

Electronic Thesis and Dissertation Repository

4-8-2022 12:00 PM

Early Solar System chronology and isotopic linkage of non-carbonaceous chondrules, clasts and achondrites

Philip M. Reger, *The University of Western Ontario*

Supervisor: Bouvier, Audrey, *The University of Western Ontario*

Co-Supervisor: Longstaffe, Frederick, *The University of Western Ontario*

A thesis submitted in partial fulfillment of the requirements for the Doctor of Philosophy degree in Geology

© Philip M. Reger 2022

Follow this and additional works at: <https://ir.lib.uwo.ca/etd>



Part of the [Cosmochemistry Commons](#)

Recommended Citation

Reger, Philip M., "Early Solar System chronology and isotopic linkage of non-carbonaceous chondrules, clasts and achondrites" (2022). *Electronic Thesis and Dissertation Repository*. 8525.
<https://ir.lib.uwo.ca/etd/8525>

This Dissertation/Thesis is brought to you for free and open access by Scholarship@Western. It has been accepted for inclusion in Electronic Thesis and Dissertation Repository by an authorized administrator of Scholarship@Western. For more information, please contact wlsadmin@uwo.ca.

Abstract

Chondrules are ubiquitous igneous spherules, the main constituents of ordinary chondrites, and are considered to be critical building blocks of planetesimals, yet their age and formation mechanism(s) remain debated. Differences between ages determined from the long-lived Pb-Pb and the short-lived ^{26}Al - ^{26}Mg chronometers have been attributed to the heterogeneous distribution of ^{26}Al in the solar nebula, a radionuclide that was responsible for early differentiation of planetesimals.

To evaluate this hypothesis, the ^{26}Al - ^{26}Mg and the ^{207}Pb - ^{206}Pb isotopic compositions were both measured by multi-collector ICP-MS in individual chondrules and igneous clasts in unequilibrated ordinary chondrites, and three achondrites. A subset of the chondrules were also analyzed by *in situ* ^{26}Al - ^{26}Mg secondary ionization mass spectrometry (SIMS), to compare with their bulk Mg model ages and Pb-Pb ages, and for ^{54}Cr isotopic anomalies. A comparison between bulk Mg model ages and Pb-Pb ages in the same chondrules suggests that the absolute ages for CAIs may be too young, and that Pb-Pb ages date precursor formation rather than time of crystallization. Precursors may have been previous generations of chondrules that were recycled by transient shock waves in the protoplanetary disk.

Chronological results of EC 002 date its crystallization at 4566 Ma which is the oldest evidence of planetary crust formation. Analysis of two angrites NWA 10463 and NWA 8535 indicate a more diverse suite of processes that shaped the evolution of the angrite parent body and differentiation of early formed planetesimals.

All together, the presented results support a homogeneous distribution of ^{26}Al in the solar nebula.

Keywords

Meteorites, chondrules, Pb-Pb chronology, Al-Mg chronology, nucleosynthetic anomalies, angrites, protoplanetary disk, Solar System

Summary for Lay Audience

This dissertation investigates the comparative chronology of the early Solar System materials using their ^{26}Al - ^{26}Mg and $^{238,235}\text{U}$ - $^{206,207}\text{Pb}$ isotopic compositions to evaluate the distribution of ^{26}Al within the protoplanetary disk. Chondrules are crystallized spherules that formed from silicate melt droplets. They are a major component of ordinary chondritic meteorites. These meteorites are sourced from tens of kilometer-sized planetary bodies formed in the early Solar System, over 4567 million years ago. Achondrite meteorites come from planetesimals that experienced wide-scale melting, with the short-lived radionuclide ^{26}Al providing an early source of radioactive heat. The distribution of ^{26}Al is a critical constraint in understanding the nebular and planetary processes that shaped the early Solar System.

The introduction (Chapter 1) presents the current state of knowledge in cosmochemistry and present the objectives of this dissertation, while Chapter 2 details the methods used to achieve those objectives.

Chapter 3 deals with chondrules that were dated using the ^{26}Al - ^{26}Mg and the Pb-Pb geochronometers and with their analyzed Cr isotope composition. The results show evidence that some chondrules formed within one million years of Solar System formation, and could be recycled by repeated heating events. Furthermore, based on ^{54}Cr isotope anomalies, chondrules were not transported between the inner and outer Solar System.

Chapter 4 highlights the chronology of the unique achondrite Erg Chech 002, whose parent asteroid experienced wide-scale melting early in its lifetime. Using ^{26}Al - ^{26}Mg and the Pb-Pb chronometry, we establish that this sample formed around 4566 million years ago, which makes it the oldest planetary crust found so far. The agreement between both chronometers is strong evidence for a homogeneous distribution of ^{26}Al in the Solar nebula.

Chapter 5 details the chronology and trace element chemistry of two angrite meteorites, NWA 8535 and NWA 10463. The angrite parent asteroid experienced full-scale melting and produced a diverse suite of rocks. The petrology, chronology and geochemistry of the

samples indicate they are unique from other angrite meteorites and that the angrite parent body may have a more complex history than previously thought.

Co-Authorship Statement

Philip Reger carried out all sample extraction, preparation, and developed the leaching and ion exchange chemistry methods for Mg and Pb and elemental analysis at Western University, and data compilation and interpretation. He carried out all Mg isotope analyses at FAU Erlangen with instruction from Dr. Marcel Regelous and Pb isotope analyses at UCA with instruction from Dr. Abdelmouhcine Gannoun, in both cases using MC-ICP-MS. Dr. Bidong Zhang and Zhiguo Guo contributed to mineral separation of the angrites NWA 8535 and NWA 10463. Philip Reger also carried out the separation of Cr isotopes at ETH Zürich as part of a Europlanet Trans-National Access supported visit and was there assisted and instructed by Dr. Précillia Morino and Katherine Murphy. Because of COVID-19-related international travel bans and laboratory closures in most parts of 2020 and 2021, absence of suitable mass spectrometric facilities set up to carry out these measurements in Canada, particular methodology or instrumentation down-time, some of the isotopic analyses had to be carried out by international collaborators. Dr. Précillia Morino carried out the analyses of the Cr isotopes. The Cr isotope composition of Pap-II was analyzed by Dr. Liping Qin at the CAS Key Laboratory in Hefei. Uranium isotope separation and analysis of Erg Chech 002 and NWA 10463 were conducted by Dr. Yvonne Roebbert and Dr. Stefan Weyer at the University of Hannover. Dr. Audrey Bouvier initially planned the project, conducted imaging of some samples using SEM and EPMA, while providing guidance during this thesis.

The Cameca ims 1280 HR2 ion probe for SIMS analysis of chondrules was set up and operated by Dr. Johan Villeneuve and Maxime Piralla at CRPG Nancy. Philip Reger and Dr. Audrey Bouvier prepared the images, selected the sampling sites of the chondrules, and attended the analytical sessions, also supported by the Europlanet program. Dr. Steven Simon imaged some chondrules and analyzed their composition by EPMA at the University of New Mexico, and has contributed to the interpretation of that data.

The O isotope composition of the Pap-II inclusion by laser-assisted infrared mass spectrometry was analyzed by Jennifer Gibson and Dr. Richard Greenwood at the Open University. Last but not least, iodine-xenon isotope analysis of Pap-II was carried out by Dr. Sarah Crowther at the University of Manchester.

A version of Chapter 3 is planned to be submitted to *Geochimica et Cosmochimica Acta*, while a short-form manuscript detailing the results from the Pap-II inclusion is in preparation to be submitted to *Nature Communications*.

A version of Chapter 4 is in preparation to be submitted to *Geochimica et Cosmochimica Acta*.

A version of Chapter 5 will be submitted to *Meteoritics & Planetary Science*.

Acknowledgments

I am deeply grateful to my supervisor Dr. Audrey Bouvier for giving me the opportunity to pursue a Ph.D. at Western, and for the support, training and patience that I have received throughout my time here. I also immensely appreciate the fantastic opportunities to attend conferences and meetings she provided me with. I am also grateful for Dr. Frederick Longstaffe for his supervision and support over the last couple of years, and for Dr. Shantanu Basu for serving on my supervisory committee.

I would also like to thank Dr. Elizabeth Webb and Dr. Patricia Corcoran for management of the GEOMETRIC clean lab from 2019 onwards, Dr. Anthony Withers, Dr. Philip McCausland and Dr. Roberta Flemming for access, instruction and assistance with their tools in BGS 1009. Marc Beauchamp and Dr. Bob Linnen are much appreciated for their assistance with the electron microprobe and benchtop SEM, respectively.

I appreciate the time and patience invested by Dr. Bastian Georg (formerly Trent University), Dr. Marcel Regelous (Friedrich Alexander Universität) and Dr. Abdelmouhcine Gannoun (Université Clermont-Auvergne) by helping me obtain my data on the Neptune multi-collector ICP-MS instruments, and Prof. Dr. Maud Boyet (Université Clermont-Auvergne) who also welcomed me regularly over four years; Dr. Johan Villeneuve and Maxime Piralla at CRPG Nancy for their assistance and operation of the SIMS; Dr. Steven Simon (University of New Mexico) and Rebecca Matthäus (Universität Bayreuth) for providing me with SEM images and EPMA analyses of my samples; Jennifer Gibson and Dr. Richard Greenwood (The Open University) for the O isotope analysis of the Paposo 004 inclusion, and Dr. Liping Qin (CAS Key Laboratory Hefei) for the Cr analysis of the same inclusion. I would also like to thank Dr. Yvonne Roebbert and Prof. Dr. Stefan Weyer at the University of Hannover for their analysis of U isotopes on a couple of samples. I would like to thank Dr. Christopher Herd at the University of Alberta for the loan of NWA 8276, and Dr. Carl Agee at the University of New Mexico for the loan of a different piece of the same meteorite, as well as for providing the two angrites NWA 8535 and NWA 10463. The Paposo 004 meteorite sample was generously donated by Rodrigo Martínez at the Museo del Meteorito in Chile, as was Erg Chech 002 from Ben Hoefnagels at Big Bang Meteorites, for which I am very grateful.

At ETH Zürich, I would like to particularly thank Dr. Précillia Morino for her organization, instruction and support revolving around my lab visit in the summer 2021, as well as Romain Alosius, Katherine Murphy and Dr. Mirjam Rüfenacht for their help in this project, and everybody else from the isotope group that welcomed me (back) so warmly. My deepest gratitude goes out to Dr. Alison Hunt and Dr. Maria Schönbacher. Without their continued support I would not be where I am now.

I would like to thank the other members of the GEOMETRIC lab with whom I crossed paths during my time at Western, Yang Shen, Matt Maloney, Peter Christoffersen, Annika van Kessel, Zhiguo Guo, Congxi Zhu, Mary Spencer, Dr. Paul Frossard, and in particular Dr. Bidong Zhang, whose efforts with the Pb chemistry prior to my arrival made my life in the lab immensely easier.

Finally, I would like to thank my family in Switzerland for all their support and everything they've done over the years; my family in Canada who had to put up with me over the last four years and convincingly pretended to enjoy my presence; my friends in Zürich for always being enthusiastic to see me again, even if only for a short time. My time in London would have been a lot less interesting and fun without my roommates of four years, who still don't exactly know what this thesis is about, the Trivia Gang, the London Area Angels baseball team, the 3rd Rocks Earth Sciences softball team, and all the friends and connections I've made during my time in London and at Western. And lastly, to Carolina: thank you for your love and support.

Table of Contents

Abstract.....	ii
Summary for Lay Audience.....	iii
Co-Authorship Statement.....	v
Acknowledgments.....	vii
Table of Contents.....	ix
List of Tables.....	xi
List of Figures.....	xiii
List of Appendices.....	xxi
1 Introduction.....	1
1.1 General Purpose.....	1
1.2 Formation of planetary systems.....	1
1.3 Chondritic Meteorites and their components.....	3
1.4 The isotopic dichotomy of the Solar System.....	6
1.5 Chondrule formation.....	8
1.6 Early Solar System chronology.....	10
1.6.1 The U-corrected Pb-Pb chronometer.....	11
1.6.2 The ^{26}Al - ^{26}Mg chronometer and distribution of ^{26}Al in the protoplanetary disk.....	15
1.7 Presentation of the next chapters.....	20
2 Methods.....	22
2.1 Sample selection.....	22
2.2 Extraction.....	22
2.3 Laboratory procedures.....	24
2.4 Sample digestion.....	24
2.5 Sample leaching for Pb analysis.....	24
2.6 Ion-exchange chromatography.....	26
2.6.1 Magnesium separation.....	26
2.6.2 Lead separation.....	28
2.6.3 Chromium.....	29
2.7 Sample analysis.....	32
2.7.1 Petrographic description.....	32
2.7.2 Mass spectrometry.....	32
3 Chronology and Cr isotope composition of chondrules and clasts in ordinary chondrites.....	42
3.1 Methods.....	43
3.2 Results.....	44
3.2.1 Petrology of chondrules and clasts.....	44
3.2.2 Bulk chemical, O isotope and I-Xe data for Pap-II.....	53
3.2.3 Bulk Mg isotope compositions and $^{27}\text{Al}/^{24}\text{Mg}$ ratios of chondrules and igneous clasts.....	55
3.2.4 <i>In situ</i> Mg isotope analyses of chondrules.....	57
3.2.5 Pb-Pb ages of chondrules.....	58
3.2.6 Cr results.....	66
3.3 Discussion.....	76

3.3.1	Comparison of $\delta^{26}\text{Mg}^*$ and ^{26}Al - ^{26}Mg model ages to other chondrule studies	76
3.3.2	Formation history of Pap-II	78
3.3.3	Pb-Pb age of QC 001-C1	80
3.3.4	Combined Al-Mg and U-Pb systematics of chondrules	81
3.3.5	Change in Cr isotope composition over time?	88
3.3.6	Implications for chondrule formation	91
4	The chronology of unique achondrite Erg Chech 002	94
4.1	Methods	96
4.2	Results	97
4.2.1	Al-Mg systematics	97
4.2.2	Uranium isotope composition	98
4.2.3	Lead isotope systematics	98
4.3	Discussion	103
4.3.1	Lead isotope systematics	103
4.3.2	Uranium-corrected Pb-Pb age of Erg Chech 002	104
4.3.3	^{26}Al - ^{26}Mg systematics	106
4.3.4	Combined ^{26}Al - ^{26}Mg and Pb-Pb chronology and EC 002 as a potential time anchor	111
5	Chronology and provenance of angrites	119
5.1	Samples and Methods	120
5.1.1	Northwest Africa 10483	120
5.1.2	Northwest Africa 8535	121
5.1.3	Methods	122
5.2	Results	122
5.2.1	Bulk and mineral REE abundances	122
5.2.2	Magnesium isotope compositions and Al/Mg ratios of achondrite fractions	123
5.2.3	U isotope composition of NWA 10463	124
5.2.4	Pb-Pb chronology of NWA 10463	125
5.3	Discussion	128
5.3.1	U-corrected Pb-Pb age of NWA 10463	128
5.3.2	Mg isotope compositions of olivine in NWA 10463 and NWA 8535	128
5.3.3	^{26}Mg excesses in NWA 10463 plagioclase: analytical artefact?	129
5.3.4	Genetic heritage of NWA 8535 and NWA 10463	130
6	Conclusions	136
6.1	Summary of Chapter 3	136
6.2	Summary of Chapter 4	138
6.3	Summary of Chapter 5	138
6.4	The wider context	139
6.5	Future work	140
	References	141
	Appendices	162
	Curriculum Vitae	173

List of Tables

Table 1: Overview of samples analyzed for their Pb, Mg and Cr isotope composition, as well as the <i>in situ</i> ^{26}Al - ^{26}Mg systematics determined by secondary ionization mass spectrometry (SIMS).....	23
Table 2: Leaching protocol for Pb analysis, following the procedure outlined in Bouvier and Wadhwa (2010).....	25
Table 3: Three-stage Mg separation scheme based on Wombacher et al. (2009), using Biorad® plastic columns and AG50W-X8 (200-400 mesh) cation exchange resin.	27
Table 4: Protocol for Pb separation chemistry, using PTFE columns and AG1-X8 (200-400 mesh) anion exchange resin, following the methods described by Bouvier and Wadhwa (2010).....	28
Table 5: Overview of Cr separation procedure using ion-exchange chromatography.	31
Table 6: Overview of cup configurations used for Pb isotope analysis between Faraday cup (FC) and Secondary Electron Multiplier (SEM) setups.	35
Table 7: Weighted average U isotope compositions of EC 002 bulk and pyroxene samples, NWA 10463 bulk leachates, and of BCR-2 terrestrial basalt standard and secondary standard IRMM 184.....	37
Table 8: Al-Mg isotope data of solution standards Cambridge-1 and the in-house Mg solution standard (“UWO ICP Std”), and terrestrial rock standard San Carlos olivine and bulk CV3 chondrite Allende.	38
Table 9: Faraday cup configuration for Cr isotope analysis by MC-ICP-MS.	40
Table 10: Average $\epsilon^{54}\text{Cr}$ composition of the DTS-2b dunite standard, measured over four sessions and compared to literature values (Schiller et al., 2014)	41
Table 11: Overview of host meteorites of chondrules and clasts.	44
Table 12: Chondrule type and Al-Mg data for analyzed chondrules, with $^{27}\text{Al}/^{24}\text{Mg}$ ratios, mass-dependent Mg isotope anomalies and mass-independent $\delta^{26}\text{Mg}^*$ listed.	68
Table 13: Overview over isochron data from SIMS analysis of chondrules. Gl: indicates glassy mesostasis or plagioclase analyses.....	69
Table 14: Overview of bulk Al-Mg data, bulk Mg model ages, <i>in situ</i> ^{26}Al - ^{26}Mg ages, Pb-Pb ages as well as the Cr isotope composition ($\epsilon^{54}\text{Cr}$).	70
Table 15: Pb isotope data for two igneous clasts Pap-I1 and NWA 12261-I1	72

Table 16: Pb isotope data for analyzed chondrules.	73
Table 17: Al-Mg data for EC 002 fractions.	98
Table 18: Mass, Pb and U elemental data, and Pb isotope data for EC 002 and full session Pb isotope data for standards NBS 981 and NBS 983.	102
Table 19: Weighted average U isotope compositions of EC 002 bulk and pyroxene samples and of BCR-2 terrestrial basalt standard.	102
Table 20: Summary of Pb-Pb ages, initial $^{26}\text{Al}/^{27}\text{Al}$ ratios and anchored Al-Mg ages for EC 002 and eight other achondrites.	118
Table 21: Rare-earth element concentrations in bulk and mineral fractions of NWA 10463 and NWA 8535. All concentrations are listed in ppm. n.m.: no measurement. ..	122
Table 22: Al-Mg data for NWA 8535 and NWA 10463 fractions.	123
Table 23: Pb isotope compositions of pyroxene and bulk leachates and residues of NWA 10463 angrite.	127

List of Figures

Figure 1: a) Scan of a slab of L3 chondrite NWA 10854, with chondrule C1 marked in red. b) extracted chondrule NWA 10854-C1 from its slab. c) BSE image of a different chondrule, showing a barred olivine texture on the right side, while the left part has a porphyritic texture. A fine-grained feldspathic mesostasis pocket lies in the middle (Source: Steve Simon, UNM).....	4
Figure 2: Overview of the dichotomy between NC and CC meteorites, potentially separated by a growing Jupiter, around 1 Ma after CAI formation (after Brennecka et al. (2020) and Kruijer et al. (2020))......	7
Figure 3: $\epsilon^{54}\text{Cr}$ - $\epsilon^{50}\text{Ti}$ plot of chondrules in NC meteorites (red) and CC meteorites (blue), with data reported by Gerber et al. (2017) and Schneider et al. (2020).....	8
Figure 4: Inverse Pb-Pb diagram (left) and standard Pb-Pb diagram (right) of pyroxene separates (leachates and residues) from the ungrouped achondrite NWA 6704. The radiogenic $^{207}\text{Pb}^*/^{206}\text{Pb}^*$ ratio is determined by the intercept of the y-axis and the slope, respectively.	13
Figure 5: Qualitative illustration of the three Pb components that make up the Pb isotope composition of a sample, and how three-component mixtures in samples can affect isochrons. The true age, calculated from the pure radiogenic Pb isotope composition, is estimated by Pb-Pb isochrons defined by samples that are binary mixtures, i.e., they are either free of modern terrestrial Pb (black ellipses) or initial Pb (orange ellipses). If samples are not binary mixtures and their Pb isotope composition is made a combination of all three Pb components, they will plot within the triangle defined by the three Pb components (red ellipses). The samples may not plot on a line, but in cases where they do, they would produce a linear array that is rotated and results in a spuriously high $^{207}\text{Pb}/^{206}\text{Pb}$ ratio representing radiogenic Pb (red line), leading to an older age than the true age of the sample.	15
Figure 6: Internal isochron of the AJEF Type B CAI analyzed by Jacobsen et al. (2008) in a $^{27}\text{Al}/^{24}\text{Mg}$ vs. $\delta^{26}\text{Mg}^*$ diagram. The slope of the trendline represents the initial $^{27}\text{Al}/^{24}\text{Mg}$ ratio of $(4.97 \pm 0.24) \times 10^{-5}$ while the y-axis intercept is equal to the initial	

$\delta^{26}\text{Mg}^*$ of -0.018 ± 0.056 ‰. Error bars for the y-axis are within the markers where not visible.....	17
Figure 7: Secondary electron microscope (SEM) image of two sample spots in plagioclase (bottom) and pyroxene (top) in NWA 12261-I1 after SIMS analysis.	33
Figure 8: Individual analyses of $^{206}\text{Pb}/^{204}\text{Pb}$ ratios of the secondary standard NBS 983 over all sessions, using both the Faraday cup and SEM setup, compared to the accepted value of 2695.4 ± 145.3 (Catanzaro et al., 1968). The concentration of the NBS997 Tl standard is 1 ppb for 0.5 ppb and 1 ppb NBS 983 measurements, and 2 ppb for measurements with 5 ppb NBS 983. Using the SEM setup, NBS 983 was 0.25 ppb and NBS 997 1 ppb. Uncertainties on individual analyses are smaller than their symbol, where not visible.	36
Figure 9: Linearized (Eq. 8) Mg isotope composition of terrestrial rock standards, with a best-fit line whose slope represents the fractionation factor $\beta = 0.521$	40
Figure 10: Image of the L3.2 chondrite Paposo 004, with the Pap-I1 inclusion marked.	43
Figure 10: a chip of NWA 8001-C1 with a barred olivine texture on the right and a porphyritic texture on the left side of the chondrule. A large mesostasis pocket is located in between the two different textures.....	45
Figure 11: BSE image of a chip of chondrule NWA 8276-C1, courtesy of Dr. Steven Simon, UNM.....	45
Figure 12: Energy-dispersed spectrum (EDS) image of a chip of NWA 8276-C2.	46
Figure 13: Energy-dispersed spectrum (EDS) image of a chip of chondrule NWA 8276-C3.....	47
Figure 14: BSE image of a chip of chondrule NWA 10854-C1, courtesy of Dr. Steven Simon, UNM.....	48
Figure 15: BSE image of chondrule C2 from NWA 10854, courtesy of Dr. Steven Simon, UNM.	48
Figure 16: Secondary electron microscope image of NWA 10854-C3. Re-crystallized plagioclase is labelled in red, low-Ca pyroxene in yellow and olivine in blue.	49
Figure 17: Backscatter electron (BSE) image of a chip of chondrule NWA 10854-C5... ..	50
Figure 18: Energy-dispersed spectrum (EDS) image of a chip of chondrule NWA 10854-C6.....	50

Figure 19: Secondary electron microscope image of NWA 11672-C1. Re-crystallized plagioclase is labelled in yellow. Olivine and pyroxene are not visually distinguishable. 51

Figure 20: Backscatter electron image of an igneous clast in H3 chondrite NWA 12261, with olivine and pyroxene grains, and quenched mesostasis (glass) in between them. 52

Figure 21: a) Backscatter electron image of the Paposo 004 inclusion Pap-I1, showing the microporphyritic texture with larger Mg-rich olivine phenocrysts ($Fa_{14.5 \pm 2.3}$; white) and more ferrous olivine groundmass ($Fa_{29.4 \pm 6.8}$; orange). Courtesy of Dr. Steven Simon, UNM. b) Electron microprobe image (at UWO) of a relict barred olivine chondrule containing low-Ca pyroxene ($Fs_{22.1 \pm 4.9}Wo_{1.5 \pm 1.3}$) embedded within the inclusion. 53

Figure 22: (a) Lithophile element abundances of Pap-I1 normalized to both CI and L chondrites (Lodders and Fegley, 1998; Barrat et al., 2012), plotted with increasing volatility. Bulk Pap-I1 shows no significant fractionation and is of the *Unfr* chemical type (Ruzicka et al., 2019); (b) No significant fractionation of REE relative to CI and L chondrites is visible for bulk Pap-I1. Error bars are within data points where not visible. 54

Figure 23: Oxygen isotope composition of Pap-I1, plotted against literature data for ordinary chondrites (Clayton et al., 1991). Uncertainties are 2SE 55

Figure 24: Overview of $\delta^{26}Mg^*$ vs. $^{27}Al/^{24}Mg$ of chondrules analyzed. Chondrules from CCs are in blue, chondrules from OCs are in red. Reference lines are isochrons representing formation times of 0 Ma and 1 Ma after CAI formation, based on the canonical $^{26}Al/^{27}Al$ of 5.23×10^{-5} (Jacobsen et al., 2008), Solar System initial $\delta^{26}Mg^*$ of -0.0340 ± 0.0016 ‰ (Schiller et al., 2010) and solar $^{27}Al/^{24}Mg$ ratio of 0.101 (Larsen et al., 2011). 57

Figure 25: Inverse Pb-Pb isochron of NWA 10854-C1 chondrule, with the compositions of primordial Pb, as represented by the the Nantan troilite (Blichert-Toft et al., 2010), and modern terrestrial Pb (Stacey and Kramers, 1975) plotted for reference. The icons of data points are larger than the uncertainties, for clarity. 59

Figure 26: Inverse Pb-Pb isochron of NWA 10854-C3, with the compositions of primordial Pb, as represented by the the Nantan troilite (Blichert-Toft et al., 2010), and modern terrestrial Pb (Stacey and Kramers, 1975) plotted for reference. The icons of data points are larger, with the exception of R, than the uncertainties, for clarity. 60

Figure 27: Inverse Pb-Pb isochron of NWA 10854-C5, with the compositions of primordial Pb, as represented by the the Nantan troilite (Blichert-Toft et al., 2010), and modern terrestrial Pb (Stacey and Kramers, 1975) plotted for reference. The icons of data points are larger than the uncertainties, for clarity. 61

Figure 28: Inverse Pb-Pb isochron of NWA 10854-C6, with the compositions of primordial Pb, as represented by the the Nantan troilite (Blichert-Toft et al., 2010), and modern terrestrial Pb (Stacey and Kramers, 1975) plotted for reference. The icons of data points are larger than the uncertainties, for clarity. 62

Figure 29: Inverse Pb-Pb isochron of chondrule NWA 8007-C1, with the compositions of primordial Pb, as represented by the the Nantan troilite (Blichert-Toft et al., 2010), and modern terrestrial Pb (Stacey and Kramers, 1975) plotted for reference. The icons of data points are larger than the uncertainties, for clarity. 63

Figure 30: Inverse Pb-Pb isochron of NWA 8276-C1, with the compositions of primordial Pb, as represented by the the Nantan troilite (Blichert-Toft et al., 2010), and modern terrestrial Pb (Stacey and Kramers, 1975) plotted for reference. The icons of data points are larger than the uncertainties, for clarity. 64

Figure 31: Inverse Pb-Pb isochron of Pap-II, with data from both analyzed fractions and the compositions of primordial Pb, as represented by the the Nantan troilite (Blichert-Toft et al., 2010), and modern terrestrial Pb (Stacey and Kramers, 1975) plotted for reference. The icons of data points are larger than the uncertainties, for clarity..... 65

Figure 32: Inverse Pb-Pb isochron of chondrule C1 from the CB_a chondrite QC 001, with the compositions of primordial Pb, as represented by the Nantan troilite (Blichert-Toft et al., 2010), and modern terrestrial Pb (Stacey and Kramers, 1975) plotted for reference. Additionally, a regression line through the data points that were not included that plots through the Nantan troilite is added. The icons of data points are larger than the uncertainties, for clarity. 66

Figure 33: Chromium isotope compositions of analyzed chondrules, compared with literature values of individual chondrules from the L3.4 ordinary chondrite Ragland (Schneider et al., 2020), H, L and LL chondrites (Trinquier et al., 2007; Qin et al., 2010; Bischoff et al., 2019), as well as CB chondrites (Yamashita et al., 2010). Uncertainties in individual chondrule data are within their marker if not visible..... 67

Figure 34: $^{27}\text{Al}/^{24}\text{Mg}$ vs. $\delta^{26}\text{Mg}^*$ diagram, with analyzed individual OC chondrules (red circles) and CC chondrules (dark blue circles) compared to literature data of Allende (CV3) chondrules (grey diamonds; Bizzarro et al., 2004), CM2 chondrules (grey squares; Bouvier et al., 2013), CV chondrules (grey crosses; Olsen et al., 2016) and CV chondrules (grey triangles; Chen et al., 2018). As references, isochrons representing formation times of 0 Ma, 1 Ma and 2 Ma after CAI formation, based on the canonical $^{26}\text{Al}/^{27}\text{Al}$ of 5.23×10^{-5} (Jacobsen et al., 2008), Solar System initial $\delta^{26}\text{Mg}^*$ of -0.0340 ± 0.0016 ‰ (Schiller et al., 2010) and solar $^{27}\text{Al}/^{24}\text{Mg}$ ratio of 0.101 (Larsen et al., 2011), are also plotted. 76

Figure 35: ^{26}Al - ^{26}Mg model ages and initial $^{26}\text{Al}/^{27}\text{Al}$ ratios of chondrules, based on their bulk $\delta^{26}\text{Mg}^*$ and $^{27}\text{Al}/^{24}\text{Mg}$ ratios, relative to the canonical initial $^{26}\text{Al}/^{27}\text{Al}$ of 5.23×10^{-5} (Jacobsen et al., 2008) and Solar System initial $\delta^{26}\text{Mg}^*$ of -0.0340 ± 0.0016 ‰ (Schiller et al., 2010). 77

Figure 36: Back-calculated $^{26}\text{Al}/^{27}\text{Al}$ ratios ($=[^{26}\text{Al}/^{27}\text{Al}]_0$) and Pb-Pb ages of chondrules, with the canonical $^{26}\text{Al}/^{27}\text{Al}$ of 5.23×10^{-5} (Jacobsen et al., 2008) added as a reference line. The empty orange symbol is NWA 8007-C1, with its large uncertainties. 83

Figure 37: Comparison of Pb-Pb ages with bulk Mg model ages of chondrules between this study (top) and chondrules from the L3.10 chondrite NWA 5697 Bollard et al. (2019, bottom). Ages are relative to the absolute age of CAIs at 4567.30 ± 0.16 Ma (Connelly et al., 2012). 85

Figure 38: Overview of $^{204}\text{Pb}/^{206}\text{Pb}$ vs $^{208}\text{Pb}/^{206}\text{Pb}$ diagrams of 8 chondrules with statistically significant isochrons, with the Nantan troilite (NT; Blichert-Toft et al., 2010) and modern terrestrial (MT; Stacey and Kramers, 1975) compositions plotted for reference. 86

Figure 39: Diagrams of $\epsilon^{54}\text{Cr}$ of OC chondrules plotted against their a) $\delta^{26}\text{Mg}^*$ values, b) Pb-Pb ages, c) bulk Mg model ages, and d) in situ ^{26}Al - ^{26}Mg ages. Included are data of two chondrules from L3.10 chondrite NWA 5697 (Connelly et al., 2012; Bollard et al., 2019). 89

Figure 40: $\epsilon^{54}\text{Cr}$ plotted against bulk Mg model ages for OC chondrules. 90

Figure 41: Secondary electron microscope image of Erg Chech 002. Large pyroxene megacrysts are visible, surrounded by groundmass of sodic plagioclase, pigeonite and accessory chromite, merrillite and silica polymorphs..... 96

Figure 42: Internal ^{26}Al - ^{26}Mg isochrons defined by a) pyroxene, bulk rock, fine-grained and plagioclase fractions, corresponding to a $^{26}\text{Al}/^{27}\text{Al}$ ratio of $(8.89 \pm 0.79) \times 10^{-6}$ and a formation age of 1.71 ± 0.12 Ma after CAI formation, based on the canonical $^{26}\text{Al}/^{27}\text{Al}$ abundance (Jacobsen et al., 2008); and b) Uncertainties are 2SE errors on $\delta^{26}\text{Mg}^*$ measurements and $\pm 5\%$ on $^{27}\text{Al}/^{24}\text{Mg}$ ratios. 99

Figure 43: Internal ^{26}Al - ^{26}Mg isochrons defined by only plagioclase fractions, corresponding to an initial $^{26}\text{Al}/^{27}\text{Al}$ ratio $(8.36 \pm 0.49) \times 10^{-6}$ and a formation age of 1.77 ± 0.08 Ma after CAI formation, based on the canonical $^{26}\text{Al}/^{27}\text{Al}$ abundance (Jacobsen et al., 2008). Uncertainties are 2SE errors on $\delta^{26}\text{Mg}^*$ measurements and $\pm 5\%$ on $^{27}\text{Al}/^{24}\text{Mg}$ ratios..... 101

Figure 44: Regression line through all analyzed Pb fractions. Also plotted are data points for the Nantan troilite, representing the primordial Pb composition of the Solar System, and the Stacey and Kramers (1975) data point representing the terrestrial Pb composition. Symbols of data points have been enlarged for clarity, larger than their uncertainties. . 103

Figure 45: Inverse Pb-Pb isochron diagram for Erg Chech 002. The uncertainty on W4 is smaller than the ellipse, as it is enlarged for clarity. The inset shows the highly radiogenic leachate W8 and residue. Leachate W7 would plot along the regression line in negative $^{204}\text{Pb}/^{206}\text{Pb}$ vs. $^{207}\text{Pb}/^{206}\text{Pb}$ space. 104

Figure 46: $\delta^{26}\text{Mg}^*$ evolution diagram of EC 002 and the bulk Solar System, calculated with the canonical $^{26}\text{Al}/^{27}\text{Al}$ ratio of 5.23×10^{-5} , a chondritic $^{27}\text{Al}/^{24}\text{Mg}$ ratio of 0.101 and a subcanonical initial Solar System $\delta^{26}\text{Mg}^*$ value of -0.128 (Wasserburg et al., 2012; MacPherson et al., 2017; see text). 108

Figure 47: $\delta^{26}\text{Mg}^*$ evolution diagram of EC 002 and the bulk Solar System, calculated with the canonical $^{26}\text{Al}/^{27}\text{Al}$ ratio of 5.23×10^{-5} , a chondritic $^{27}\text{Al}/^{24}\text{Mg}$ ratio of 0.101 and a canonical initial $\delta^{26}\text{Mg}^*$ value of -0.034 (Jacobsen et al., 2008; Schiller et al., 2010b). 110

Figure 48: Comparison between absolute Pb-Pb ages of seven achondrites and their ^{26}Al - ^{26}Mg ages anchored to EC 002 (Pb-Pb age: 4565.87 ± 0.28 , initial $^{26}\text{Al}/^{27}\text{Al}$: (8.89 ± 0.87)

$\times 10^{-6}$). For clarity, the error bars of the Pb-Pb age of NWA 7325 (4563.4 ± 2.6 Ma; Koefoed et al., 2016) are not visible in their entirety. Literature data have been used for Pb-Pb ages and ^{26}Al - ^{26}Mg ages of the angrites Sahara 99555 (Al-Mg: Spivak-Birndorf et al., 2009; Schiller et al., 2015; U-corrected Pb-Pb ages: Amelin et al., 2008b; Tissot et al., 2017), NWA 1670 (Schiller et al., 2015), D’Orbigny (Spivak-Birndorf et al., 2009; Schiller et al., 2015; Amelin et al., 2008a; Tissot et al., 2017), Asuka 881394 (Wadhwa et al., 2009; Wimpenny et al., 2019), NWA 6704 (Amelin et al., 2019; Sanborn et al., 2019), NWA 7325 (Koefoed et al., 2016) and NWA 2976 (Schiller et al., 2010b; Bouvier et al., 2011a)..... 112

Figure 49: False-color EDS image of NWA 10463, with Al-Ti-bearing pyroxene (fassaite) in yellow, olivine in green, plagioclase in orange-brown and Cr-spinel in red. Accessory mineral phases include kirschsteinite, ilmenite, troilite and tsangpoite (Ca-phosphate)..... 120

Figure 50: Image of NWA 8535 under cross-polarized light, from Santos (2016). This particular thin section is made up of ~ 96% olivine and 3% spinel, with accessory metal, sulfides, pyroxene and phosphates..... 121

Figure 51: Al-Mg data of NWA 10463 and NWA 8535 fractions. Uncertainties in $^{27}\text{Al}/^{24}\text{Mg}$ ratios are $\pm 5\%$, and are within symbols where not visible. The regression line through PL3 and PL4 has a slope that corresponds to an initial $^{26}\text{Al}/^{27}\text{Al}$ ratio of $\sim 5.4 \times 10^{-7}$, in the range of the volcanic angrites. 124

Figure 52: Pb-Pb isochron of Px fractions of NWA 10463 angrite..... 125

Figure 53: Pb-Pb isochron of pyroxene and bulk fractions of NWA 10463 angrite. 126

Figure 54: Comparison of U-corrected Pb-Pb ages of angrites, showing the age clusters of the volcanic angrites at ~4560 Ma, the plutonic angrites at ~4556-4557 Ma, and also the “intermediate” group of angrites at ~ 4560 Ma. Error bars are within the symbols if not visible, and include uncertainties of the U isotope compositions. Black diamonds are literature data from Tissot et al. (2017), black circles from Brennecka and Wadhwa (2012)..... 131

Figure 55: Bulk REE patterns for NWA 10463, NWA 2999, and the volcanic and plutonic angrites, represented by D’Orbigny and Angra dos Reis, respectively. R+ 2012: Riches et al. (2012). S&W 2021: Sanborn and Wadhwa (2021). 133

Figure 56: Olivine REE patterns for NWA 8535 and NWA 10463 compared to NWA 2999, volcanic angrite Sahara 99555 and plutonic angrite LEW 86010. F+ 2003: Floss et al. (2003). S&W 2021: Sanborn and Wadhwa (2021)..... 134

Figure 57: REE patterns in clinopyroxene of the angrites NWA 10463, NWA 2999, as well as volcanic angrite Sahara 99555 and plutonic angrite LEW 86010. ‘h’ and ‘l’ denote measurements with higher (filled symbols) or lower (empty symbols) REE concentration. Ytterbium and Lu measurements were reported as “below detection limit.” F+ 2003: Floss et al. (2003). S&W 2021: Sanborn and Wadhwa (2021)..... 135

List of Appendices

Appendix 1: SIMS data points of chondrules and clasts	162
Appendix 2: NWA 8276-C1 EPMA data from UNM [in wt%]	165
Appendix 3: NWA 10854-C1 EPMA data from UNM [in wt%]	166
Appendix 4: NWA 10854-C3 EPMA data from BGI [in wt%].....	166
Appendix 5: NWA 10854-C5 EPMA data from BGI [in wt%].....	168
Appendix 6: NWA 11672-C1 EPMA data from BGI [in wt%].....	169
Appendix 7: Pap-I1 EPMA Data from UWO [in wt%]: Olivine.....	170
Appendix 8: Pap-I1 EPMA Data from UWO [in wt%]: Pyroxene (relict chondrule)....	171
Appendix 9: Pap-I1 EPMA Data from UWO [in wt%]: Glassy mesostatis	171

1 Introduction

1.1 General Purpose

The study of early Solar System materials allows us to infer how its planets formed and evolved, as a complement to astronomical observations and astrophysical modelling. The discovery of thousands of exoplanets over the last two decades and the advent of astronomical observations of protoplanetary disks around young stars has fundamentally changed our understanding of the architecture of planetary systems and challenged preconceptions of how our own Solar System formed. Meteorites, and samples returned from a handful of space missions, are the only materials available to us that record the processes that took place at the beginning of our Solar System. The meteoritic record has been a key to not only unlocking answers about the early history of the Solar System (e.g., the age of the Solar System at 4.567 billion years) but has also provided important constraints on planetary formation models.

1.2 Formation of planetary systems

Stars form by gravitational collapse of denser, colder regions of molecular clouds. The process of star formation can be divided into four classes, based on astronomical observations of young stellar objects: *Class 0* objects are characterized by the core of the protostar being enveloped in a dense accretion disk, with bipolar outflows and periodic outbursts ejecting mass and removing angular momentum from rotating accretion disk. This is the early main accretion phase. In *Class I* objects, protostars are in the late accretion phase, with diminishing density of the accretion disk and strength of the bipolar outflows. *Class II* objects, also referred to as classical T Tauri stars, continue to exhibit bipolar outflows, but also strong stellar winds. They are surrounded by a protoplanetary disk initially made up primarily of gas with about 1% of dust (by mass) (Williams and Cieza, 2011), but are not embedded in their parent molecular cloud material anymore. Finally, in *Class III* objects, the gaseous protoplanetary disk has dissipated and made way for a debris disk, rocky bodies (McSween Jr and Huss, 2010). The duration of these four stages increases by roughly one order of magnitude per stage: *Class 0* stage lasts on the order of 10^4 years, *Class I* on the order of 10^5 years. Protoplanetary disk lifetimes, the

Class II stage, last from less than 1 Myr in high-mass stars, up to 10 Myr in lower-mass stars, with median timescales around 3 Myr (Williams and Cieza, 2011). In the case of our Solar System, it is still unclear how particularly *Class 0* and *Class I* stages relate to chronological data from meteorites. The dissipation of the gas in the protoplanetary disk, thus concluding the *Class II* stage, has been estimated to have occurred around 4 to 5 Ma after the first solids formed in the Solar System (Bollard et al., 2015; Wang et al., 2017; Weiss et al., 2017), while the debris disk around the Sun has been estimated to have lasted for about 40-50 Myr (Gilmour and Filtner, 2019).

Observations of ringed substructures in protoplanetary disks around young stellar objects imply that the building blocks of planets and planetesimals formed early, during the *Class II* stage, but that dust-grain growth may have begun even earlier during the *Class I* stage (e.g., Andrews, 2020; Segura-Cox et al., 2020). Cosmochemical evidence via the short-lived ^{182}Hf - ^{182}W chronometer has similarly indicated that the parent bodies of iron meteorites accreted within the first 1 Myr of the Solar System (Kruijer et al., 2014; Spitzer et al., 2021) and that Mars may have grown to ca. 90% of its current mass within the first 4 Myr (Dauphas and Pourmand, 2011). Such rapid accretion timescales of planetesimals and planetary embryos require a mechanism for dust grains to grow quickly and efficiently. The pebble accretion growth model suggests that initially, coagulation and growth of sub-micron-sized dust grains to mm- to cm-sized “pebbles” occurs, but is limited by bouncing, fragmentation and drift barriers (Johansen and Lambrechts, 2017). These barriers can be overcome through locally concentrated pebble zones (i.e., higher dust-to-gas ratios) induced by pressure bumps, vortex trapping or more likely the streaming instability (with a combination of the former two), leading to gravitational collapse that can form planetesimals on the order of hundreds of kilometers (Birnstiel et al., 2016; Liu et al., 2019). These planetesimals then grow due to collisions between them (planetesimal accretion), before pebble accretion becomes the dominant mechanism of planetary bodies at the size of Ceres or Mars which eventually leads to runaway gas accretion and the formation of gas and ice giants (Johansen and Lambrechts, 2017). The formation of the terrestrial planets on the other hand may have been restricted to planetesimal accretion (Izidoro et al., 2021), or could be explained by pebble accretion

outside of Mars' current orbit and subsequent inward migration (Johansen et al., 2021) for them to escape runaway accretion.

1.3 Chondritic Meteorites and their components

Meteorites are pieces of planetary bodies that were ejected from their parent body and were subsequently found on Earth. Commonly, meteorites are primarily classified by the presence or absence of chondrules, μm - to mm-sized igneous spherules, into chondrites or achondrites, respectively. Meteorites classified as chondrites are considered to be the most primitive meteorites, as they have not undergone any full-scale melting or differentiation. Chondrites are divided into the carbonaceous chondrite (CC), ordinary chondrite (OC), enstatite chondrite (EC), Rumuruti-like chondrite classes (R) and into the Kakangari-like chondrite grouplet (K) where they may be further divided into groups according to various chemical or petrologic properties (Weisberg et al., 2006). The carbonaceous chondrites of the Ivuna (CI) group are thought to generally reflect solar abundances in their composition (e.g. Anders and Grevesse, 1989).

Key components of most chondrite groups are refractory inclusions, which include Ca-Al-rich inclusions (CAIs) and amoeboid olivine aggregates (AOAs), chondrules and matrix. Most AOAs and some CAIs show fine-grained textures and are thought to have condensed directly from the gas of the Solar nebula, while other CAIs show more coarse-grained textures, indicating crystallization after (re-)melting events (McSween and Huss, 2010). CAIs are believed to be the first solids that condensed out of the Solar nebula, and CAI formation is generally understood to represent the beginning of the Solar system, at absolute ages of ~ 4567 to 4568 Ma (Amelin et al., 2010; Bouvier and Wadhwa, 2010; Connelly et al., 2012).

Chondrules are igneous spherules (Figure 1), generally mm-sized, largely composed of olivine and low-Ca pyroxene, and can constitute up to 80% of some ordinary chondrites (Weisberg et al., 2006). Most chondrules are porphyritic in texture and can be divided into type I for Mg-rich chondrules and type II for chondrules with X_{Mg} values lower than 0.9). Some rare Al-rich chondrules are thought to have evolved from CAI precursors (Scott, 2007). Due to their texture, it is generally assumed that chondrules formed by the

melting of nebular dust aggregates and cooled rapidly thereafter (e.g., Alexander et al., 2008).

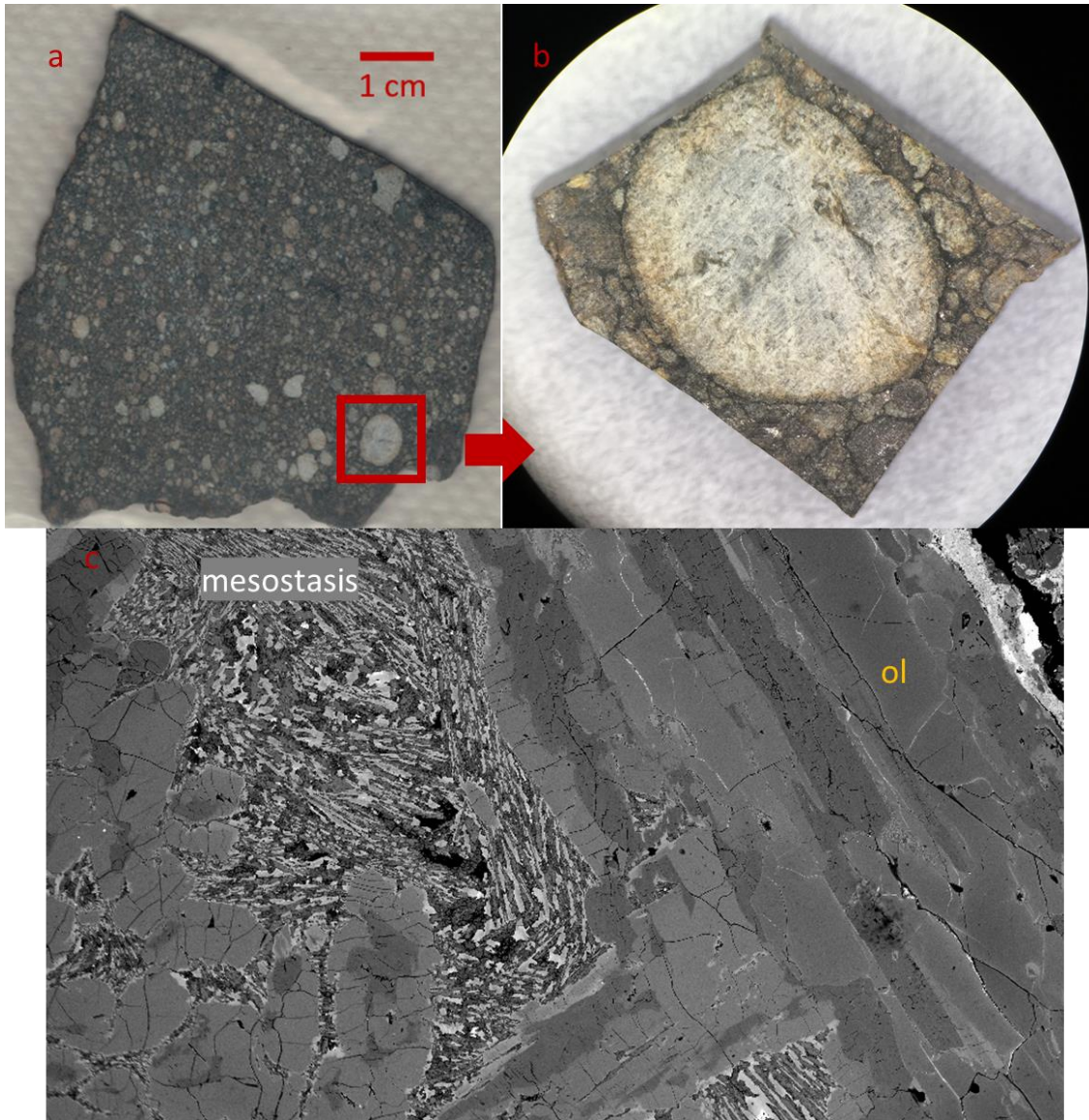


Figure 1: a) Scan of a slab of L3 chondrite NWA 10854, with chondrule C1 marked in red. b) extracted chondrule NWA 10854-C1 from its slab. c) BSE image of chondrule C2 from NWA 10854, showing a barred olivine texture on the right side, while the left part has a porphyritic texture. A fine-grained feldspathic mesostasis pocket lies in the middle (Source: Steve Simon, UNM).

Matrix is the fine-grained material surrounding chondrules and refractory inclusions, and may contain fine-grained silicates, metals, organic matter, sulfides and presolar grains.

Compositions of matrix can vary significantly. It was long suggested that matrix and chondrules formed in the same environments due to the chemical complementarity between them (Bland et al., 2005; Hezel and Palme, 2010), however, based on Pb-Pb ages of chondrules, Bollard et al. (2017) argued that a genetic link between matrix and chondrules is not supported by the data and that the complementarity could be preserved over longer timescales without the need for coeval formation.

Ordinary chondrites make up the vast majority (ca. 85%) of meteorites found on Earth and are classified into the high-Fe (H), low-Fe (L) and very low-Fe (LL) groups based on their bulk Fe contents which is distributed in the forms of metal, sulfide, and as fayalite and ferrosilite components in olivine and orthopyroxene, respectively. Abundances of chondrules in OCs range from 60 to 80 vol%, whereas CAIs are very uncommon at less than 1 vol% (Weisberg et al., 2006). The parent bodies of the H and LL chondrites are suggested to have been smaller asteroids (10 to 50 km radii), whereas the L chondrite parent body may have been a large asteroid with a radius of more than 100 km (Bouvier et al., 2007).

Chondritic meteorite parent bodies formed through the accretion of the meteoritic components described above, before secondary processes modified their pristine mineralogy and composition. Thermal metamorphism, aqueous alteration and shock metamorphism all played varying roles for different chondrite groups. In addition to the classification of a chondritic meteorite into its chemical group, they can also be divided into six petrologic types based on the level of secondary processes that they have undergone (Van Schmus and Wood, 1967). Meteorites that experienced increasing levels of thermal metamorphism would be classified into petrologic types 3 to 6, with 3 meaning no metamorphism nor alteration occurred and 6 meaning that metamorphic conditions reached points near partial melting. On the other hand, petrologic types 1 and 2 describe the amount of aqueous alteration the meteorite experienced (Huss et al., 2006). Not all chondrite groups experienced the full range of these secondary processes. For example, some carbonaceous chondrite groups experienced aqueous alteration (e.g., CI, CM), and only two (the CV and CK chondrite groups) experienced thermal metamorphism at all. Ordinary chondrites on the other hand have experienced the full range of thermal metamorphism, but no aqueous alteration (Weisberg et al., 2006).

Unequilibrated ordinary chondrites (i.e., OCs of petrologic type 3) are thought to represent the most primitive and pristine meteorites available.

Achondrite meteorites are rock samples that were formed through melting and differentiation of their parent body. They can be remnants of metallic cores (iron meteorites), of the crust and mantles of planets and planetesimals (stony achondrites, such as angrites, eucrites, or the SNC meteorites from Mars), or mixtures thereof (stony-iron meteorites, such as pallasites or mesosiderites). The breadth of variety in achondrite meteorites reveals not only the diverse asteroid population in the Solar System, but also the different processes that shaped the planets and asteroids.

1.4 The isotopic dichotomy of the Solar System

The first comprehensive isotopic anomalies between different meteorite groups were detected in O isotopes, where meteoritic materials plotted off of the terrestrial fractionation line and were consistent among their classification (Clayton et al., 1976). These anomalies however, are more likely to be products of self-shielding in the solar nebula rather than inherited signatures of presolar carriers (Lyons and Young, 2005). Heterogeneity in the Cr and Ti isotope compositions of meteorites between groups were first measured by Trinquier et al. (2007, 2009), before Warren (2011) described an isotopic dichotomy between carbonaceous and non-carbonaceous meteorites when comparing reported Cr, Ti and O isotopic anomalies for various meteorite groups, with a distinct gap existing between the isotope compositions of non-carbonaceous and carbonaceous chondrite groups.

Primordial nucleosynthetic isotope anomalies have since been reported for a variety of other elements, such as Ca (Schiller et al., 2015b; Schiller et al., 2018; Valdes et al., 2021), Ni (Regelous et al., 2008; Steele et al., 2011; Render et al., 2018; Nanne et al., 2019), Ru (Chen et al., 2010; Fischer-Gödde and Kleine, 2017; Bermingham et al., 2018; Fischer-Gödde et al., 2018) and Mo (Burkhardt et al., 2011; Budde et al., 2016; Bermingham et al., 2018; Spitzer et al., 2020). Of those elements, particularly Ni and Mo isotope anomalies also show clear evidence of the isotopic dichotomy between CC and NC meteorites (Nanne et al., 2019; Worsham et al., 2019). The dichotomy has been suggested to have formed by early infall of material with CAI-like isotope composition

near the sun, as CAIs were forming (likely during the *Class I* stage of stellar formation: Brennecke et al., 2020), which then spread viscously through the protoplanetary disk. The isotopic composition of the infalling material evolved to NC-like composition, and began to transport and mix with the outer disk (with early infall composition). Before the protoplanetary disk was well-mixed and homogenized, transport and mixing ceased, likely due to the separation of the protoplanetary disk, by either the early growth of Jupiter (Kruijer et al., 2017), or the presence of a pressure bump (Brasser and Mojzsis, 2020). This separation created the NC reservoir, with its isotopic composition representing the late infalling material, and the CC reservoir, whose isotopic composition was a mix of CAI-like and NC-like material (Figure 2; Burkhardt et al., 2019).

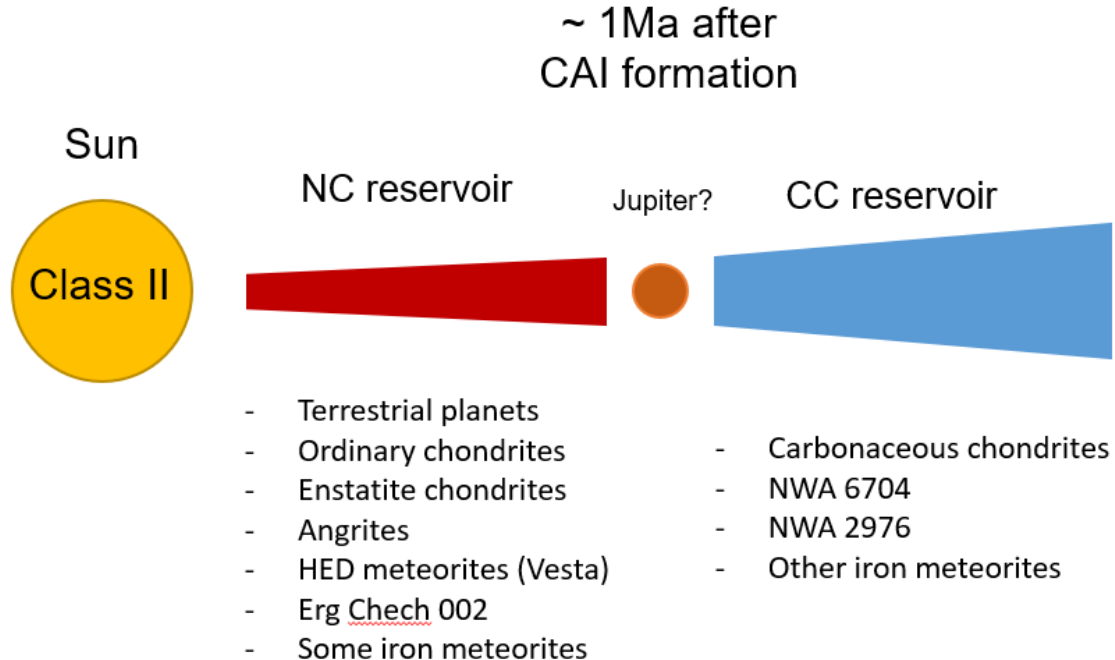


Figure 2: Overview of the dichotomy between NC and CC meteorites, potentially separated by a growing Jupiter, around 1 Ma after CAI formation (after Brennecke et al. (2020) and Kruijer et al. (2020)).

Recent studies have expanded these isotopic studies to chondrules to investigate any mixing and transport processes that potentially took place between the NC and CC reservoirs. Results from combined Cr-Ti-O isotope systematics in chondrules from both

ordinary and carbonaceous chondrites have demonstrated that while their isotope compositions can overlap those formed in the other reservoir for a single element, there is no overlapping between NC and CC chondrules when plotted in multi-isotope space (Figure 3; Schneider et al., 2020). These results prove the existence of an effective barrier and negligible exchange of material after the separation of the two formation reservoirs, at least during chondrule formation. The analysis of Cr isotope compositions of chondrules along with chronological data could be used to constrain the timing of infall, mixing and thermal processing in the protoplanetary disk.

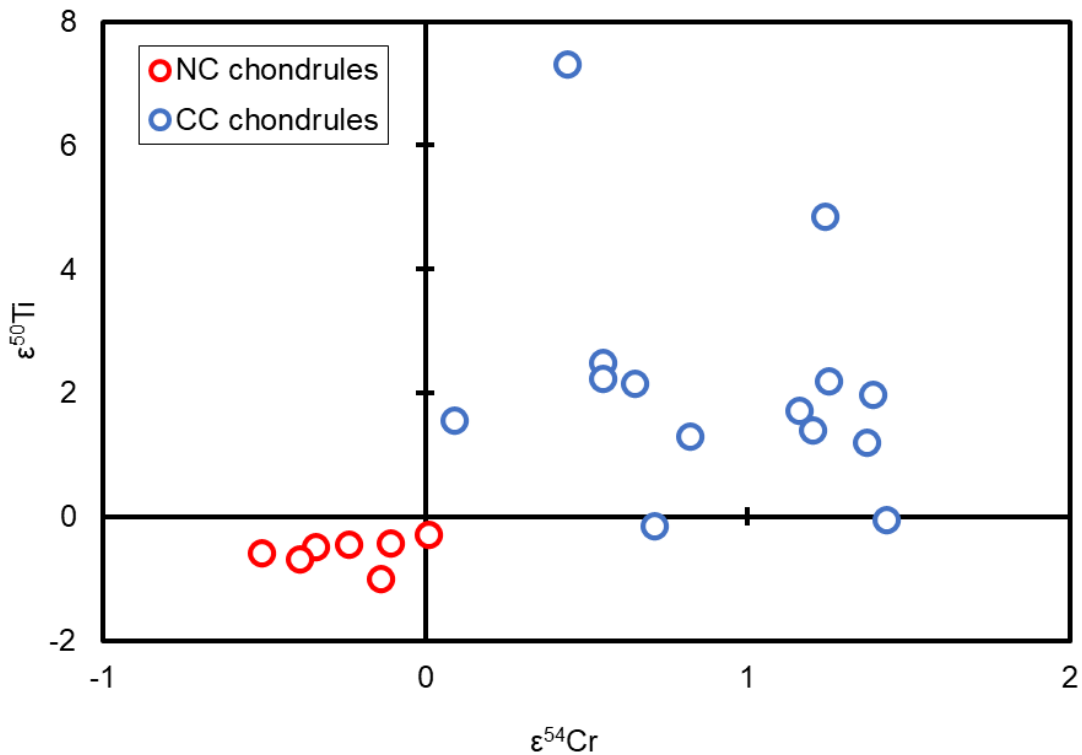


Figure 3: $\epsilon^{54}\text{Cr}$ - $\epsilon^{50}\text{Ti}$ plot of chondrules in NC meteorites (red) and CC meteorites (blue), with data reported by Gerber et al. (2017) and Schneider et al. (2020).

1.5 Chondrule formation

Based on their abundance in chondritic meteorites, chondrules may have played a substantial role in the formation of planetesimals (e.g. Johansen et al., 2015). Whereas a general consensus on the formation mechanisms of CAIs has been reached, the debate about the formation of chondrules is far from settled. While CAIs are believed to have

condensed from the gas in the solar nebula before experiencing some re-melting (e.g. MacPherson et al., 2010), chondrules show textural evidence for high-temperature melting of nebular dust aggregates and other precursors, and subsequent, rapid cooling (e.g., Alexander et al., 2008; Desch & Connolly, 2002; Hewins & Connolly, 1996). Relict grains in chondrules suggest that re-heating and interactions with the gas and dust from the protoplanetary disk occurred before chondrules were accreted onto their parent bodies (Metzler et al., 1992).

The chronology of chondrules has been studied with a variety of chronometers, and will be discussed in more detail below. In short, *in situ* ^{26}Al - ^{26}Mg ages as determined by secondary ionization mass spectrometry (SIMS) analysis of ~ 80 chondrules show a roughly 1.5 Myr gap between the formation of CAIs and OC chondrules (Kita et al., 2000; Villeneuve et al., 2009; Pape et al., 2019), whereas ages determined by Pb-Pb chronometry on ~ 15 OC chondrules indicate contemporaneous formation with CAIs, while lasting for about 4 Myr (Bollard et al., 2017). The differences in formation ages have been attributed to ^{26}Al heterogeneity in the Solar System (Bollard et al., 2019), the Pb-Pb chronometer dating precursor formation, rather than the last melting event (Blichert-Toft et al., 2020), or resetting of the Al-Mg systematics due to thermal metamorphism (MacPherson et al., 2012; Van Orman et al., 2014).

Suitable mechanisms fulfilling the aforementioned conditions may involve shock wave heating (Connolly Jr. and Love, 1998) generated through nebular lightning (Desch and Cuzzi, 2000), gravitational disk instabilities (Youdin and Shu, 2002) and bow shocks created by passing planetesimals on their orbits (Morris et al., 2012). Gravitational instabilities are thought to occur more prominently early in the lifetime of the protoplanetary disk while material is still accreting to it and is relatively massive compared to the mass of the proto-sun (Kratte and Lodato, 2016). This could explain more efficient, early formation of chondrules, but requires an additional source for chondrule formation after 1 Myr after CAIs, when disk instabilities become less efficient due to the relative decrease in mass of the protoplanetary disk. Bow shocks generated by planetary embryos and planetesimals passing through the protoplanetary disk may account for the formation of younger chondrules (Morris et al., 2012). In addition, the timescales of accretion of such planetary embryos (Dauphas and Pourmand, 2011) match

the ca. 4 Myr period of chondrule formation. Other formation mechanisms proposed include X-winds (Shu et al., 1997), magnetized disk winds (Salmeron and Ireland, 2012), and impact splashes from colliding planetesimals (Asphaug et al., 2011; Olsen et al., 2013; Lichtenberg et al., 2018). The enigmatic, metal-rich CB chondrites do show petrological, Mg and Pb isotopic evidence of chondrule formation by the cooling of a vapour plume caused by collisions between planetesimals (Krot et al., 2005; Olsen et al., 2013; Bollard et al., 2015), indicating that different mechanisms may be involved in chondrule formation.

Identifying and understanding the mechanisms of chondrule formation remains an important aspect in the evolution of the early Solar system. Chondrules represent, if not a critical step towards planetary accretion, as suggested by Johansen et al. (2015), then at the very least the remnants of widespread processes occurring in the protoplanetary disk, as is evident by the sheer abundance of chondrules in meteoritic material.

1.6 Early Solar System chronology

Radiometric dating provides chronological constraints about the formation and evolution of early Solar System materials. Long-lived radionuclides (LLR) are those where the parent nuclides have a long enough half-life to still be present in a significant amount in present day. On the contrary, short-lived radionuclides (SLR) are all extinct today due to their shorter half-lives (in the range of 10^5 to 10^8 years for geochemical applications). The long-lived chronometers provide us with absolute ages for the dated materials, whereas the short-lived chronometers give only ages relative to a different reference material called “anchor”. The “anchors” most commonly used are CAIs and achondrites, including rapidly-cooled volcanic angrites.

The existence of SLR in the early Solar system has been demonstrated by measuring the excesses of daughter isotopes in early Solar system materials, such as CAIs (e.g., Lee et al., 1976; Halliday et al., 1999). Because of the short lifespans of some SLR (e.g., ^{10}Be , ^{26}Al , ^{41}Ca , ^{182}Hf), they must have been introduced into the Solar nebula during, shortly before or shortly after the collapse of the solar molecular cloud. The SLR were synthesized by stellar sources before being injected into the Solar nebula (e.g., Goswami, 2004; Wasserburg et al., 2017) or by solar energetic particle irradiation reactions of dust

and gas near the proto-Sun (e.g., ^{10}Be , ^{26}Al ; Shu et al., 1997; Lee et al., 1998). More details on the synthesis of ^{26}Al will be provided in section 1.6.2.

1.6.1 The U-corrected Pb-Pb chronometer

This introduction of the U-corrected Pb-Pb chronometer is largely based on the comprehensive article published by Connelly et al. (2017). In contrast to the use of SLR as chronometers, those utilizing LLR do not necessitate parent nuclide homogeneity, only the knowledge of parent-to-daughter isotope ratios. However, the usage of the Pb-Pb chronometer is hampered by issues of its own: most notably, almost all samples have been affected by atmospheric Pb contamination (Pb_c) aggravated in the past with the use of leaded gasoline; and secondly, the $^{238}\text{U}/^{235}\text{U}$ ratio, long assumed to be constant at 137.88, has been shown to exhibit significant variations in CAIs (Brennecka et al., 2010) and even terrestrial rocks (Weyer et al., 2008; Brennecka et al., 2010).

The application of U-corrected Pb-Pb dating is based on the dual decay chains involving ^{235}U and ^{238}U decaying to ^{207}Pb and ^{206}Pb , respectively, via a series of intermediate short-lived radiogenic nuclides and their subsequent decay. The ^{235}U - ^{207}Pb decay chain has a half-life of 0.7038 Gyr (Jaffey et al., 1971), whereas the ^{238}U - ^{206}Pb decay chain has a half-life of 4.4683 Gyr (Villa et al., 2016). The isotopic composition of Pb is additionally altered by the decay of ^{232}Th to ^{208}Pb , with a half-life of 14.01 Gyr (Le Roux and Glendenin, 1963). As such, of the four naturally occurring isotopes of Pb, only ^{204}Pb is not increased from its primordial abundance by means of radioactive decay, meaning that radiogenic ingrowth affects the Pb isotope compositions, expressed as $^{206}\text{Pb}/^{204}\text{Pb}$, $^{207}\text{Pb}/^{204}\text{Pb}$ and $^{208}\text{Pb}/^{204}\text{Pb}$ ratios. The half-life of ^{232}Th is too long to provide precise ages, limiting its use as a chronometer, but the $^{208}\text{Pb}/^{204}\text{Pb}$ ratio can be used to constrain the long-term Th/U ratio of planets and their reservoirs (Blichert-Toft et al., 2020). The evolution of the $^{206}\text{Pb}/^{204}\text{Pb}$ and $^{207}\text{Pb}/^{204}\text{Pb}$ ratios over time can be expressed by the following equations (Eqs. 1 and 2), where t represents the age and λ represents the decay constant of the parent nuclide:

$$\left(\frac{^{206}\text{Pb}}{^{204}\text{Pb}}\right)_{\text{present}} = \left(\frac{^{206}\text{Pb}}{^{204}\text{Pb}}\right)_{\text{initial}} + \left(\frac{^{238}\text{U}}{^{204}\text{Pb}}\right)_{\text{present}} * (e^{\lambda_{238}t} - 1) \quad (\text{Eq. 1})$$

$$\left(\frac{^{207}\text{Pb}}{^{204}\text{Pb}}\right)_{\text{present}} = \left(\frac{^{207}\text{Pb}}{^{204}\text{Pb}}\right)_{\text{initial}} + \left(\frac{^{235}\text{U}}{^{204}\text{Pb}}\right)_{\text{present}} * (e^{\lambda_{235}t} - 1) \quad (\text{Eq. 2})$$

By dividing the two decay equations for the present-day $^{206}\text{Pb}/^{204}\text{Pb}$ and $^{207}\text{Pb}/^{204}\text{Pb}$ ratios (Eqs. 1 and 2), resulting in Eq. 3, the U/Pb is not required to obtain an age date:

$$\left[\frac{\left(\frac{^{207}\text{Pb}}{^{204}\text{Pb}}\right)_{\text{present}} - \left(\frac{^{207}\text{Pb}}{^{204}\text{Pb}}\right)_{\text{initial}}}{\left(\frac{^{206}\text{Pb}}{^{204}\text{Pb}}\right)_{\text{present}} - \left(\frac{^{206}\text{Pb}}{^{204}\text{Pb}}\right)_{\text{initial}}} \right] = \left(\frac{^{235}\text{U}}{^{238}\text{U}}\right)_{\text{present}} * \left(\frac{e^{\lambda_1 t} - 1}{e^{\lambda_2 t} - 1}\right) \quad (\text{Eq. 3})$$

The left side of Eq. 3 is equal to the ratio of radiogenic $^{207}\text{Pb}^*/^{206}\text{Pb}^*$ ratio (Eq. 4).

$$\left(\frac{^{207}\text{Pb}}{^{206}\text{Pb}}\right)_{\text{radiogenic}} = \left(\frac{^{235}\text{U}}{^{238}\text{U}}\right)_{\text{present}} * \left(\frac{e^{\lambda_1 t} - 1}{e^{\lambda_2 t} - 1}\right) \quad (\text{Eq. 4})$$

The radiogenic $^{207}\text{Pb}^*/^{206}\text{Pb}^*$ ratio corresponds to the slope of the isochron in a $^{206}\text{Pb}/^{204}\text{Pb}$ vs. $^{207}\text{Pb}/^{204}\text{Pb}$ diagram (“standard Pb-Pb diagram”) and to the y-axis intercept in a $^{204}\text{Pb}/^{206}\text{Pb}$ vs. $^{207}\text{Pb}/^{206}\text{Pb}$ diagram (“inverse Pb-Pb diagram”) (Figure 4). Inverse Pb-Pb diagrams are more commonly used for meteoritic samples, as radiogenic phases will plot nearer to the intercept and yield smaller age uncertainties from more precise ^{207}Pb and ^{206}Pb isotopic measurements, compared to the minor ^{204}Pb isotope. Due to the aforementioned pervasive atmospheric Pb contamination of samples, the Pb isotope composition of a sample is a mixture of various amounts of three different Pb components: Pb that was initially incorporated into the sample (Pb_i), Pb produced radiogenically due to the decay of U (and Th) isotopes (Pb_r), and a modern terrestrial component (Pb_c). In samples that originate from the beginning of the Solar System, initial Pb (Pb_i) is often approximated by the Pb isotope composition of U-free meteoritic troilite (FeS) that were separated from iron meteorites such as Canyon Diablo (Tatsumoto et al., 1973) and Nantan (Blichert-Toft et al., 2010). The modern terrestrial component (Pb_c) is generally represented by the average modern crustal Pb isotope composition, as determined by Stacey and Kramers (1975), and is often abbreviated by the letters “SK”. In order to obtain reliable absolute Pb-Pb ages based on radiogenic $^{207}\text{Pb}/^{206}\text{Pb}$ ratios, four conditions need to be met:

1. the system remained closed from diffusion and was not reset.

2. same initial Pb isotopic composition was incorporated into the different mineral phases of a sample.
3. the reduction of the three-component system of Pb to a two-component system (i.e., $Pb_i + Pb_r$ or $Pb_c + Pb_r$); and
4. the $^{238}\text{U}/^{235}\text{U}$ ratio of the sample is known.

The first two points are general conditions for radiometric dating. The third point is a critical aspect for successful application of the Pb-Pb chronometer. Substantial efforts to remove either modern terrestrial Pb contamination, or in some cases initial Pb (Connelly et al., 2008), are necessary in order to acquire reliable measurements. This is commonly achieved through a step-leaching procedure, starting with dilute acids and increasing their strength as the procedure progresses (see chapter 2.5).

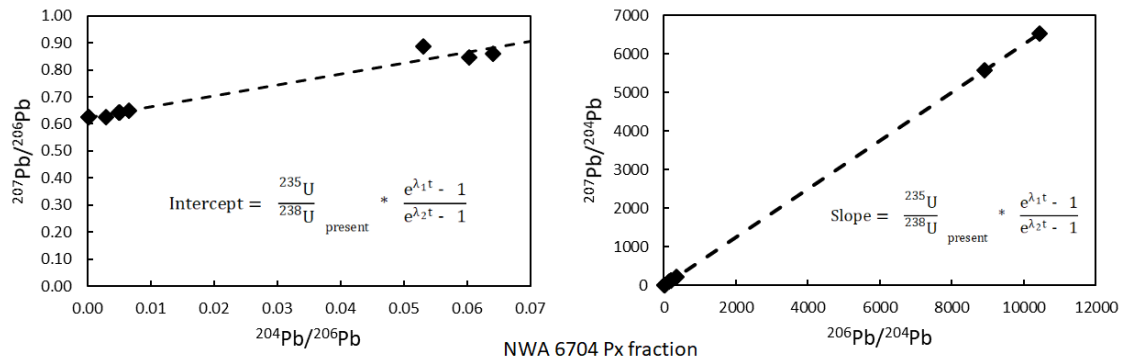


Figure 4: Inverse Pb-Pb diagram (left) and standard Pb-Pb diagram (right) of pyroxene separates (leachates and residues) from the ungrouped achondrite NWA 6704. The radiogenic $^{207}\text{Pb}^*/^{206}\text{Pb}^*$ ratio is determined by the intercept of the y-axis and the slope, respectively.

In “inverse” Pb-Pb diagrams, the radiogenic Pb component (Pb_r) is the isochron intercept of the y-axis where the amount of ^{204}Pb equals 0 (i.e., pure radiogenic Pb). In reality, it is unlikely that samples are completely radiogenic and ^{204}Pb -free. The pure radiogenic Pb component can be estimated from linear arrays (isochrons) defined by samples whose Pb isotope compositions are binary mixtures of either $Pb_r + Pb_i$, or $Pb_r + Pb_c$. If their Pb isotope compositions are mixtures of a third component, they either do not show any collinearity, or if they do, the “isochron” would be rotated and show a spuriously high $^{207}\text{Pb}/^{206}\text{Pb}$ ratio at the y-axis intercept (Figure 5). This illustrates the paramount

importance of step-leaching protocols for removal of one Pb component in order to determine accurate Pb-Pb ages.

The fourth point has been a recent major breakthrough in cosmochemistry and U-Pb chronometry in particular. It was long assumed that the $^{238}\text{U}/^{235}\text{U}$ ratio was invariant at 137.88 in geological and meteoritic materials. In meteorites, Brennecka et al. (2010 a) reported variations of the $^{238}\text{U}/^{235}\text{U}$ ratio in CAIs separated from the CV chondrite Allende, with values ranging from 137.409 ± 0.039 and 137.885 ± 0.009 . Variations of that magnitude result in corresponding Pb-Pb age corrections up to 5 Myr older than reported for samples with an assumed $^{238}\text{U}/^{235}\text{U}$ uniform ratio of 137.88. These variations were proposed to be the result of the decay of ^{247}Cm ($t_{1/2}=15.6$ Ma) (Brennecka et al., 2010; Tissot et al. 2015), isotope fractionation of U during CAI formation caused by redox reactions or evaporation and/or condensation (Connelly et al., 2012), or a combination of any of them for CAIs (Amelin et al., 2010). Connelly et al. (2017) suggested that the variations in U isotopic compositions may only be attributed to the CAI forming region of the solar nebula, as the $^{238}\text{U}/^{235}\text{U}$ ratios of analyzed chondrules converge to a value of 137.786 ± 0.013 (Connelly et al., 2012; Brennecka et al., 2015), as do whole-rock eucrites, angrites and achondrites (Goldmann et al., 2015). Large $^{238}\text{U}/^{235}\text{U}$ variations in bulk ordinary chondrites reported by Goldmann et al. (2015) show a positive correlation with U content. Nevertheless, Connelly et al. (2017) concluded that this correlation was likely due to secondary processes such as fractionation during metamorphism, and that a $^{238}\text{U}/^{235}\text{U}$ ratio of 137.786 ± 0.013 can be used as the present bulk Solar System value. Nonetheless, U isotopic compositions should be analyzed for calculating robust Pb-Pb ages whenever possible, owing to sample U concentrations and sizes.

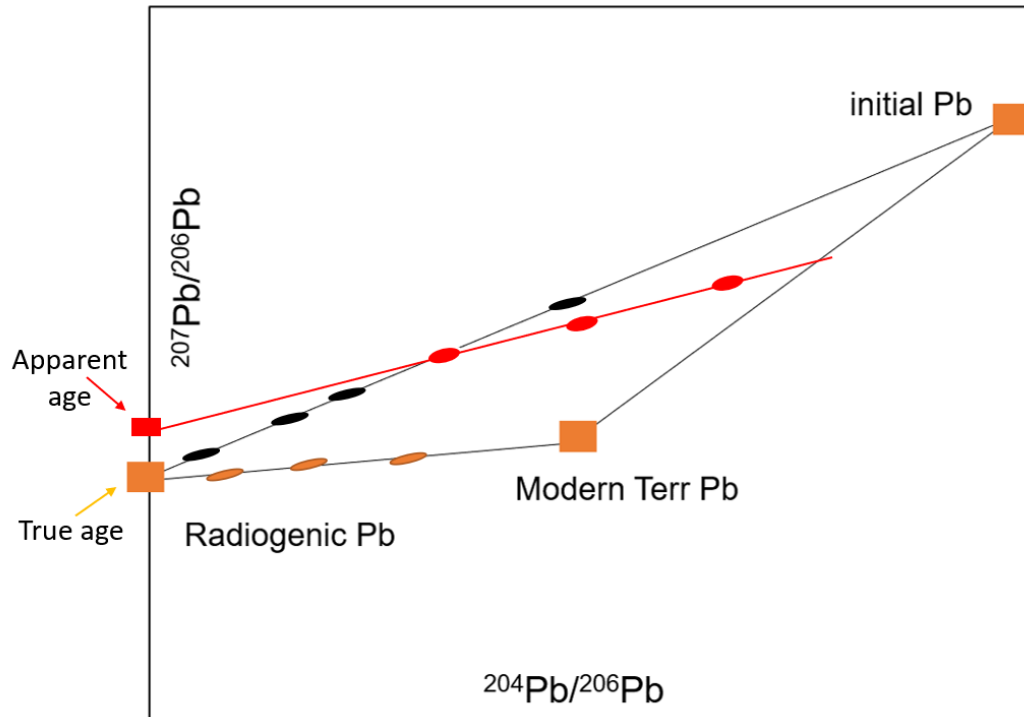


Figure 5: Qualitative illustration of the three Pb components that make up the Pb isotope composition of a sample, and how three-component mixtures in samples can affect isochrons. The true age, calculated from the pure radiogenic Pb isotope composition, is estimated by Pb-Pb isochrons defined by samples that are binary mixtures, i.e., they are either free of modern terrestrial Pb (black ellipses) or initial Pb (orange ellipses). If samples are not binary mixtures and their Pb isotope composition is made a combination of all three Pb components, they will plot within the triangle defined by the three Pb components (red ellipses). The samples may not plot on a line, but in cases where they do, they would produce a linear array that is rotated and results in a spuriously high $^{207}\text{Pb}/^{206}\text{Pb}$ ratio representing radiogenic Pb (red line), leading to an older age than the true age of the sample.

1.6.2 The ^{26}Al - ^{26}Mg chronometer and distribution of ^{26}Al in the protoplanetary disk

The radioactive decay of ^{26}Al to ^{26}Mg ($t_{1/2}=0.717$ Ma; National Nuclear Data Center NuDat v3.0, 2021) is thought to have been the driving force behind thermal heating leading to planetary melting and differentiation during the first 5 Myr of the Solar System (e.g. Lee et al., 1976; Macpherson et al., 1995; Russell et al., 1996). Since all primordial

^{26}Al went extinct within the first 10 Myr of the Solar system, excesses of ^{26}Mg ($^{26}\text{Mg}^*$) relative to what would be expected by mass-dependent processes are quantified, from which initial $^{26}\text{Al}/^{27}\text{Al}$ ratios at the time of formation are inferred. This is traditionally plotted in a $^{27}\text{Al}/^{24}\text{Mg}$ vs. $\delta^{26}\text{Mg}^*$ isochron diagram, where the slope is the initial $^{26}\text{Al}/^{27}\text{Al}$ ratio, and the intercept of the y-axis the initial $\delta^{26}\text{Mg}^*$ value (Figure 6). Equation 5 shows the calculation of age relative to the CAIs in Myr, where $T_{1/2}$ is the half-life of ^{26}Al in Myr:

$$\Delta t(\text{Myr}) = \ln \left(\frac{\frac{^{26}\text{Al}}{^{27}\text{Al}}_{\text{CAI}}}{\frac{^{26}\text{Al}}{^{27}\text{Al}}_{\text{Sample}}} \right) * \frac{T_{1/2}}{\ln(2)} \quad (\text{Eq. 5})$$

However, while the ^{26}Al - ^{26}Mg chronometer has the potential to provide high-resolution relative ages, its chronologically-meaningful use relies on a homogeneous distribution of the parent nuclide, ^{26}Al , in the solar nebula. In sub-chapter 1.4, a multitude of elements, such as Cr, Ti and Mo are explained to exhibit isotopic variations depending on their formation reservoir. It was generally thought that ^{26}Al was indeed homogeneously distributed throughout the protoplanetary disk, with the so-called “canonical” initial $^{26}\text{Al}/^{27}\text{Al}$ value of 5×10^{-5} , as found in CAIs (Figure 6; Jacobsen et al., 2008; MacPherson et al., 2010; Kita et al., 2013).

Notable exceptions to the “canonical” value were found in CAIs with Fractionation and Unknown Nuclear effects (FUN CAIs), their low abundance among the oldest materials in the solar nebula alone however would have not significantly affected the degree of homogeneity in the CAI-forming region of the protoplanetary disk (Macpherson et al., 1995). Larsen et al. (2011) reported widespread heterogeneities in mass-independent excess ^{26}Mg values among refractory inclusions and by comparing Al-Mg ages to U-Pb ages, they concluded that the variations in $^{26}\text{Mg}^*$ were the result of a heterogeneous distribution of ^{26}Al in the solar nebula. This conclusion has since been a topic of considerable debate, as other studies argue that the visible heterogeneities are due to variations of the Mg isotopic composition in the solar nebula, and that the assumption of CAIs and AOAs forming coevally is flawed and the combined isochron is therefore chronologically insignificant (Wasserburg et al., 2012; Kita et al., 2013).

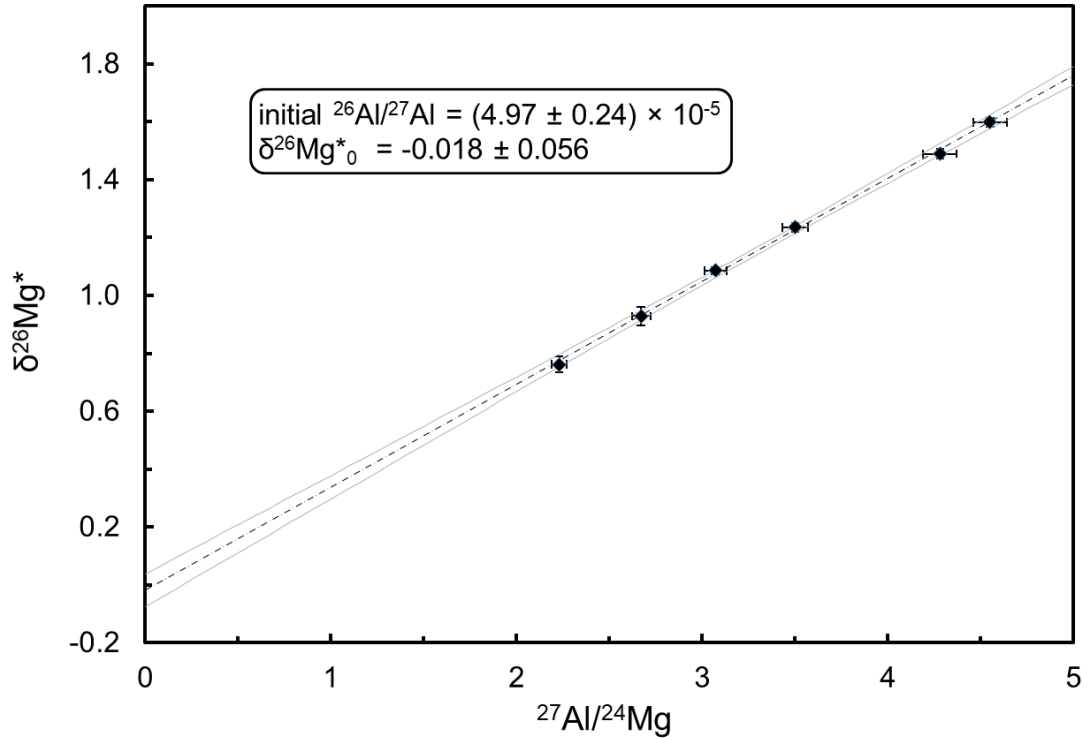


Figure 6: Internal isochron of the AJEF Type B CAI analyzed by Jacobsen et al. (2008) in a $^{27}\text{Al}/^{24}\text{Mg}$ vs. $\delta^{26}\text{Mg}^*$ diagram. The slope of the trendline represents the initial $^{27}\text{Al}/^{24}\text{Mg}$ ratio of $(4.97 \pm 0.24) \times 10^{-5}$ while the y-axis intercept is equal to the initial $\delta^{26}\text{Mg}^*$ of -0.018 ± 0.056 ‰. Error bars for the y-axis are within the markers where not visible.

Other studies have attempted to use combined Pb-Pb and ^{26}Al - ^{26}Mg chronology on various meteorites and components to test for a homogeneous distribution of ^{26}Al . Common targets of such investigations are achondrites, in particular angrites (Schiller et al., 2015a) and unique achondrites (Bouvier et al., 2011; Koefoed et al., 2016; Amelin et al., 2019; Sanborn et al., 2019; Wimpenny et al., 2019), but also OC chondrules (Bollard et al., 2019). The ^{26}Al - ^{26}Mg ages of volcanic angrites (Spivak-Birndorf et al., 2009; Schiller et al., 2015a) are, when anchored to CAIs, about 1 Myr younger than the U-corrected Pb-Pb ages (Amelin, 2008a,b; Connelly et al., 2008; Tissot et al., 2017), implying $^{26}\text{Al}/^{27}\text{Al}$ ratios $\sim 1 \times 10^{-5}$. This is reflected as well in OC chondrules that were dated by both U-corrected Pb-Pb and *in situ* ^{26}Al - ^{26}Mg dating by SIMS (Bollard et al., 2019), and other achondrites that formed in the inner Solar System (NC reservoir), however, in some of those achondrites, there is evidence of secondary processes (e.g., metamorphism, impacts) affecting the Al-Mg systematics (Koefoed et al., 2016;

Wimpenny et al., 2019). This is potentially also the case for the angrites (Sanborn et al., 2015), and could account for the differences in formation ages between the Pb-Pb and ^{26}Al - ^{26}Mg chronometers, rather than ^{26}Al heterogeneity. The two unique achondrites NWA 2976 and NWA 6704 that formed in the CC reservoir, on the other hand, do not show any age differences (Bouvier et al., 2011; Amelin et al., 2019; Sanborn et al., 2019). Evaluation of the distribution of ^{26}Al is not just limited to comparison of the Pb-Pb and ^{26}Al - ^{26}Mg chronometers. Some studies have utilized the ^{182}Hf - ^{182}W or ^{53}Mn - ^{53}Cr chronometers to compare to ^{26}Al - ^{26}Mg ages, particularly in angrites (e.g., Glavin et al., 2004; Kleine et al., 2012; Kruijer et al., 2014), but also in chondrites and chondrules (e.g., Schrader et al., 2017; Budde et al., 2018). Kleine et al. (2012) concluded that ^{26}Al indeed was distributed heterogeneously due to significant age differences between CAIs and angrites using the ^{182}Hf - ^{182}W and ^{26}Al - ^{26}Mg chronometers. However, after the revision of the initial ^{182}Hf - ^{180}Hf ratio by Kruijer et al. (2014), the ^{182}Hf - ^{182}W ages for the studied angrites were no longer distinct from the ^{26}Al - ^{26}Mg ages, supporting a homogeneous distribution of ^{26}Al . Budde et al. (2018) came to the same conclusion when using ^{182}Hf - ^{182}W ages for CR chondrules. This interpretation may be problematic, however: Schiller et al. (2015) pointed out that in the case of the angrites, both ^{182}Hf - ^{182}W ages and ^{26}Al - ^{26}Mg ages disagreed with Pb-Pb ages (e.g., Amelin, 2008) and argued that the use of assumption-free, absolute chronometers (such as Pb-Pb dating) combined with the ^{26}Al - ^{26}Mg chronometer would provide a more scrupulous test of ^{26}Al variability. There is, however, still disagreement, if the Pb-Pb chronometer dates the last chondrule melting event or chondrule precursor formation (Bollard et al., 2019; Blichert-Toft et al., 2020). All these different studies indicate that the matter is far from settled and requires further study.

The fact that ^{26}Al as well as other short-lived radionuclides even existed at the time of formation of our Solar system indicates that they must have been synthesized and possibly transported to the solar nebula around that time. Abundances of nuclides such as ^{235}U , ^{238}U , ^{146}Sm and ^{53}Mn match the predictions of long-term galactic nucleosynthesis as their production mechanism (Wasserburg et al., 2006). Other, short-lived nuclides (e.g., ^{10}Be , ^{26}Al , ^{107}Pd) do not, and require addition into the Solar nebula. Two different mechanisms have been proposed for SLR addition: synthesis by spallation reactions

caused by galactic and/or solar irradiation, or stellar sources, such as injection from a nearby supernova event. Irradiation of solids in the Solar nebula can account for the observed abundance of ^{10}Be , as this nuclide is not formed through stellar nucleosynthesis (Gounelle et al., 2005). Conversely, production by irradiation cannot account for the abundances of ^{26}Al within the same parameters. This would indicate a stellar source as more likely (Duprat and Tatischeff, 2007). Aluminium-26 being injected into the protoplanetary disk from a nearby supernova has been another hypothesis that has been offered (e.g. Pan et al., 2012). This has been argued against due to missing collateral effects that such an event would cause, such as a remarkable shift in O isotopic composition (Gounelle and Meibom, 2007). While Ellinger et al. (2010) cautioned against immediate dismissal of the supernova hypothesis, Wasserburg et al. (2006) pointed out that supernova-injected material would require significant dilution, and in the process could not contribute enough to observed initial $^{60}\text{Fe}/^{56}\text{Fe}$ ratios. Another potential stellar source for ^{26}Al is the ejection of gas envelopes of asymptotic giant branch (AGB) and super-asymptotic giant branch (SAGB) stars (Wasserburg et al., 2006; Ventura et al., 2011; Wasserburg et al., 2017). Aluminium-26 is most efficiently synthesized by hot bottom burning in stars with masses in the range of 6 Solar masses (Ventura et al., 2011), but models indicate stars in that mass range or higher would produce too little ^{182}Hf and ^{107}Pd , and that stars with lower masses produce too little ^{26}Al and would outlive the lifetime of molecular clouds, thereby running out of time to contribute to the molecular cloud out of which the proto-sun and the protoplanetary disk evolved (Wasserburg et al., 2017).

Irradiation by galactic and solar cosmic rays can also produce ^{26}Al in meteoroids between their ejection from the parent asteroid and arrival on Earth, but also during their residence time on Earth's surface (as meteorites) at lower production rates. The amount of cosmogenic ^{26}Al atoms produced by neutron capture however is negligible compared to abundance at the beginning of the early Solar System ($^{26}\text{Al}/^{27}\text{Al} \sim 5 \times 10^{-5}$, e.g., Jacobsen et al., 2008) and does not affect the ^{26}Al - ^{26}Mg chronometer (Leya and Masarik, 2009).

1.7 Presentation of the next chapters

As outlined in this chapter, the timing, abundance and distribution of ^{26}Al in the protoplanetary disk were crucial factors in the evolution of the early Solar system and planetary bodies, and that the processes that took place in the protoplanetary disk are far from fully understood.

In order to better constrain and further our knowledge of the processes that shaped the early Solar System, this dissertation provides new chronological and nucleosynthetic data on chondrules, igneous clasts and achondrite meteorites, obtained through the analysis of their Mg, Pb and Cr isotope compositions using state-of-the-art analytical techniques. These are described in Chapter 2, which covers sample selection, sample preparation, chemical separation of Mg, Pb and Cr, as well as their analysis by multi-collector inductively-coupled plasma mass spectrometry (MC-ICP-MS), and Mg isotope analysis by secondary ionization mass spectrometry (SIMS)

In chapter 3, the results of these analyses on chondrules and igneous clasts from unequilibrated ordinary chondrites are presented. These samples have undergone very little if any alteration on their parent bodies and record the conditions in which their formation took place, making them well-suited to help us understand the processes that shaped the early Solar System.

In chapter 4, chronological results that were obtained by the application of Pb-Pb and ^{26}Al - ^{26}Mg chronometry on the unique achondrite Erg Chech 002 are presented. This meteorite is mineralogically unusual and so far, no meteorites are believed to have been found that originated from the same parent asteroid. A previous study (Barrat et al., 2021) has shown that the meteorite formed within the first 2.5 million years of the Solar System, giving it the potential to be a critical piece of evidence when evaluating the abundance and distribution of ^{26}Al in the Solar nebula.

Chapter 5 presents the chronological and chemical results of two distinctive angrite meteorites, Northwest Africa 8535 and Northwest Africa 10463. These two samples expand the suite of samples from the angrite parent body, which in the past have broadly been categorized into the older, volcanic angrites and the younger, plutonic angrites. NWA 10463 appears texturally to be more closely related to the plutonic angrites, but exhibits mineral characteristics that are not found in those samples. NWA 8535 is the

first dunitic angrite found, which likely samples an unknown part of the angrite parent body. Understanding their chemical and chronological relation to other angrites will advance our knowledge of the parent body processes that formed the angrites.

Chapter 6 summarizes the results and their interpretation, and places them into the broader context.

2 Methods

2.1 Sample selection

Chondrules with unusually large sizes (at least 1 cm diameter) were selected from unequilibrated (type 3) ordinary chondrites, with sufficient mass for Pb chemistry (> 40 mg) prioritized. Based on the Pb-Pb age dating results and petrologic type of the chondrules, some were selected for *in situ* ^{26}Al - ^{26}Mg SIMS analysis. In addition to OC chondrules, two large igneous inclusions from the Paposo 004 L3 chondrite and the Northwest Africa 12261 H3 chondrite, a chondrule-like fraction of the CBa chondrite Quebrada Chimborazo 001 and a chondrule from the ungrouped C2 chondrite Tarda were selected. For achondrites, the angrites Northwest Africa 10463 and NWA 8535, and the ungrouped achondrite Erg Chech 002 were selected for analyses. All samples and their host meteorites are listed in Table 1, along with the analyses performed on them.

2.2 Extraction

Chondrules and inclusions were extracted from slabs of their host chondrites by use of a diamond-coated wire saw (Diamond Wire Tech) and a low-speed Buehler IsoMet saw with a diamond-coated wafering blade. Once grossly separated from the slabs, the chondrules were further cleaned up from adhering matrix using diamond-coated dental tools. A small fragment of each chondrule was separated using dental tools to be polished and mounted in epoxy for petrographic description by scanning electron microscopy (SEM) and electron probe microanalysis (EPMA). The remainder of the chondrules were cleaned with acetone and water, prior to being crushed in an agate mortar into a homogenized powder. Mineral fractions of bulk achondrite meteorites were hand-picked under binoculars after crushing gently the bulk sample under a desired grain size. Single use nylon sieves were cut to size and cleaned with ethanol before usage. Fines (< 60 μm grain size) were sieved out and a hand magnet was used to remove any magnetic minerals prior to mineral separation. In the case of angrite NWA 10463, density separation using heavy liquids such as bromoform and diiodomethane were used to separate mafic minerals (pyroxene and olivine; $\rho \approx 3.2 \text{ g/cm}^3$) and feldspar minerals ($\rho \approx 2.9 \text{ g/cm}^3$) that were then washed with clean acetone. Plagioclase and pyroxene-olivine fractions were

then hand-picked under binoculars, with multiple plagioclase fractions (~ 1 mg or less) picked to ensure variable $^{27}\text{Al}/^{24}\text{Mg}$ ratios for Mg isotope analysis.

Table 1: Overview of samples analyzed for their Pb, Mg and Cr isotope composition, as well as the in situ ^{26}Al - ^{26}Mg systematics determined by secondary ionization mass spectrometry (SIMS).

Meteorite	Sample	Pb	bulk Mg	SIMS Mg	Cr
<i>Chondrules/clasts</i>					
Northwest Africa 8007 (L3.2)	C1	x	x	x	x
Northwest Africa 8276 (L3.00)	C1	x	x	x	x
	C2		x	x	x
	C3		x		
Northwest Africa 10854 (L3)	C1	x	x	x	x
	C2	x	x	x	
	C3	x	x		
	C5	x	x		
	C6	x	x	x	x
Northwest Africa 11672 (L3)	C1	x	x	x	x
Northwest Africa 12261 (H3)	I1	x	x	x	x
Paposo 004 (L3.1)	I1	x	x	x	x
Quebrada Chimborazo 001 (Cb _a)	C1	x	x		x
Tarda (C2-ung)	C2		x		x
<i>achondrites</i>					
Northwest Africa 8535 (ang)			Olivine fraction		
Northwest Africa 10463 (ang)		x	Various fractions		
Erg Chech 002 (achon-ung)		x	Various fractions		

NWA 8276-C1 was provided by Dr. Steven Simon, University of New Mexico, NWA 8276-C2 and -C3 by Dr. Christopher Herd, University of Alberta. Paposo 004 was donated by Rodrigo Martínez, Museo del Meteorito, San Pedro de Atacama, Chile. The angrites NWA 8535 and 10463 were provided by Dr. Carl Agee, University of New Mexico. Erg Check 002 was donated from Ben Hoefnagels (Big Bang Meteorites). Other samples were acquired from private dealers by Dr. Audrey Bouvier

2.3 Laboratory procedures

All water used during cleaning and chemistry procedures was ultrapure water (18.2 M Ω), filtered by a Milli-Q® and Q-POD Element water purification systems. Acids used during chemistry include hydrochloric acid (HCl), nitric acid (HNO₃), hydrofluoric acid (HF) and hydrobromic acid (HBr). HCl and HNO₃ were distilled in the lab from trace metal grade and were subsequently titrated and analyzed for a whole suite of element concentrations before use and dilution. High-purity Aristar Ultra concentrated acids were purchased for HF and HBr and diluted assuming 29M and 9M, respectively.

Chemistry procedures were performed under Class 10 ULPA filtered fume hood or filtered laminar flow hoods that were rigorously wiped clean. Cleanroom nitrile and/or vinyl gloves were used throughout the procedures to reduce contamination during handling.

For most samples, Savillex® PFA Teflon beakers were used and cleaned in hot 50% HNO₃, hot Milli-Q® water and 6 M HCl. Beakers used for Pb chemistry were cleaned in subsequent steps of hot 50% HNO₃, a 1:9 mixture of 16 M HNO₃ and 8 M HF, 6 M HCl, 0.5 M HBr and finally in a 6 M HCl-1 M HF mixture.

2.4 Sample digestion

Powdered samples were digested in a 5:1 mixture of 29 M HF and 15 M HNO₃ while heated on a hotplate at 120°C for 48 hours. The samples are subsequently ultrasonicated for an hour and then dried down before being re-fluxed in 15 M HNO₃ for 24 hours at 120°C. Ultrasonication and drying are repeated for this step, before the sample is converted to its chloride form and taken up in 6 M HCl prior to chromatographic separation.

2.5 Sample leaching for Pb analysis

Samples destined for Pb analysis undergo a leaching protocol with progressively stronger acids, designed to remove terrestrial Pb contamination (**Error! Reference source not found.**). A volume of 0.5 ml of acid per 50 mg of sample is added to the powdered sample and then collected after undergoing its designated leaching step, before the next acid is added to the sample. In between subsequent steps involving different acids, the

sample is rinsed with Milli-Q water which is then collected with the prior wash. The powdered sample is ultrasonicated for 15 minutes first in 0.5 M HBr (Wash-1), then Milli-Q water (Wash-2) and then twice in 0.5 M HNO₃ (Wash-3). Subsequently, 6 M HCl (Wash-4) and then 7 M HNO₃ (twice; Wash-5 and Wash-6) are added to the sample and heated at 120°C for 1 hour. Finally, 1 M HF is first added to the sample and ultrasonicated for an hour (Wash-7), then added again and heated at 90°C for 12 hours (Wash-8). The fraction of the sample that is left after the complete leaching procedure is labelled as the residue (R). Leachates and residue are dried down and then dissolved in the same manner as described in chapter 2.4, with an added step of uptake in 1.5 M HBr prior to Pb separation.

Table 2: Leaching protocol for Pb analysis, following the procedure outlined in Bouvier and Wadhwa (2010).

Step	Acid	Processing	Duration	Repeat	Collected as...	
1	0.5 M HBr	Ultrasonication washing	15 min	once	Wash-1 (W1)	Often combined to W1-3
2	Water	Ultrasonication washing	15 min	once	Wash-2 (W2)	
3	0.5 M HNO ₃	Ultrasonication washing	15 min	twice	Wash-3 (W3)	
4	6 M HCl	Hot plate fluxing at 120°C	1 hr	once	Wash-4 (W4)	
5	7 M HNO ₃	Hot plate fluxing at 120°C	1 hr	once	Wash-5 (W5)	Often combined to W5+6
6	7 M HNO ₃	Hot plate fluxing at 120°C	1 hr	once	Wash-6 (W6)	
7	1 M HF	Ultrasonication washing	1 hr	once	Wash-7 (W7)	
8	1 M HF	Hot plate fluxing at 90°C	12 hrs	once	Wash-8 (W8)	

2.6 Ion-exchange chromatography

Ion-exchange chromatography is used to separate targeted elements from other elements (matrix elements) in dissolved samples. This involves the successive addition of different acids with different molarities into plastic or PTFE columns which are loaded with anionic or cationic exchange resin. The polymeric exchange resin contains “counter-ions” that are released as introduced ions (the sample) of the same charge are trapped (thus exchanging them). The trapped ions can be eluted from the resin when the pH is changed through addition of a different acid or the same acid with different molarity. During cationic exchange chromatography, the negatively charged resin (AG50W resin) exchanges its positive “counter-ions” for positive ions from the sample (e.g., Mg^{2+}) during sample loading, and vice versa for anion-exchange resin (AG1 resin).

All samples were processed in the GEOMETRIC laboratory at Western University for Mg and Pb separation.

2.6.1 Magnesium separation

All Mg samples were processed at the GEOMETRIC lab at Western University. The protocol for separating Mg from matrix elements in samples was adapted from protocol used by Wombacher et al. (2009) and consisted of three stages (Table 3): the first two separated Mg from Ca and Fe, while the third stage separated Mg from the remaining matrix elements. Plastic BioRad® columns were filled with water prior to loading 1.2 ml of cationic exchange resin AG50W-X8 (200-400 mesh). The resin is activated by adding ca. 6 ml 6 M HCl before rinsing the acid out with Milli-Q water. The columns and the resin are cleaned with 20 ml of 4 M HCl before a conditioning step of 3.6 ml 10 M HCl is added prior to sample loading. Sample aliquots containing 20-100 μg of Mg are dried down and taken up in 0.3 ml 10 M HCl for loading onto the columns. Magnesium, along with some matrix elements, is first eluted with 3.2 ml 10 M HCl, followed by a post-Mg fraction of 0.8 ml 8 M HCl that is later dried down and taken up again in 0.3 ml 10 M HCl for loading onto the second stage. Calcium and Fe are separated afterwards with 14.2 ml 8 M HCl and 10 ml 4 M HCl, respectively, before the columns are washed out with 10 ml of each 4 M HCl, then rinsed with ca. 10 ml 6 M HCl and 2 M HF.

Table 3: Three-stage Mg separation scheme based on Wombacher et al. (2009), using Biorad® plastic columns and AG50W-X8 (200-400 mesh) cation exchange resin.

Stage 1 + 2			Stage 3		
<i>Step</i>	<i>Acid</i>	<i>Volume [ml]</i>	<i>Step</i>	<i>Acid</i>	<i>Volume [ml]</i>
Resin cleaning	4 M HCl	ca. 20	resin conditioning	0.4 M HCl	3.6
Resin conditioning	10 M HCl	3.6	Load sample in	0.4 M HCl	0.3
Load sample in	10 M HCl	0.3	matrix elution	0.4 M HCl	33.6
Mg + matrix elution	10 M HCl	3.2	Be, Ti, Al elution	0.15 M HF	7.2
post-Mg step	8 M HCl	0.8	pre-Mg step	1 M HCl	1
Ca elution	8 M HCl	14.2	Mg elution	1 M HCl	20
Fe elution	4 M HCl	10	Wash out	6 M HCl	5
Wash	4 M HCl	10			

The second stage is a repeat of the first stage, but only the post-Mg fraction is loaded onto the columns. The Mg fraction is collected together with the Mg fraction from the first stage and the dried down.

The third stage, separating Mg from matrix elements like Al and Cr, among others, uses the same columns and resin as the first two. After activating and cleaning, the resin is conditioned with 3.6 ml 0.4 M HCl. The dried-down Mg fraction from the first two stages is taken up in 0.3 ml 0.4 M HCl and loaded onto the column. This is followed by 33.6 ml 0.4 M HCl for elution of multiple matrix elements, before 7.2 ml 0.15 M HF elutes Be, Ti and Al. A pre-Mg step of 1 ml 1 M HCl is added prior to Mg elution with 20 ml 1 M HCl. After this the columns are washed out with 5 ml of 6 M HCl and then rinsed with ca. 10 ml 6 M HCl and 2 M HF.

The procedure was tested with multi-element and Mg solution standards, as well as terrestrial rock standards (including the San Carlos olivine, the United States Geological

Survey (USGS) basalt standards BCR-2 and BIR-1, and the Geological Survey of Japan (GSJ) rhyolite standard JR-1). Additionally, Mg-free processed rock standard matrices were doped with a Mg solution “UWO ICP Std” solution and processed again through column chemistry to control any potential fractionation effects from our methods. Results from those tests are listed along with other standard data in **Table 8**.

2.6.2 Lead separation

The separation of Pb from samples involves a two-stage anion-exchange chromatography protocol, following the protocols of Bouvier and Wadhwa (2010) and is summarized in Table 4. It uses 50 μ l of AG1-X8 (200-400 mesh) anionic exchange resin in PTFE columns. The column and resin are cleaned with a full column reservoir volume (cv) of 6 M HCl, 0.5 ml of Milli-Q water, 1 ml 0.5 M HNO₃ and 0.2 ml of Milli-Q water, before the sample is loaded in 0.3 ml 1.5 M HBr. Depending on the size of the sample, it may be loaded in a larger volume to ensure sufficient flow through the resin.

Table 4: Protocol for Pb separation chemistry, using PTFE columns and AG1-X8 (200-400 mesh) anion exchange resin, following the methods described by Bouvier and Wadhwa (2010).

Step:	Eluent:	Volume (ml):	
		Stage 1	Stage 2
Clean resin and column	6M HCl	1 cv	1 cv
	H ₂ O	500 μ l	500 μ l
	0.5M HNO ₃	1ml	1ml
	H ₂ O	200 μ l	200 μ l
Condition column	1.5M HBr	200 μ l	200 μ l
Load sample and collect matrix elements	1.5M HBr	300 μ l	300 μ l
rinse and collect matrix elements	1.5M HBr	2*200 μ l	500 μ l
Collect Pb and dry down	0.5M HNO ₃	2ml	2+1ml

Matrix elements are eluted by adding 0.2 ml 1.5 M HBr twice, before 2 ml 0.5 M HNO₃ elutes Pb. This procedure is repeated to purify the Pb fraction. For that, the Pb cut is dried down and then taken up again in 0.3 ml 1.5 M HBr prior to loading. For the second stage, the matrix is eluted in a single 0.5 ml 1.5 M HBr step, and the Pb fraction is eluted with a total of 3 ml 0.5 M HNO₃.

2.6.3 Chromium

Separation of Cr was carried out alongside Ti separation by a combined chemistry protocol, following the first part of the method described by Williams et al. (2019) and the method for Cr developed by Dr. Précillia Morino and collaborators at ETH Zürich. The purification of Cr is comprised of three different columns (Table 5). The first set separates the fractions containing Ti from Cr and the matrix. PTFE columns are filled with 0.7 ml of AG1-X8 (100-200 mesh) cationic exchange resin. The resin is cleaned with 2 cv of 0.5 M HCl, 5 ml of 6 M HCl + 1 M HF and finally 1 cv of MQ water. The pre-conditioning step involves 6 ml of 4 M HF, before the samples, taken up in 10.5 ml 4 M HF, are loaded onto the columns with 5 ml, 0.5 ml and another 5 ml step. The sample load (SL1) is collected, as fluorides and matrix elements including Cr are eluted during this step. The next fraction, containing Ti, Hf and Zr, is eluted by adding 3 ml 6 M HCl + 1 M HF. A post-Ti fraction is eluted with an additional 2 ml of 6 M HCl + 1 M HF, before the Mo fraction is eluted with 9 ml 3 M HNO₃.

At this point, the Cr fraction (collected as SL1 with the fluorides and matrix fraction) undergoes a separate procedure from the Ti and other fractions. The Cr fraction (SL1) undergoes two columns, first separating Cr from most matrix elements, and then purifying Cr.

The first column uses 4 ml of AG50-X8 (200-400 mesh) in PTFE columns, which is cleaned with repeated 0.5 cv of 6 M HCl and pre-conditioned in 20 ml 1 M HCl. The SL1 fraction is taken up in 0.4 ml of 9 M HCl and then diluted to 1 M HCl prior to loading. The sample is then washed in with 3.4 ml of 1 M HCl before Cr is eluted in 12 ml 1 M HCl, which is all collected in one beaker. Further matrix elements are eluted in 18 ml of 6 M HCl, before rinsing and washing out the columns.

The Cr cut is dried down and taken up in 0.4 ml of 1 M HNO₃, with 20 µl of H₂O₂ added to the samples to change the oxidation state from Cr(III) to Cr(VI) and are stored in the dark to prevent the decomposition of H₂O₂ for 5 days to prior to loading onto the second Cr column.

The second column for separating Cr uses 0.4 ml of AG50-X8 (200-400 mesh) that are added to micro-BioSpinTM columns. They are cleaned with 1 cv of 6 M HCl, additional 2

ml of 6 M HCl and 1 cv of Milli-Q water. The columns are then pre-conditioned in 1 ml of 1 M HNO₃, before the sample is loaded. Matrix elements are eluted in 16.4 ml of 1 M HNO₃, after which Cr is eluted and collected in 2.4 ml of 6 M HCl.

Table 5: Overview of Cr separation procedure using ion-exchange chromatography.

Ti + Cr column			Cr column 1			Cr column 2		
Step	Amount	Acid	Step	Amount	Acid	Step	Amount	Acid
Cleaning	2 CV	0.5 M HCl	Cleaning	2*0.5 CV	6 M HCl	Cleaning	1 cv	6 M HCl
	5 ml	6 M HCl +1 M HF		5 ml	H ₂ O		2 ml	6 M HCl
	1 CV	H ₂ O		5 ml	0.25 M HCl		1 cv	H ₂ O
Pre-con	6 ml	4 M HF	Pre-con	20 ml	1 M HCl	Pre-con	1 ml	1 M HNO ₃
Sample load (Cr+matrix)	10.5 ml	4 M HF	Sample load	3.6 ml	1 M HCl	Sample load	0.4 ml	1 M HNO ₃
Ti elution	3 ml	6 M HCl +1 M HF	Wash in	3.4 ml	1 M HCl	Matrix elution	16,4 ml	1 M HNO ₃
Post-Ti	2 ml	6 M HCl +1 M HF	Cr elution	12 ml	1 M HCl	Cr elution	2.4 ml	6 M HCl
Mo elution	9 ml	3 M HNO ₃	Matrix elution	18 ml	6 M HCl			

Colour-coded are the collected cuts that are loaded onto the next column. Precon: pre-conditioning.

2.7 Sample analysis

2.7.1 Petrographic description

Fragments from chondrule and clast samples were polished and carbon-coated for petrographic description using Scanning Electron Microscopy (SEM) and/or Electron Probe Microanalysis (EPMA) at Western, the University of New Mexico, and University of Bayreuth. These mounts were further used for Secondary Ionization Mass Spectrometry (SIMS) ^{26}Al - ^{26}Mg analyses at CRPG Nancy.

2.7.2 Mass spectrometry

2.7.2.1 Quadrupole inductively-coupled plasma-mass spectrometry (qICP-MS)

Major, minor and trace element analyses of samples were conducted using a Thermo *iCap* quadrupole ICP-MS with 100 $\mu\text{L}/\text{mn}$ nebuliser and glass spray chamber and ESI FAST autosampler at Western. Multi-element standards were used for calibration, generally ranging from concentrations of 0.1 ppb to 500 ppb. Additionally, for $^{27}\text{Al}/^{24}\text{Mg}$ ratio determination, gravimetric Al-Mg solutions were prepared to calibrate samples and rock standards. The range of $^{27}\text{Al}/^{24}\text{Mg}$ ratios was adjusted for each analytical session, depending on the types of samples. Over the entire time, they ranged from 0.001 to 500. For major and minor elements, as well as $^{27}\text{Al}/^{24}\text{Mg}$ ratios, analysis was performed using kinetic energy discrimination (KED) in collision cell mode, while trace element analysis was performed in standard mode. Collision cell mode reduces polyatomic interferences in lower mass ranges (e.g., $^{12}\text{C}^{14}\text{N}$ on ^{26}Mg) by using an inert gas (helium, in this case) to cause collisions that reduce the energy of polyatomic ions based on their larger size than analyte ions of the same mass. Terrestrial standards BCR-2 and San Carlos olivine, and bulk CV3 chondrite Allende were analyzed along with the samples to verify the accuracy of the elemental analysis. Uncertainties associated with $^{27}\text{Al}/^{24}\text{Mg}$ ratios are estimated to be $\pm 5\%$ based on repeat measurements of rock standards, with some exceptions for samples that were analyzed multiple times.

2.7.2.2 In situ ^{26}Al - ^{26}Mg analysis

The Mg isotope compositions of selected chondrules and clasts on polished mounts were analyzed by secondary ionization mass spectrometry (SIMS) using a Cameca ims 1280 HR2 ion probe at the Centre de Recherches Pétrologique et Géologique (CRPG) in Nancy, France, using procedures previously reported by Villeneuve et al. (2009). In short, $^{24}\text{Mg}^+$, $^{25}\text{Mg}^+$, $^{26}\text{Mg}^+$ and $^{27}\text{Al}^+$ were measured simultaneously in multi-collection mode using Faraday cups over 50 cycles, each lasting 10 s, after 240 s of pre-sputtering. Typical vacuum conditions during analysis were below 3×10^{-9} Torr. The primary O^- beam intensity was ~ 6 nA and typical spot sizes were ~ 10 μm , resulting between 1 and 2×10^8 counts per second on $^{24}\text{Mg}^+$ in olivine. Instrumental mass fractionation was corrected by repeated and interspersed analysis of terrestrial rock standards San Carlos olivine, BHVO and the Gold enstatite standard prior to, during, and after each analytical session.

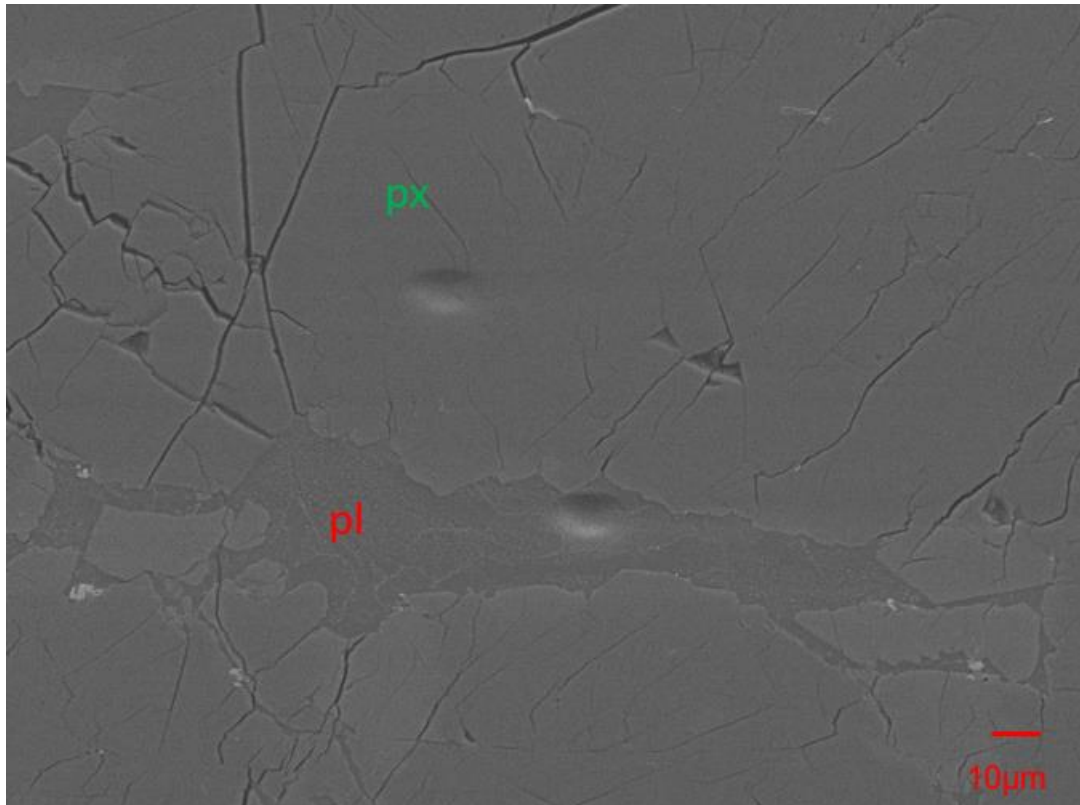


Figure 7: Scanning electron microscope (SEM) image of two sample spots in plagioclase (red) and pyroxene (green) in NWA 12261-I1 after SIMS analysis.

After SIMS analysis, samples and spots were inspected using scanning electron microscopy (SEM) to evaluate if the spots sampled pure mineral phases, or if mineral mixtures or cracks were present during sampling (Figure 7). Mixtures and cracks can affect the instrumental mass fractionation corrections and lead to high scatter amongst the data (Pape et al., 2019).

2.7.2.3 Multi-collector inductively-coupled plasma-mass spectrometry (MC-ICP-MS)

2.7.2.3.1 Lead isotope analysis

Lead isotope compositions were measured using a Thermo Fisher *Neptune Plus* MC-ICP-MS equipped with a Cetac Aridus II desolvating nebulizer at Université Clermont-Auvergne (UCA). In general, the protocols of Ancellin et al. (2019) were followed. The Pb samples were taken up in 0.5 to 1.5 ml of 0.05M HNO₃, depending on their Pb concentrations. Sample and standard solutions were both doped with the NBS 997 Tl standard ($^{205}\text{Tl}/^{203}\text{Tl} = 2.3871$; White et al., 2000) to a concentration of 1 ppb, and samples were bracketed with the NBS 981 Pb standard (Abouchami et al., 2000) to correct internally and externally for instrumental mass fractionation. In addition, the radiogenic NBS 983 Pb standard (Catanzaro et al., 1968) was included in the analytical sessions as a secondary standard owing to its higher $^{206}\text{Pb}/^{204}\text{Pb}$ more representative of the measurements of radiogenic samples such as achondrites, and is plotted in Figure 8. Before every standard and sample measurement, a background measurement with baseline analysis was taken, which was subtracted from the standards or samples during data reduction. Peak center and baseline analysis were performed on all standard measurements but only on samples diluted in 1.5 ml of 0.05M HNO₃, to ensure sufficient material for was available for the isotopic analysis.

Samples were introduced by a Cetac Aridus II desolvating nebulizer at an uptake rate of 100 $\mu\text{l}/\text{min}$. Sample gas flow was ~ 1 l/min, while N₂ gas was added to the at ~ 0.8 l/min to increase stability of the plasma. With 1 ppb NBS 981 standard solutions, the typical intensity on ^{204}Pb was ~ 20 mV, and ~ 0.4 V on ^{206}Pb , while the radiogenic NBS 983 standard produced intensities of ~ 0.8 mV and ~ 2 V on ^{204}Pb and ^{206}Pb , respectively.

Some samples were analyzed with a secondary electron multiplier (SEM) on ^{204}Pb , as the intensity in a Faraday cup (FC) setup would be below 0.3 mV. Using the SEM setup allows for better quantification of low ^{204}Pb ($0.3 \text{ mV} \approx 25000$ counts per second) but has the disadvantage that ^{208}Pb cannot be measured (Table 6). Sample analyses consisted of 60 cycles with 8.4 s integration time in the FC setup, whereas the analyses in the SEM setup consisted of only 25 cycles, with no peak center or baseline analysis. Samples analyzed using the SEM setup were later analyzed in the FC setup over 10 cycles to roughly quantify $^{208}\text{Pb}/^{206}\text{Pb}$, if enough material was available. For ^{206}Pb , ^{207}Pb and ^{208}Pb , $10^{11} \Omega$ amplifiers were used, whereas a $10^{12} \Omega$ amplifier was used for ^{204}Pb .

Table 6: Overview of cup configurations used for Pb isotope analysis between Faraday cup (FC) and Secondary Electron Multiplier (SEM) setups.

Analysis	L3	L2	L1	C (or IC1)	H1	H2	H3
Pb (FC)	^{202}Hg	^{203}Tl	^{204}Pb	^{205}Tl	^{206}Pb	^{207}Pb	^{208}Pb
Pb (SEM)		^{202}Hg	^{203}Tl	^{204}Pb	^{205}Tl	^{206}Pb	^{207}Pb

The measured Pb isotopic data were reduced offline in Excel and R using a self-written code, and “inverse” isochrons were calculated using Model 1 York regressions in IsoplotR (Vermeesch, 2018) and using the Isoplot 4.15 add-in in Excel (Ludwig, 2008). Total procedural blanks, including chemistry, generally ranged from 0.3 to 2.4 pg, with one outlier blank from the processing of the QC 001-C1 sample being 14 pg, and compositions were corrected according to their sample-to-blank ratios, following the equations provided in the Appendix of Bouvier et al. (2007). Errors on $^{204}\text{Pb}/^{206}\text{Pb}$ and $^{207}\text{Pb}/^{206}\text{Pb}$ ratios for isochron regression were either the correlated errors or the daily external reproducibility of the NBS 981 or NBS 983 standards (depending on which standard is more representative of the sample ratios), whichever is larger. Measurements of the $^{206}\text{Pb}/^{204}\text{Pb}$ ratios of secondary standard NBS 983 over all sessions are within uncertainty of the accepted value (Catanzaro et al., 1968: Figure 8). The uncertainty of the Pb-Pb ages determined from isochron regressions include the propagated uncertainty

of the U isotope composition. For chondrules, the bulk Solar System $^{238}\text{U}/^{235}\text{U}$ ratio of 137.786 ± 0.013 (Connelly et al., 2012) was used to calculate their age.

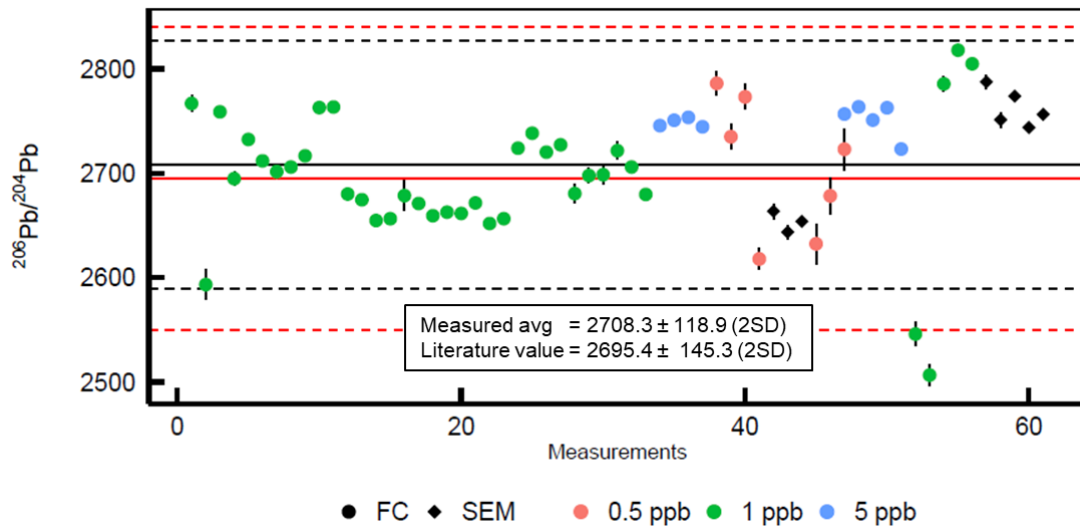


Figure 8: Individual analyses of $^{206}\text{Pb}/^{204}\text{Pb}$ ratios of the secondary standard NBS 983 over all sessions, using both the Faraday cup and SEM setup, compared to the accepted value of 2695.4 ± 145.3 (Catanzaro et al., 1968). The concentration of the NBS997 TI standard is 1 ppb for 0.5 ppb and 1 ppb NBS 983 measurements, and 2 ppb for measurements with 5 ppb NBS 983. Using the SEM setup, NBS 983 was 0.25 ppb and NBS 997 1 ppb. Uncertainties on individual analyses are smaller than their symbol, where not visible.

2.7.2.3.2 Uranium isotope analysis

Analysis of the U isotope composition of a bulk sample and leached pyroxenes (included W5+6, W7, W8 and R) of EC 002, as well as leached bulk sample of NWA 10463 (included W4 to R), were performed by Dr. Yvonne Roebbert at the Leibniz Universität Hannover, following the protocols of Roebbert et al. (2021). The collected matrix elements of two aliquots of the terrestrial standard BCR-2, equal to ~ 5 ng and ~ 20 ng of U that underwent prior Pb separation (as for EC 002), were analyzed to ensure that no U isotope fractionation occurred during the Pb chemistry. The double-spike solution IRMM 3636 was used to correct for mass-bias (Richter et al., 2010). Each sample was analyzed twice, bracketed by the CRM-112a standard, over 60 cycles at 4 s integration time. Concentrations between standards and samples were individually matched and intensities

on ^{238}U were between 2.5 V and 12 V. The standard IRMM 184 was analyzed along with the samples (Table 7).

Table 7: Weighted average U isotope compositions of EC 002 bulk and pyroxene samples, NWA 10463 bulk leachates, and of BCR-2 terrestrial basalt standard and secondary standard IRMM 184.

Sample	Mass [mg]	U [ng]	$^{238}\text{U}/^{235}\text{U}$	2σ	n	^{238}U intensity [V]
EC 002 Bulk	~120	15	137.819	0.007	2	12
EC 002 Px leachates	~160	3	137.766	0.027	2	2.5
NWA 10463 bulk leachates	~ 210	3	137.770	0.110	2	2.8
BCR-2 a	11.8	20	137.797	0.017	2	15
BCR-2 b	2.9	5	137.815	0.046	2	4
IRMM 184			137.668	0.008	8	2.5 - 15

2.7.2.3.3 Magnesium isotope analysis

Initial analyses of the Mg isotope standards were conducted at the Water Test Centre at Trent University in Peterborough, using a Thermo Fischer *Neptune* multi-collector inductively-coupled plasma mass spectrometry (MC-ICP-MS). The Mg isotope compositions chondrules, clasts and achondrite fractions were subsequently analyzed by a Thermo Fisher *Neptune Plus* MC-ICP-MS at the Friedrich-Alexander-Universität (FAU) in Erlangen. The ^{24}Mg , ^{25}Mg and ^{26}Mg ion beams were measured simultaneously on the L4, Center and H4 Faraday cups, respectively, with a $10^{10} \Omega$ amplifier on the L4 cup, and run in medium resolution mode ($M/\Delta M \sim 4000$) with a Jet sample cone and H skimmer cone interface. This combination resulted in lower sensitivity than with a Jet + X skimmer cone setup, but increased signal stability over multiple standard analyses, similar to the findings of Chen et al. (2018) and Gou et al. (2019).

The sample and standard solutions were diluted to approximately 300 ppb (≈ 90 V on ^{24}Mg), where feasible, in 2% HNO_3 and matched to within 5% or less of their concentrations. Solutions were introduced using a Cetac Aridus II desolvating nebulizer

system at an uptake rate of 50 $\mu\text{l}/\text{min}$. The sample gas flow was $\sim 1 \text{ L}/\text{min}$, while the use of N_2 gas, used to stabilize the plasma, was avoided due to potential polyatomic interferences with C affecting Mg isotope measurements. Standard-sample bracketing with the DSM3 standard was used to correct for mass fractionation and instrumental drift. Generally, analyses consisted of four sample measurements bracketed by five standard measurements, with each measurement consisting of a peak center, 20 cycles at 8.4 s of integration time followed by 150 s of wash time. The instrumental background was measured prior to each sample and standard analysis. Total procedural blanks, including chemistry, were less than 5 ng, a negligible amount relative to the amount of Mg in the samples ($\approx 75 \mu\text{g}$).

Table 8: Al-Mg isotope data of solution standards Cambridge-1 and the in-house Mg solution standard (“UWO ICP Std”), and terrestrial rock standard San Carlos olivine and bulk CV3 chondrite Allende.

Standards	$^{27}\text{Al}/$ ^{24}Mg	\pm	$\delta^{25}\text{Mg}$ [‰]	2SE	$\delta^{26}\text{Mg}$ [‰]	2SE	$\delta^{26}\text{Mg}$ * [‰]	2SE	n
Cambridge-1			-1.365	0.020	-2.645	0.040	-0.002	0.007	27
<i>literature</i> ^a			-1.343	0.036	-2.597	0.042	n.r.	n.r.	49
<i>literature</i> ^b			-1.335	0.032	-2.606	0.040	n.r.	n.r.	
San Carlos olivine	0.0021	0.0009	-0.149	0.012	-0.322	0.025	-0.008	0.007	15
<i>literature</i> ^c	0.0031	0.0004	-0.16	0.01	-0.31	0.02	0.00	0.01	36
Allende	0.1300	0.0039	-0.171	0.027	-0.323	0.052	0.013	0.008	12
<i>literature</i> ^c	0.1294	0.0007	-0.16	0.01	-0.29	0.02	0.03	0.02	7
<i>literature</i> ^d			-0.15	0.01	-0.30	0.02	n.r.	n.r.	
UWO ICP Std ^d			-0.329	0.027	-0.627	0.037	0.018	0.022	12
UWO ICP Std ^e			-0.296	0.027	-0.594	0.030	-0.013	0.031	8
UWO ICP Std ^f			-0.323	0.020	-0.626	0.016	0.006	0.041	8
UWO ICP Std ^g			-0.309	0.023	-0.610	0.024	-0.003	0.033	16
UWO ICP Std ^h			-0.318	0.018	-0.617	0.021	0.006	0.021	28

n.r.: not reported.

^a An and Huang (2014)

^b Vogl et al. (2020)

^c Bouvier et al. (2013)

^d Teng et al. (2010)

^e unprocessed

^f column processed

^g added to Mg-free matrices of terrestrial standards BCR-2 and BIR-1, column processed

^h all column-processed combined (f+g)

ⁱ all standard solution measurements combined (f+g+h)

Magnesium isotope data is reported in δ -notation (in per mil), the relative differences of $^x\text{Mg}/^{24}\text{Mg}$ ratios of the sample to the bracketing standard, where $x = 25$ or 26 :

$$\delta \text{ } ^x\text{Mg} = \left(\frac{(^x\text{Mg}/^{24}\text{Mg})_{\text{sample}}}{(^x\text{Mg}/^{24}\text{Mg})_{\text{standard}}} - 1 \right) \times 1000 \quad (\text{Eq. 6})$$

Mass-independent variations in ^{26}Mg due to ^{26}Al decay ($\delta^{26}\text{Mg}^*$) were determined by internally normalizing the measured $^{26}\text{Mg}/^{24}\text{Mg}$ ratio to $^{25}\text{Mg}/^{24}\text{Mg} = 0.12663$ (Catanzaro et al., 1966) using the exponential law with fractionation factor $\beta = 0.511$:

$$\delta^{26}\text{Mg}^* = (\delta^{26}\text{Mg} - \left(1 + \frac{\delta^{25}\text{Mg}}{1000} \right)^{\left(\frac{1}{\beta} \right)} - 1) \times 1000 \quad (\text{Eq. 7})$$

To assess instrumental mass fractionation and the fractionation factor, the standard average values were plotted in linearized versions (Figure 9), with $\delta^{26}\text{Mg}$ vs. $\delta^{25}\text{Mg}$ (Eq. 3, after Young et al., 2004).

$$\delta' \text{ } ^x\text{Mg} = 1000 \times \ln \left(\frac{\delta \text{ } ^x\text{Mg}}{1000} + 1 \right) \quad (\text{Eq. 8})$$

The best-fit line has a slope of 0.521 ± 0.014 (Figure 9) within error of the equilibrium (0.521), kinetic (0.511) and Rayleigh (0.516) fractionation factors (Davis et al., 2015).

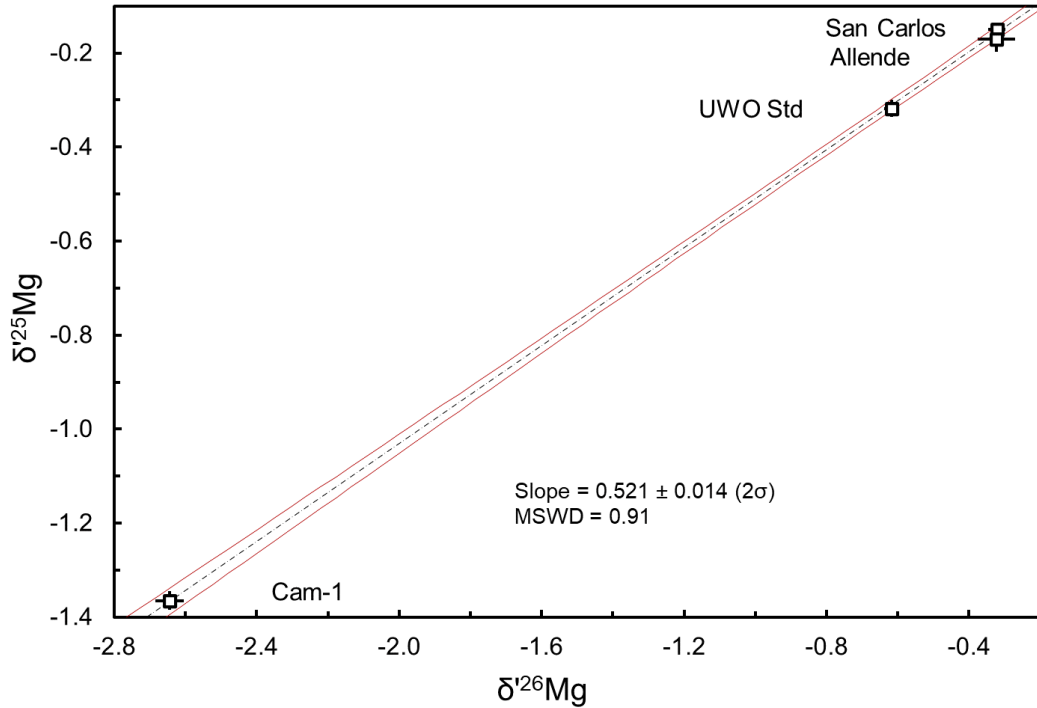


Figure 9: Linearized (Eq. 8) Mg isotope composition of terrestrial rock standards, with a best-fit line whose slope represents the fractionation factor $\beta = 0.521$.

2.7.2.3.4 Chromium isotope analysis

Chondrules and clasts were analyzed for their Cr isotope composition at ETH Zürich using a Thermo Scientific *Neptune Plus* MC-ICP-MS with a Cetac Aridus II desolvating nebulizer introduction system following the protocols described in Bischoff et al. (2019). Total Cr masses of the samples ranged from ~ 25 to $50 \mu\text{g}$, with procedural blanks in the range. Samples were diluted in 2% HNO_3 to a concentration of approximately 6 ppm, corresponding to a signal intensity of ~ 60 V on ^{52}Cr in medium-resolution. The four Cr isotopes ^{50}Cr , ^{52}Cr , ^{53}Cr and ^{54}Cr are measured on the H2, C, L1 and L2 cups, respectively, while ^{49}Ti , ^{51}V and ^{56}Fe are measured on cups H4, H1 and L4, respectively, to monitor any potential interferences of their isotopes on the Cr isotopes (Table 9).

Table 9: Faraday cup configuration for Cr isotope analysis by MC-ICP-MS.

H4	H3	H2	H1	C	L1	L1	L3	L4
^{49}Ti		^{50}Cr	^{51}V	^{52}Cr	^{53}Cr	^{54}Cr		^{56}Fe

Measurements are acquired over 100 cycles with 4s integration time each, with sample measurements repeated between 4 to 9 times over multiple sessions. Measured ratios are normalized to $^{50}\text{Cr}/^{52}\text{Cr} = 0.051859$ (Shields et al., 1966) using the exponential law to correct for instrumental mass bias and are reported as parts per ten thousand deviations from the NIST SRM 979 bracketing standard ($\epsilon^{53}\text{Cr}$ and $\epsilon^{54}\text{Cr}$), where $x = 53$ or 54 (Eq. 9):

$$\epsilon^{x\text{Cr}} = \left(\frac{(^{x}\text{Cr}/^{52}\text{Cr})_{\text{sample}}}{(^{x}\text{Cr}/^{52}\text{Cr})_{\text{standard}}} - 1 \right) \times 10^4 \text{‰} \quad (\text{Eq. 9})$$

The external reproducibility for $\epsilon^{53}\text{Cr}$ and $\epsilon^{54}\text{Cr}$ are 14 and 26 ppm (2SE), respectively, based on repeated analysis of the DTS-2b dunite standard (Table 10) Total procedural blanks, including chemistry, were less 5 ng, insignificant compared to the 25 to 50 μg of Cr in the samples.

Table 10: Average $\epsilon^{54}\text{Cr}$ composition of the DTS-2b dunite standard, measured over four sessions and compared to literature values (Schiller et al., 2014)

	$\epsilon^{54}\text{Cr}$	2SE
this study	0.076	0.026
Schiller et al. (2014)	0.077	0.028

3 Chronology and Cr isotope composition of chondrules and clasts in ordinary chondrites

The main components of ordinary chondrites are chondrules and matrix, with rare refractory inclusions, such as Ca-Al-rich inclusions (CAIs) or amoeboid olivine aggregates (AOAs), making up less than 1% (e.g., Weisberg et al., 2006). In addition to chondrules, which are covered in the introduction chapter, large igneous inclusions and clasts are found in ~ 4% of ordinary chondrites (Bridges and Hutchison, 1997). These large igneous clasts, also referred to in the literature as “mega-” or “macrochondrules” (e.g. Ruzicka et al., 1998), “large igneous-textured inclusions” (Ruzicka et al., 2000; Ruzicka et al., 2012) and “melt-rock clasts” (e.g., Rubin et al., 1983), among others, are somewhat enigmatic regarding their formation and heritage and have been the subject of various studies over the past couple of decades.

Some clasts are proposed to have formed via the same mechanisms as chondrules have, and show vapour-fractionated bulk elemental trends, while other clasts and inclusions may have been the result of impacts and localized melting (Ruzicka et al., 2019). Oxygen isotope studies of chondrules, clasts and fragments have not only shown substantial accretionary mixing among the H, L and LL chondrite reservoirs (Clayton et al., 1991; Ruzicka et al., 2019) but also fragments from the eucrite parent body (Hyde et al., 2019) and the outer Solar System (Kebukawa et al., 2019) embedded in ordinary chondrites. These findings demonstrate the potential impact that studying such inclusions can have on our understanding of processes taking place in the early Solar System. Recently, inclusions and clasts have been studied by using the I-Xe and Hf-W chronometers, showing that many inclusions formed during the same time interval as chondrules, but also that some inclusions may have experienced a protracted thermal history lasting up to 50 Ma after CAI formation (Almeida et al., 2017; Crowther et al., 2018; Ruzicka et al., 2018). In order to further expand our knowledge of the origin and heritage of large igneous inclusions, we investigated two anomalously large inclusions in L3.2 chondrite Paposo 004 (hereafter Pap-I1; Figure 10) and in the H3 chondrite NWA 12261 (NWA 12261-I1 hereafter). We analyzed selected individual chondrules and clasts for their Pb isotope compositions to determine their absolute ages, their mineral isochron ^{26}Al - ^{26}Mg

age by SIMS and bulk Mg and Cr isotope compositions of the clasts. Additionally, for Pap-II, the bulk triple O isotope composition and I-Xe systematics were obtained.

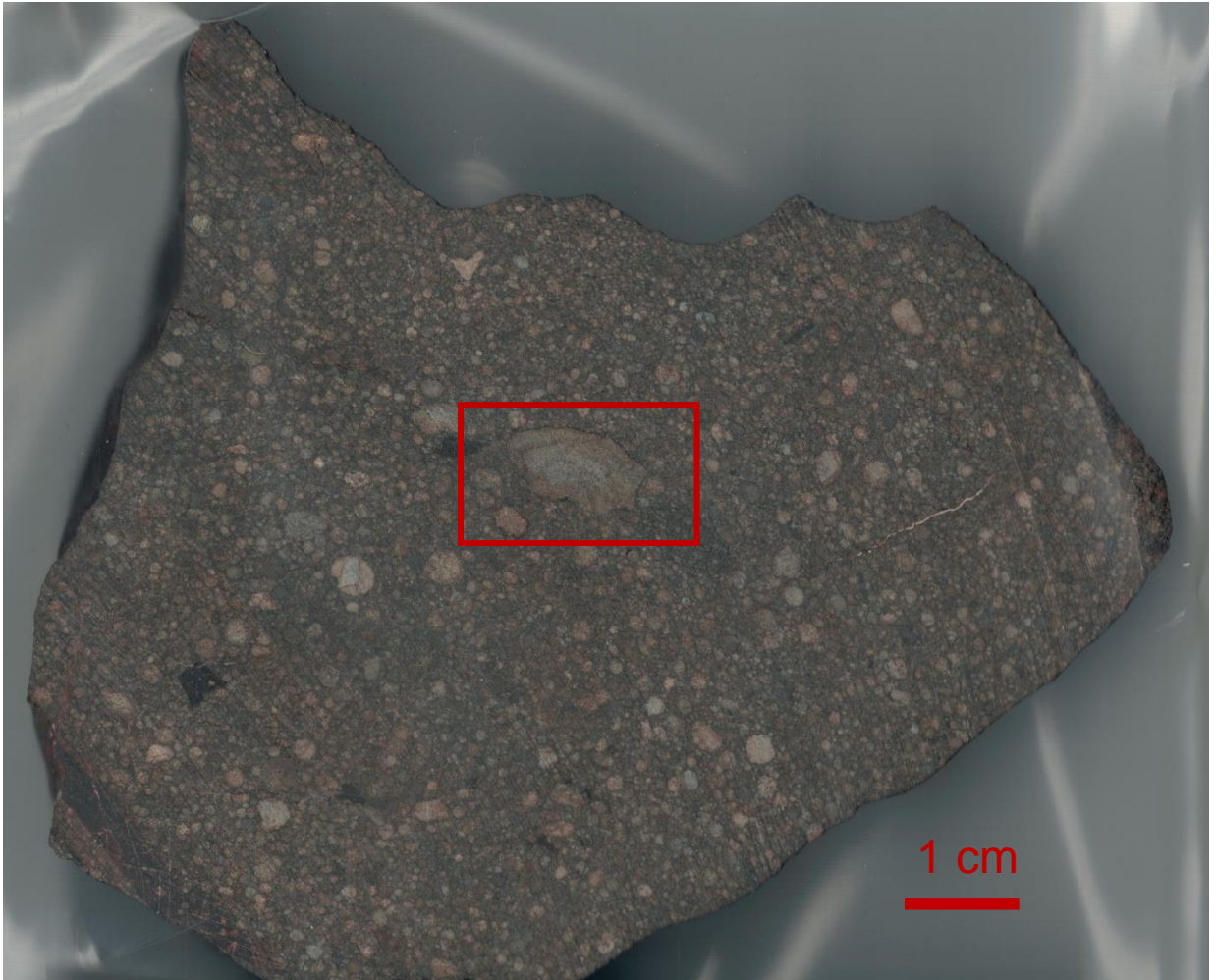


Figure 10: Image of the L3.2 chondrite Paposo 004, with the Pap-II inclusion marked.

3.1 Methods

For the Pap-II, in addition to the methods described in chapter 2, the O and Cr isotope compositions, as well as the I-Xe age, were obtained by collaborators (see Co-Authorship statement). The sample was crushed and homogenized from a 10 mg whole-rock chip, and the triple O isotope composition was analyzed by infrared laser-assisted fluorination by Jennifer Gibson and Dr. Richard Greenwood at the Open University, United Kingdom, following the protocols of Greenwood et al. (2017).

The Cr isotope composition was obtained on a ~ 5 mg aliquot from the fraction dissolved at UWO, and underwent Cr separation and analysis by Dr. Liping Qin at the CAS Key Laboratory and CAS Center for Excellence in Comparative Planetology in Hefei, China. The analysis followed the protocols of Qin et al. (2010).

The I-Xe age was determined from a whole-rock chip by nuclear irradiation and analyzed by Dr. Sarah Crowther using the Refrigerator Enhanced Laser Analyser for Xenon (RELAX) mass spectrometer at the University of Manchester, United Kingdom and followed the protocols described in Crowther et al. (2008).

For the other clast and chondrule samples, the Methods described in Chapter 2 were used.

3.2 Results

3.2.1 Petrology of chondrules and clasts

Listed in **Table 11** are all analyzed samples, with petrological information, shock and weathering stages and origin of the meteorite samples.

Table 11: Overview of host meteorites of chondrules and clasts.

Meteorite	total mass [g]	Petrologic type	Weathering grade	Shock stage	from
Northwest Africa 8007 ^a	664	L3.2	W1	n.a.	SkyFall Meteorites
Northwest Africa 8276 ^b	789	L3.00	W1	n.a.	UNM, UAlberta
Northwest Africa 10854 ^c	741	L3	W1	S2	Aras Jonikas Meteorites
Northwest Africa 11672 ^d	282	L3	W0/1	S2	Aras Jonikas Meteorites
Northwest Africa 12261 ^e	21600	H3	W1/2	S2	Big Bang Meteorites
Paposo 004 ^a	8250	L3.1	W1	n.a.	Museo del Meteorito
Quebrada Chimborazo 001 ^f	598	Cba	n.a.	n.a.	Labenne Meteorites
Tarda ^g	4000	C2-ung	W0	low	UNM

UNM: Carl Agee, University of New Mexico; UAlberta: Chris Herd, University of Alberta. ^a Meteoritical Bulletin 102 (Ruzicka et al., 2015); ^b Meteoritical Bulletin 103 (Ruzicka et al., 2017); ^c Meteoritical Bulletin 105 (Bouvier et al., 2017); ^d Meteoritical Bulletin 107 (Gattacceca et al., 2020a); ^e Meteoritical

Bulletin 108 (Gattacceca et al., 2020b); ^f Meteoritical Bulletin 104 (Bouvier et al., 2017); ^g Meteoritical Bulletin 109 (Gattacceca et al., 2021).

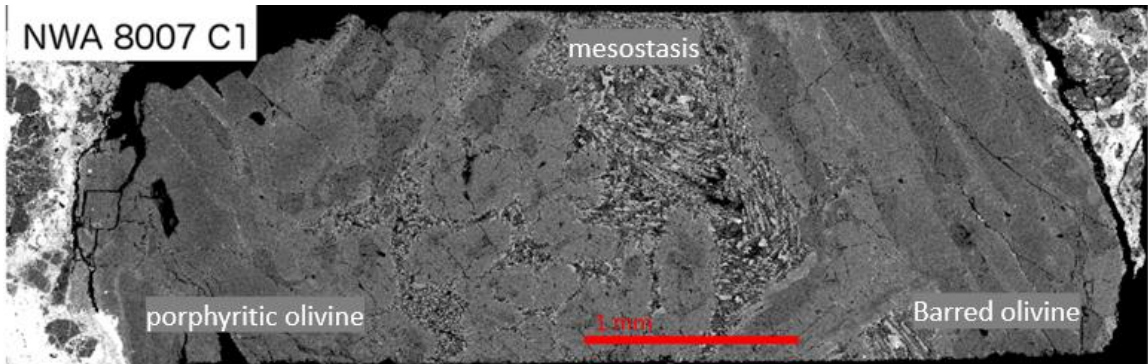


Figure 11: Backscatter electron (BSE) image of a chip of NWA 8001-C1 with a barred olivine texture on the right and a porphyritic texture on the left side of the chondrule. A large mesostasis pocket is located in between the two different textures.

NWA 8007-C1: The chondrule has a barred olivine and porphyritic texture with Mg-rich olivine and enstatite and a large (~ 1 mm × 0.8 mm) mesostasis pocket with sodic plagioclase and Ca-rich clinopyroxene (Figure 11)

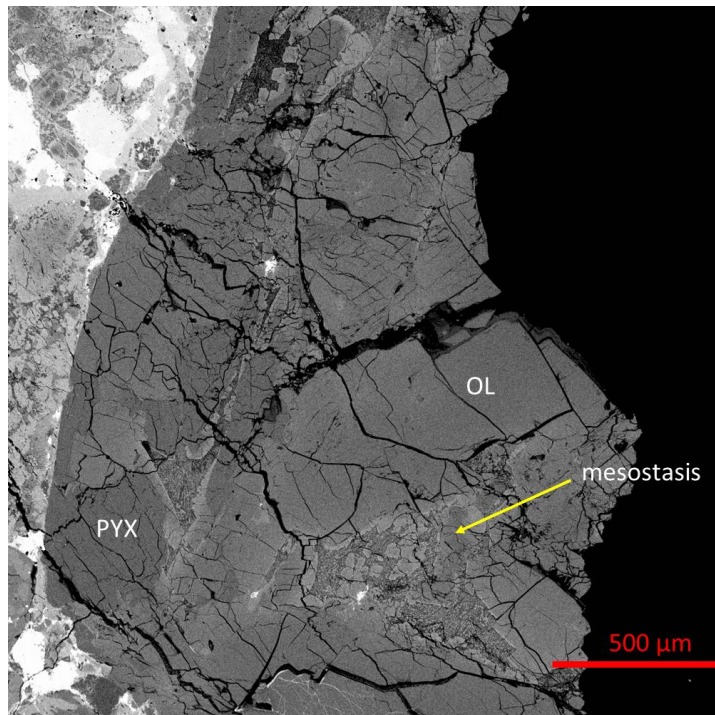


Figure 12: BSE image of a chip of chondrule NWA 8276-C1, courtesy of Dr. Steven Simon, UNM.

NWA 8276-C1: Porphyritic type II AB chondrule that is made up mostly of olivine ($Fa_{14.0} \pm 1.4$ ($n=4$)) and pyroxene (both Ca-rich and -poor). Several large pockets of Al-rich mesostasis are present, some of which included quenched crystals (Figure 12, Appendix 2).

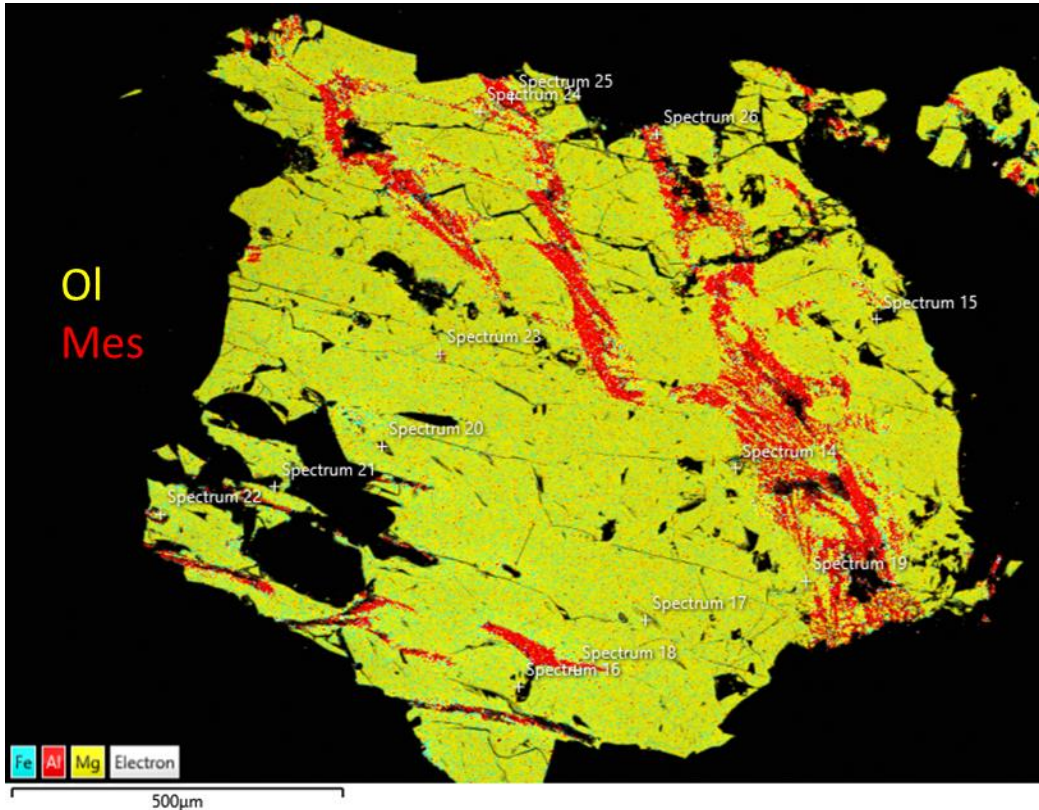


Figure 13: Energy-dispersed spectrum (EDS) image of a chip of NWA 8276-C2.

NWA 8276-C2: Type II AB chondrules, porphyritic with mostly olivine and some glassy mesostasis (Figure 13).

NWA 8276-C3: Type II AB PO(P) chondrule with a porphyritic texture, dominated by olivine with some pyroxene (Figure 14).

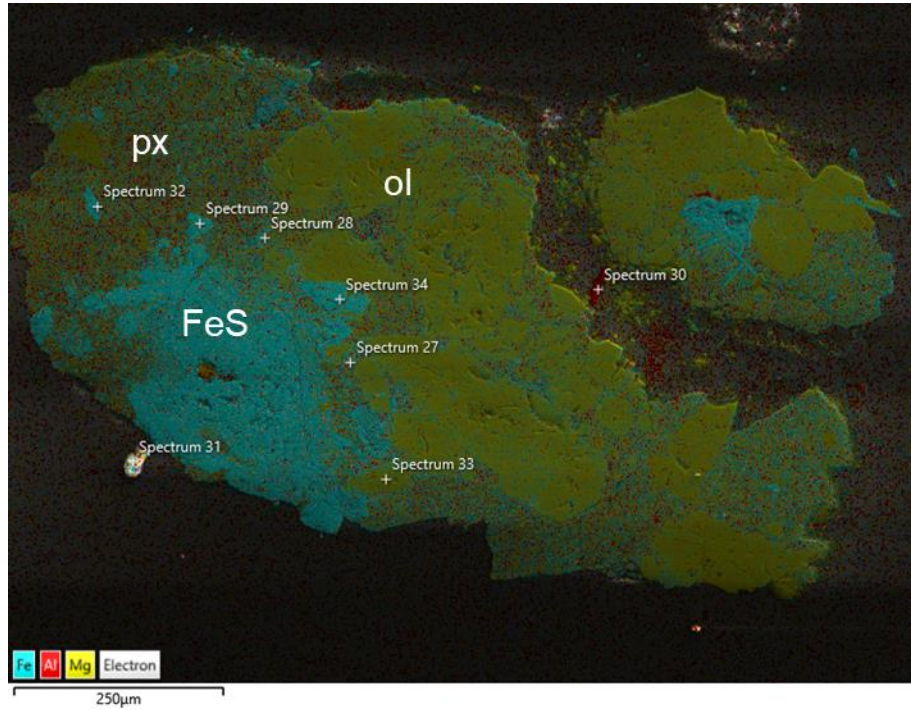


Figure 14: Energy-dispersed spectrum (EDS) image of a chip of chondrule NWA 8276-C3

NWA 10854-C1: Barred olivine chondrule with olivine ($\text{Fa}_{11.6 \pm 5.8}$, $n=5$), some pyroxene ($\text{Fs}_{7.1 \pm 9.1} \text{Wo}_{1.9 \pm 2.4}$, $n=5$) and small plagioclase pockets ($\sim 10 \mu\text{m}$). Type I AB chondrule (Figure 15, Appendix 3).

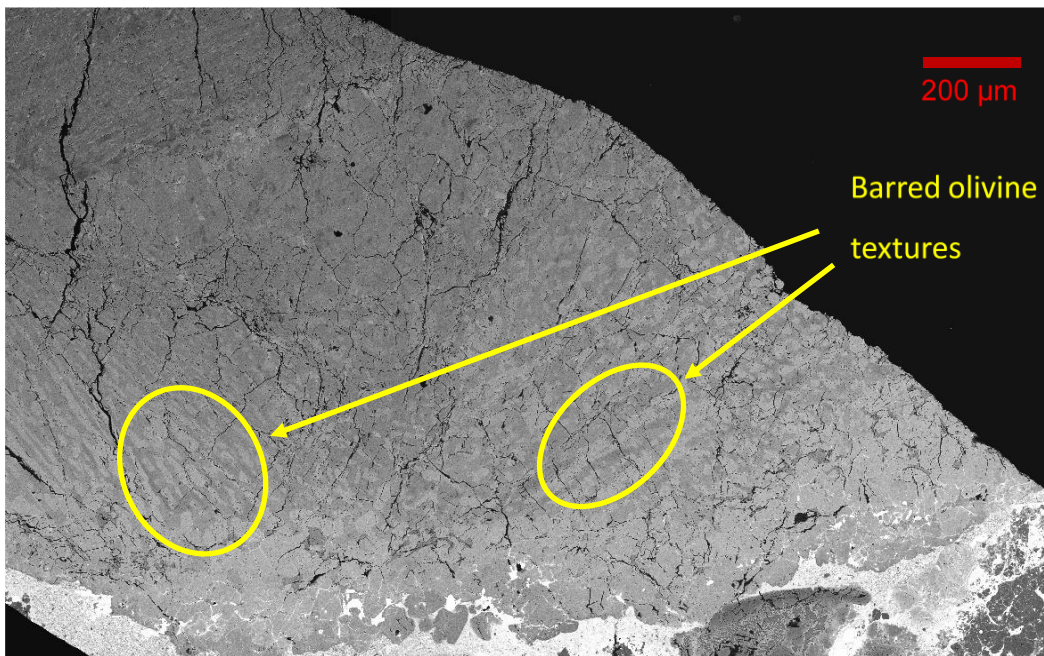


Figure 15: BSE image of a chip of chondrule NWA 10854-C1, courtesy of Dr. Steven Simon, UNM.

NWA 10854-C2: Porphyritic type II AB chondrule, with forsteritic phenocrysts, surrounded by finer olivine and pyroxene. Feldspathic glass in ~ 20 μm large pockets is present between mafic grains (Figure 16).

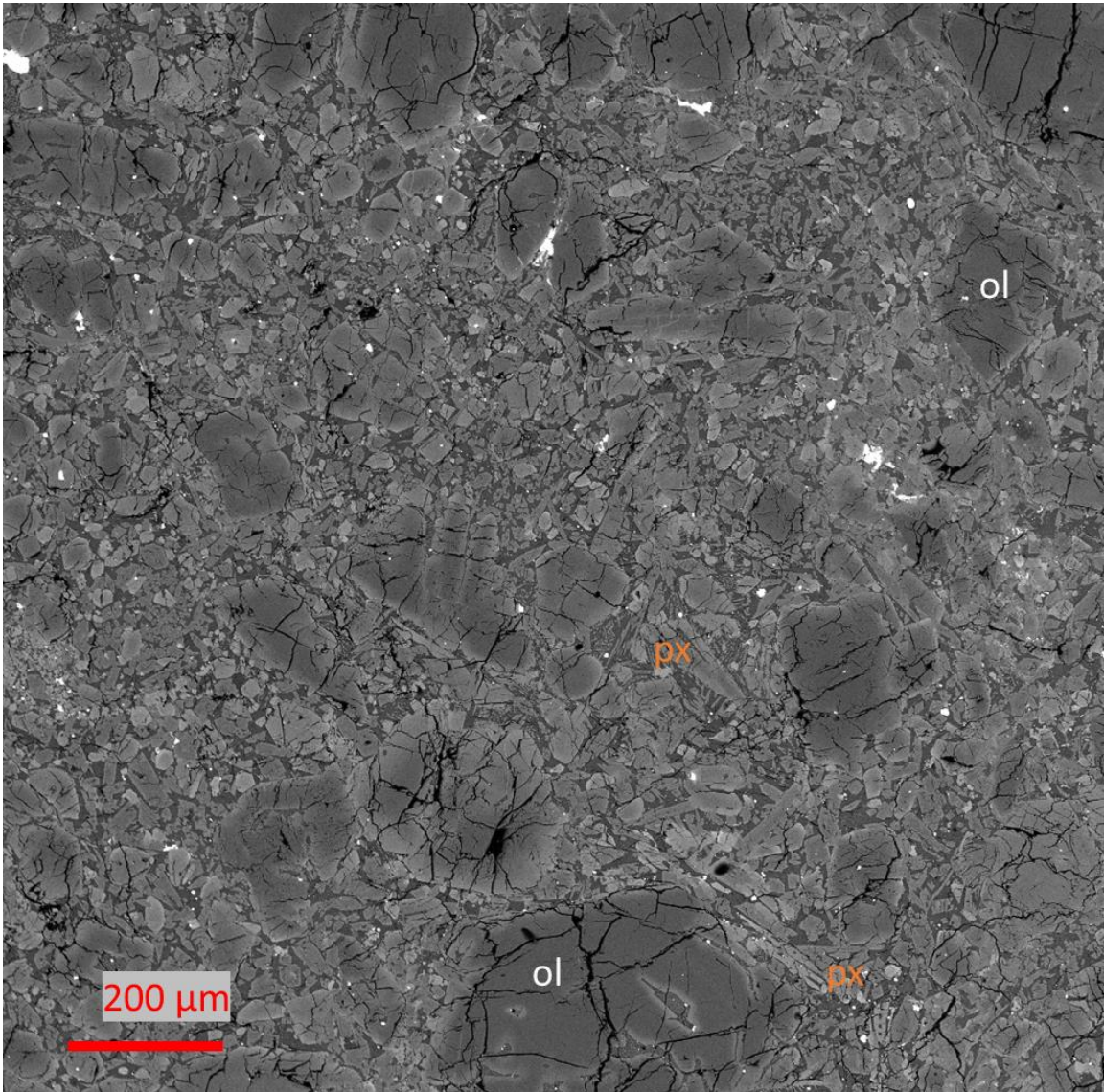


Figure 16: BSE image of chondrule C2 from NWA 10854, courtesy of Dr. Steven Simon, UNM.

NWA 10854-C3: Type II AB chondrule with porphyritic texture of similarly sized (~ 100 μm) olivine ($\text{Fa}_{22.7\pm 2.7}$, $n=12$) and low-Ca pyroxene grains ($\text{Fs}_{19.1\pm 5.6}\text{Wo}_{3.4\pm 4.5}$, $n=14$). Recrystallized low-Na plagioclase ($\text{An}_{84.4\pm 1.2}$, $n=4$) filled in between the olivine and pyroxene grains (Figure 17, Appendix 4).

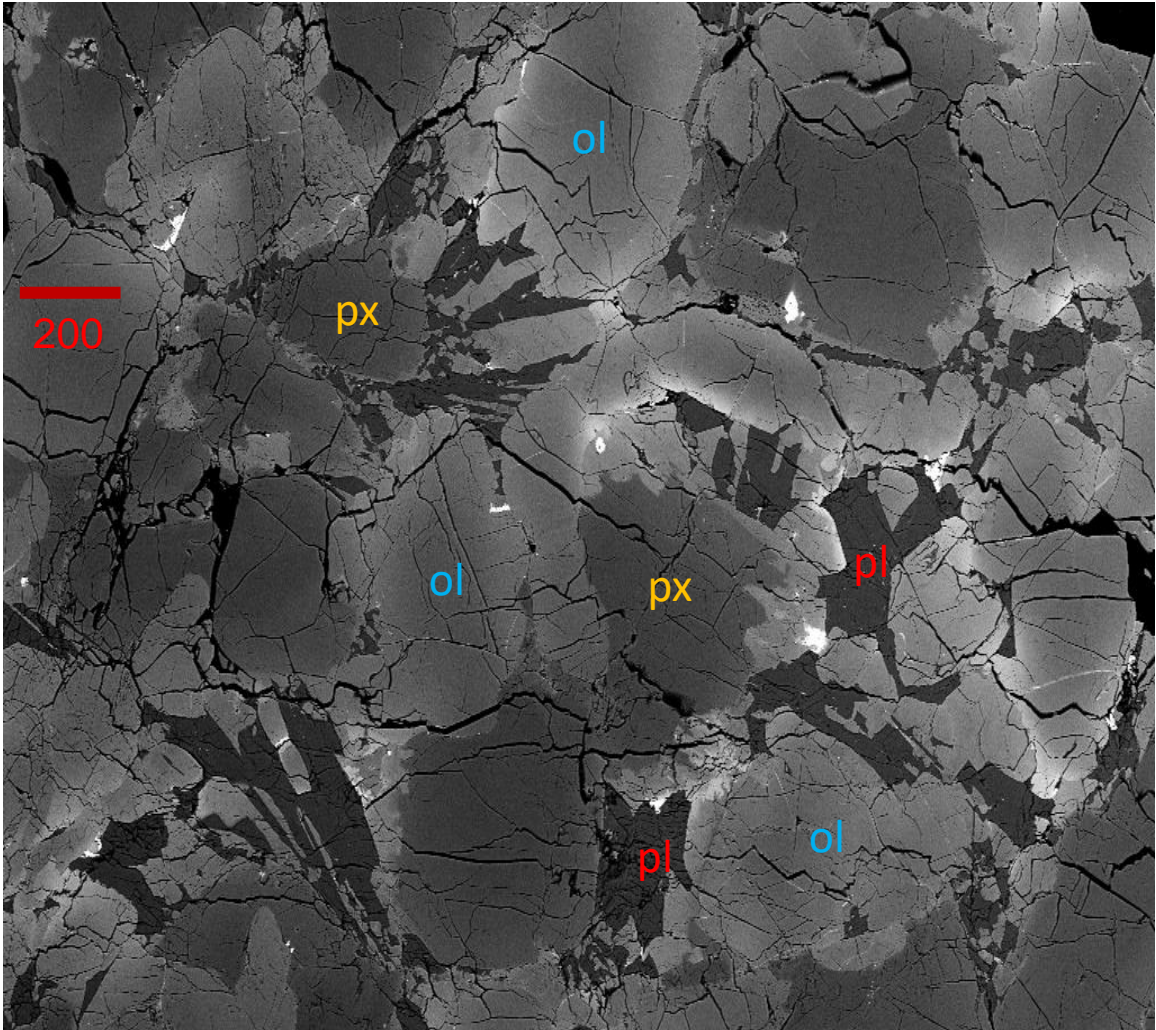


Figure 17: Secondary electron image of NWA 10854-C3. Re-crystallized plagioclase is labelled in red, low-Ca pyroxene in yellow and olivine in blue.

NWA 10854-C5: Type I AB chondrule, with Fe-poor olivine ($\text{Fa}_{8.8\pm 0.7}$, $n=11$) and pyroxene ($\text{Fs}_{7.8\pm 1.7}\text{Wo}_{20.2\pm 20.0}$, $n=17$) compositions. Both Ca-rich and Ca-poor pyroxene are present, though Fe content stays consistent between the two phases (Figure 18, Appendix 5).

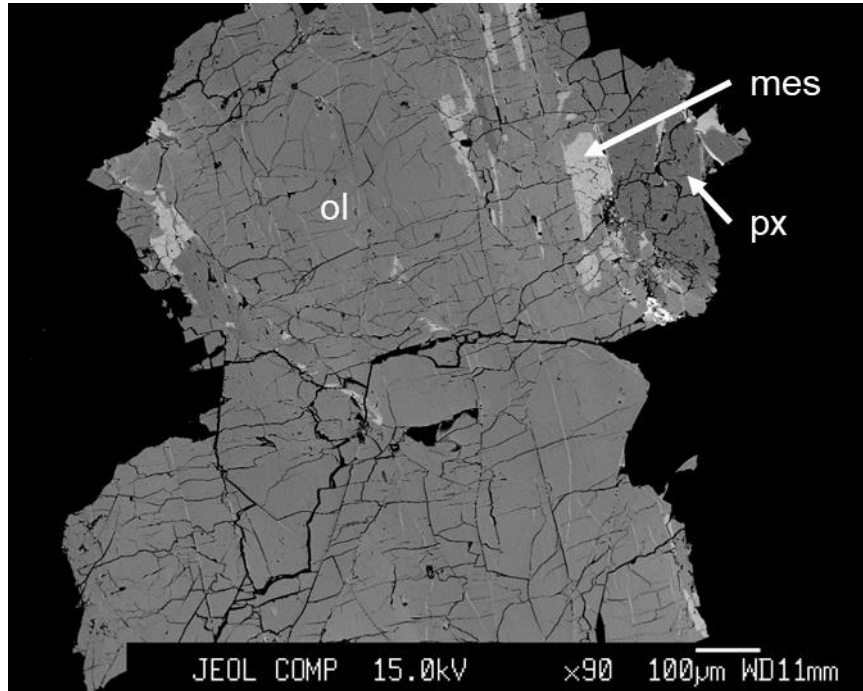


Figure 18: Backscatter electron (BSE) image of a chip of chondrule NWA 10854-C5
 NWA 10854-C6: Type II AB chondrule, mostly olivine with some pyroxene and mesostasis pockets (Figure 19)

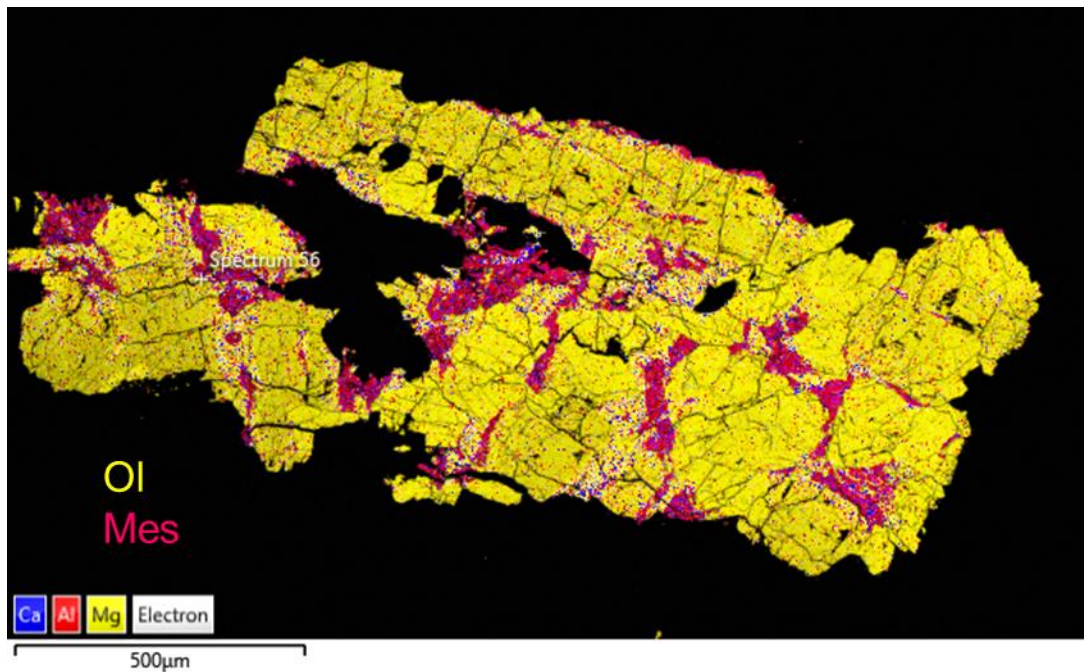


Figure 19: Energy-dispersed spectrum (EDS) image of a chip of chondrule NWA 10854-C6.

NWA 11672-C1: Type II AB chondrule with a porphyritic texture and ~ 5% metal and sulfide nodules, consistent olivine compositions ($\text{Fa}_{16.0\pm 0.7}$, $n=15$), both low- and high-Ca pyroxene ($\text{Fs}_{12.7\pm 3.7}\text{Wo}_{28.6\pm 24.0}$, $n=7$), and re-crystallized plagioclase ($\text{An}_{86.3\pm 1.2}$, $n=8$). Olivine and pyroxene are visually not discernible (Figure 20, Appendix 6).

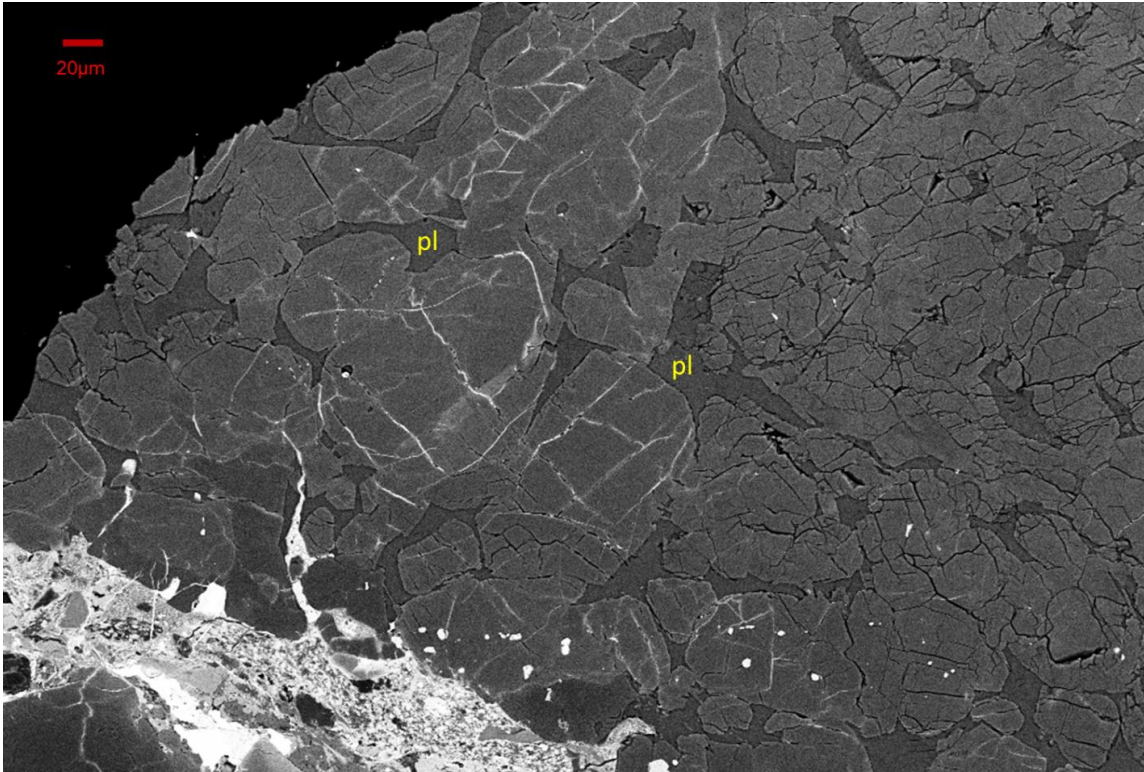


Figure 20: Secondary electron image of NWA 11672-C1. Re-crystallized plagioclase is labelled in yellow. Olivine and pyroxene are not visually distinguishable.

NWA 12261-II: Large igneous inclusion in H3 chondrite NWA 12261, contains zoned olivine with Fe contents at 10 wt% in the core and 30 wt% in the rim. Pyroxene is Ca-free in the core and more Ca-rich in the rims, with consistent Fe content of 10 wt% throughout the grains. Quenched mesostasis has plagioclase composition with additional FeO. Olivine and pyroxene are visually hard to distinguish (Figure 21).

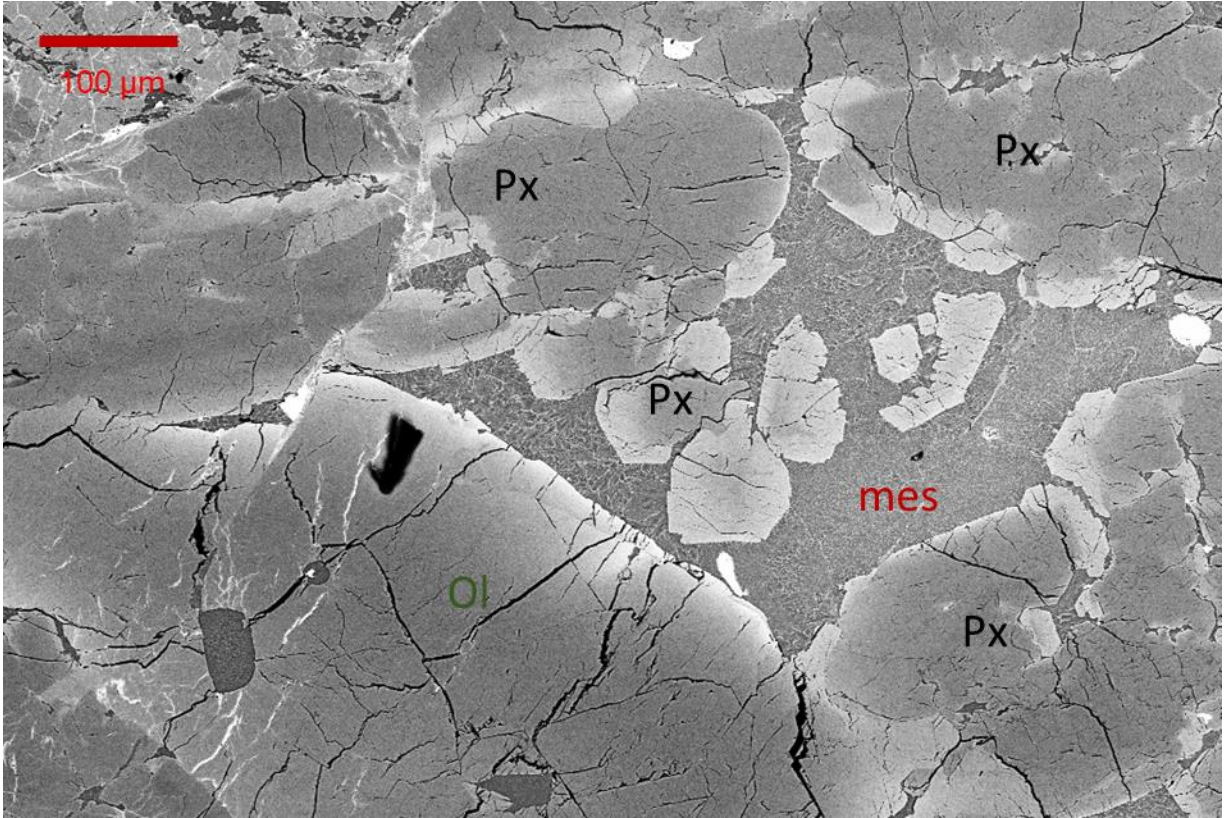


Figure 21: Backscatter electron image of an igneous clast in H3 chondrite NWA 12261, with olivine and pyroxene grains, and quenched mesostasis (glass) in between them.

Pap-II: The texture of the large igneous inclusion from Paposo 004 is dominated by microporphyritic olivine grains ($< 100 \mu\text{m}$) and some larger olivine phenocrysts ($> 250 \mu\text{m}$). The larger phenocrysts are zoned with decreasing Mg content from the centre ($\text{Fa}_{14.5 \pm 2.3}$) to the rim, equal to the smaller olivine grains ($\text{Fa}_{29.4 \pm 6.8}$). Sulfides and metals form an igneous rim of the inclusion and are also present in the form of troilite, kamacite and taenite nodules, respectively, and are depleted in comparison to bulk ordinary chondrites. The glass has a predominantly sodic plagioclase composition ($\text{Na}_2\text{O} = 8.8 \pm 3.0 \text{ wt\%}$) with interstitial high-Ca pyroxene needles ca. $1 \mu\text{m}$ in width and $10 \mu\text{m}$ in length.

Contained within the inclusion is a $0.2 \times 0.5 \text{ mm}$ relict barred olivine chondrule with low-Ca pyroxene $\text{Fs}_{22.1 \pm 4.9}\text{Wo}_{1.5 \pm 1.3}$ (Figure 22).

Electron microprobe analysis data of Pap-II can be found in Appendix 7, Appendix 8 and Appendix 9.

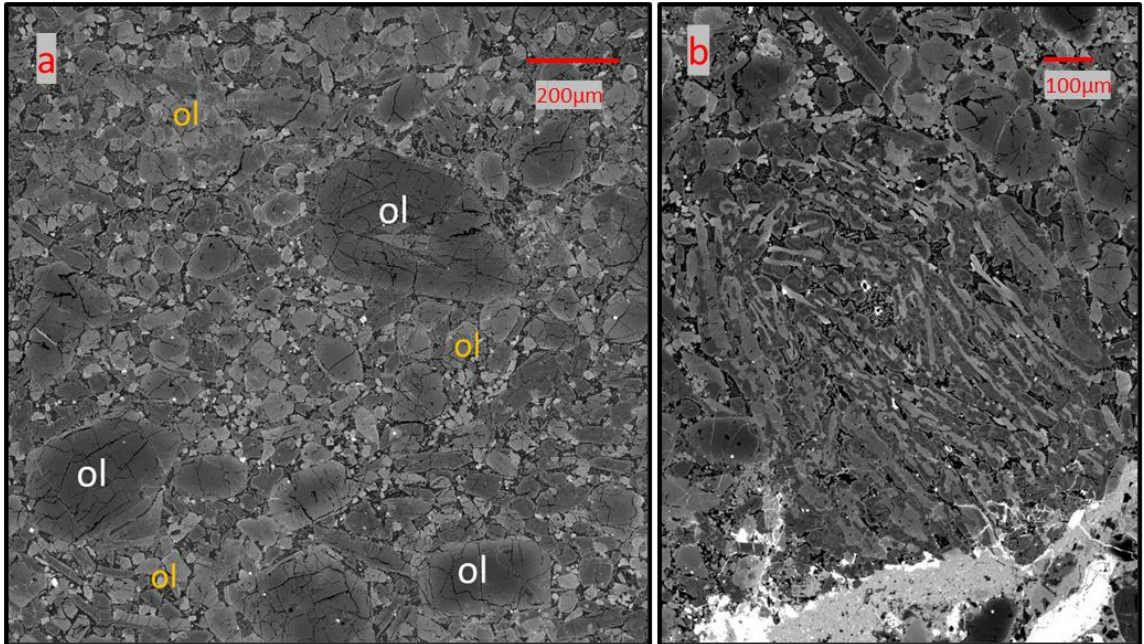


Figure 22: a) Backscatter electron image of the Paposo 004 inclusion Pap-I1, showing the microporphyritic texture with larger Mg-rich olivine phenocrysts ($\text{Fa}_{14.5 \pm 2.3}$; white) and more ferrous olivine groundmass ($\text{Fa}_{29.4 \pm 6.8}$; orange). Courtesy of Dr. Steven Simon, UNM. b) Electron microprobe image (at UWO) of a relict barred olivine chondrule containing low-Ca pyroxene ($\text{Fs}_{22.1 \pm 4.9}\text{Wo}_{1.5 \pm 1.3}$) embedded within the inclusion.

3.2.2 Bulk chemical, O isotope and I-Xe data for Pap-I1

Bulk chemical type: Major lithophile elements in Pap-I1 are enriched by about 50% compared to CI chondrites and show no signs of significant fractionation with increasing volatility, with the notable exception of Ca, which is depleted by about 80%. There is also no enrichment in K, indicating that Pap-I1 is of the *Unfr* chemical type, after the framework of (Ruzicka et al., 2019). Regarding REE, Pap-I1 is on average enriched by about 40% compared to CI chondrites without showing any significant fractionation. Comparing to average L chondrite composition (Lodders and Fegley, 1998), Pap-I1 shows neither depletion nor enrichment (Figure 23).

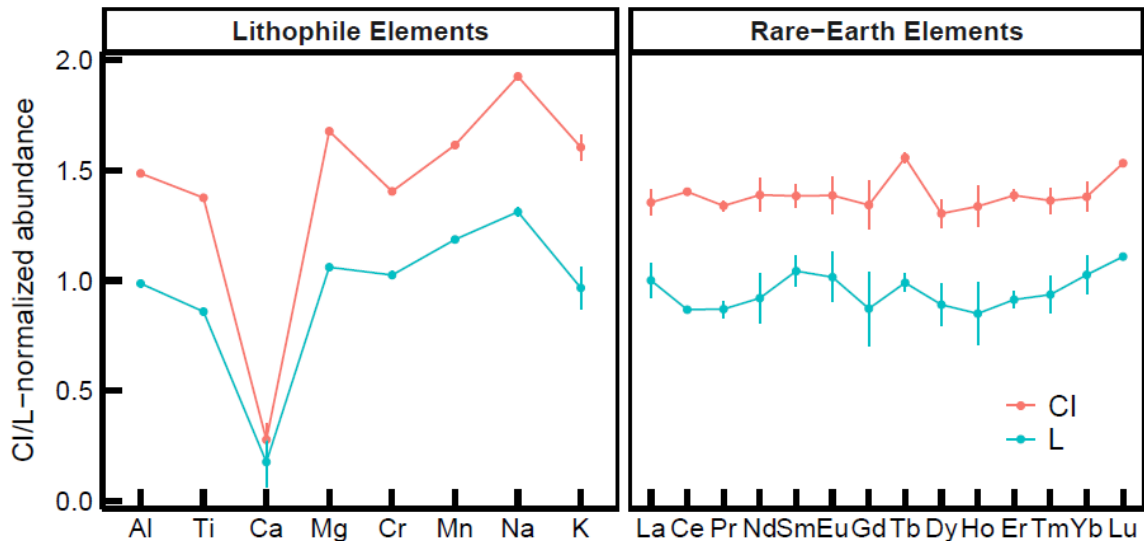


Figure 23: (a) Lithophile element abundances of Pap-I1 normalized to both CI and L chondrites (Lodders and Fegley, 1998; Barrat et al., 2012), plotted with increasing volatility. Bulk Pap-I1 shows no significant fractionation and is of the *Unfr* chemical type (Ruzicka et al., 2019); (b) No significant fractionation of REE relative to CI and L chondrites is visible for bulk Pap-I1. Error bars are within data points where not visible.

Oxygen isotopes: Four replicate O isotope analyses of the bulk Pap-I1 resulted in a triple O isotope composition of $\delta^{17}\text{O} = 3.413 \pm 0.166 \text{ ‰}$, $\delta^{18}\text{O} = 4.537 \pm 0.144 \text{ ‰}$ and $\Delta^{17}\text{O} = 1.054 \pm 0.092 \text{ ‰}$ (all uncertainties are 2SE), consistent with formation in the L chondrite reservoir (Clayton et al., 1991; Figure 24).

I-Xe age: The isochron determined from $^{132}\text{Xe}/^{129}\text{Xe}$ and $^{128}\text{Xe}^*/^{129}\text{Xe}$ ratios from two Pap-I1 fractions gives an age of $121.8 \pm 4.5 \text{ Ma}$ after Shallowater, equivalent to $126.4 \pm 4.5 \text{ Ma}$ after CAI formation and an absolute age of $4440.9 \pm 4.5 \text{ Ma}$ (Gilmour and Crowther, 2017).

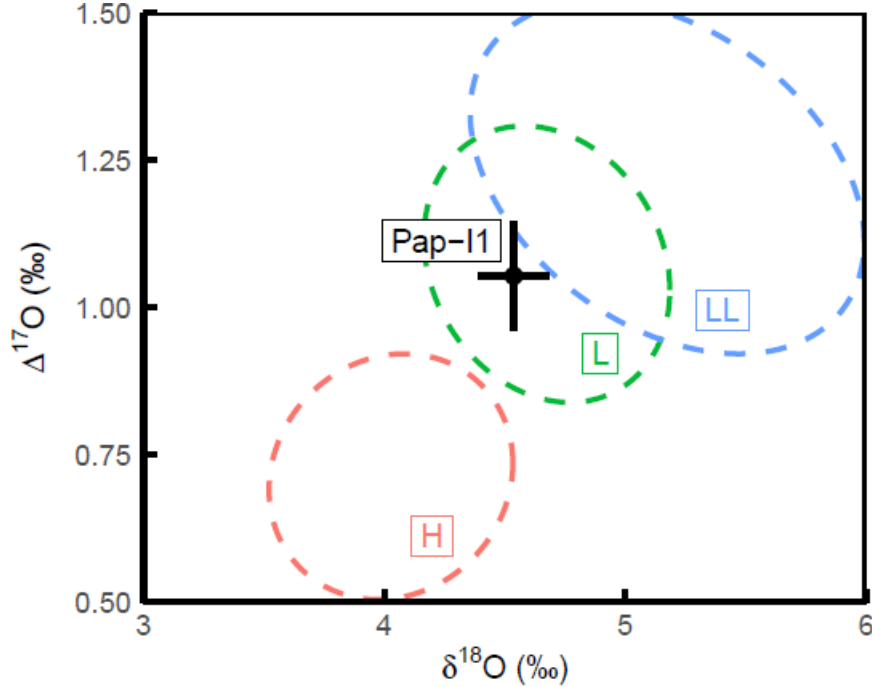


Figure 24: Oxygen isotope composition of Pap-II, plotted against literature data for ordinary chondrites (Clayton et al., 1991). Uncertainties are 2SE

3.2.3 Bulk Mg isotope compositions and $^{27}\text{Al}/^{24}\text{Mg}$ ratios of chondrules and igneous clasts

We measured the bulk Mg composition of eleven chondrules and two igneous clasts from ordinary chondrites, as well as one chondrule from both the CB_b chondrite QC 001 and the ungrouped carbonaceous chondrite Tarda. Their $^{27}\text{Al}/^{24}\text{Mg}$ ratios, mass-dependent $\delta^{25}\text{Mg}$ and $\delta^{26}\text{Mg}$ and mass-independent $\delta^{26}\text{Mg}^*$ compositions are reported in Table 12: Chondrule type and Al-Mg data for analyzed chondrules, with $^{27}\text{Al}/^{24}\text{Mg}$ ratios, mass-dependent Mg isotope anomalies and mass-independent $\delta^{26}\text{Mg}^*$ listed.

Sample	Type	$^{27}\text{Al}/^{24}\text{Mg}$	2SE	$\delta^{25}\text{Mg}$ (‰)	2SE	$\delta^{26}\text{Mg}$ (‰)	2SE	$\delta^{26}\text{Mg}^*$
NWA8007-C1	BO IAB	0.086	0.005	-0.230	0.005	-0.471	0.007	
NWA8276-C1	POP IIAB	0.226	0.011	-0.200	0.025	-0.411	0.039	
NWA8276-C2	POP IIAB	0.113	0.006	-0.531	0.045	-1.040	0.090	
NWA8276-C3	PO(P) IIAB	0.077	0.004	-0.106	0.013	-0.218	0.028	
NWA10854-C1	BO IAB	0.069	0.001	0.004	0.024	-0.022	0.046	
NWA10854-C2	PO(P) IIAB	0.083	0.001	-0.300	0.029	-0.559	0.048	
NWA10854-C3	POP IIAB	0.138	0.014					
NWA10854-C5	POP IAB	0.083	0.013	-0.670	0.023	-1.312	0.033	
NWA10854-C6	POP IIAB	0.141	0.007	-0.230	0.193	-0.463	0.375	

NWA11672-C1	POP IIAB	0.101	0.009	0.169	0.023	0.309	0.050
NWA12261-I1	Ign. Clast	0.138	0.014	-0.206	0.027	-0.426	0.040
Pap-I1 bulk	Ign. Clast	0.089	0.001	-0.255	0.009	-0.520	0.013
QC 001 Sill	CBa	0.118	0.006	-0.256	0.012	-0.526	0.022
Tarda-C2		0.101	0.005	-0.033	0.019	-0.056	0.026

. The $^{27}\text{Al}/^{24}\text{Mg}$ ratios of most chondrules are close to the solar ratio as defined by CI chondrites of 0.101 (Lodders, 2003; Luu et al., 2019) and range from 0.069 to 0.226. The mass-independent $\delta^{26}\text{Mg}^*$ compositions of the ordinary chondrite chondrules cover a range from -0.035 ± 0.020 ‰ to 0.002 ± 0.015 ‰. The CB chondrite chondrule from QC 001 has a $^{27}\text{Al}/^{24}\text{Mg}$ ratio of 0.118 and a $\delta^{26}\text{Mg}^*$ value of -0.025 ± 0.021 ‰. The carbonaceous chondrite chondrule Tarda-C2 has a solar $^{27}\text{Al}/^{24}\text{Mg}$ ratio of 0.101 and a $\delta^{26}\text{Mg}^*$ value of 0.010 ± 0.022 ‰. In total, none of the chondrules exhibit resolvable $\delta^{26}\text{Mg}^*$ excesses compared to the DSM-3 terrestrial standard but given the dearth of chondrules with supracanonical $^{27}\text{Al}/^{24}\text{Mg}$ ratios (5 chondrules with $^{27}\text{Al}/^{24}\text{Mg}$ ratios > 0.101 , and only one > 0.2) that is not unexpected. However, 8 out the 14 chondrules and clasts are resolved from the initial $\delta^{26}\text{Mg}^*$ of the Solar System (-0.0340 ± 0.0016 ‰; Schiller et al., 2010), evidence of radiogenic ingrowth of ^{26}Mg due to the decay of ^{26}Al (Figure 25). Model ages calculated from the bulk Mg data are reported in **Table 14**.

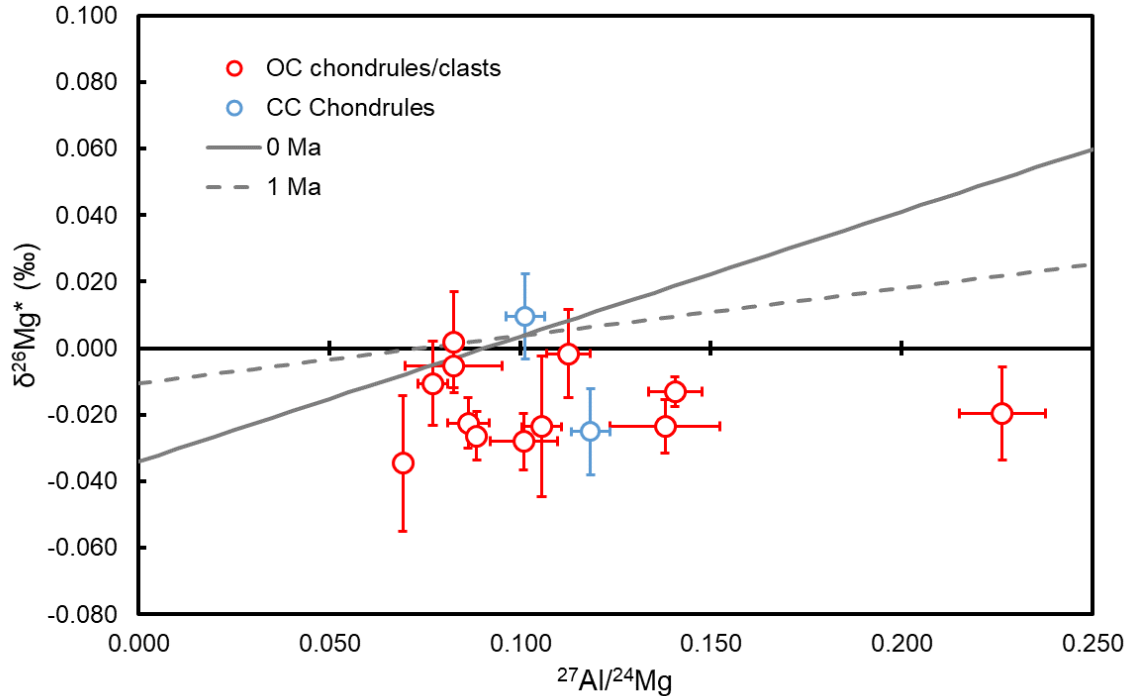


Figure 25: Overview of $\delta^{26}\text{Mg}^*$ vs. $^{27}\text{Al}/^{24}\text{Mg}$ of chondrules analyzed. Chondrules from CCs are in blue, chondrules from OCs are in red. Reference lines are isochrons representing formation times of 0 Ma and 1 Ma after CAI formation, based on the canonical $^{26}\text{Al}/^{27}\text{Al}$ of 5.23×10^{-5} (Jacobsen et al., 2008), Solar System initial $\delta^{26}\text{Mg}^*$ of $-0.0340 \pm 0.0016 \%$ (Schiller et al., 2010) and solar $^{27}\text{Al}/^{24}\text{Mg}$ ratio of 0.101 (Larsen et al., 2011).

3.2.4 *In situ* Mg isotope analyses of chondrules

The polished mounts of six chondrules and two igneous clasts were analyzed by secondary ionization mass spectrometry (SIMS) to determine the *in situ* Al-Mg isotope systematics. Chondrules were selected based on how pristine the chondrules appeared from their mineralogy. In practice, this meant that chondrules with glassy (uncrystallised) mesostasis present were prioritized. Some chondrules with re-crystallized plagioclase (an indication of post-formational thermal metamorphism) that were large enough to sample were also analyzed. Mineral isochrons generally included all data points that did not exhibit any obvious signs of mineral phase mixtures (i.e., large uncertainties on $^{27}\text{Al}/^{24}\text{Mg}$ ratios). Later, SEM observations of the analysis spots were also used to evaluate the quality of the data points, i.e., if cracks or mineral mixtures were present. Bulk Mg measurements of samples (**Table 14**) were also included in isochrons. In some

samples, measurements of mafic phases (olivine and pyroxene) accounted for much of the scatter in the dataset. For comparison, isochrons were also calculated using only glass or plagioclase fractions on their own, and with the bulk chondrule Mg isotope composition. All isochron data are listed in Table 13, while individual analyses can be found in Appendix 1. Ages are calculated relative to the canonical $^{26}\text{Al}/^{27}\text{Al}$ ratio of $(5.23 \pm 0.13) \times 10^{-5}$ (Jacobsen et al., 2008) and under the assumption of homogeneous ^{26}Al distribution in the protoplanetary disk.

Of the eight samples analyzed, two chondrules (NWA 8276-C1 and NWA 11672-C1) exhibit no resolvable initial $^{26}\text{Al}/^{27}\text{Al}$ abundances (i.e., the slope of the isochron). The four remaining chondrules show resolved initial $^{26}\text{Al}/^{27}\text{Al}$ abundances, some albeit with high scatter (MSWD). Their ages range from $1.70^{+0.81}/_{-0.44}$ Ma to $2.27^{+0.52}/_{-0.34}$ Ma after CAI formation, in the same range as previous reports in OC chondrules (e.g., Pape et al., 2019).

The two igneous clasts, NWA 12261-I1 and Pap-I1, also exhibit resolvable initial $^{26}\text{Al}/^{27}\text{Al}$ abundances, but different formation ages. NWA 12261-I1 has an ^{26}Al - ^{26}Mg age of $2.92^{+1.03}/_{-0.49}$ Ma after CAI formation, on the late end of the reported chondrule ages. Pap-I1 on the other hand, has one of the oldest ages of any object dated, with an age of $0.89^{+1.56}/_{-0.56}$ Ma after CAI formation. The large uncertainty and scatter are driven primarily by the large range of $^{26}\text{Mg}/^{24}\text{Mg}$ ratios in olivine. An isochron including only glass and bulk analyses corresponds to a more restricted age of $0.73^{+0.29}/_{-0.22}$ Ma after CAI formation.

3.2.5 Pb-Pb ages of chondrules

All Pb-Pb chondrule and clast ages have been calculated using the bulk Solar System $^{238}\text{U}/^{235}\text{U}$ ratio of 137.786 ± 0.013 (Connelly et al., 2012), with uncertainties of the U isotope composition propagated into the Pb-Pb age uncertainties. The Pb isotope compositions of leachates and residues of the two igneous clasts and individual chondrules are listed in **Table 15** and Table 16, respectively, with their calculated Pb-Pb ages reported in **Table 14**. Most chondrules are characterized by unradiogenic $^{206}\text{Pb}/^{204}\text{Pb}$ ratios, a common phenomenon in olivine-rich meteoritic materials (such as chondrules), as U generally is not hosted in olivine (Merle et al., 2020).

Isochrons were calculated using Isoplot 4.15 and a York regression (Ludwig, 2008). Only statistically significant regressions (probability of fit > 0.05) with at least three data points are shown and discussed. Data points are omitted if they reduce the fit of the regression line beyond the statistically accepted threshold.

NWA 10854-C1: The Pb isotope compositions in the leachates and residues of NWA 10854-C1 are relatively more radiogenic and show $^{206}\text{Pb}/^{204}\text{Pb}$ ratios ranging between 14.8 and 843.7. The Pb-Pb age was determined from a three-point isochron using the relatively radiogenic fractions W7, W8 and R, resulting in an age of 4566.73 ± 0.94 Ma. Using W5+6 instead of W7 results in an equal age, but with a larger spread of data points, less scatter and slightly higher precision of 4566.99 ± 0.74 Ma (Figure 26).

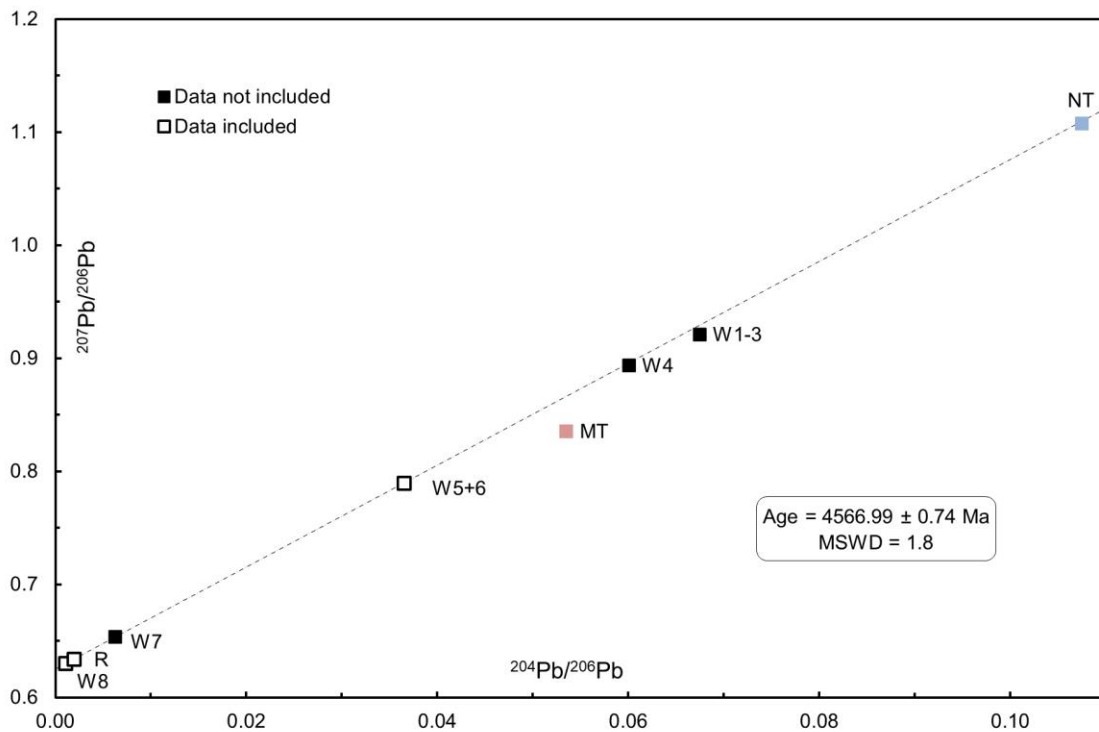


Figure 26: Inverse Pb-Pb isochron of NWA 10854-C1 chondrule, with the compositions of primordial Pb, as represented by the the Nantan troilite (Blichert-Toft et al., 2010), and modern terrestrial Pb (Stacey and Kramers, 1975) plotted for reference. The icons of data points are larger than the uncertainties, for clarity.

NWA 10854-C2: Ratios of $^{206}\text{Pb}/^{204}\text{Pb}$ range from 12.4 to 71.8. No significant isochron can be plotted, as data points are overdispersed.

NWA 10854-C3: The regression line through the three most radiogenic fractions seems to be rotated due to a lack of complete terrestrial Pb removal during leaching, as it passes in between NT and MT, resulting in an old apparent age distinct from other previously reported chondrules at 4569.6 ± 1.8 Ma (Figure 27), but technically within uncertainty of “old” CAI ages/estimates (Bouvier and Wadhwa, 2010; Desch et al., 2021) and chondrule *NWA 8276-C1*. Most likely, this Pb-Pb age is unreliable and too imprecise for further discussion.

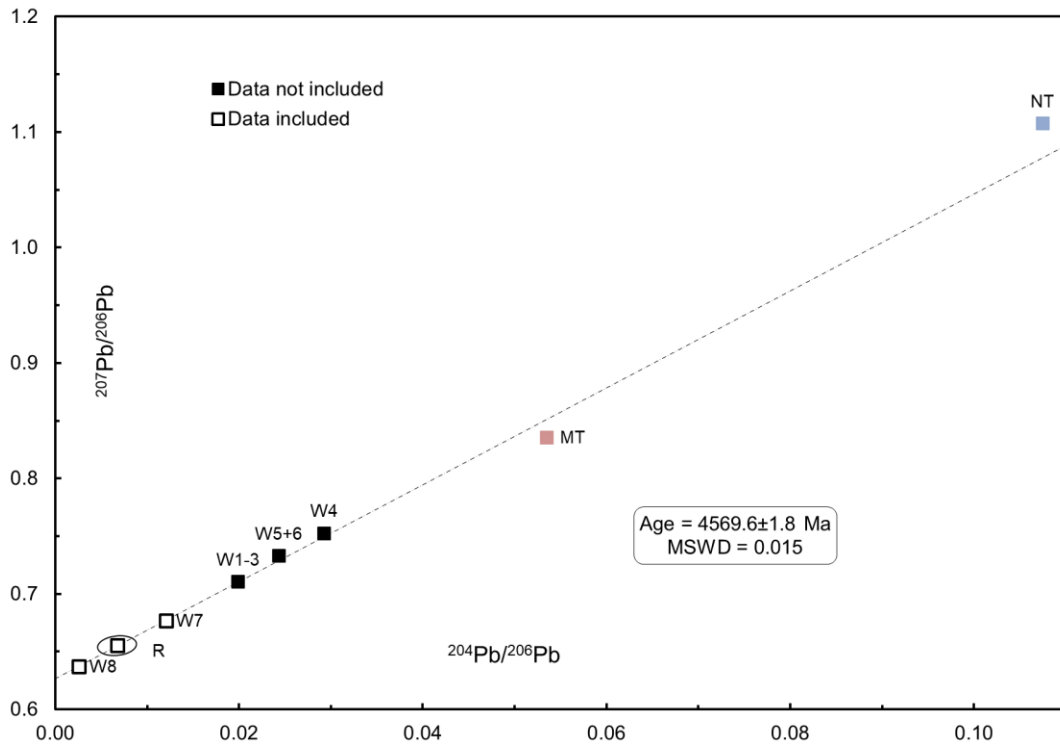


Figure 27: Inverse Pb-Pb isochron of *NWA 10854-C3*, with the compositions of primordial Pb, as represented by the the Nantan troilite (Blichert-Toft et al., 2010), and modern terrestrial Pb (Stacey and Kramers, 1975) plotted for reference. The icons of data points are larger, with the exception of R, than the uncertainties, for clarity.

NWA 10854-C5: Imprecise Pb-Pb age at 4564.7 ± 7.5 Ma, determined from an isochron with leachates W4, W7 and W8 (Figure 28). The residue and leachate W5+6 plot far off the isochron, and have sample-to-blank ratios less than 100.

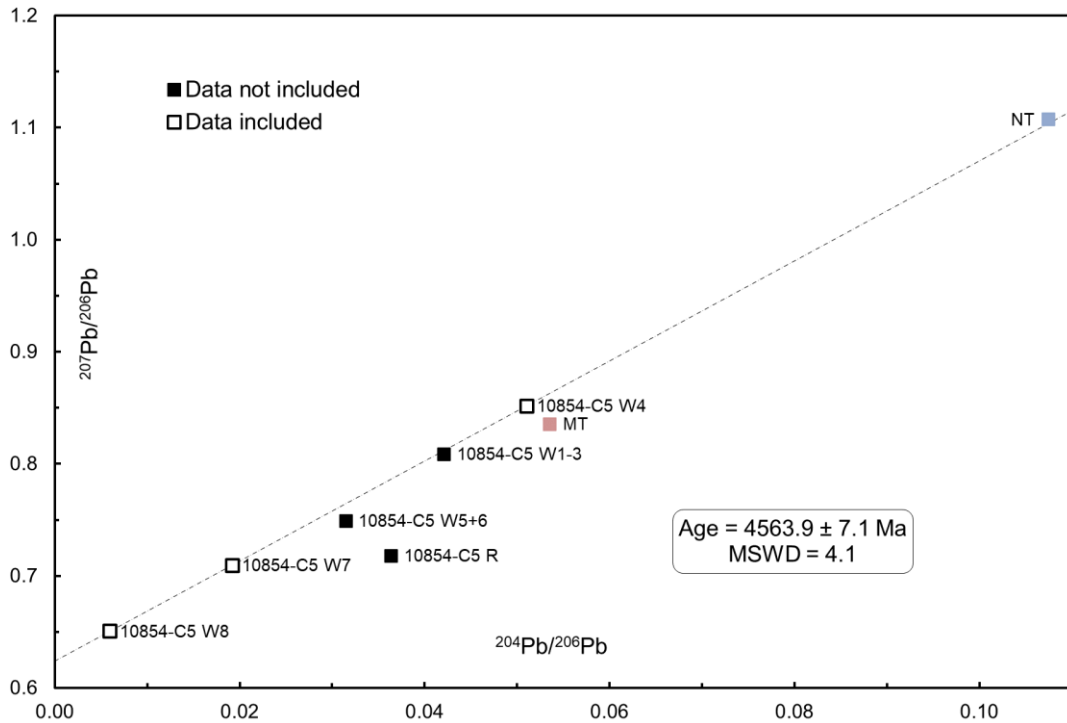


Figure 28: Inverse Pb-Pb isochron of NWA 10854-C5, with the compositions of primordial Pb, as represented by the the Nantan troilite (Blichert-Toft et al., 2010), and modern terrestrial Pb (Stacey and Kramers, 1975) plotted for reference. The icons of data points are larger than the uncertainties, for clarity.

NWA 10854-C6: The leachates are more radiogenic than most other chondrules, with blank-corrected $^{206}\text{Pb}/^{204}\text{Pb}$ ratios up 387. An isochron determined by the last four leaching steps (W5+6, W7, W8 and R) gives an age 4567.82 ± 0.57 Ma and plots through the Nantan troilite composition (Figure 29). The first two leachates, W1-3 and W4, seem to be affected by terrestrial Pb contamination, as they are pulled off the isochron towards the composition of modern terrestrial Pb.

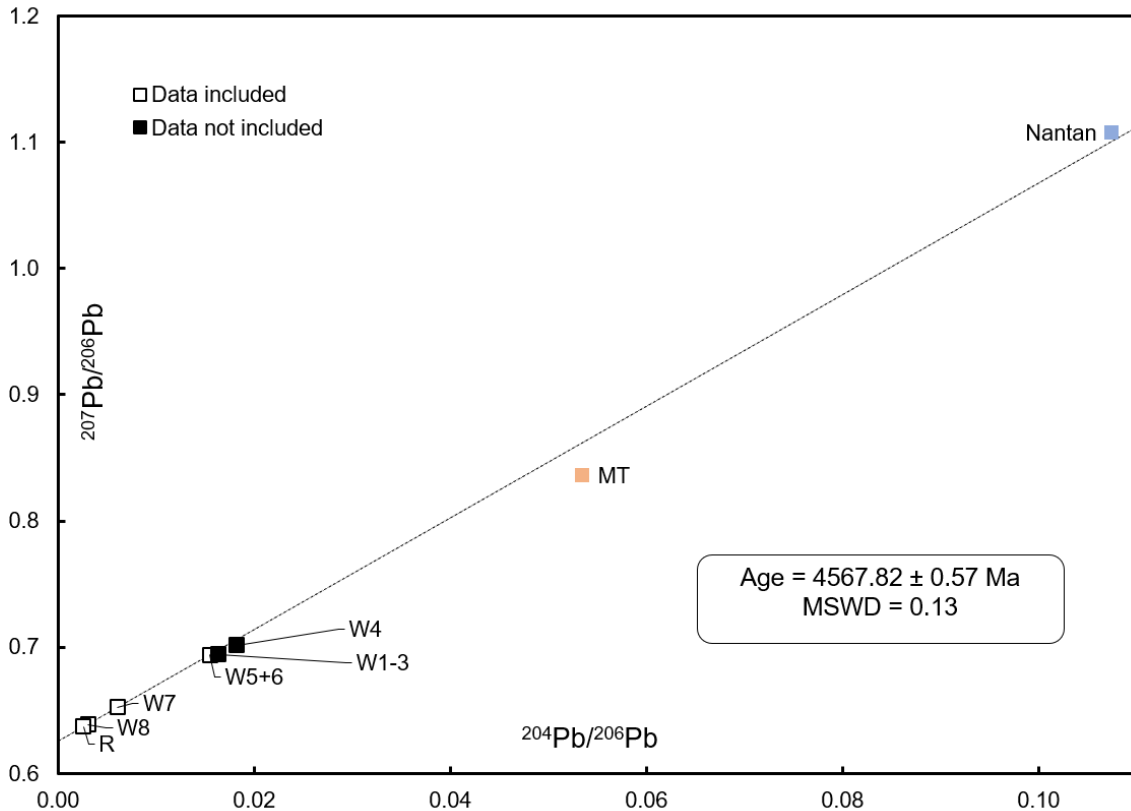


Figure 29: Inverse Pb-Pb isochron of NWA 10854-C6, with the compositions of primordial Pb, as represented by the the Nantan troilite (Blichert-Toft et al., 2010), and modern terrestrial Pb (Stacey and Kramers, 1975) plotted for reference. The icons of data points are larger than the uncertainties, for clarity.

NWA 11672-C1: No meaningful isochrons including three or more points can be determined from this sample. Three-point isochrons give varying ages between 4567 Ma and 4565 Ma.

NWA 12261-II: No age can be determined. Isotopic compositions are very primitive for all leachates and the residue, near the primordial Pb composition, between 9.87 and 11.5 for $^{206}\text{Pb}/^{204}\text{Pb}$.

NWA 8007-C1: The Pb isotopic composition of the leachates and residue are unradiogenic, with $^{206}\text{Pb}/^{204}\text{Pb}$ ratios ranging from 11.3 to 44.1. A rather imprecise Pb-Pb age was determined from the last three leachates and residue, giving an age of 4567.3 ± 1.6 Ma (Figure 30).

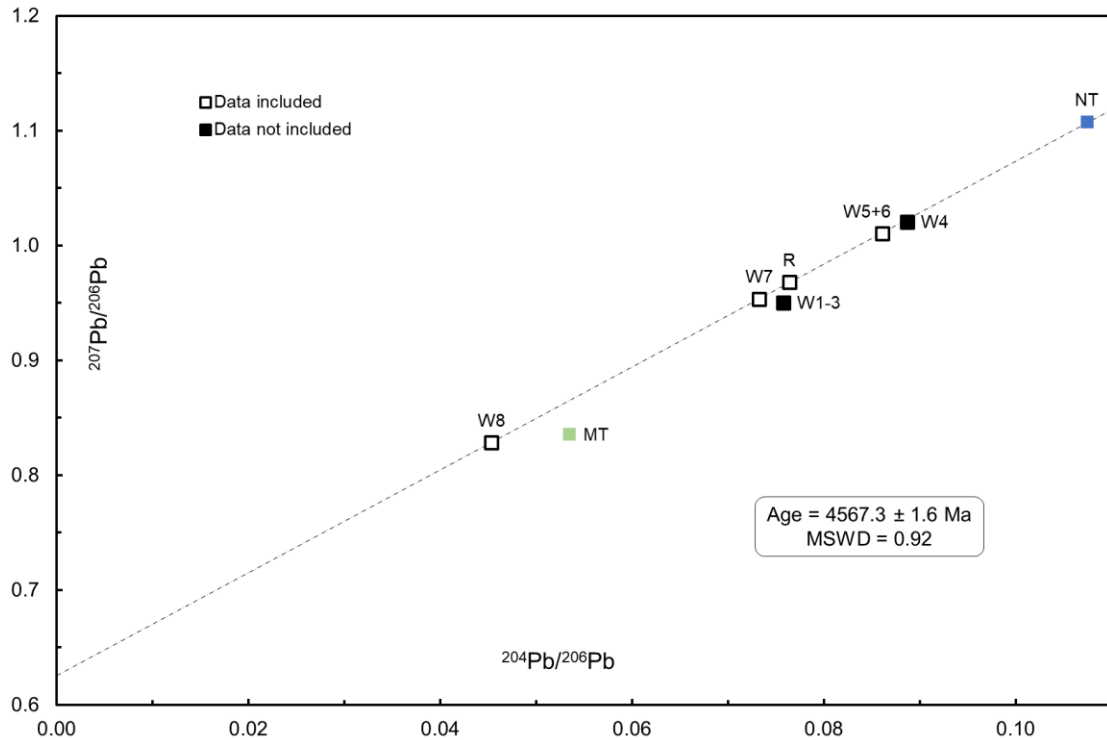


Figure 30: Inverse Pb-Pb isochron of chondrule NWA 8007-C1, with the compositions of primordial Pb, as represented by the the Nantan troilite (Blichert-Toft et al., 2010), and modern terrestrial Pb (Stacey and Kramers, 1975) plotted for reference. The icons of data points are larger than the uncertainties, for clarity.

NWA 8276-C1: The only meaningful isochron is determined from three points, W4, W8 and R, resulting in an age of 4568.21 ± 0.29 Ma (Figure 31). This age is resolvably older than the currently accepted CAI average age of 4567.30 ± 0.16 (Connelly et al., 2012), but is comparable to two “older” CAI ages around ~ 4568 Ma (Bouvier and Wadhwa, 2010; Bouvier et al., 2011b).

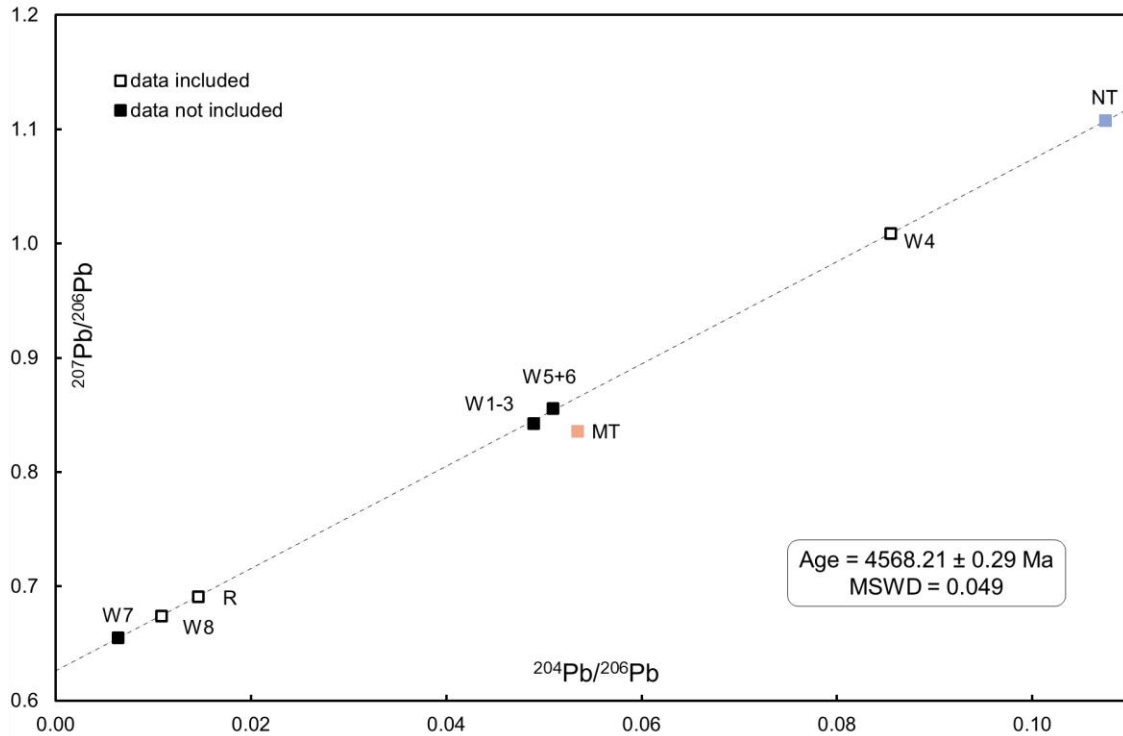


Figure 31: Inverse Pb-Pb isochron of NWA 8276-C1, with the compositions of primordial Pb, as represented by the the Nantan troilite (Blichert-Toft et al., 2010), and modern terrestrial Pb (Stacey and Kramers, 1975) plotted for reference. The icons of data points are larger than the uncertainties, for clarity.

Pap-II: Two separate fractions of the sample were leached and analyzed for their Pb isotope composition. Their $^{206}\text{Pb}/^{204}\text{Pb}$ isotope ratios range from 11.5 to 44.1. Isochrons through leachates and residues of individual fractions do not result in any meaningful ages. The best-fit regression line includes data combined from both fractions (F1-W7, F1-R, F2-W7, F2-W8), passes through the Nantan troilite composition and yields a young age of 4529.3 ± 2.1 Ma (Figure 32).

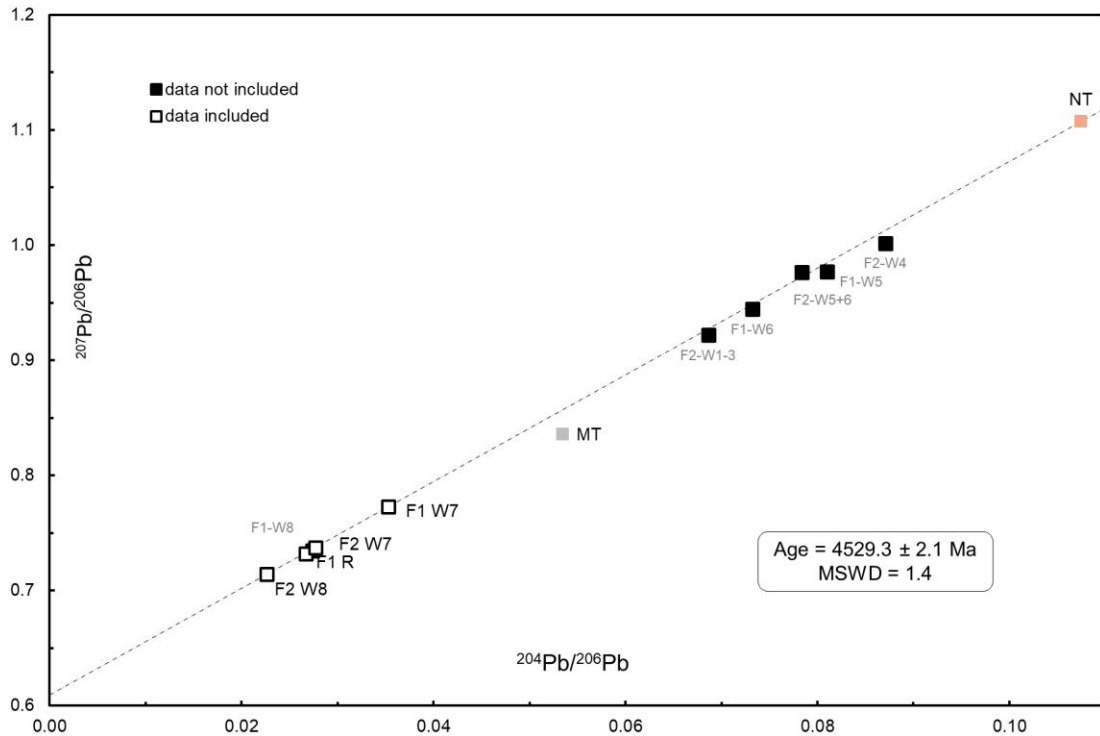


Figure 32: Inverse Pb-Pb isochron of Pap-I1, with data from both analyzed fractions and the compositions of primordial Pb, as represented by the the Nantan troilite (Blichert-Toft et al., 2010), and modern terrestrial Pb (Stacey and Kramers, 1975) plotted for reference. The icons of data points are larger than the uncertainties, for clarity.

QC 001-C1: The leachates and residue make up a three-component mixture, but W7, W8 and R plot on a line with the modern terrestrial (MT) composition, and along with W1-3 define an isochron with an age of 4563.39 ± 0.56 Ma (Figure 33).

In summary, unradiogenic Pb isotope compositions in chondrules remain a limiting factor in determining meaningful Pb-Pb ages with small uncertainties (i.e., < 1 Ma) by isochron regression. Four out of eight OC chondrules have Pb-Pb ages with uncertainties < 1 Ma, with three additional chondrules with larger uncertainties. The Pb-Pb ages do cover the same range as previously reported Pb-Pb ages in individual chondrules, within their stated uncertainties (Connelly et al., 2012; Bollard et al., 2017). The Pap-I1 igneous inclusion has a Pb-Pb age that is substantially younger at ~ 4529 Ma than chondrules and its corresponding Al-Mg age. The chondrule 8276-C1 has an older Pb-Pb age (4568.21 ± 0.29 Ma) than the absolute age of Allende and Efremovka CAIs ($4567.30 \pm$

0.16 Ma; Connelly et al., 2012), suggesting that the Pb isotope systematics in those CAIs may have been affected by secondary processes on their parent body (e.g., Krot et al., 1998).

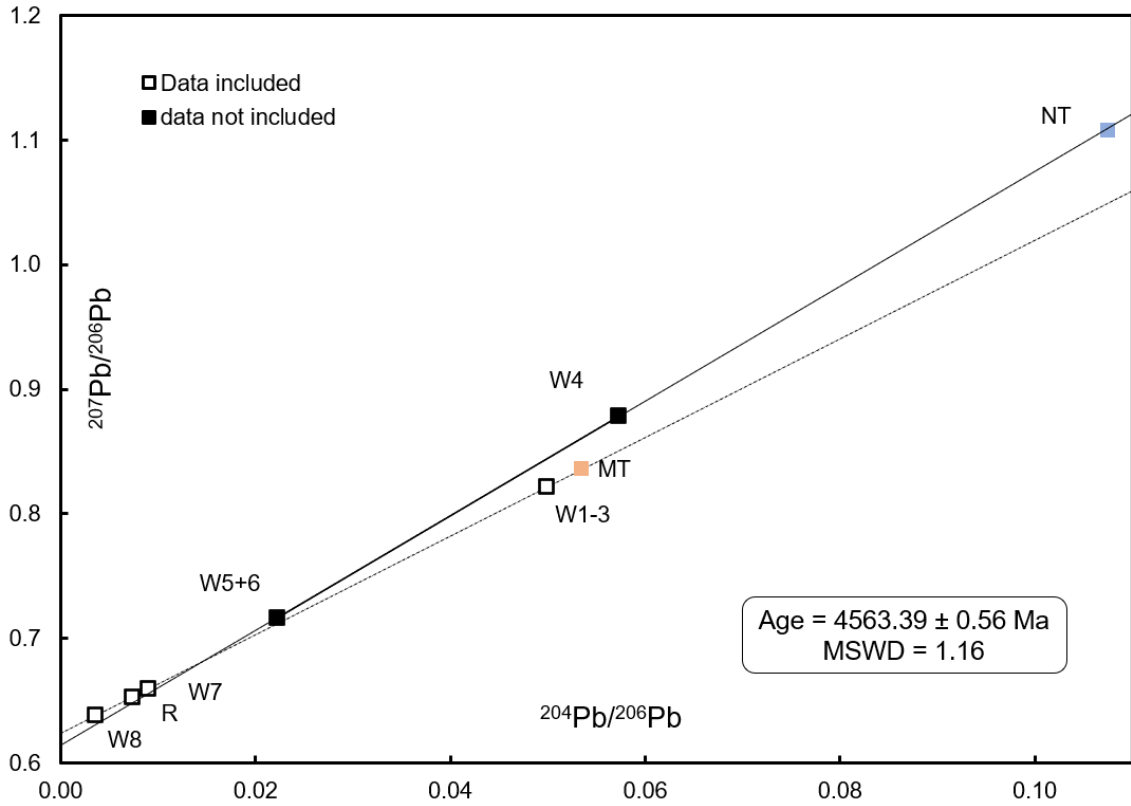


Figure 33: Inverse Pb-Pb isochron of chondrule C1 from the CB_a chondrite QC 001, with the compositions of primordial Pb, as represented by the Nantan troilite (Blichert-Toft et al., 2010), and modern terrestrial Pb (Stacey and Kramers, 1975) plotted for reference. Additionally, a regression line through the data points that were not included that plots through the Nantan troilite is added. The icons of data points are larger than the uncertainties, for clarity.

3.2.6 Cr results

The Cr isotope compositions of 6 chondrules and 2 large igneous inclusions are reported in **Table 14** and Figure 34. The chondrule from CB_a chondrite QC 001 is the only sample with a positive $\epsilon^{54}\text{Cr}$ value of 1.29 ± 0.08 , while the values of the remaining chondrules and inclusions range from -0.59 ± 0.05 to -0.20 ± 0.13 . The data for QC 001-C1 is

consistent with the $\epsilon^{54}\text{Cr}$ values reported in earlier studies for chondrules of the CB_a chondrite Gujba (Yamashita et al., 2010), as are the OC chondrules with literature data (Trinquier et al., 2007; Schneider et al., 2020).

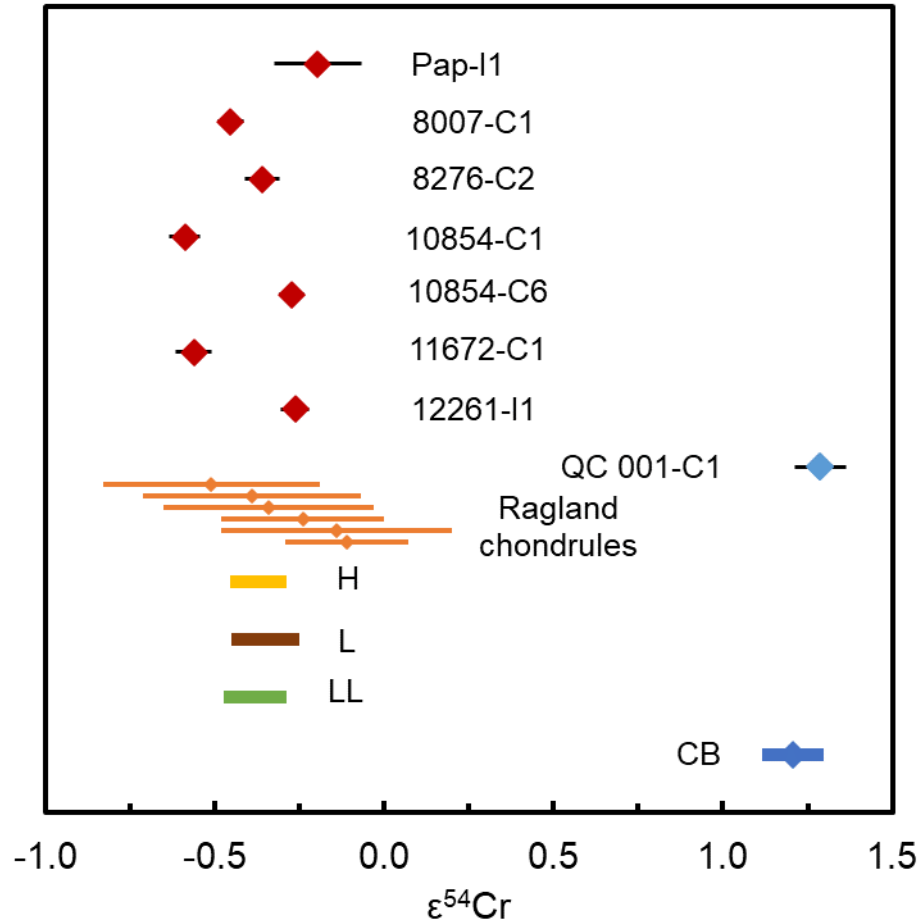


Figure 34: Chromium isotope compositions of analyzed chondrules, compared with literature values of individual chondrules from the L3.4 ordinary chondrite Ragland (Schneider et al., 2020), H, L and LL chondrites (Trinquier et al., 2007; Qin et al., 2010; Bischoff et al., 2019), as well as CB chondrites (Yamashita et al., 2010). Uncertainties in individual chondrule data are within their marker if not visible.

Table 12: Chondrule type and Al-Mg data for analyzed chondrules, with $^{27}\text{Al}/^{24}\text{Mg}$ ratios, mass-dependent Mg isotope anomalies and mass-independent $\delta^{26}\text{Mg}^*$ listed.

Sample	Type	$^{27}\text{Al}/^{24}\text{Mg}$	2SE	$\delta^{25}\text{Mg}$ (‰)	2SE	$\delta^{26}\text{Mg}$ (‰)	2SE	$\delta^{26}\text{Mg}^*$ (‰)	2SE
NWA8007-C1	BO IAB	0.086	0.005	-0.230	0.005	-0.471	0.007	-0.022	0.008
NWA8276-C1	POP IIAB	0.226	0.011	-0.200	0.025	-0.411	0.039	-0.020	0.014
NWA8276-C2	POP IIAB	0.113	0.006	-0.531	0.045	-1.040	0.090	-0.002	0.013
NWA8276-C3	PO(P) IIAB	0.077	0.004	-0.106	0.013	-0.218	0.028	-0.011	0.013
NWA10854-C1	BO IAB	0.069	0.001	0.004	0.024	-0.022	0.046	-0.035	0.020
NWA10854-C2	PO(P) IIAB	0.083	0.001	-0.300	0.029	-0.559	0.048	0.002	0.015
NWA10854-C3	POP IIAB	0.138	0.014					-0.024	0.008
NWA10854-C5	POP IAB	0.083	0.013	-0.670	0.023	-1.312	0.033	-0.005	0.007
NWA10854-C6	POP IIAB	0.141	0.007	-0.230	0.193	-0.463	0.375	-0.013	0.004
NWA11672-C1	POP IIAB	0.101	0.009	0.169	0.023	0.309	0.050	-0.028	0.008
NWA12261-I1	Ign. Clast	0.138	0.014	-0.206	0.027	-0.426	0.040	-0.024	0.008
Pap-I1 bulk	Ign. Clast	0.089	0.001	-0.255	0.009	-0.520	0.013	-0.026	0.007
QC 001 Sill	CBa	0.118	0.006	-0.256	0.012	-0.526	0.022	-0.025	0.011
Tarda-C2		0.101	0.005	-0.033	0.019	-0.056	0.026	0.010	0.013

Table 13: Overview over isochron data from SIMS analysis of chondrules. Gl: indicates glassy mesostasis or plagioclase analyses.

Samples	isochron	Initial $^{26}\text{Al}/^{27}\text{Al}$		Initial $\delta^{26}\text{Mg}$ [‰]		MSWD	Age after CAI [Ma]		
			\pm		\pm			+	-
NWA	all	9.06×10^{-6}	5.15×10^{-6}	-0.026	0.024	9.3	1.70	0.81	0.44
8007-C1	bulk + gl	9.06×10^{-6}	9.89×10^{-6}	-0.027	0.048	24	1.70	inf	0.71
NWA	all	5.02×10^{-6}	8.22×10^{-6}	-0.015	0.045	12	2.27	inf	0.94
8276-C1	bulk + gl	5.99×10^{-6}	1.02×10^{-4}	-0.028	0.066	14	2.09	inf	2.79
NWA	all	5.02×10^{-6}	2.09×10^{-6}	-0.001	0.022	3.6	2.27	0.52	0.34
8276-C2	bulk + gl	5.15×10^{-6}	3.20×10^{-6}	-0.004	0.038	5.5	2.24	0.94	0.47
NWA	all	5.15×10^{-6}	9.20×10^{-6}	0.002	0.039	5.8	2.24	inf	0.99
10854-C2	bulk + gl	5.99×10^{-6}	3.20×10^{-6}	-0.002	0.015	0.008	2.09	0.74	0.41
NWA	all	6.97×10^{-6}	1.53×10^{-6}	-0.020	0.008	2.7	1.95	0.24	0.19
10854-C6	bulk + gl	6.97×10^{-6}	1.81×10^{-6}	-0.020	0.009	2.9	1.95	0.29	0.22
NWA	all	2.37×10^{-6}	1.07×10^{-5}	-0.029	0.046	11.8	2.99	inf	1.65
11672-C1	bulk + gl	1.49×10^{-6}	1.95×10^{-6}	0.142	0.068	1.05	3.44	inf	0.81
NWA	all	2.55×10^{-6}	1.67×10^{-6}	-0.018	0.017	1.03	2.92	1.03	0.49
12261-I1	bulk + gl	4.18×10^{-7}	3.62×10^{-6}	-0.023	0.047	3.3	4.67	inf	2.19
Pap-I1	all	2.09×10^{-5}	1.67×10^{-5}	-0.034	0.02	6.1	0.89	1.56	0.57
	bulk + gl	2.45×10^{-5}	6.27×10^{-6}	-0.042	0.0085	0.29	0.73	0.29	0.22

Table 14: Overview of bulk Al-Mg data, bulk Mg model ages, *in situ* ^{26}Al - ^{26}Mg ages, Pb-Pb ages as well as the Cr isotope composition ($\epsilon^{54}\text{Cr}$).

Sample	Type	$^{27}\text{Al}/^{24}\text{Mg}$	2SE	$\delta^{26}\text{Mg}^*$ (‰)	2SE	Mg model age [Ma after CAI]	<i>in situ</i> ^{26}Al - ^{26}Mg age [Ma after CAI]	Pb-Pb age [Ma]	2SE	$\epsilon^{54}\text{Cr}$	2SE
NWA 8007-C1	BO IAB	0.086	0.005	-0.022	0.008	1.00 $^{+1.06}_{-0.51}$	1.70 $^{+0.81}_{-0.44}$	4567.3	1.6	-0.45	0.04
NWA 8276-C1	POP IIAB	0.226	0.011	-0.020	0.014	1.71 $^{+2.98}_{-0.67}$	n.i.	4568.21	0.26	tbd	
NWA 8276-C2	POP IIAB	0.113	0.006	-0.002	0.013	0.26 $^{+0.55}_{-0.36}$	2.27 $^{+0.52}_{-0.34}$	n.a.		-0.36	0.05
NWA 8276-C3	PO(P) IIAB	0.077	0.004	-0.011	0.013	0.20 $^{+0.75}_{-0.43}$	n.d.	n.a.			
NWA 10854-C1	BO IAB	0.069	0.001	-0.035	0.020	Inf $^{+inf}_{0.26}$ Ma *	n.d.	4566.99	0.73	-0.59	0.05
NWA 10854-C2	PO(P) IIAB	0.083	0.001	0.002	0.015	-0.14 $^{+0.54}_{-0.36}$	2.09 $^{+0.74}_{-0.41}$	no significant age			
NWA 10854-C3	POP IIAB	0.138	0.014	-0.024	0.008	1.54 $^{+1.47}_{-0.58}$	n.d.	4569.6	1.8		
NWA 10854-C5	POP IAB	0.083	0.013	-0.005	0.007	0.07 $^{+0.34}_{-0.26}$	n.d.	4564.4	7.5		
NWA 10854-C6	POP IIAB	0.141	0.007	-0.013	0.004	0.89 $^{+0.27}_{-0.22}$	1.95 $^{+0.24}_{-0.19}$	4567.82	0.55	-0.27	0.04
NWA 11672-C1	POP IIAB	0.101	0.009	-0.028	0.008	1.77 $^{+inf}_{-0.87}$	n.i.	no significant age		-0.56	0.05
NWA 12261-I1	Ign. Clast	0.138	0.014	-0.024	0.008	1.28 $^{+inf}_{-1.09}$	2.92 $^{+1.06}_{-0.51}$	no significant age		-0.26	0.04
Pap-I1 bulk	Ign. clast	0.089	0.001	-0.026	0.007	1.42 $^{+3.27}_{-0.68}$	0.73 $^{+0.29}_{-0.22}$	4529.3	2.1	-0.20	0.13
QC 001 Sill	CB _a	0.118	0.006	-0.025	0.011	1.54 $^{+inf}_{-0.77}$	n.d.	4563.39	0.54	1.29	0.08
Tarda-C2		0.101	0.005	0.010	0.013	-0.13 $^{+0.37}_{-0.28}$	n.d.	n.a.		tbd	

BO: barred olivine chondrule; POP: porphyritic olivine-pyroxene chondrule; PO(P): porphyritic chondrule, with mostly olivine; IAB: type I chondrule ($X_{Mg} > 0.9$), contains both olivine and pyroxene; IIAB: type II chondrule ($X_{Mg} < 0.9$), contains both olivine and pyroxene. * denotes the oldest possible age. n.a. = not analyzed, n.d. = not determined, n.i.= no isochron regression was obtained.

Table 15: Pb isotope data for two igneous clasts Pap-I1 and NWA 12261-I1

Sample	Pb (ng)	Sample/Blank	$^{206}\text{Pb}/^{204}\text{Pb}$ raw	$^{204}\text{Pb}/^{206}\text{Pb}$	2SE (%)	$^{207}\text{Pb}/^{206}\text{Pb}$	2SE (%)	$^{208}\text{Pb}/^{206}\text{Pb}$	2SE (%)	
Pap-I1 Fraction 1										
W5	2.5	1222	12.5	0.08103	0.011	0.976708	0.006	2.64062	0.030	
W6	0.3	180	13.8	0.07324	0.065	0.944549	0.030	2.47536	0.197	
W7	4.9	2734	28.6	0.03527	0.010	0.772758	0.004	1.67708	0.039	
W8	3.2	917	36.9	0.02738	0.033	0.734732	0.008	1.50438	0.240	
R	4.0	5348	37.8	0.02670	0.007	0.732265	0.004	1.49140	0.055	
Pap-I1 Fraction 2										
W1-3	4.4	4882	14.7	0.06863	0.211	0.921760	0.014	2.36063	0.017	
W4	3.3	3685	11.6	0.08709	0.173	1.001720	0.004	2.72265	0.004	
W5+6	0.5	563	12.9	0.07837	0.100	0.976523	0.016	2.58334	0.106	
W7	2.8	3125	36.4	0.02768	0.152	0.737535	0.002	1.51343	0.042	
W8	0.7	757	44.4	0.02265	1.221	0.714202	0.006	1.40530	0.310	
R	0.2	210	37.2	0.02680	4.559	0.734311	0.017	1.48252	---	
NWA 12261-Incl 1										
W1-3	42.3	42675	11.5	0.086617	0.002	1.011101	0.0010	2.74887	0.0006	
<i>Fraction 1</i>										
W4	3.3	3066	10.0	0.100346	0.009	1.075514	0.0048	3.02463	0.0010	
W5+6	0.5	483	10.5	0.095177	0.047	1.052025	0.0263	2.91893	0.0021	
W7	7.9	6405	10.8	0.092594	0.004	1.039359	0.0022	2.85946	0.0006	
W8	9.4	2926	11.4	0.087553	0.008	1.016920	0.0040	2.74983	0.0010	
R	7.3	7211	11.5	0.086993	0.003	1.013662	0.0018	2.73501	0.0006	
<i>Fraction 2</i>										
W4	3.0	2040	9.9	0.101301	0.006	1.081666	0.0036	3.04782	0.0009	
W5+6	0.6	206	10.4	0.096233	0.055	1.057994	0.0314	2.93569	0.0028	
W7	6.3	5105	10.8	0.092184	0.002	1.038075	0.0013	2.85309	0.0005	
W8	9.9	4978	11.4	0.087675	0.002	1.017686	0.0012	2.75396	0.0006	
R	5.1	3495	11.4	0.087989	0.003	1.019000	0.0018	2.75999	0.0008	

Table 16: Pb isotope data for analyzed chondrules.

Sample	Pb (ng)	Sample/Blank	²⁰⁶ Pb/ ²⁰⁴ Pb raw	²⁰⁴ Pb/ ²⁰⁶ Pb	2SE (%)	²⁰⁷ Pb/ ²⁰⁶ Pb	2SE (%)	²⁰⁸ Pb/ ²⁰⁶ Pb	2SE (%)
Northwest Africa 8007-C1									
W1-3	4.2	5668	13.2	0.075761	0.005	0.950283	0.002	2.52345	0.0028
W4	3.8	2525	11.3	0.088714	0.014	1.020565	0.008	2.79709	0.0156
W5+6	0.7	201	16.7	0.086072	0.079	1.010445	0.060	2.71392	0.0092
W7	1.0	492	44.1	0.073252	0.025	0.953480	0.019	2.52842	0.0051
W8	0.7	209	22.0	0.045353	0.104	0.828497	0.016	2.03684	0.0063
R	0.5	153	13.1	0.076390	0.317	0.968056	0.379	2.50873	0.0056
Northwest Africa 8276-C1									
W1-3	0.8	447	20.5	0.048885	0.020	0.842997	0.004	1.99142	0.0051
W4	1.2	2141	11.7	0.085443	0.011	1.008847	0.005	2.71186	0.0051
W5+6	0.2	197	19.6	0.050880	0.044	0.855801	0.009	2.71392	---
W7	0.4	979	156	0.006388	0.219	0.655568	0.009	1.12737	0.0061
W8	0.4	822	92.0	0.010832	0.139	0.674408	0.010	1.11771	0.0072
R	0.0	90	67.1	0.014604	0.876	0.691237	0.078	1.13876	---
Northwest Africa 10854-C1									
W1-3	2.2	2846	14.8	0.067474	0.007	0.921417	0.002	2.39927	0.0042
W4	0.6	248	16.7	0.060051	0.041	0.893887	0.008	2.19446	0.0057
W5+6	0.1	71	27.2	0.036496	0.298	0.789855	0.052	1.78075	---
W7	0.4	193	155	0.006249	1.212	0.654045	0.050	1.32992	---
W8	0.2	231	844	0.001024	6.508	0.630090	0.046	1.21981	---
R	0.2	166	460	0.001954	4.692	0.633852	0.063	---	---
Northwest Africa 10854-C2									
W2-4	1.4	1489	15.5	0.064707	0.014	0.917070	0.015	2.27790	0.0014
W5	0.2	132	12.4	0.080595	0.144	0.994279	0.173	2.60304	0.0034
W6	0.1	34	13.8	0.073280	0.564	0.955886	0.667	2.43039	0.0461
W7	0.8	1118	43.4	0.023030	0.041	0.716091	0.020	1.41092	0.0016
W8	0.7	1103	71.8	0.013904	0.068	0.672394	0.021	1.21724	0.0012

R	0.6	1372	70.8	0.014099	0.054	0.672548	0.019	1.21595	0.0014
Northwest Africa 10854-C3									
W1-3	3.3	3099	50.4	0.019842	0.020	0.710751	0.003	1.396699	0.0032
W4	0.9	527	34.2	0.029234	0.058	0.752799	0.009	1.499932	0.0037
W5+6	0.1	165	40.9	0.024325	0.246	0.733085	0.032	1.305343	---
W7	0.3	526	82.7	0.012029	0.210	0.676913	0.016	1.329920	---
W8	0.1	121	352	0.002563	4.44	0.637192	0.074	0.922270	---
R	0.01	45	135	0.006726	25.5	0.655239	1.086	0.947999	---
Northwest Africa 10854-C5									
W1-3	2.3	4266	23.8	0.042085	0.009	0.809037	0.004	1.990872	0.0106
W4	1.1	1769	19.6	0.051032	0.010	0.851728	0.003	2.043836	0.0048
W5+6	0.2	86	31.6	0.031452	0.360	0.749339	0.062	1.570759	---
W7	0.7	460	52.0	0.019159	0.133	0.709383	0.015	1.564642	0.0051
W8	0.3	212	164	0.005928	1.16	0.650767	0.045	1.333875	---
R	0.2	85	27.4	0.036341	0.277	0.718286	0.082	1.573922	---
Northwest Africa 10854-C6									
W1-3	6.8	9322	61.2	0.016333	0.010	0.694452	0.001	1.304508	0.0004
W4	1.0	1052	54.8	0.018225	0.071	0.701833	0.006	1.209826	0.0009
W5+6	0.4	199	64.0	0.015445	0.447	0.693993	0.032	1.101179	---
W7	1.0	874	164	0.006041	0.293	0.652410	0.009	0.991488	0.0012
W8	0.5	239	315	0.003014	2.18	0.638953	0.037	0.918753	---
R	0.3	93	333	0.002582	6.60	0.637241	0.093	0.918778	---
Northwest Africa 11672-C1									
W1-3	8.8	3663	13.0	0.077209	0.231	0.946090	0.031	2.488663	0.0873
W4	5.8	5330	12.2	0.082097	0.077	0.988963	0.005	2.665926	0.0082
W5+6	1.6	2438	13.8	0.072437	0.009	0.949640	0.003	2.438302	0.0046
W7	2.0	3726	24.5	0.040852	0.007	0.808835	0.002	1.715888	0.0032
W8	1.6	2646	27.3	0.036596	0.012	0.789113	0.002	1.776366	0.0036
R	0.3	204	18.1	0.055302	0.102	0.873611	0.012	1.187027	---

Quebrada Chimborazo 001-C1

W1-3	4.5	809	20.0	0.049927	0.009	0.821450	0.003	1.971731	0.0007
W4	4.7	544	17.5	0.057255	0.009	0.878343	0.003	2.105516	0.0009
W5+6	1.4	171	44.7	0.022198	0.310	0.716707	0.038	1.440506	0.0016
W7	1.3	350	110	0.008999	0.453	0.659400	0.025	1.178227	0.0010
W8	0.6	108	257	0.003535	3.98	0.638132	0.089	1.068828	0.0017
R	0.7	91	128	0.007418	2.15	0.652668	0.099	1.116710	0.0023

3.3 Discussion

3.3.1 Comparison of $\delta^{26}\text{Mg}^*$ and ^{26}Al - ^{26}Mg model ages to other chondrule studies

The Mg isotope composition of ordinary chondrite chondrules measured by solution MC-ICPMS are characterized by $\delta^{26}\text{Mg}^*$ values that show no resolvable excess ^{26}Mg compared to the terrestrial value (= 0 ‰). These results can be compared to the bulk Mg isotope compositions of both CC chondrules reported by other studies (Bizzarro et al., 2004; Bouvier et al., 2013; Olsen et al., 2016; Chen et al., 2018). There do not appear to be any significant differences between datasets and the chondrules of OCs and CCs (Figure 35).

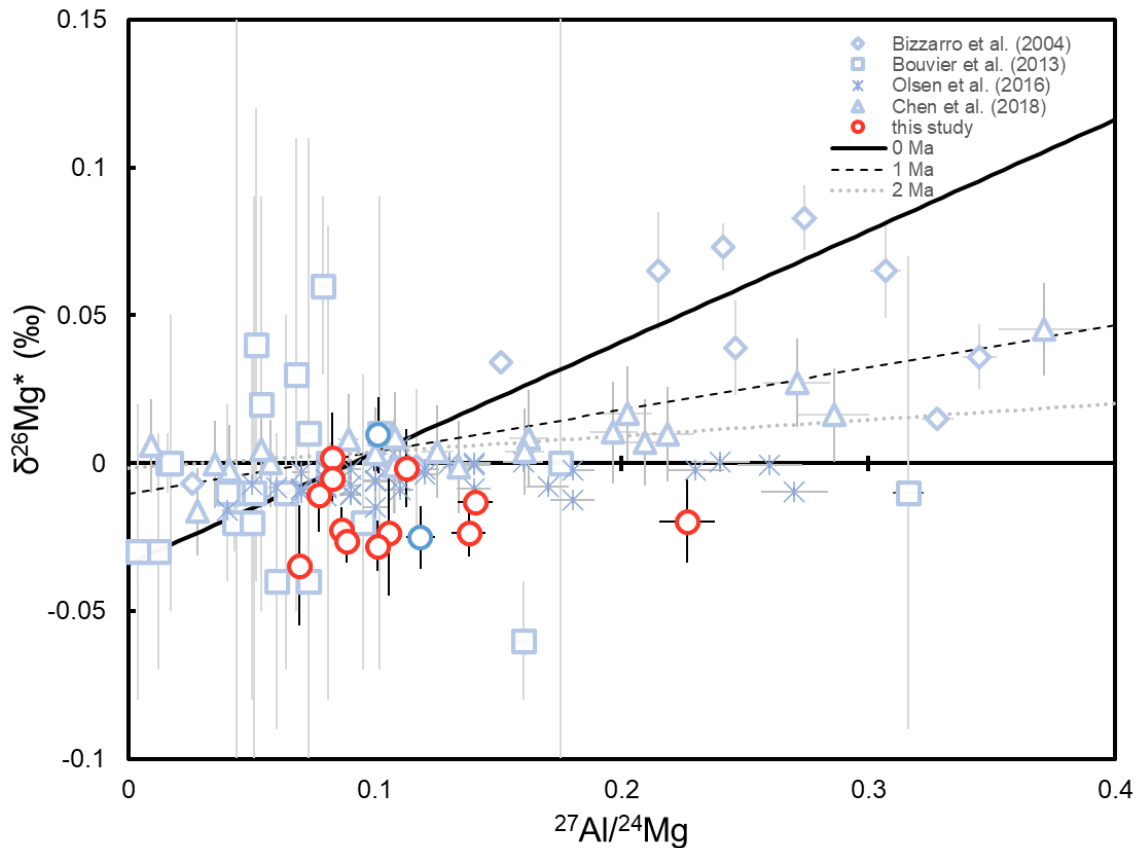


Figure 35: $^{27}\text{Al}/^{24}\text{Mg}$ vs. $\delta^{26}\text{Mg}^*$ diagram, with analyzed individual OC chondrules (red circles) and CC chondrules (dark blue circles) compared to literature data of Allende (CV3) chondrules (grey diamonds; Bizzarro et al., 2004), CM2 chondrules (grey squares; Bouvier

et al., 2013), CV chondrules (grey crosses; Olsen et al., 2016) and CV chondrules (grey triangles; Chen et al., 2018). As references, isochrons representing formation times of 0 Ma, 1 Ma and 2 Ma after CAI formation, based on the canonical $^{26}\text{Al}/^{27}\text{Al}$ of 5.23×10^{-5} (Jacobsen et al., 2008), Solar System initial $\delta^{26}\text{Mg}^*$ of $-0.0340 \pm 0.0016 \text{ ‰}$ (Schiller et al., 2010) and solar $^{27}\text{Al}/^{24}\text{Mg}$ ratio of 0.101 (Larsen et al., 2011), are also plotted.

The model ages calculated from the Solar System initial of $-0.0340 \pm 0.0016 \text{ ‰}$ (Schiller et al., 2010b) are hence also comparable to those reported by Bizzarro et al. (2004) and Chen et al. (2018). Some chondrules have not fully resolved model ages, as their Mg isotope compositions (including uncertainty) overlap with that of the initial Solar System, meaning their model “ages” define the oldest possible formation age (maximum age). Importantly, model ages date the Al/Mg fractionation event, often interpreted to be the formation of chondrule precursors (e.g., Luu et al., 2015; Chen et al., 2018), and can thus not be directly compared to internal mineral ^{26}Al - ^{26}Mg isochrons of chondrules.

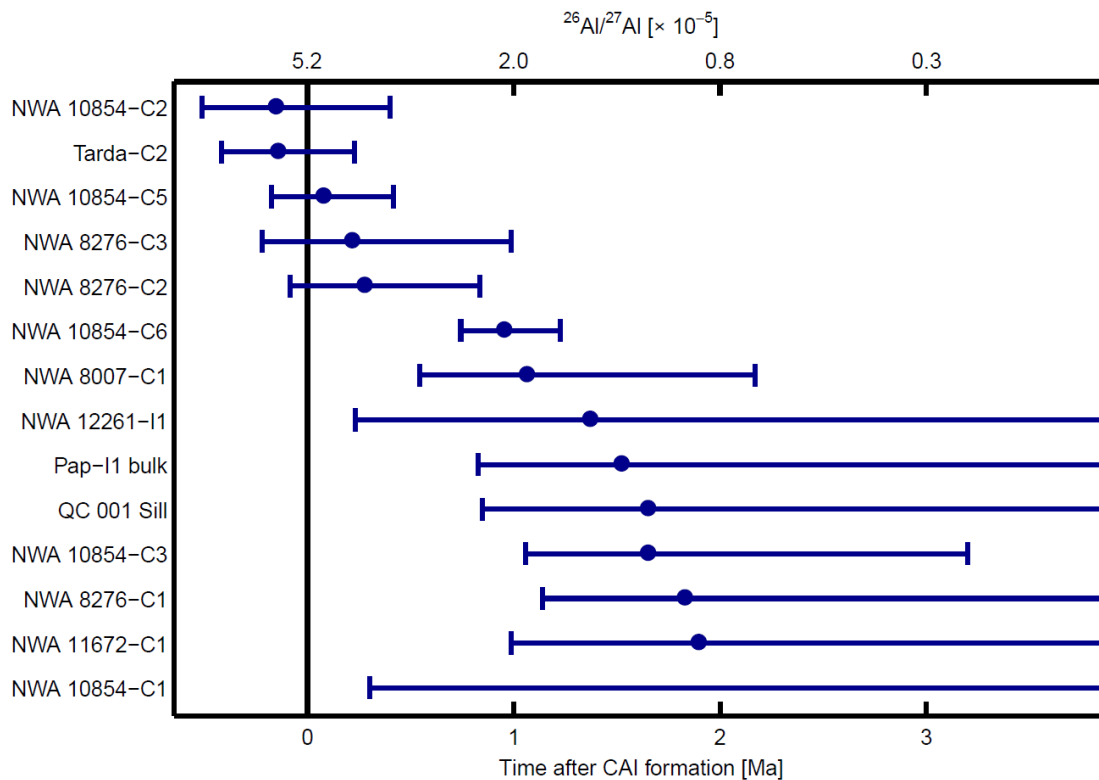


Figure 36: ^{26}Al - ^{26}Mg model ages and initial $^{26}\text{Al}/^{27}\text{Al}$ ratios of chondrules, based on their bulk $\delta^{26}\text{Mg}^*$ and $^{27}\text{Al}/^{24}\text{Mg}$ ratios, relative to the canonical initial $^{26}\text{Al}/^{27}\text{Al}$ of 5.23×10^{-5}

(Jacobsen et al., 2008) and Solar System initial $\delta^{26}\text{Mg}^*$ of $-0.0340 \pm 0.0016 \text{ ‰}$ (Schiller et al., 2010).

The model ages of the analyzed chondrules are displayed in Figure 36 and range from 0 to 2 Ma after CAI, with one chondrule (NWA 10854-C1) only having a resolved maximum age 0.26 Ma after CAI formation. These model ages are comparable to previous studies in CV3 chondrites (Chen et al., 2018; Bizzarro et al., 2004) and indicate that chondrule precursor formation took place coevally with CAI formation, and likely lasted at least 2 Myr.

3.3.2 Formation history of Pap-I1

One sample stands out from the Pb isotope dataset: The igneous clast Pap-I1 has a statistically significant Pb-Pb age that is ~ 35 Myr younger than typical chondrule Pb-Pb ages. This age is not only inconsistent with the petrological observations, it is also seemingly incongruent with our current understanding of parent body formation timescales: iron meteorites parent bodies having accreted within the first Myr after CAI formation (Kruijer et al., 2014) and the chondrite parent bodies between 2-4 Ma after CAI formation (e.g., Hellmann et al., 2019). Earlier chronological work on large igneous clasts/inclusions, showed that the majority of them formed early within the first ~ 4 Myr of the solar system, as does the internal mineral ^{26}Al - ^{26}Mg isochrons of the other igneous clast analyzed, NWA 12261-I1 (Almeida et al., 2017; Crowther et al., 2018; Ruzicka et al., 2018). Nonetheless, the young Pb-Pb age of Pap-I1 (4529.3 ± 2.1 Ma) is not unusual compared to Hf-W ages where a group of four inclusions with young Hf-W model ages (~ 7 to >50 Ma after CAI formation), share many of the same characteristics as Pap-I1: they are either of the *Unfr* or *Unfr+K* chemical type, have microporphyritic textures and O isotope compositions similar to those of their host meteorites and are thus believed to have formed through impact melting of their host meteorites, followed by rapid cooling to preserve the heterogeneity in olivine and the glass in the inclusions (Ruzicka et al., 2018). However, the Paposo 004 host meteorite and Pap-I1 show no signs of brecciation, shock effects or any other evidence for post-accretionary formation, questioning the idea that the Pb-Pb age could reflect late (~ 35 Ma) impact melting of its host meteorite. The I-

Xe age of 126.5 Ma after CAI formation is also unusually young (Gilmour and Filtness, 2019), but does not rule out an impact event at 35 Ma after CAI formation. It does provide evidence of an event ~ 90 Myr later that reset the I-Xe chronometer, but did not affect the U-Pb chronometer.

This would indicate that the Pb-Pb of Pap-I1 does not reflect its formation age, but that the U-Pb system may not have closed until the waning of thermal metamorphism. A number of studies have shown that metamorphism on the L chondrite parent body may have lasted up to 60 Ma after CAI formation, based on U-Pb phosphate ages (Göpel et al., 1994; Amelin, 2000; Blackburn et al., 2017) as well as whole-rock and chondrule CDT- $^{207}\text{Pb}/^{206}\text{Pb}$ model ages (Bouvier et al., 2007). It is notable that these young ages (ranging from 4509.55 ± 1.36 Ma for L6 Bruderheim to 4542.6 ± 2.4 Ma for L5 Knyahinya) were determined on equilibrated L chondrites (petrologic types 4 to 6) and show some degree of correlation between their age and petrologic type. As previously stated, Paposo 004 is classified as a type 3.1 L chondrite (Ruzicka et al., 2015) where little evidence of thermal metamorphism is expected to be visible from mineralogy and composition. This holds true for the inclusion Pap-I1 where the lack of olivine homogenization and lack of widespread devitrification of glass indicate that temperatures likely would not have reached above 400°C (Miyamoto et al., 1986; Huss et al., 2006), below estimates for the closure temperature of Pb diffusion in various minerals (e.g. Amelin et al., 2005; Göpel et al., 1994). It therefore seems that the petrologic characteristics, as well as the *in situ* ^{26}Al - ^{26}Mg isochron age which was not reset, and the young Pb-Pb age (consistent with U-Pb and Pb-Pb ages of other L chondrites) cannot be easily reconciled.

A possible source of age uncertainty is the U isotope composition of Pap-I1. While the use of the bulk solar $^{238}\text{U}/^{235}\text{U}$ value of 137.786 ± 0.013 to calculate the Pb-Pb age is considered to be acceptable for inner solar system materials other than CAIs (Connelly et al., 2012), the potential age difference can be significant if the true value of Pap-I1 deviates from the solar value. In this particular case, deviations could potentially account for a change of ~ 1 Ma in the Pb-Pb age when covering the range of compositions reported by Brennecka et al. (2010) in CAIs. While the wide range of these values are likely inapplicable for chondritic materials due to the enrichment of refractory elements

in CAIs, we consider this to be a conservative estimate. A change of that magnitude in age is insignificant compared to our stated uncertainty of 2.1 Ma. In any case, while the U isotope composition may require a correction of the Pb-Pb age, a potential change of 1-2 Ma at an age around 35 Ma after CAI formation does not alter any scenarios in a meaningful way and would not be enough to reconcile the apparent differences between petrology and chronology.

The implications of these discordant results between various chronometers may be that the application of Pb-Pb chronology to date formation could be significantly hampered in L chondrite samples that have undergone even minimal thermal metamorphism. While this should not disqualify Pb-Pb chronology from being used on meteoritic material from pristine L chondrites, it does suggest that caution should be exercised when selecting samples for purely chronological purposes.

3.3.3 Pb-Pb age of QC 001-C1

The chondrule from CB_a chondrite QC 001 is another sample that warrants a closer look at its Pb-Pb isochron. The isochron is defined by the W1-3, W7 and W8 leachates, as well as the residue, and corresponds to an age of 4563.39 ± 0.56 Ma. This age is 0.90 ± 0.60 Myr older than the mean age of four chondrules in the CB_a chondrite Gujba, whose ages range from 4562.32 ± 0.52 Ma to 4562.66 ± 0.43 Ma, but it does overlap within uncertainties the ages of the two older chondrules (Bollard et al., 2015). This would be at odds with a single impact producing the chondrules in CB chondrites, but could be resolved if another impact event occurred 0.5 to 1 Myr earlier. Alternatively, the gap between the Pb-Pb ages could be explained by faster cooling of some CB chondrules compared to others. It has been suggested that some CB chondrites formed in different locales of an impact-produced vapour plume (Weyrauch et al., 2019). However, the cooling rates calculated from metals (on the scale of hours to years; Florin et al., 2021) are not nearly low enough to account for an age gap of 0.5 to 1 Myr.

Perhaps a better explanation is that the fractions that defined the isochron of QC 001 were not binary mixtures of terrestrial and radiogenic Pb, but still contained some primordial Pb. This could rotate the isochron and result in a spuriously old age. A regression line through the two leachates that were not included in the isochron plot

towards the Nantan troilite and point towards a comparatively young age of ~ 4542 Ma (Figure 33). Omitting the W1-3 leachate fraction from the isochron results in an age of 4564.3 ± 2.7 Ma, an older but more imprecise age that lies within uncertainty of the Pb-Pb ages reported in the Gujba chondrules (Bollard et al., 2015). The older age indicates that the W1-3 is made up primarily of terrestrial Pb, whereas the leachates W7 and W8 and the residue may have incorporated a proportionally larger share of primordial Pb compared to terrestrial Pb. Since it cannot be fully confirmed that the isochron was indeed rotated, the age of 4563.39 ± 0.56 Ma should be interpreted as the older limit for chondrule formation of CB chondrites, or, less likely, could date a previous impact event.

3.3.4 Combined Al-Mg and U-Pb systematics of chondrules

The Pb-Pb ages of individual chondrules in prior studies range from coeval formation with CAIs to about ~ 4 Ma after CAI formation (Connelly et al., 2012; Bollard et al., 2017). In particular, the Pb-Pb ages within the first ~ 1.7 Ma after CAI formation have been a source of discussion, as there are only very few chondrules with ^{26}Al - ^{26}Mg ages determined from internal mineral isochrons during that interval (Pape et al., 2019). The chondrules dated in this dataset primarily fall into that early category.

Only two chondrules have both meaningful Pb-Pb ages and *in situ* ^{26}Al - ^{26}Mg ages. In both cases, the ^{26}Al - ^{26}Mg ages are younger than the Pb-Pb ages. Chondrule NWA 10854-C6 has a Pb-Pb age of 4567.82 ± 0.57 and a ^{26}Al - ^{26}Mg age of $1.95^{+0.24}_{-0.19}$ Ma after CAI formation, that translates to an absolute age of $4565.35^{+0.29}_{-0.25}$ Ma, relative to the absolute CAI age of 4567.30 ± 0.16 Ma (Connelly et al., 2012), and an age gap of 2.5 ± 0.6 Myr. Both Pb-Pb and ^{26}Al - ^{26}Mg ages are less precise for NWA 8007-C1, with 4567.3 ± 1.6 Ma and $1.70^{+0.81}_{-0.44}$ Ma after CAI formation, respectively. The ^{26}Al - ^{26}Mg age translates to an absolute age of $4565.60^{+0.46}_{-0.83}$ Ma, but given the imprecise Pb-Pb age results in an age gap of $1.7^{+1.7}_{-1.8}$ Myr and is thus not an ideal sample. The results from NWA 10854-C6 are consistent with the data of Bollard et al. (2019) that showed similar age gaps between Pb-Pb ages and *in situ* ^{26}Al - ^{26}Mg ages. They found that chondrules with older ages, averaging around 4567.5 Ma, had lower inferred $^{26}\text{Al}/^{27}\text{Al}$ ratios at the time of CAI formation ($[\text{}^{26}\text{Al}/\text{}^{27}\text{Al}]_0 = 4.75^{+1.99}_{-1.21} \times 10^{-5}$) than chondrules that averaged ages of 4566.2 Ma ($[\text{}^{26}\text{Al}/\text{}^{27}\text{Al}]_0 = 1.82^{+0.57}_{-0.40} \times 10^{-5}$). This observation was explained

by an initial heterogeneous distribution of ^{26}Al in the Solar nebula, caused by thermal processing of primordial molecular cloud material in the inner Solar System that selectively depleted the carriers of ^{26}Al (and ^{54}Cr). CI chondrite-like, ^{26}Al -enriched dust was subsequently admixed to the depleted inner disk (Larsen et al., 2011; Schiller et al., 2018), resulting in higher $[\text{}^{26}\text{Al}/\text{}^{27}\text{Al}]_0$ ratios when calculated back to CAI formation. Adding the data from the two chondrules studied here (Figure 37) fits into the described trend. There are, however, some reservations with the interpretation from Bollard et al. (2019). Firstly, the proposed mechanism of selective destruction of ^{26}Al and ^{54}Cr from thermal processing to achieve the lower initial ^{26}Al abundance and lower $\epsilon^{54}\text{Cr}$ values is based on the correlation of ^{26}Mg excesses and $\epsilon^{54}\text{Cr}$ values in Solar System materials, where the inner Solar System (NC reservoir) is characterized by negative $\delta^{26}\text{Mg}^*$ and $\epsilon^{54}\text{Cr}$ values, whereas the outer Solar System (CC reservoir) has positive values for both (Larsen et al., 2011; Van Kooten et al., 2016). This correlation has been shown to not hold up with the analysis of ungrouped NC achondrites Asuka 881394 and NWA 7325 with positive $\delta^{26}\text{Mg}^*$ and negative $\epsilon^{54}\text{Cr}$ values (Koefoed et al., 2016; Goodrich et al., 2017; Wimpenny et al., 2019). In addition to these data points that refute the proposed relationship, ^{26}Mg excesses are not only controlled by ^{26}Al abundances, but also by Al/Mg ratios of samples, and different thermal histories in different objects can modify $\delta^{26}\text{Mg}^*$, i.e., prolonged magma residence vs. rapid cooling (Wimpenny et al., 2019).

Secondly, all but one Allende chondrule analyzed by both Pb-Pb and *in situ* ^{26}Al - ^{26}Mg chronometry have been from the L3.10 chondrite NWA 5697, formed in the NC reservoir in the inner Solar System (Bollard et al., 2019). Bollard et al. (2017) reported Pb-Pb ages of chondrules from two CR2 chondrites and CV3 Allende, as well as the NWA 5697 chondrules that were subsequently analyzed by SIMS for their ^{26}Al - ^{26}Mg age in Bollard et al. (2019). If ^{26}Al heterogeneity is indeed responsible for the discordance between Pb-Pb and ^{26}Al - ^{26}Mg ages, chondrules from carbonaceous chondrites would be predicted to have higher $^{26}\text{Al}/^{27}\text{Al}$ ratios than OC chondrules with equal Pb-Pb ages. This is not the case for the one Allende chondrule in Bollard et al. (2019), whose age offset between Pb-Pb and ^{26}Al - ^{26}Mg age is in fact the largest of the dated chondrules. Furthermore, the Pb-Pb ages of individual CR2 chondrules analyzed by Bollard et al. (2017) span the same age range from 0 to 4 Ma after CAI formation. Compared to OC chondrules, CR

chondrule formation has been independently dated by *in situ* ^{26}Al - ^{26}Mg chronometry to have occurred later than 2.2 Ma after CAI formation, and may have lasted until >3.9 Ma after CAI formation (Schrader et al., 2017; Tenner et al., 2019). While no ^{26}Al - ^{26}Mg data on the CR chondrules dated by Bollard et al. (2017) is available yet, for the CR chondrules with Pb-Pb ages within 1 Myr of CAI formation, the initial $^{26}\text{Al}/^{27}\text{Al}$ ratios would have to be at least $\sim 2 \times 10^{-5}$, about 3 times higher than the highest initial $^{26}\text{Al}/^{27}\text{Al}$ ratios determined for CR chondrules so far.

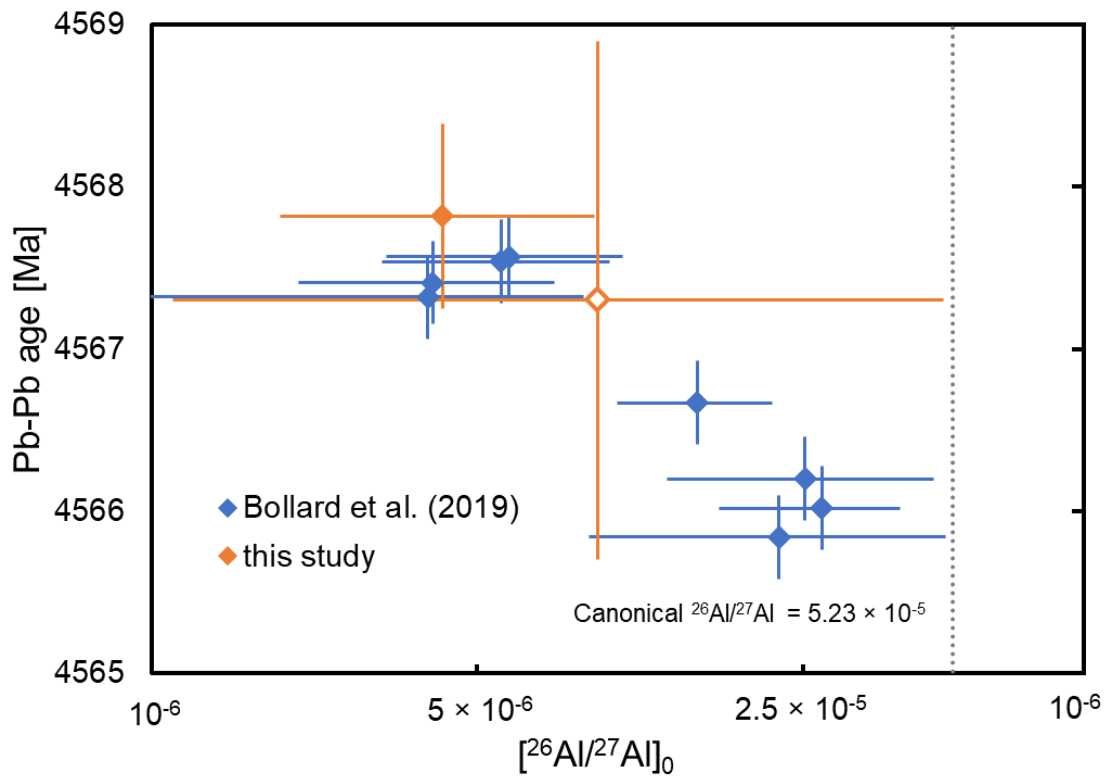


Figure 37: Back-calculated $^{26}\text{Al}/^{27}\text{Al}$ ratios ($=[\text{}^{26}\text{Al}/\text{}^{27}\text{Al}]_0$) and Pb-Pb ages of chondrules, with the canonical $^{26}\text{Al}/^{27}\text{Al}$ of 5.23×10^{-5} (Jacobsen et al., 2008) added as a reference line. The empty orange symbol is NWA 8007-C1, with its large uncertainties.

If the lower-than-expected initial $^{26}\text{Al}/^{27}\text{Al}$ ratios (relative to the Pb-Pb ages) are not caused by ^{26}Al heterogeneity, a different scenario must explain the results. One such scenario that has been proposed is that the absolute ages of CAIs, determined from CAIs from CV3 chondrites Efremovka and Allende at 4567.30 ± 0.16 Ma (Connelly et al.,

2012), are spuriously young due to later-stage aqueous and thermal alteration on the CV parent body (Krot et al., 1998; Krot et al., 2021). Older ages have been proposed in the past, but U isotope correction was estimated from the U/Th correlation with U isotopic compositions in CV3 CAIs (Bouvier and Wadhwa, 2010) or have not been published in a peer-reviewed journal yet (Bouvier et al., 2011b). Desch et al. (2021) in a conference abstract used a statistical approach of short-lived chronometers in achondrites to estimate the absolute age of CAIs at 4568.61 ± 0.26 Ma. However, a change in the absolute age of CAIs only affects $[\text{}^{26}\text{Al}/\text{}^{27}\text{Al}]_0$ of the chondrules, which would shift all points in Figure 37 to the right and maintain the differences between them. Furthermore, the age differences between Pb-Pb and ^{26}Al - ^{26}Mg mineral isochron ages are not constant and vary by up to 2 Myr, so that older absolute CAI ages cannot account for those differences.

The most straightforward explanation of the difference between Pb-Pb and ^{26}Al - ^{26}Mg SIMS ages is that, given the consistency between various studies of UOC chondrules (including this data and that of Bollard et al. (2019)), *in situ* ^{26}Al - ^{26}Mg chronometry dates the last crystallization event of chondrules, between 1.8 and 2.9 Ma after CAI formation. The Pb-Pb chronometer, on the other hand, may date chondrule precursor formation, analog to bulk Mg model ages with ages in the same range. If the Pb-Pb ages date the same precursor formation as bulk Mg model ages do, it is not visible in our dataset, nor in the dataset of Bollard et al. (2019), as seen in Figure 38. There may well have been timing differences between Al/Mg and U/Pb fractionation of chondrule precursors.

On the other hand, $^{204}\text{Pb}/^{206}\text{Pb}$ - $^{207}\text{Pb}/^{206}\text{Pb}$ isochrons may not be chronologically significant, as Blichert-Toft et al. (2020) have shown that Th/U variations exist within individual chondrules that could break the condition necessary of a single initial Pb composition at time of formation to obtain a chronologically valid age. These variations are likely due to the incorporation of different Th and U carriers, which may or may not be cogenetic. Their conclusion suggest that caution should be exercised when interpreting linear arrays in $^{204}\text{Pb}/^{206}\text{Pb}$ - $^{207}\text{Pb}/^{206}\text{Pb}$ space as isochrons. Isochrons can be evaluated by plotting the $^{208}\text{Pb}/^{206}\text{Pb}$ ratios against $^{204}\text{Pb}/^{206}\text{Pb}$ ratios, where the radiogenic $^{208}\text{Pb}^*/^{206}\text{Pb}^*$ intercept allows for calculation of κ ($= \text{}^{232}\text{Th}/\text{}^{232}\text{U}$). If the analyzed fractions do not align in $^{204}\text{Pb}/^{206}\text{Pb}$ - $^{208}\text{Pb}/^{206}\text{Pb}$ space, that would indicate multiple radiogenic phases in the sample.

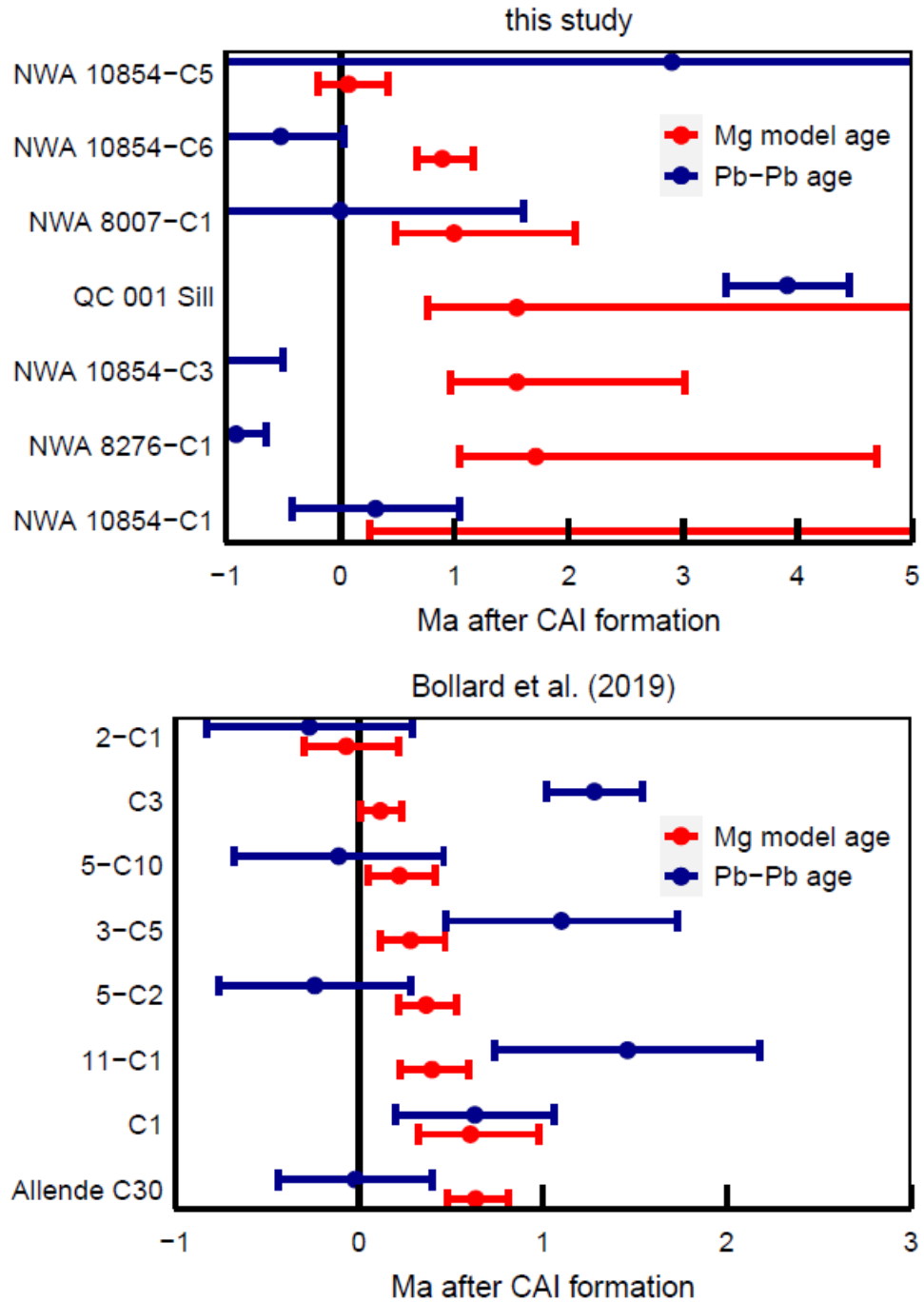


Figure 38: Comparison of Pb-Pb ages with bulk Mg model ages of chondrules between this study (top) and chondrules from the L3.10 chondrite NWA 5697 Bollard et al. (2019, bottom). Ages are relative to the absolute age of CAIs at 4567.30 ± 0.16 Ma (Connelly et al., 2012).

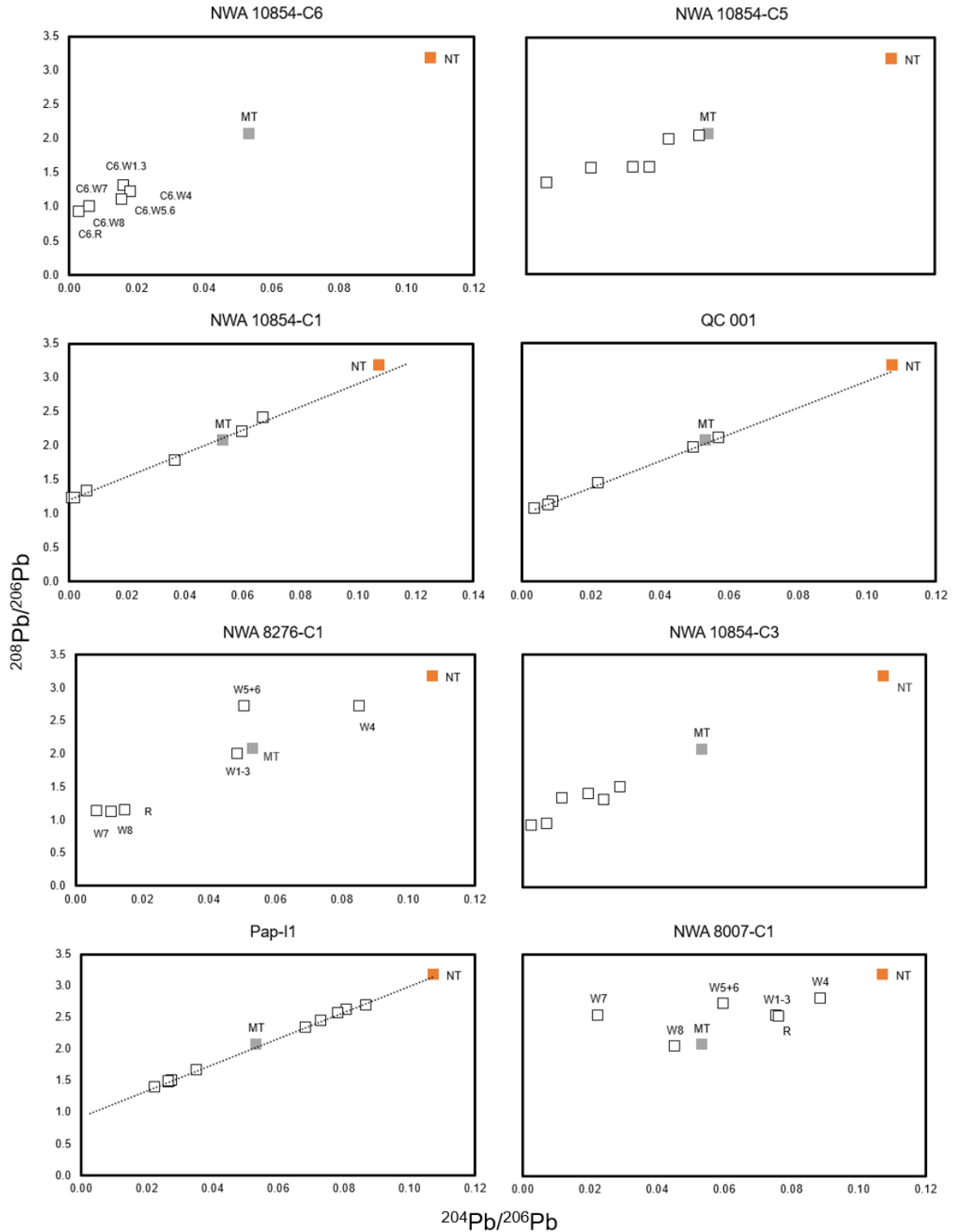


Figure 39: Overview of $^{204}\text{Pb}/^{206}\text{Pb}$ vs $^{208}\text{Pb}/^{206}\text{Pb}$ diagrams of 8 chondrules with statistically significant isochrons, with the Nantan troilite (NT; Blichert-Toft et al., 2010) and modern terrestrial (MT; Stacey and Kramers, 1975) compositions plotted for reference.

In this case, ^{208}Pb was not measured in every sample due to the use of the SEM setup, where the positioning and number of the high-end Faraday cups does not allow for analysis of ^{208}Pb . Most samples that were analyzed this way were subsequently analyzed with a Faraday cup setup, however, those analyses were limited to a short-number of cycles with low concentrations. On a first-order scale, those results should be sufficient to evaluate if they align linearly in a $^{204}\text{Pb}/^{206}\text{Pb}$ - $^{208}\text{Pb}/^{206}\text{Pb}$ diagram, though the calculation of a precise κ value may not be warranted.

The $^{204}\text{Pb}/^{206}\text{Pb}$ vs $^{208}\text{Pb}/^{206}\text{Pb}$ diagrams shown in Figure 39 suggest that for at least three samples, Pap-II, NWA 10854-C1 and QC 001-C1 the $^{207}\text{Pb}/^{206}\text{Pb}$ isochrons remain valid. For the two samples NWA 10854-C3 and -C5, their “isochrons” are characterized by a suspiciously old Pb-Pb age and large age uncertainties, respectively. Their non-linearity in $^{204}\text{Pb}/^{206}\text{Pb}$ vs $^{208}\text{Pb}/^{206}\text{Pb}$ space suggests that those $^{207}\text{Pb}/^{206}\text{Pb}$ “isochrons” are invalid. The same can be said for NWA 8007-C1, as there seem to be two visible carriers with distinct Th/U ratios. The remaining two chondrules, NWA 10854-C6 and NWA 8276-C1, are not as straightforward to evaluate. For the latter, W7 and W5+6 were not included in the Pb-Pb isochron regression and plot off a line through the three included fractions (R+W8+W4). Given that those leachates and the residue that determine the Pb-Pb isochron also plot on a straight line in $^{204}\text{Pb}/^{206}\text{Pb}$ - $^{208}\text{Pb}/^{206}\text{Pb}$ space and the $^{208}\text{Pb}^*/^{206}\text{Pb}^*$ intercept defines a close to planetary (~ 3.9) Th/U value, the age should not be discarded, though doubts about its validity may persist, particularly as its old age (4568.21 ± 0.29 Ma) is older than the currently accepted absolute age of CAIs (4567.30 ± 0.16 Ma; Connelly et al., 2012). This would suggest that chondrules (or their precursors), and potentially CAIs, formed earlier than that time. While the dataset is not the most robust, it could be a further piece of evidence that the absolute age of some CAIs is older than the one calculated by Connelly et al. (2012).

The situation for NWA 10854-C6 is similar, as there is some variation among the early leachates, but those included in the Pb-Pb isochron appear to plot on a straight line and the $^{208}\text{Pb}^*/^{206}\text{Pb}^*$ intercept defines a Th/U ratio that is similarly close to the planetary value.

These observations, along with the anomalous Pb-Pb age of Pap-II, suggest that Pb-Pb chronology in bulk samples from meteorites needs to be evaluated carefully. In addition

to heterogeneous incorporation of Th and U carriers, secondary processes such as impact events, thermal metamorphism and aqueous alteration, played a role in all but the most pristine chondritic materials. These processes could have conceivably affected the isotope systematics of various chronometers in some samples, necessitating the assessment of their petrological setting as well. On the other hand, the re-heating and recycling of chondrules does not cause any significant mass-dependent fractionation effects on Pb isotopes, as demonstrated by Zn isotope analysis of chondrules (Bollard et al., 2017)

3.3.5 Change in Cr isotope composition over time?

Chromium isotopes are useful tracers of the genetic relationship between meteoritic samples. Warren (2011) first classified meteorites and their parent bodies into the non-carbonaceous chondrite (NC) and carbonaceous chondrite (CC) reservoirs based on their distinct O, Cr and Ti isotope anomalies. More recent work by Schneider et al. (2020) studied chondrules from both reservoirs and found that the Cr compositions in CC chondrules were influenced by the admixture of more ^{54}Cr -enriched material and, more generally, that the isotopic anomalies reflected heterogeneity among the chondrule precursor.

The range of $\epsilon^{54}\text{Cr}$ values of the analyzed chondrules are consistent with previous observations for both OC chondrules and the CB chondrules. The OC chondrules have characteristic negative ^{54}Cr anomalies, consistent with their formation in the NC reservoir, whereas the CB_a chondrule from QC 001 is enriched in ^{54}Cr , as CC material is. The individual chondrule analyses, however, reveal distinct Cr isotope compositions between them, which had previously not been reported. Of particular interest are the two chondrules from NWA 10854, which have distinct $\epsilon^{54}\text{Cr}$ values (-0.59 ± 0.05 and -0.27 ± 0.04 for C1 and C6, respectively). If the $\epsilon^{54}\text{Cr}$ variations are reflective of different source reservoirs of chondrules within the NC reservoir, this would suggest that chondrules were transported substantially before accretion into their parent bodies. On the other hand, $\epsilon^{54}\text{Cr}$ variations may be caused by a temporal difference of precursor (or chondrule) formation.

To evaluate these distinct Cr isotope composition, $\epsilon^{54}\text{Cr}$ values are plotted against chronological information that could potentially reveal a change in the Cr isotope

composition in the NC reservoir over time. To broaden the dataset, two chondrules from the L3.10 chondrite NWA 5697, which have been chronologically dated and had their $\epsilon^{54}\text{Cr}$ values analyzed (Connelly et al., 2012; Bollard et al., 2019), are added. The $\epsilon^{54}\text{Cr}$ values are plotted against $\delta^{26}\text{Mg}^*$, bulk Mg model ages, *in situ* ^{26}Al - ^{26}Mg ages and Pb-Pb ages in Figure 40.

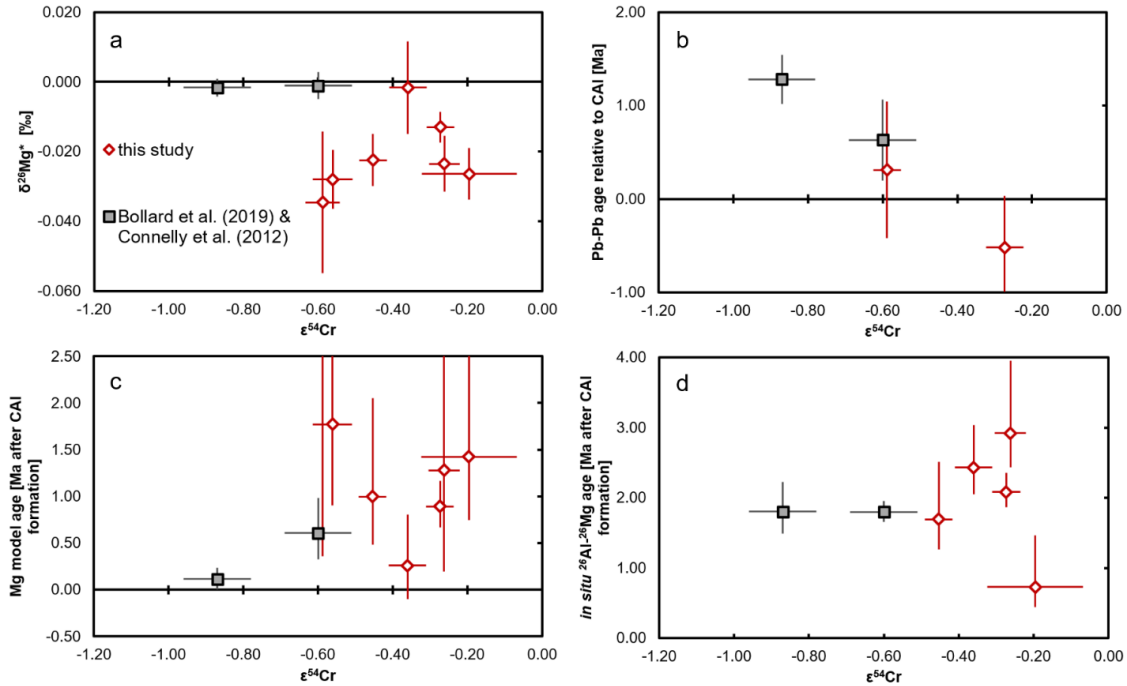


Figure 40: Diagrams of $\epsilon^{54}\text{Cr}$ of OC chondrules plotted against their a) $\delta^{26}\text{Mg}^*$ values, b) Pb-Pb ages, c) bulk Mg model ages, and d) *in situ* ^{26}Al - ^{26}Mg ages. Included are data of two chondrules from L3.10 chondrite NWA 5697 (Connelly et al., 2012; Bollard et al., 2019).

Judging from the diagrams, a trend between Pb-Pb ages and $\epsilon^{54}\text{Cr}$ and, to a lesser extent, a trend between bulk Mg model ages and $\epsilon^{54}\text{Cr}$ are discernible. It is notable, however, that the trends are reversed, i.e., $\epsilon^{54}\text{Cr}$ values become more negative over time when plotted against Pb-Pb ages (those determined to be meaningful in the previous chapter), whereas the opposite is visible when plotted against bulk Mg model ages. While York model regressions judge both of these trends to be statistically significant by Isoplot 4.15 (Ludwig, 2008) based on the available data (MSWD = 0.17, $n = 4$), the lack of additional data in the $\epsilon^{54}\text{Cr}$ vs. Pb-Pb age diagram could skew the probability of fit and outliers have a disproportionate effect on the regression. Furthermore, the magnitude of the linear trend

would suggest chondrules with Pb-Pb ages younger than 2 Ma after CAI formation have $\epsilon^{54}\text{Cr}$ values more negative than -1. This is doubtful, given no such $\epsilon^{54}\text{Cr}$ values have been reported for any chondrules. Considering this, the dearth of data points and questions surrounding the accuracy of Pb-Pb ages in mind, the Pb-Pb vs $\epsilon^{54}\text{Cr}$ trend may not be meaningful.

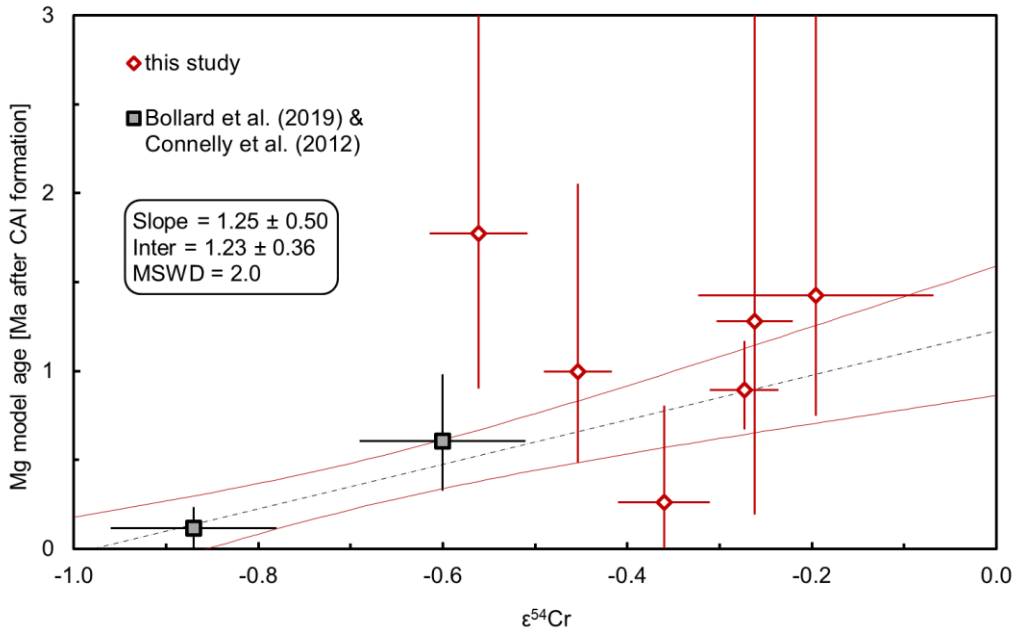


Figure 41: $\epsilon^{54}\text{Cr}$ plotted against bulk Mg model ages for OC chondrules.

On the other hand, the regression between the bulk Mg model ages and $\epsilon^{54}\text{Cr}$ is more tenuous (MSWD = 2.0, $n = 8$) and does not account for chondrules with “infinite” model ages (Figure 41). The trend suggests an increase of $\sim 0.8 \pm 0.3$ ϵ -units over 1 Myr and an initial $\epsilon^{54}\text{Cr}$ value in the NC reservoir of $\sim -1 \pm 0.2$. It is possible that this increase could reflect the admixing of CAI- or AOA-like material ($\epsilon^{54}\text{Cr} \sim 6$) to the NC reservoir. Ordinary chondrites generally have less than 1 vol% of CAIs or AOAs (Weisberg et al., 2006), likely even less, in the range of a couple of ppm (Haugbølle et al., 2019). However, in order to reproduce chondrules with $\epsilon^{54}\text{Cr}$ values around -0.3, CAI or AOAs would have to contribute 10% to the chondrules at the time of their precursor formation, as a simple mass-balance calculation returns. This would also conflict with the findings of Ebert et al. (2018), who suggested that refractory minerals without excesses in ^{50}Ti (and, by extension likely ^{54}Cr) were present in the NC reservoir. Finally, the trend could

reflect thermal processing, where carriers with more negative $\epsilon^{54}\text{Cr}$ values were selective sublimated during nebular processes, or a change in composition of infalling molecular cloud material. As more data becomes available, this potential relationship between the ^{54}Cr anomalies and precursor formation could be evaluated in more detail.

3.3.6 Implications for chondrule formation

Chondrules are proposed to have formed through flash heating events, where precursors were heated above 1500°C (Hewins and Connolly, 1996) and cooled quickly within hours to days (Desch and Connolly, 2002). Precursors of chondrules are believed to include silicate dust aggregates that sublimated from the nebular gas, CAIs (Russell et al., 1996), AOAs (Marrocchi et al., 2019), as well as other chondrules (Villeneuve et al., 2015) and even planetesimal material (Libourel and Krot, 2007). Along with the presence of relict grains (e.g., Jones and Danielson, 1997) and refractory forsterite grains in chondrules that formed within the first 3 Ma after CAI formation (Gregory et al., 2020), this suggests that materials that formed coevally with CAIs were reworked and incorporated into chondrules. Furthermore, petrologic and geochemical evidence has suggested that chondrules themselves underwent substantial recycling (Libourel et al., 2006; Ruzicka et al., 2007; Ruzicka et al., 2008; Mahan et al., 2018).

We have measured one of the oldest ^{26}Al - ^{26}Mg SIMS ages for an ordinary chondritic component as the Pap-I1 inclusion formed $0.73^{+0.29}/_{-0.22}$ Ma after CAIs. The inclusion contains a relict chondrule preserved inside which is a contextual proof that chondrules did form earlier than 1.7 Ma after CAI formation and were subsequently incorporated or reprocessed until accretion during the suggested “time gap” between CAIs and chondrules observed by *in situ* ^{26}Al - ^{26}Mg chronometry by SIMS. It suggests that chondrule formation occurred continuously or regularly from ~ 0.7 Ma after CAI formation onwards. This can nonetheless be reconciled with *in situ* ^{26}Al - ^{26}Mg ages, that suggest chondrule formation began only after ~ 1.7 Ma: chondrules may have undergone continuous recycling by transient heating events (e.g., Connolly et al., 2006), where Mg diffusion between the minerals would have reset the ^{26}Al - ^{26}Mg chronometer (but not affected the Mg isotope composition of the bulk chondrule), until ~ 1.7 Ma after CAI formation, when the efficiency of chondrule recycling began to wane (potentially, due to

decreasing gas and dust density in the Solar nebula), and radiogenic ingrowth of ^{26}Mg could accumulate in minerals undisturbed. The survival of the old age determined from the mineral isochron of Pap-I1 is extraordinary and can be attributed to its large size that may have prevented re-setting of the ^{26}Al - ^{26}Mg systematics.

This would be compatible with the range of model ages of chondrules determined from their bulk Mg isotope composition, which is understood to date Al/Mg fractionation and the formation of chondrule precursors, as well as with the range of model ages (0 to ~3 Ma after CAI formation) of refractory forsterite grains (Gregory et al., 2020). These chronological constraints could feasibly be satisfied by nebular chondrule formation models, such as bow shocks generated by planetary embryos passing through regions with higher gas and dust densities (Morris et al., 2012).

Alternatively, the ^{26}Al - ^{26}Mg ages of chondrules could indicate the timing of their accretion onto the chondrite parent bodies, which could have shielded chondrules from further re-setting of the ^{26}Al - ^{26}Mg chronometer. The earliest iron meteorite parent bodies accreted within the first 0.5 Myr of the Solar System (Kruijer et al., 2014), while accretion of chondrites is constrained by chondrule ages that lasted up to 2.9 Ma after CAI formation for ordinary chondrites (e.g., Pape et al., 2018) and 3.9 Ma after CAI formation for carbonaceous chondrites (e.g., Schrader et al., 2017). This is consistent with the ^{26}Al - ^{26}Mg age of NWA 12261-I1 at $2.92^{+1.03}_{-0.49}$ Ma after CAI formation that provides an upper limit on the accretion age of the H chondrite parent body at ~ 4 Ma after CAI formation. If chondrules formed in a planetary setting, e.g., from impacts (e.g., Villeneuve et al., 2015; Lichtenberg et al., 2018), our data suggests that those occurred from the timing of CAI formation onwards and lasted until ~ 4 Ma after CAI formation for CC chondrules, and until ~ 5 Ma for CB chondrules.

The Pb-Pb ages of chondrules themselves have been and continue to be controversial inasmuch as there has been disagreement on what event the Pb-Pb ages date. Bollard et al. (2019) made the case that they date the time of crystallization, whereas other have argued that they date the U/Pb fractionation event, i.e., chondrule precursor formation (Blichert-Toft et al., 2020). The consistency and extent of OC chondrule analyses by *in situ* ^{26}Al - ^{26}Mg chronometry suggest that the ages are more representative of chondrule formation ages (i.e., last crystallization event), whereas Pb-Pb ages likely date processes

occurring earlier or at the same time, such as precursor formation. Furthermore, previously published Pb-Pb ages of chondrules also need to be evaluated by analyzing $^{208}\text{Pb}/^{206}\text{Pb}$ ratios compared to $^{204}\text{Pb}/^{206}\text{Pb}$ ratios, to evaluate if the Pb isotope composition of the samples evolve from a single initial Pb composition. The exact role that the Pb-Pb ages play in the protoplanetary puzzle of chondrule chronology is still unclear.

4 The chronology of unique achondrite Erg Chech 002

The use of radiometric dating has been a cornerstone of unravelling the mysteries surrounding the formation and early evolution of the Solar System. Of the various chronometers, the absolute Pb-Pb chronometer and the short-lived, relative ^{26}Al - ^{26}Mg chronometer have been particularly useful in dating extraterrestrial materials. The ^{26}Al - ^{26}Mg chronometer can resolve events that took place within $\sim 30,000$ years, while the Pb-Pb chronometer has, among other milestones, established the age of the Solar System between ~ 4567 and 4568 Ma by dating Ca-Al-rich inclusions in CV3 chondrites (CAIs; Amelin et al., 2010; Connelly et al., 2012; Bouvier & Wadhwa, 2010). Despite the promise of both these chronometers, some issues have questioned their significance. On one hand, as a relative chronometer based on the decay of the short-lived parent nuclide ^{26}Al , the ^{26}Al - ^{26}Mg chronometer relies on a homogeneous abundance of ^{26}Al throughout the protoplanetary disk at the time of formation for its successful application to the entire Solar System. On the other hand, to determine accurate absolute ages using the dual decay chains from ^{235}U to ^{207}Pb and ^{238}U to ^{206}Pb , the $^{238}\text{U}/^{235}\text{U}$ ratio needs to be known. Until recently, it was assumed that the $^{238}\text{U}/^{235}\text{U}$ ratio was invariant at 137.88 among early Solar System materials, when significant variations in different objects were discovered (Amelin et al., 2010; G. A. Brennecka et al., 2010). The assumption of a homogeneous distribution of ^{26}Al in the protoplanetary disk has repeatedly been challenged, without a consensus in the scientific community emerging. Studies involving CAIs, ameboid olivine aggregates (AOAs), bulk meteorites (Larsen et al., 2011), chondrules (Bollard et al., 2019) and angrites (Schiller et al., 2015a) suggested an initial $^{26}\text{Al}/^{27}\text{Al}$ ratio in the inner Solar System around 1×10^{-5} , around 80% lower than the canonical value of 5×10^{-5} (Jacobsen et al., 2008). Other studies have disagreed with these conclusions (e.g., Wasserburg et al., 2012; Kita et al., 2013; Gregory et al., 2020). In particular, combined Pb-Pb and ^{26}Al - ^{26}Mg dating of achondrites, e.g., angrites or unique, ungrouped meteorites, have been frequently utilized to test the hypothesis of ^{26}Al heterogeneity (e.g., Bouvier et al., 2011; Schiller et al., 2015; Wimpenny et al., 2019). The Pb-Pb and ^{26}Al - ^{26}Mg ages of some meteorites that formed in the non-carbonaceous inner Solar System (NC reservoir; Warren, 2011), such as the angrite D'Orbigny

(Amelin, 2008b; Schiller et al., 2015a; Tissot et al., 2017), a common anchor meteorite, and the unique achondrite Asuka 881394 (Wadhwa et al., 2009; Wimpenny et al., 2019) do not match when anchored to CAIs from the CV3 chondrites Efremovka and Allende (Connelly et al., 2012). Conversely, the Pb-Pb and ^{26}Al - ^{26}Mg ages achondrites that formed in the carbonaceous chondrite (CC) reservoir of the outer Solar System, such as NWA 6704 (Amelin et al., 2019; Sanborn et al., 2019) and NWA 2976 (Bouvier et al., 2011), are concordant when anchored to the same CAI age. The discordance in the data of some NC meteorites have been interpreted by different studies to reflect either heterogeneity of ^{26}Al in the Solar System (Schiller et al., 2015a), or that in particular the Al-Mg systematics were disturbed through thermal metamorphism or shock heating from impact events (Koefoed et al., 2016; Sanborn et al., 2019; Wimpenny et al., 2019).

In order to further evaluate the distribution of ^{26}Al in the early Solar System, we have used both the Pb-Pb and ^{26}Al - ^{26}Mg chronometers to date the formation of the unique achondrite Erg Chech 002. EC 002 is a recent meteorite find with an unusual chemistry and mineralogy: its composition is enriched in alkaline elements (comparable to terrestrial andesites) (Barrat et al., 2021) and contains large (up to 9 cm) orthopyroxene megacrysts (Gattacceca et al., 2021) in a groundmass of sodic plagioclase and pigeonite (Figure 42). Geochemically, EC 002 exhibits a distinct trace element pattern compared to other andesitic meteorites, with no significant anomalies in alkali and high field-strength elements (Barrat et al., 2021). Highly siderophile elements show fractionation between the compatible and incompatible elements that suggest metal-silicate separation occurred on the parent body of EC 002 (Nicklas et al., in review).

Mass-independent $\Delta^{17}\text{O}$ values suggest affinity with four anomalous eucrites, Bunburra Rockhole, EET 92023, Emmaville and Asuka 881394, but they are mineralogically very different from EC 002 (Gattacceca et al., 2021). The O isotope composition along with the negative Tm anomaly of the whole-rock indicate formation in the NC reservoir. The elemental composition supports formation by partial melting of a chondritic precursor, followed by rapid cooling after cooling to 900°C, likely by excavation or ejection from an impact event (Barrat et al., 2021).

EC 002 has until now only been dated by in situ ^{26}Al - ^{26}Mg analysis by secondary ionization mass spectrometry (SIMS), as well as noble gas geochemistry. The Al-Mg

systematics result in an initial $^{26}\text{Al}/^{27}\text{Al}$ ratio of 5.72×10^{-6} and an age of 2.139 ± 0.013 Ma after CAI formation, making it the oldest igneous meteorite found to date. The K-Ar age is equal within uncertainty at 4534^{+117}_{-125} Ma, indicating the absence of disruption by impact on the parent body of EC 002 after that time, and both ^3He and ^{21}Ne exposure ages of ~ 25 Ma (Barrat et al., 2021). To get a better constraint on the crystallisation history of EC 002 and assess its potential as a new anchor for short-lived radionuclides, we analyzed the Mg, Pb and U isotope compositions by multi collector inductively coupled plasma mass spectrometry (MC-ICP-MS) to determine the ^{26}Al - ^{26}Mg and U-corrected Pb-Pb ages to further evaluate the formation of EC 002 and the distribution of ^{26}Al in the early Solar System.

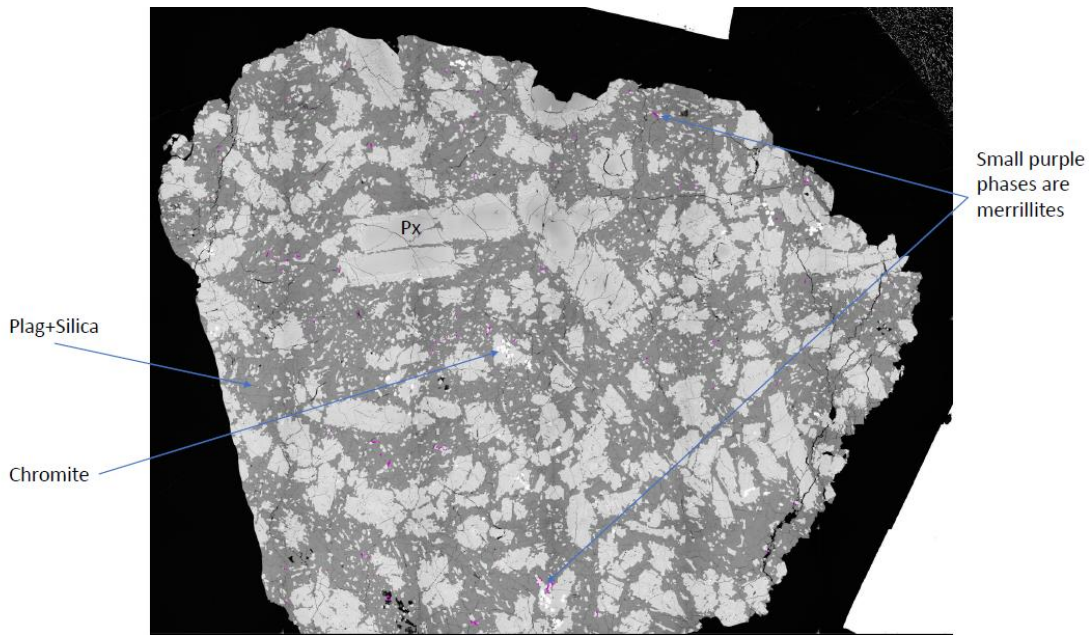


Figure 42: Secondary electron image of Erg Chech 002. Large pyroxene megacrysts are visible, surrounded by groundmass of sodic plagioclase, pigeonite and accessory chromite, merrillite and silica polymorphs.

4.1 Methods

For U-Pb and Al-Mg studies, a ~ 600 mg section of Erg Chech 002 (donated by Ben Hoefnagels, Big Bang Meteorites) was rinsed in acetone and water, prior to being

crushed in an agate mortar. Roughly 120 mg were taken as a bulk rock fraction. Pyroxene and feldspar minerals were separated by hand-picking under binoculars, with repeated crushing and sieving. Eight feldspar fractions were picked, along with a pyroxene and a fine-grained (<60 μm) fraction for Mg isotope analysis.

The protocols for Mg, Pb and U isotope analysis are described in Chapter 2.

4.2 Results

4.2.1 Al-Mg systematics

Magnesium isotope compositions and $^{27}\text{Al}/^{24}\text{Mg}$ ratios of the analyzed mineral fractions of EC 002 are summarized in Table 17. The $^{27}\text{Al}/^{24}\text{Mg}$ ratios span a range from 0.98 for the Px fraction to 34.4 in feldspars. Excesses in ^{26}Mg are not resolved from the terrestrial fractionation line for the bulk and Px fractions at $\delta^{26}\text{Mg}^* = 0.013 \pm 0.020\text{‰}$ and $0.010 \pm 0.010\text{‰}$, respectively. In the feldspar fractions and fines fraction, radiogenic ^{26}Mg excesses are resolved and range from $0.132 \pm 0.010\text{‰}$ to $2.058 \pm 0.015 \text{‰}$. A regression line through the data is obtained with Isoplot 4.15 (Ludwig, 2008), with a slope corresponding to the $^{26}\text{Al}/^{27}\text{Al}$ at the time of crystallization of $(8.89 \pm 0.79) \times 10^{-6}$ and an y-intercept ($\delta^{26}\text{Mg}^*_0$) of $-0.058 \pm 0.026\text{‰}$, representing the initial Mg isotope composition at time of crystallization (MSWD = 4.6). This $^{26}\text{Al}/^{27}\text{Al}_0$ corresponds to a crystallization age of $1.71 \pm 0.12 \text{ Ma}$ after CAI formation (Figure 43). This corresponds to an absolute age of $4565.59 \pm 0.19 \text{ Ma}$ when anchored to the canonical $^{26}\text{Al}/^{27}\text{Al}$ value of $(5.23 \pm 0.13) \times 10^{-5}$ (Jacobsen et al., 2008) and the absolute age of CAIs at $4567.30 \pm 0.16 \text{ Ma}$ (Connelly et al., 2012). When anchored to the D'Orbigny angrite (Pb-Pb age: 4563.51 ± 0.29 [Amelin, 2008; Tissot et al., 2017], initial $^{26}\text{Al}/^{27}\text{Al}$: $(3.98 \pm 0.15) \times 10^{-7}$ [Schiller et al., 2015] or $(5.06 \pm 0.92) \times 10^{-7}$ [Spivak-Birndorf et al., 2009]), the $^{26}\text{Al}-^{26}\text{Mg}$ formation age of EC 002 is $4566.51 \pm 0.32 \text{ Ma}$ or $4566.28 \pm 0.39 \text{ Ma}$, depending on whether the initial $^{26}\text{Al}/^{27}\text{Al}$ ratios of Schiller et al. (2015 or Spivak-Birndorf et al. (2009) is used. The ages are $0.92 \pm 0.37 \text{ Myr}$ and $0.69 \pm 0.44 \text{ Myr}$, respectively, older than when anchored to CAIs.

Regressing the subset of feldspar fractions results in an initial $^{26}\text{Al}/^{27}\text{Al}$ of $(8.36 \pm 0.49) \times 10^{-6}$ and a $\delta^{26}\text{Mg}^*_0$ of $-0.010 \pm 0.032\text{‰}$ (MSWD = 0.0017), equal within the stated uncertainties of the regression through the complete dataset (Figure 44).

The $\delta^{25}\text{Mg}$ values of EC 002 fractions are all distinctly lighter than the terrestrial rock standard San Carlos olivine and the bulk CV3 chondrite Allende, and lie between $-0.729 \pm 0.012\%$ and $-1.104 \pm 0.013\%$.

Table 17: Al-Mg data for EC 002 fractions.

Sample	$^{27}\text{Al}/^{24}\text{Mg}$	\pm	$\delta^{25}\text{Mg}$ [‰]	2SE	$\delta^{26}\text{Mg}$ [‰]	2SE	$\delta^{26}\text{Mg}^*$ [‰]	2SE	n
EC Px	0.98	0.05	-0.825	0.014	-1.603	0.030	0.010	0.010	4
EC Bulk	1.05	0.18	-0.736	0.037	-1.427	0.085	0.013	0.020	7
EC fines	3.45	0.17	-0.840	0.054	-1.571	0.101	0.139	0.006	8
EC fsp2-4	6.33	0.32	-0.729	0.012	-1.056	0.021	0.370	0.004	4
EC fsp1+8	9.03	0.45	-1.104	0.013	-1.627	0.022	0.532	0.005	4
EC fsp7	10.7	0.54	-0.957	0.010	-1.236	0.014	0.636	0.016	4
EC fsp6	34.4	1.72	-0.956	0.015	0.187	0.033	2.058	0.015	4

4.2.2 Uranium isotope composition

The results for the $^{238}\text{U}/^{235}\text{U}$ ratios in both the bulk and the W5-R leachates of EC 002 are summarized in Table 19. Both samples were measured twice, with their weighted average $^{238}\text{U}/^{235}\text{U}$ ratios being 137.819 ± 0.007 for the bulk, and 137.766 ± 0.027 for the leachates. The uncertainty associated with the analyses, particularly on the leachates, is mainly due to the low U concentration of this sample (2.5 V on ^{238}U from ≈ 5 ng U).

4.2.3 Lead isotope systematics

Lead isotope data for leachates and residue of a pyroxene fraction are presented in Table 18: Mass, Pb and U elemental data, and Pb isotope data for EC 002 and full session Pb isotope data for standards NBS 981 and NBS 983.

Sample	mass [mg]	Pb [ng]	U [ng]	Sample/ Blank	$^{206}\text{Pb}/^{204}\text{Pb}$ raw	$^{204}\text{Pb}/^{206}\text{Pb}$	2SE [%]	$^{207}\text{Pb}/^{206}\text{Pb}$	2SE [%]	Nantan model age
EC-W1-3	1.6	3.2	2.2	3808	41.5	0.0240	0.015	0.721208	0.002	4529.73
EC-W4	1.0	1.3	6.5	1549	42.5	0.0235	0.035	0.637959	0.004	4526.74
EC-W5+6	0.3	0.1	0.2	131	343.9	0.00268	3.42	0.717551	0.045	4567.91
EC-W7	4.1	0.6	0.3	302	10902.7	-0.000007	612	0.625026	0.021	4566.22
EC-W8	44.2	0.8	0.8	1331	6953.1	0.000122	7.25	0.625378	0.005	4565.64
EC-R	42.9	1.2	1.0	1366	16604.9	0.000039	21.3	0.625128	0.005	4565.92

. Leachates W7 and W8, as well as the residues are highly radiogenic, with raw $^{206}\text{Pb}/^{204}\text{Pb}$ ratios ranging from 7584 to 23487. Sample-to-blank ratios in these range from 302 to 1549. The first leachates (W1-3 to W5+6) have $^{206}\text{Pb}/^{204}\text{Pb}$ ratios in the range of 41 to 344, with a low sample-to-blank ratio of 131 for W5+6 and 1549 to 3808 for the remaining leachates. In an “inverse” $^{204}\text{Pb}/^{206}\text{Pb}$ - $^{207}\text{Pb}/^{206}\text{Pb}$ space, the leachates and residues are significantly overdispersed (MSWD = 391). Nevertheless, they plot along a line projecting towards the point of terrestrial Pb as defined by the model of Stacey and Kramers (1975), indicating that the pyroxene in the sample is free of initial, primordial Pb (Figure 45) and that the Pb isotope compositions of the leachates and residues are a mixture of only radiogenic Pb ($^{204}\text{Pb} = 0$) and terrestrial Pb. This has been previously observed in the angrites Sahara 99555 (Amelin 2008b, Connelly et al., 2008) and NWA 1670 (Schiller et al., 2015), as well as some chondrules (Bollard et al., 2017).

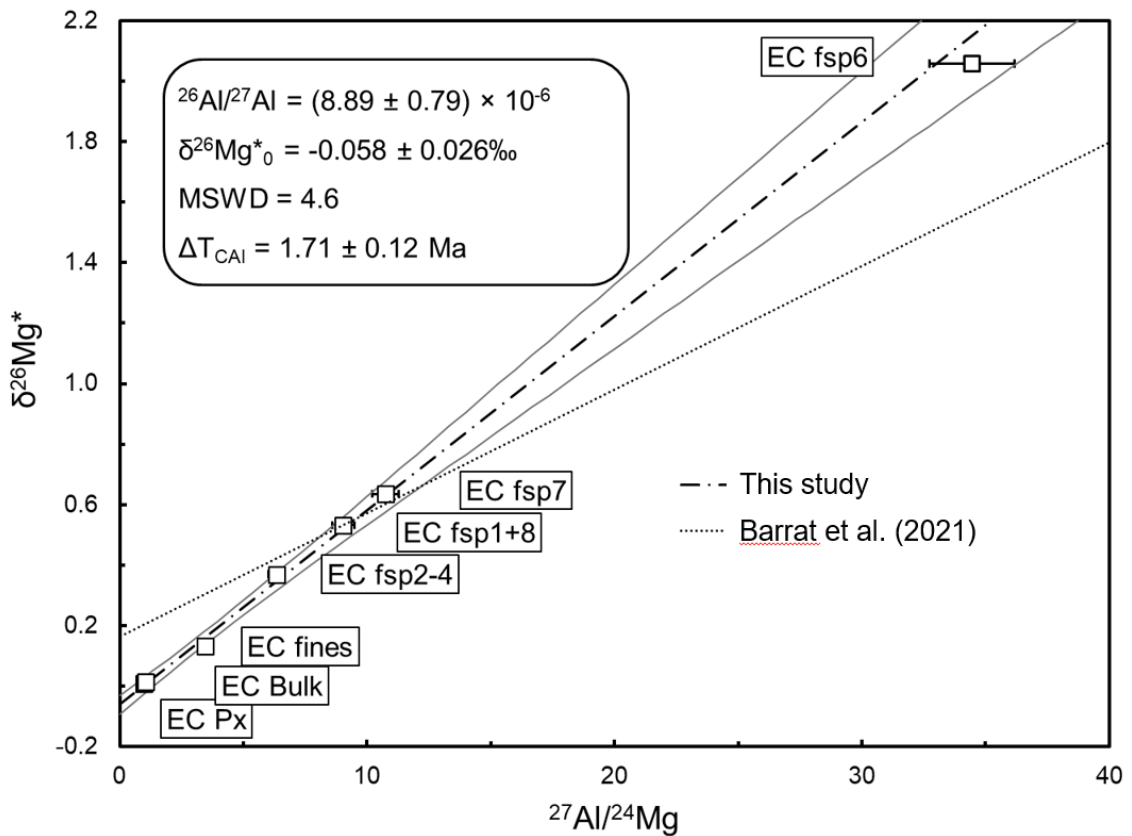


Figure 43: Internal ^{26}Al - ^{26}Mg isochrons defined by a) pyroxene, bulk rock, fine-grained and plagioclase fractions, corresponding to a $^{26}\text{Al}/^{27}\text{Al}$ ratio of $(8.89 \pm 0.79) \times 10^{-6}$ and a formation age of 1.71 ± 0.12 Ma after CAI formation, based on the canonical $^{26}\text{Al}/^{27}\text{Al}$

abundance (Jacobsen et al., 2008); and b) Uncertainties are 2SE errors on $\delta^{26}\text{Mg}^*$ measurements and $\pm 5\%$ on $^{27}\text{Al}/^{24}\text{Mg}$ ratios.

A statistically meaningful isochron (probability of fit > 0.05) can be calculated using leachates W4, W7, W8 and the residue R, however, W7 is omitted due to its negative $^{204}\text{Pb}/^{206}\text{Pb}$ ratio after background- and blank-correction, despite it still plotting along the isochron. This leaves three fractions defining the isochron (MSWD = 3.3), resulting in an age of 4565.87 ± 0.28 Ma (Figure 46), calculated with the $^{238}\text{U}/^{235}\text{U}$ ratio 137.766 ± 0.027 , determined from the pyroxene leachates. All ages given include error propagation on the U isotope composition, except for $^{207}\text{Pb}^*/^{206}\text{Pb}^*$ model ages of individual leachates.

The $^{207}\text{Pb}^*/^{206}\text{Pb}^*$ model ages () calculated from both initial Pb as represented by the Nantan troilite (Blichert-Toft et al., 2010) and the Stacey & Kramers (SK) point representing terrestrial Pb, show no age difference for a given highly radiogenic leachate or the residue, as they plot close enough to the y-axis to not make any significant difference in y-intercept ($= ^{207}\text{Pb}^*/^{206}\text{Pb}^*$). For the less radiogenic leachate W4, the Nantan and SK model ages differ significantly, the SK model ages being in line with the other leachates and residue of its respective fraction, indicating once again that there likely was no primordial Pb present in the sample. The weighted average of the SK model ages for W4, W8 and R results in an Pb-Pb age of 4565.88 ± 0.40 Ma. Adding the SK model age for W7, where only its $^{207}\text{Pb}/^{206}\text{Pb}$ ratio is considered, to the weighted average gives an age of 4565.90 ± 0.36 Ma.

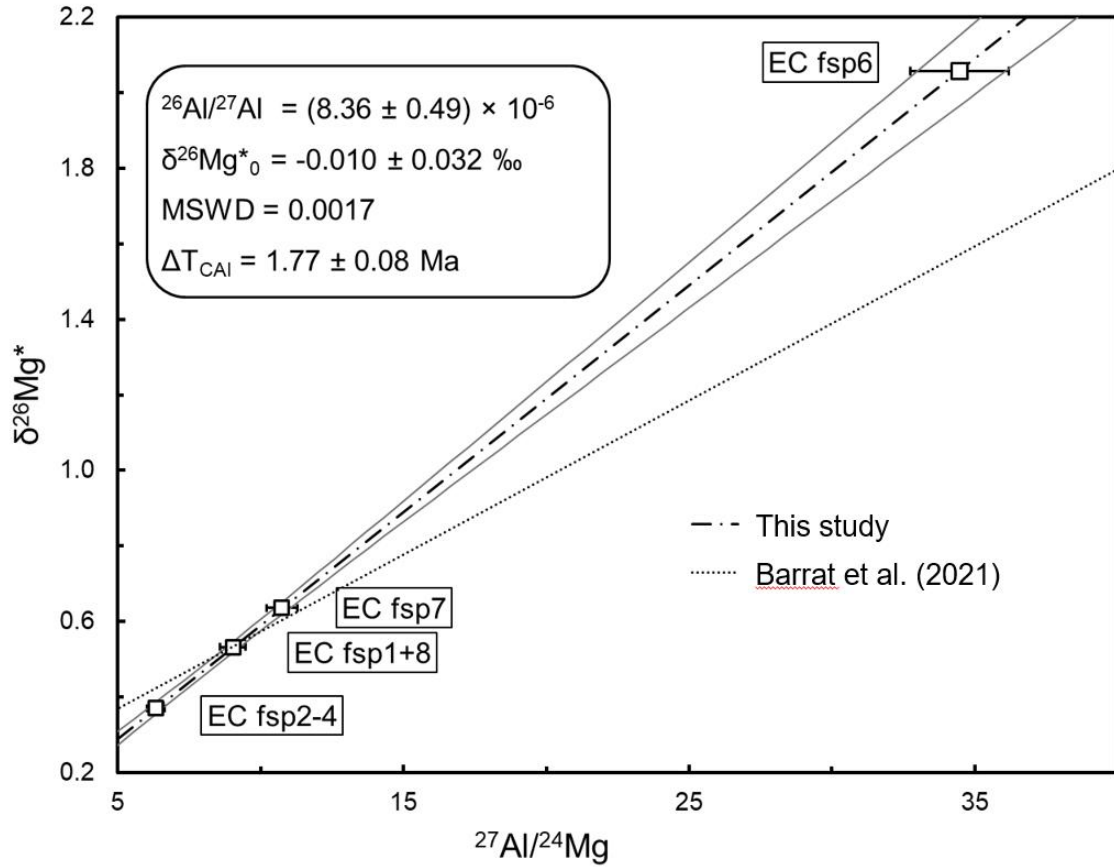


Figure 44: Internal ^{26}Al - ^{26}Mg isochrons defined by only plagioclase fractions, corresponding to an initial $^{26}\text{Al}/^{27}\text{Al}$ ratio $(8.36 \pm 0.49) \times 10^{-6}$ and a formation age of $1.77 \pm 0.08 \text{ Ma}$ after CAI formation, based on the canonical $^{26}\text{Al}/^{27}\text{Al}$ abundance (Jacobsen et al., 2008). Uncertainties are 2SE errors on $\delta^{26}\text{Mg}^*$ measurements and $\pm 5\%$ on $^{27}\text{Al}/^{24}\text{Mg}$ ratios.

Table 18: Mass, Pb and U elemental data, and Pb isotope data for EC 002 and full session Pb isotope data for standards NBS 981 and NBS 983.

Sample	mass [mg]	Pb [ng]	U [ng]	Sample/Blank	$^{206}\text{Pb}/^{204}\text{Pb}$ raw	$^{204}\text{Pb}/^{206}\text{Pb}$	2SE [%]	$^{207}\text{Pb}/^{206}\text{Pb}$	2SE [%]	Nantan model age	±	SK model age	±
EC-W1-3	1.6	3.2	2.2	3808	41.5	0.0240	0.015	0.721208	0.002	4529.73	0.20	4571.38	1.56
EC-W4	1.0	1.3	6.5	1549	42.5	0.0235	0.035	0.637959	0.004	4526.74	0.18	4565.58	1.49
EC-W5+6	0.3	0.1	0.2	131	343.9	0.00268	3.42	0.717551	0.045	4567.91	0.62	4571.46	0.58
EC-W7	4.1	0.6	0.3	302	10902.7	-0.000007	612	0.625026	0.021	4566.22	0.35	4566.18	0.35
EC-W8	44.2	0.8	0.8	1331	6953.1	0.000122	7.25	0.625378	0.005	4565.64	0.15	4565.79	0.14
EC-R	42.9	1.2	1.0	1366	16604.9	0.000039	21.3	0.625128	0.005	4565.92	0.15	4565.97	0.14

Nantan model ages are calculated from the primordial Pb isotope composition, represented by the Nantan troilite (Blichert-Toft et al., 2010). SK model ages are calculated from the modern terrestrial Pb composition as given by Stacey and Kramers (1975).

Table 19: Weighted average U isotope compositions of EC 002 bulk and pyroxene samples and of BCR-2 terrestrial basalt standard.

Sample	Mass [mg]	U [ng]	$^{238}\text{U}/^{235}\text{U}$	2σ	n	^{238}U intensity [V]
EC 002 Bulk	~120	15	137.819	0.007	2	12
EC 002 Px leachates	~160	5	137.766	0.027	2	2.5

4.3 Discussion

4.3.1 Lead isotope systematics

Even though only three fractions make up our ^{207}Pb - ^{206}Pb isochron, with a rather non-radiogenic leachate and a highly radiogenic leachate and residue, it is statistically meaningful (MSWD = 3.3, probability of fit = 0.068). The weighted average of their $^{207}\text{Pb}^*/^{206}\text{Pb}^*$ SK model ages are consistent with the isochron age. Hence, we interpret the absolute age of 4565.87 ± 0.28 Ma as defined by the isochron as the crystallization age of EC 002 (Figure 46).

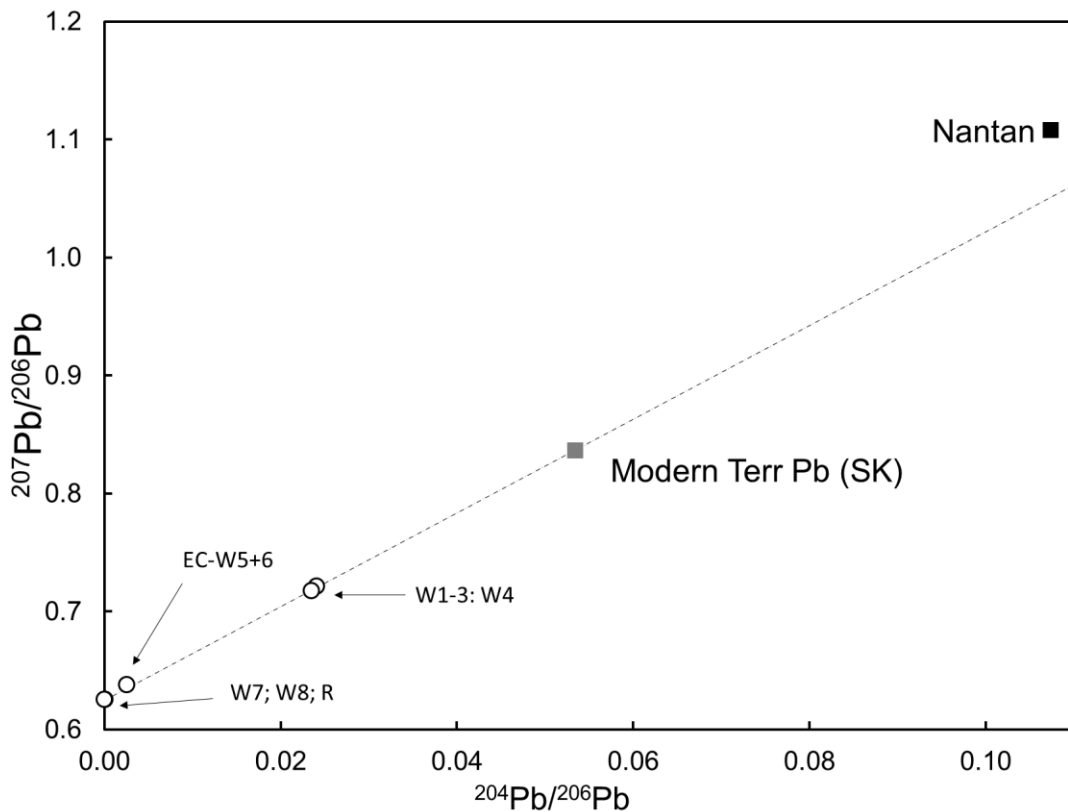


Figure 45: Regression line through all analyzed Pb fractions. Also plotted are data points for the Nantan troilite, representing the primordial Pb composition of the Solar System, and the Stacey and Kramers (1975) data point representing the terrestrial Pb composition. Symbols of data points have been enlarged for clarity, larger than their uncertainties.

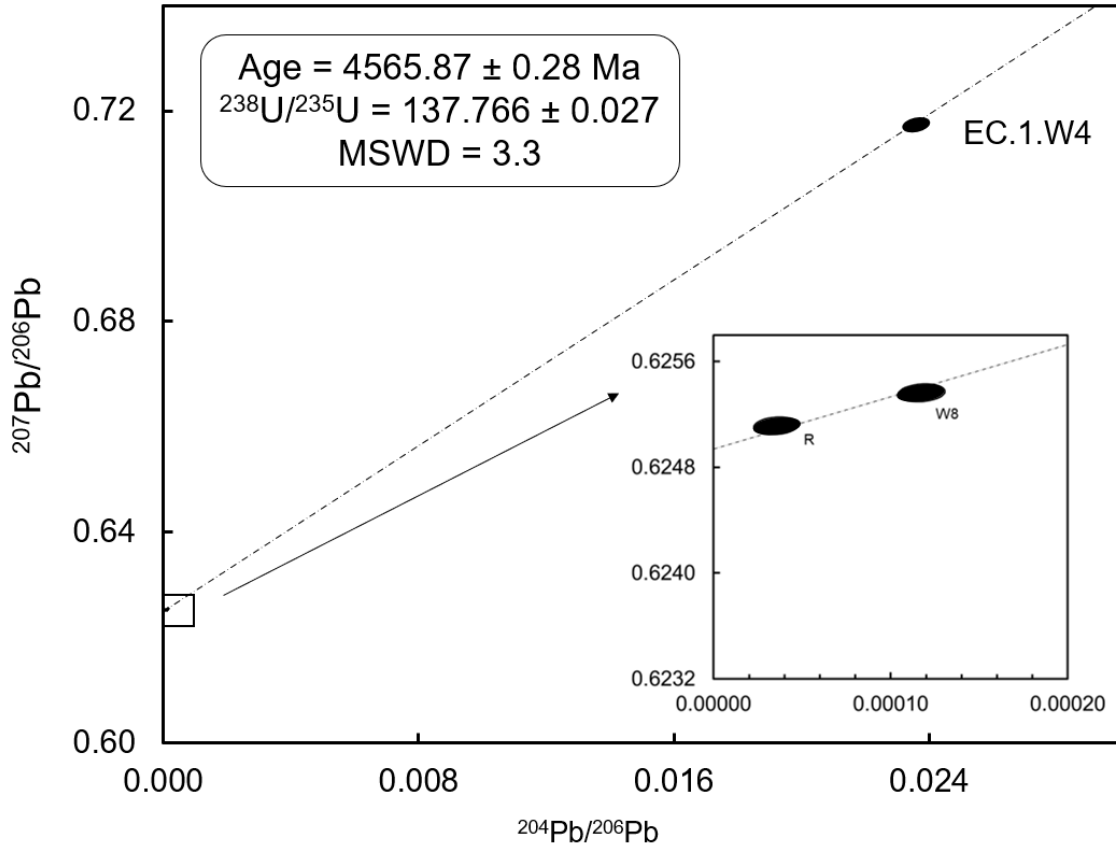


Figure 46: Inverse Pb-Pb isochron diagram for Erg Chech 002. The uncertainty on W4 is smaller than the ellipse, as it is enlarged for clarity. The inset shows the highly radiogenic leachate W8 and residue. Leachate W7 would plot along the regression line in negative $^{204}\text{Pb}/^{206}\text{Pb}$ vs. $^{207}\text{Pb}/^{206}\text{Pb}$ space.

4.3.2 Uranium-corrected Pb-Pb age of Erg Chech 002

The bulk $^{238}\text{U}/^{235}\text{U}$ ratio of EC 002 is 137.819 ± 0.010 , distinct from the combined leachates (W5 to R) of the Px fractions at 137.766 ± 0.027 . The resulting age difference in the Pb-Pb ages of EC 002, depending on which $^{238}\text{U}/^{235}\text{U}$ ratio is used, is 0.56 ± 0.28 Myr.

Our difference in measured $^{238}\text{U}/^{235}\text{U}$ ratio is likely due to internal heterogeneity of U isotopes in different minerals of the bulk sample and potential effect of secondary minerals formed during terrestrial weathering in the Sahara desert. Newly formed secondary U-rich minerals (e.g., Fe-oxides, carbonates) could potentially affect Pb-Pb ages quite significantly: many Pb-Pb ages in achondrites are determined from leachates and residues of pyroxene fractions, whereas the U isotope compositions of those samples

were determined on bulk fractions, often by different studies and workers (Tissot et al., 2017). If U isotope heterogeneity between pyroxenes and bulk samples exist in dated samples, U-corrected Pb-Pb ages would need to be further corrected. Brennecka and Wadhwa (2012) reported no resolvable differences between the bulk and pyroxenes from the angrite D'Orbigny, but recently, Huyskens et al. (2020) reported some heterogeneities between mineral phases (pyroxene, phosphate) and bulk fractions in some slowly cooled, plutonic angrites.

Alternatively, U isotope fractionation between the bulk and pyroxene fraction could (also) have plausibly occurred during Pb column chemistry, though two terrestrial BCR-2 standard aliquots that underwent the same Pb separation procedure as the pyroxene leachates were analyzed along with the samples and their U isotope composition lies within error of previously reported values (e.g., Goldmann et al., 2015), making this scenario unlikely. Another option could be that the leaching steps in dilute acid, designed to remove terrestrial Pb contamination, also removed carriers of terrestrial U contamination. While EC 002 was classified with a low weathering grade (Gattacceca et al., 2021), evidence of iron metal oxidation and secondary minerals such as carbonates (calcite) is visible by eye. A simple mass balance calculation between the bulk, the leached pyroxene and a terrestrial U component (assumed value equal to the CRM-112a standard; Richter et al., 2010) does not conclusively rule out that the U isotope composition of the bulk sample is a mixture of terrestrial U and the U composition given by the pyroxene leachates. Results from past studies on U isotope fractionation due to acid leaching are mixed: Brennecka and Wadhwa (2012) and Huyskens et al. (2020) reported no resolvable differences between the leachates and residues in their studied angrites, whereas Krestianinov et al. (2021) recently did report a resolvable difference in the volcanic angrite NWA 12774. That same study however reported no differences between the U isotope composition of leachates and residues of a bulk EC 002 sample.

It therefore seems most likely that the difference in U isotope composition between the bulk and leached pyroxene fractions of EC 002 are caused by variations of U isotopes in different minerals. Given that the Pb-Pb isochron of EC 002 was determined on leached pyroxene fractions, it is appropriate to use the $^{238}\text{U}/^{235}\text{U}$ ratio of the same pyroxene

fractions to calculate the U-corrected Pb-Pb age, resulting in an absolute age of 4565.87 ± 0.28 Ma.

While the resolution on $^{238}\text{U}/^{235}\text{U}$ ratios often is not sufficient to resolve smaller variations between mineral and bulk fractions, given the large sample mass needed for precise analysis, potential significant age corrections could have far-reaching consequences on the interpretation of results. In the case of EC 002, the age difference of 0.56 ± 0.28 Myr is enough to change the concordance of ^{26}Al - ^{26}Mg and U-corrected Pb-Pb ages between EC 002 and D'Orbigny, as will be demonstrated below.

4.3.3 ^{26}Al - ^{26}Mg systematics

Regressing the ^{26}Al - ^{26}Mg data from seven fractions of EC 002 results in an isochron with excess scatter (MSWD = 4.6) and a crystallization age of 1.71 ± 0.12 Ma after CAI formation (Figure 43). The excess scatter likely signifies an underestimation of the errors associated with their data points. The four plagioclase fractions of our dataset define an isochron with an age of 1.77 ± 0.08 Ma after CAI formation, identical within the stated uncertainties but with no excess scatter (MSWD = 0.002; Figure 44). The difference in MSWD could be a product of an underestimation of the errors associated with the bulk, pyroxene and fine-grained fraction data points. Alternatively, the excess scatter in the isochron containing all fractions could be due to geological reasons, that the mineral fractions did not crystallize at the same time, or re-distribution and diffusion occurred after crystallization through metamorphism or impact events. Since it is estimated that EC 002 cooled rapidly, intuitively it may seem unlikely that the excess scatter is due to differences in the timing of crystallization. The excess scatter of the full dataset is driven mostly by the fine-grained fraction, which lies below the isochron. Its removal from the isochron calculation lowers the MSWD to 1.4, while the age stays the same at 1.71 ± 0.07 Ma after CAI formation. The fine-grained fraction (~ 20 mg) was taken after crushing and initial sieving (< 60 μm) of the bulk sample. Visually, it was dominated by sodic plagioclase and pigeonite from the groundmass of the meteorite, but no further mineral separation was undertaken due to the small grain sizes. This fraction could therefore include small accessory mineral grains that are present in the groundmass, such as merrillite. Merrillite is commonly associated with metamorphic or shock event on

meteorites, and may have formed at a later stage (e.g., Adcock et al., 2017; Koike et al., 2020). Furthermore, the large orthopyroxene megacrysts, reportedly up to 9 cm in size in some EC 002 samples (Gattacceca et al., 2021), have been interpreted as xenocrysts (Barrat et al., 2021): residual pyroxenes from a prior melting event that potentially got incorporated into a rapidly ascending melt (Nicklas et al., in review). Since anorthite-poor, sodic plagioclase, as is present in EC 002, was likely to be the last major mineral to allow Mg diffusion during cooling (Van Orman et al., 2014), the plagioclase isochron could be interpreted as the time of final closure of the ^{26}Al - ^{26}Mg system in major minerals of EC 002.

With our dataset, these potential differences cannot be resolved in a statistically meaningful manner, but they may be of interest for further evaluation, with the analysis of additional pyroxene fractions that span a range of $^{27}\text{Al}/^{24}\text{Mg}$ ratios. The isochron that includes all fractions (1.71 ± 0.12 Ma after CAI formation) is therefore used for chronological purposes going forward.

The crystallization age of 1.71 ± 0.12 Ma after CAI formation as determined by ^{26}Al - ^{26}Mg chronology using MC-ICPMS is 0.43 ± 0.12 Myr older than the ^{26}Al - ^{26}Mg age of 2.14 ± 0.01 Ma after CAI formation (re-calculated with a ^{26}Al half-life of 0.717 Myr) reported by Barrat et al. (2021), determined by secondary ionization mass spectrometry (SIMS). Our age is strengthened by the analysis of different plagioclase fractions with a good spread in $^{27}\text{Al}/^{24}\text{Mg}$ ratios, and with that subset of our data in agreement with our overall isochron. The difference to the result of Barrat et al. (2021) is hard to reconcile.

Potentially, when analyzing sample spots with very low amounts of Mg by SIMS, such as those with $^{27}\text{Al}/^{24}\text{Mg}$ ratios between 2000 and 5000, counting statistics errors could become a factor, where background corrections could hypothetically overcorrect the amount of Mg isotopes, leading to spuriously lower ^{26}Mg excesses. Furthermore, the calibrating standard used, Miyake-Jima plagioclase, has a $^{27}\text{Al}/^{24}\text{Mg}$ ratio of 396.3, an order of magnitude lower than the plagioclase analyzed in their sample of EC 002, which could lead to miscalibration for the measurements with higher $^{27}\text{Al}/^{24}\text{Mg}$ ratios.

An alternative interpretation is that the isochron determined by Barrat et al. (2021) represents the time of closure of pure plagioclase ($^{27}\text{Al}/^{24}\text{Mg} > 1500$), whereas our isochron with fractions that contain at least some proportion of other minerals represents

the time of closure of a mineral mixture with a higher closure temperature for Mg diffusion. Closure temperatures of pyroxene and anorthite have been estimated at 900°C to 1000°C and 700°C to 800°C, respectively (Wadhwa et al., 2009). With the age difference of 0.43 ± 0.12 Myr between isochrons, based on those closure temperatures as an upper limit, the cooling rate would be 465°C/Myr, several orders of magnitude slower than what Barrat et al. (2021) estimated from the petrology of EC 002 (5°C/yr from 1200°C to 1000°C, and >0.1 to 1°C/day below 900°C). Such a large difference can't be explained by the isochrons representing different times of closure of minerals and still satisfy the petrological constraints established on the cooling rate of EC 002.

By the same method, if the plagioclase-only isochron were more representative in a canonical Solar System (initial $\delta^{26}\text{Mg}^*$ of -0.034 ‰), partial melting could have commenced not before 1.37 Ma after CAI formation.

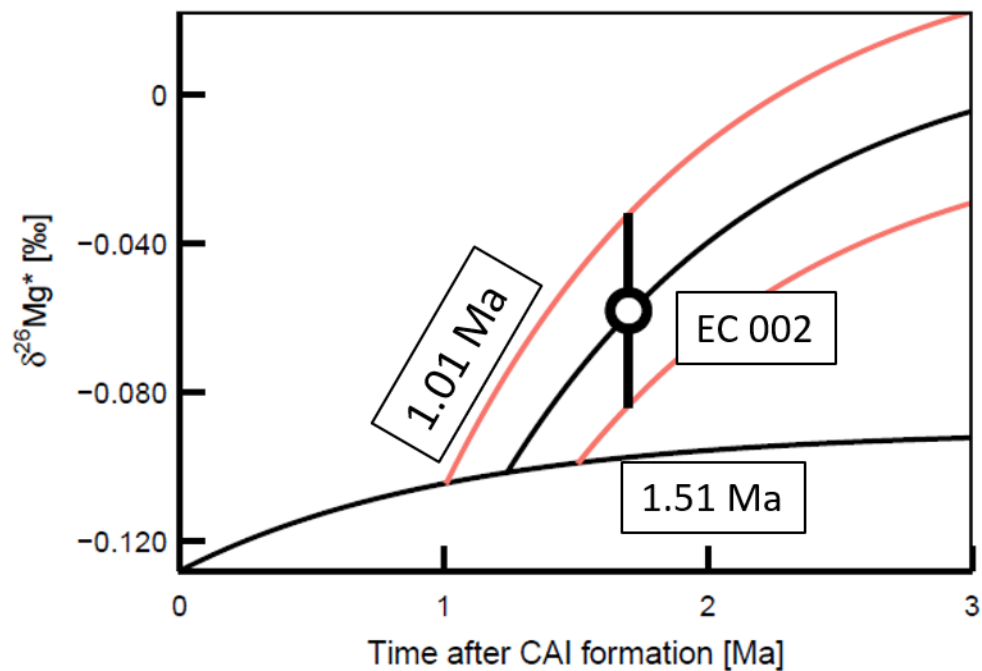


Figure 47: $\delta^{26}\text{Mg}^*$ evolution diagram of EC 002 and the bulk Solar System, calculated with the canonical $^{26}\text{Al}/^{27}\text{Al}$ ratio of 5.23×10^{-5} , a chondritic $^{27}\text{Al}/^{24}\text{Mg}$ ratio of 0.101 and a subcanonical initial Solar System $\delta^{26}\text{Mg}^*$ value of -0.128 (Wasserburg et al., 2012; MacPherson et al., 2017; see text).

Not only is the initial $^{26}\text{Al}/^{27}\text{Al}$ ratio between our results and those of Barrat et al. (2021) different, but also the initial ^{26}Mg composition ($\delta^{26}\text{Mg}^*_0$). The $\delta^{26}\text{Mg}^*_0$ value is $-0.058 \pm 0.026\text{‰}$, for the full isochron or $-0.010 \pm 0.032\text{‰}$ for the plagioclase-only isochron. Both are within uncertainty of the initial ^{26}Mg composition of the Solar System (Jacobsen et al., 2008; Schiller et al., 2010b). The low $\delta^{26}\text{Mg}^*_0$ value from the full isochron implies that crystallization took place before any significant radiogenic ingrowth of ^{26}Mg due to the decay of ^{26}Al could occur. Assuming that the parent body of EC 002 accreted with a chondritic $^{27}\text{Al}/^{24}\text{Mg}$ ratio of 0.101 (Palme et al., 2014), crystallization would have to occur coevally with CAI formation, which is in disagreement with our ^{26}Al - ^{26}Mg age determined from the initial $^{26}\text{Al}/^{27}\text{Al}$ ratio. One explanation could be $\delta^{26}\text{Mg}^*$ heterogeneity in the early Solar System; both Wasserburg et al. (2012) and Macpherson et al. (2017) analyzed CAIs with canonical $^{26}\text{Al}/^{27}\text{Al}$ ratios but lower than canonical $\delta^{26}\text{Mg}^*_0$ values ($-0.127 \pm 0.032 \text{‰}$ and $-0.128 \pm 0.037 \text{‰}$, respectively). If the Mg isotope composition of EC 002 evolved from such a low initial $\delta^{26}\text{Mg}^*$ value, we can calculate the time interval between partial melting and crystallization that could have produced the $\delta^{26}\text{Mg}^*_0$ of our dataset, analog to Barrat et al. (2021). The $\delta^{26}\text{Mg}^*$ evolution curves of EC 002 and the bulk Solar System (with an initial $\delta^{26}\text{Mg}^*$ of -0.128‰) intersect at 1.01 Ma and 1.51 Ma after CAI formation, the time interval during which partial melting could have commenced to form EC 002 (Figure 47).

By the same method, if the plagioclase-only isochron were more representative in a canonical Solar System (initial $\delta^{26}\text{Mg}^*$ of -0.034‰), partial melting could have commenced not before 1.37 Ma after CAI formation (Figure 48).

Alternatively, two-stage differentiation could have produced a low $\delta^{26}\text{Mg}^*_0$ value by initially forming an Al-poor melt with only little radiogenic ^{26}Mg ingrowth, from which EC 002 then differentiated with the bulk $^{27}\text{Al}/^{24}\text{Mg}$ ratio of 1.05 ± 0.18 . This, however, contradicts the findings of Barrat et al. (2021) and Nicklas et al. (in review), who argue that EC 002 must be a primitive or primary melt. Finally, alteration or contamination with terrestrial Mg, as has been observed in angrite Sahara 99555 (e.g., Floss et al., 2003), could have shifted the isochron of EC 002 towards lower $\delta^{26}\text{Mg}^*$ values and $^{27}\text{Al}/^{24}\text{Mg}$ ratios. This would not affect the slope of the isochron (Spivak-Birndorf et al., 2009), and could furthermore explain the light $\delta^{25}\text{Mg}$ values of the EC 002 fractions compared to

terrestrial rocks, bulk chondrites (Table 17: Al-Mg data for EC 002 fractions) and other achondrites (e.g., Sedaghatpour and Teng, 2016). This is a plausible explanation, considering that oxidation, as well as secondary weathering products, can be found in the sample (Gattacceca et al., 2021) and samples were processed without leaching for Al-Mg analyses. Given that terrestrial standards Cambridge-1 and San Carlos olivine, as well as a bulk fraction of the Allende CV chondrite, were analyzed alongside the samples, underwent the same Mg separation protocols, and do not show any deviation from the values of previously published studies, unusually light mass-dependent Mg isotope composition is unlikely an analytical artefact. Rather, additional attention should be given to samples with visibly weathered surfaces, potentially using short cleaning procedures with dilute acids to remove most of any terrestrial contamination but without fractionating the elemental parent/daughter ratios.

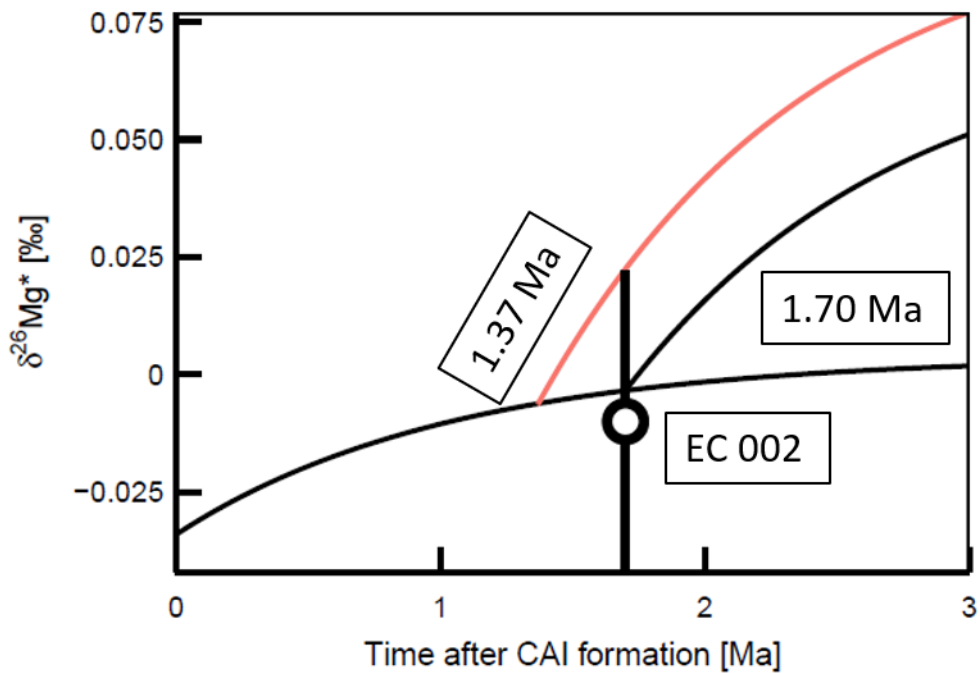


Figure 48: $\delta^{26}\text{Mg}^*$ evolution diagram of EC 002 and the bulk Solar System, calculated with the canonical $^{26}\text{Al}/^{27}\text{Al}$ ratio of 5.23×10^{-5} , a chondritic $^{27}\text{Al}/^{24}\text{Mg}$ ratio of 0.101 and a canonical initial $\delta^{26}\text{Mg}^*$ value of -0.034 (Jacobsen et al., 2008; Schiller et al., 2010b).

4.3.4 Combined ^{26}Al - ^{26}Mg and Pb-Pb chronology and EC 002 as a potential time anchor

The early formation, rapid cooling history and fairly undisturbed history (Barrat et al., 2021) of EC 002 makes it a prime candidate as an anchor meteorite. Both the Pb-Pb age and initial $^{26}\text{Al}/^{27}\text{Al}$ are well constrained with relatively small uncertainties. We compared EC 002 with the initial $^{26}\text{Al}/^{27}\text{Al}$ ratios of seven other achondrites with peer-reviewed and published Pb-Pb ages (Table 20: Summary of Pb-Pb ages, initial $^{26}\text{Al}/^{27}\text{Al}$ ratios and anchored Al-Mg ages for EC 002 and eight other achondrites).

Sample	Pb-Pb age		Initial $^{26}\text{Al}/^{27}\text{Al}$		Al-Mg age rel. EC 002 [Ma]		Al-Mg age rel. D'Orbigny (2,3) [Ma]		Al-Mg age rel. EC 002 [Ma]
	\pm		\pm	\pm	\pm	\pm	\pm	\pm	\pm
Erg Chech 002	4565.87	0.28	8.89×10^{-6}	7.90×10^{-7}			4566.51	0.31	4566.51
			5.72×10^{-6}	0.07×10^{-6}			4566.09	0.29	4566.09
D'Orbigny	4563.51	0.29	3.98×10^{-7}	1.50×10^{-8}	4562.87	0.31			4562.87
			5.06×10^{-7}	9.20×10^{-8}	4563.10	0.38			4563.10
Sahara 99555	4564.07	0.48	3.64×10^{-7}	1.80×10^{-8}	4562.78	0.31	4563.42	0.30	4562.78
	4563.79	0.33	5.13×10^{-7}	1.90×10^{-7}	4563.11	0.54	4563.76	0.50	4563.11
NWA 1670	4564.39	0.24	5.92×10^{-7}	5.90×10^{-8}	4563.25	0.33	4563.89	0.32	4563.25
NWA 7325	4563.4	2.6	3.03×10^{-7}	1.40×10^{-8}	4562.60	0.31	4563.25	0.30	4562.60
Asuka 881394	4564.95	0.53	1.48×10^{-6}	1.80×10^{-8}	4564.14	0.30	4564.78	0.29	4564.14
			1.28×10^{-6}	7.00×10^{-8}	4564.00	0.31	4564.64	0.30	4564.00
NWA 11119			1.69×10^{-6}	9.00×10^{-8}	4564.27	0.31	4564.91	0.30	4564.27
		+0.22/-							
NWA 6704	4562.76	0.30	3.15×10^{-7}	3.80×10^{-8}	4562.64	0.35	4563.28	0.33	4562.64
NWA 2976	4562.89	0.59	3.94×10^{-7}	1.60×10^{-8}	4562.86	0.31	4563.50	0.30	4562.86
			4.91×10^{-7}	4.60×10^{-8}	4563.07	0.33	4563.71	0.32	4563.07

): the three angrites D'Orbigny, Sahara 99555 and NWA 1670 (Amelin, 2008a, 2008b; Connelly et al., 2008; Spivak-Birndorf et al., 2009; Schiller et al., 2015a; Tissot et al., 2017); two (likely) ungrouped non-carbonaceous achondrites Asuka 881394 (Wadhwa et al., 2009; Wimpenny et al., 2019) and NWA 7325 (Koefoed et al., 2016) and two ungrouped carbonaceous achondrites NWA 2976 (Schiller et al., 2010a; Bouvier et al., 2011) and NWA 6704 (Amelin et al., 2019; Sanborn et al., 2019). Of these samples, only NWA 1670 and NWA 7325 have not had their U isotope composition analyzed. Additionally, we calculate a new ^{26}Al - ^{26}Mg formation age for the ungrouped achondrite NWA 11119 of 4564.27 ± 0.31 anchored to EC 002, based on the $^{26}\text{Al}/^{27}\text{Al}$ initial of $(1.69 \pm 0.09) \times 10^{-6}$ for NWA 11119 (Srinivasan et al., 2018). This age is consistent with

a preliminary Pb-Pb age reported in abstract form (4563.3 ± 2.9 Ma; Dunlap et al., 2018) but not with a different one (4559.4 ± 2.6 Ma; Huyskens et al., 2018).

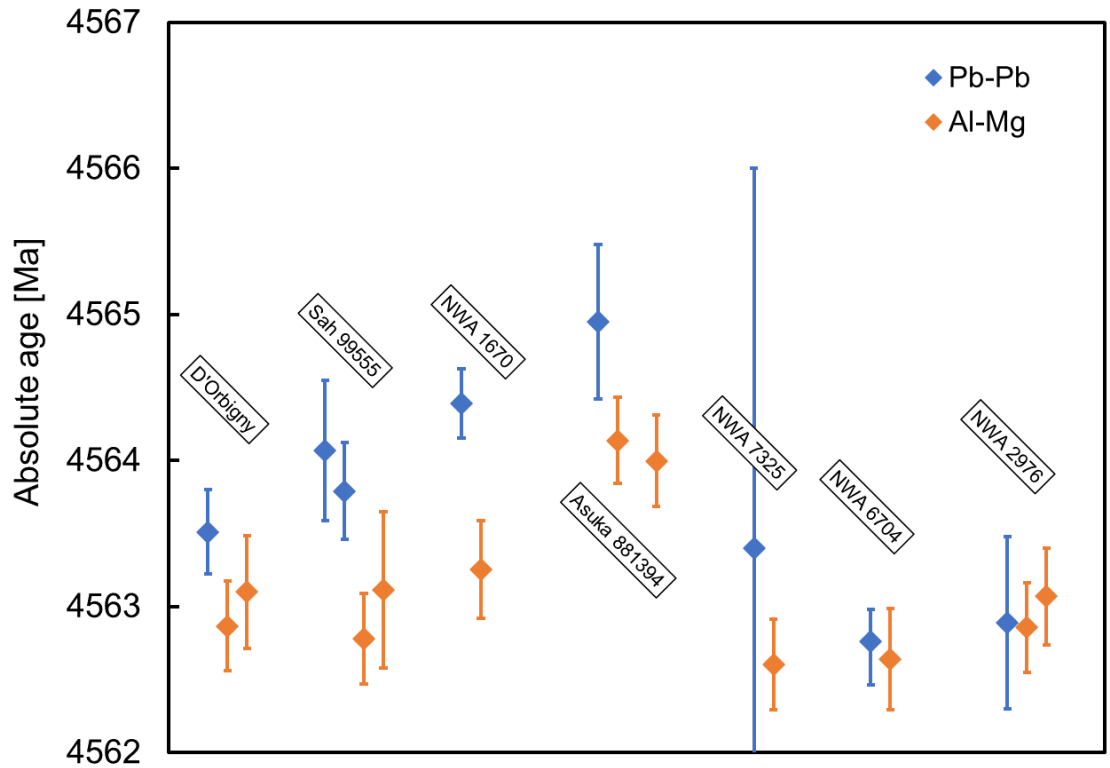


Figure 49: Comparison between absolute Pb-Pb ages of seven achondrites and their ^{26}Al - ^{26}Mg ages anchored to EC 002 (Pb-Pb age: 4565.87 ± 0.28 , initial $^{26}\text{Al}/^{27}\text{Al}$: $(8.89 \pm 0.87) \times 10^{-6}$). For clarity, the error bars of the Pb-Pb age of NWA 7325 (4563.4 ± 2.6 Ma; Koefoed et al., 2016) are not visible in their entirety. Literature data have been used for Pb-Pb ages and ^{26}Al - ^{26}Mg ages of the angrites Sahara 99555 (Al-Mg: Spivak-Birndorf et al., 2009; Schiller et al, 2015; U-corrected Pb-Pb ages: Amelin et al., 2008a; Tissot et al., 2017), NWA 1670 (Schiller et al., 2015), D'Orbigny (Spivak-Birndorf et al., 2009; Schiller et al., 2015; Amelin et al., 2008b; Tissot et al., 2017), Asuka 881394 (Wadhwa et al., 2009; Wimpenny et al., 2019), NWA 6704 (Amelin et al., 2019; Sanborn et al., 2019), NWA 7325 (Koefoed et al., 2016) and NWA 2976 (Schiller et al., 2010b; Bouvier et al., 2011c).

The Pb-Pb ages of the seven achondrites and their ^{26}Al - ^{26}Mg ages anchored to EC 002 are displayed in Figure 49 and reported in Table 20: Summary of Pb-Pb ages, initial $^{26}\text{Al}/^{27}\text{Al}$ ratios and anchored Al-Mg ages for EC 002 and eight other achondrites.

Sample	Pb-Pb age	Initial $^{26}\text{Al}/^{27}\text{Al}$	Al-Mg age rel. EC 002 [Ma]	Al-Mg age rel. D'Orbigny (2,3) [Ma]	Al-Mg age rel. EC 002 [Ma]
--------	-----------	---	----------------------------	-------------------------------------	----------------------------

		±		±		±		±	
Erg Chech 002	4565.87	0.28	8.89×10^{-6}	7.90×10^{-7}			4566.51	0.31	45
			5.72×10^{-6}	0.07×10^{-6}			4566.09	0.29	45
D'Orbigny	4563.51	0.29	3.98×10^{-7}	1.50×10^{-8}	4562.87	0.31			45
			5.06×10^{-7}	9.20×10^{-8}	4563.10	0.38			45
Sahara 99555	4564.07	0.48	3.64×10^{-7}	1.80×10^{-8}	4562.78	0.31	4563.42	0.30	45
	4563.79	0.33	5.13×10^{-7}	1.90×10^{-7}	4563.11	0.54	4563.76	0.50	45
NWA 1670	4564.39	0.24	5.92×10^{-7}	5.90×10^{-8}	4563.25	0.33	4563.89	0.32	45
NWA 7325	4563.4	2.6	3.03×10^{-7}	1.40×10^{-8}	4562.60	0.31	4563.25	0.30	45
Asuka 881394	4564.95	0.53	1.48×10^{-6}	1.80×10^{-8}	4564.14	0.30	4564.78	0.29	45
			1.28×10^{-6}	7.00×10^{-8}	4564.00	0.31	4564.64	0.30	45
NWA 11119			1.69×10^{-6}	9.00×10^{-8}	4564.27	0.31	4564.91	0.30	45
		+0.22/-							
NWA 6704	4562.76	0.30	3.15×10^{-7}	3.80×10^{-8}	4562.64	0.35	4563.28	0.33	45
NWA 2976	4562.89	0.59	3.94×10^{-7}	1.60×10^{-8}	4562.86	0.31	4563.50	0.30	45
			4.91×10^{-7}	4.60×10^{-8}	4563.07	0.33	4563.71	0.32	45

. The angrite NWA 1670 is the only sample that is unambiguously discordant, with a difference of 1.13 ± 0.53 Myr between the Pb-Pb age and anchored ^{26}Al - ^{26}Mg age. Of the other two angrites, the anchored ^{26}Al - ^{26}Mg ages reported by both Spivak-Birndorf et al. (2009) and Schiller et al. (2015) for D'Orbigny are both concordant with the U-corrected Pb-Pb age (Amelin, 2008a; Tissot et al., 2017), whereas the ^{26}Al - ^{26}Mg data from Schiller et al. (2015) of Sahara 99555 is discordant with the Pb-Pb ages of both Amelin (2008b) and Connelly et al. (2008), but the less precise ^{26}Al - ^{26}Mg data from Spivak-Birndorf et al. (2009) is concordant within its uncertainty. The data for unique basaltic achondrite Asuka 881394 is also conflicting: the U-corrected Pb-Pb age of 4564.95 ± 0.53 (Wimpenny et al., 2019) includes data points of Wadhwa et al. (2009). The anchored ^{26}Al - ^{26}Mg age is only concordant with the data from Wimpenny et al. (2019), but not with the data from Wadhwa et al. (2009), which is younger by 0.95 ± 0.64 Myr. For NWA 7325, the non-radiogenic Pb isotope composition of the leachates and residues is responsible for a comparatively less precise Pb-Pb age of 4563.4 ± 2.6 Ma, calculated with an assumed $^{238}\text{U}/^{235}\text{U}$ ratio of 137.794 (Goldmann et al., 2015) due to the low U concentration of the sample (Koefoed et al., 2016). With this larger uncertainty, the ^{26}Al - ^{26}Mg age anchored to EC 002 is concordant with the Pb-Pb age of NWA 7325.

The two ungrouped CC achondrites, NWA 6704 and NWA 2976, are both concordant between their U-corrected Pb-Pb ages (Amelin et al., 2019; Bouvier et al., 2011c) and

their anchored ^{26}Al - ^{26}Mg age (Sanborn et al., 2019; Schiller et al., 2010b; Bouvier et al., 2011c).

It is surprising to see that, when anchored to EC 002, the ^{26}Al - ^{26}Mg ages of CC achondrites are fully concordant with their Pb-Pb ages, and that NC achondrites show some discordance. While no data regarding nucleosynthetic anomalies of EC 002 have been reported as of yet, the O isotope composition (Gattacceca et al., 2021) and negative Tm abundance anomalies (Barrat et al., 2021) indicate that EC 002 formed in the NC reservoir, as did the angrites and the Asuka 881394 and NWA 7325 achondrites. That ^{26}Al - ^{26}Mg ages of Asuka 881394 and some of the angrites are not concordant when anchored to EC 002 is not expected, since it is assumed that they formed in the same formation reservoir with the same initial $^{26}\text{Al}/^{27}\text{Al}$ abundance, regardless if ^{26}Al was distributed homogeneously or heterogeneously between the NC and CC reservoirs. Angrites have repeatedly shown a temporal discordance between their U-corrected Pb-Pb ages and ^{26}Al - ^{26}Mg ages when anchored to the current best age estimate of CAIs at 4567.30 ± 0.16 Ma (Connelly et al., 2012), which has been explained by a lower $^{26}\text{Al}/^{27}\text{Al}$ ratio ($\sim 1 \times 10^{-5}$) at that time in the inner Solar System, where angrites formed (Schiller et al., 2015). In this scenario, the inner Solar System was depleted in ^{26}Al through thermal processing due to it being closer to the proto-Sun (Schiller et al., 2018), before CI-like, ^{26}Al -enriched dust was admixed to that formation reservoir (Bollard et al., 2019). The angrite parent body is proposed to have accreted within the first 0.25 ± 0.15 Ma after CAI formation (Schiller et al., 2015), at which time the depletion of ^{26}Al would have to have already been in place. Since EC 002 formed with a canonical $^{26}\text{Al}/^{27}\text{Al}$ ratio and crystallized within the first 2 Myr of the Solar System, as determined from our Al-Mg and Pb data, in the inner Solar System, this depletion must have occurred after accretion of the EC 002 parent body and prior to that of the angrite parent body, all within the first 0.25 ± 0.15 Ma after CAI formation. While the accretion of the EC 002 parent body likely occurred within the first 1 Myr, as the parent bodies of other achondrites have (Kruijer et al., 2014; Spitzer et al., 2021), a depletion of 75% of the initial ^{26}Al over a maximum time interval of 0.4 Myr, would require an efficient, large-scale mechanism that would likely have been recorded in other meteorites and their components as well. Ordinary chondrite chondrules that were dated by both the Pb-Pb

and ^{26}Al - ^{26}Mg chronometer, whose Pb-Pb ages show coeval formation with CAIs and cover the first 2 Myr, show no evidence of such a depletion occurring during the first 0.25 ± 0.15 Myr (Bollard et al., 2019). Therefore, given these arguments, and the concordance of ^{26}Al - ^{26}Mg and Pb-Pb ages in achondrites across the NC-CC dichotomy, we do not find evidence that ^{26}Al was distributed heterogeneously in the Solar nebula.

Regarding the angrite NWA 1670, a couple of explanations for the discordance between ^{26}Al - ^{26}Mg and Pb-Pb ages could be viable: firstly, the Pb-Pb age of 4564.39 ± 0.24 Ma (Schiller et al., 2015) was calculated with an assumed U isotope composition of 137.786 ± 0.013 (Connelly et al., 2012) which could potentially lead to an inaccurate Pb-Pb age. However, NWA 1670 is a quenched angrite, and with the average U isotope composition of quenched angrites being 137.797 ± 0.010 (Tissot et al., 2017), it is more likely that the actual $^{238}\text{U}/^{235}\text{U}$ ratio of NWA 1670 would correct the Pb-Pb age to an older age, if at all. Secondly, the initial $^{26}\text{Al}/^{27}\text{Al}$ ratio of NWA 1670 was determined on fractions with $^{27}\text{Al}/^{24}\text{Mg}$ ratios that ranged from 0.003 to 3.2, an order of magnitude lower than in EC 002 and other achondrite samples, and with resolvable ^{26}Mg excesses in only two of nine feldspar/pyroxene fractions (Schiller et al., 2015). How robust the Al-Mg dataset of NWA 1670 is in light of this, is not completely certain. Thirdly, NWA 1670 may have been shocked (Keil, 2012 and references therein), which could have caused disturbance of the radiometric systems.

The other angrite with discordant ^{26}Al - ^{26}Mg and Pb-Pb ages, Sahara 99555, may have suffered from broader disturbance, including re-distribution of Pb on the mineral grain scale (Amelin, 2008a). Sahara 99555 also exhibits evidence of terrestrial alteration in the form of LREE enrichment in some olivine and kirschsteinite (Floss et al., 2003). Spivak-Birndorf et al. (2009) however, noted that terrestrial Mg contamination would not affect slope of the isochron, and therefore would not be able to resolve the age difference between the ^{26}Al - ^{26}Mg and Pb-Pb chronometers on its own.

Sanborn et al. (2015) also reported disturbances in the Sm-Nd systematics for some angrites, including D'Orbigny, indicating that resetting events for at least that chronometer did occur on the angrite parent body. These concerns regarding the accuracy of the chronology of angrites suggest that the comparison of their ^{26}Al - ^{26}Mg and Pb-Pb ages may not be suitable as an anchor meteorite and for drawing broad conclusions

regarding the distribution and abundance of ^{26}Al in the Solar System. For Asuka 881394, Wimpenny et al. (2019) furthermore interpret their ^{26}Al - ^{26}Mg age as disturbed by slow cooling or low-grade metamorphism, supported by the petrography of the sample, explaining the apparent age difference to their Pb-Pb age. All these concerns could potentially account for the chronological discordance between the ^{26}Al - ^{26}Mg and Pb-Pb systems.

A further alternative to ^{26}Al heterogeneity and disturbance of ^{26}Al - ^{26}Mg systematics has been offered, where the commonly used absolute age of CAIs may be spuriously young (Bouvier and Wadhwa, 2010; Bouvier et al., 2011b; Sanborn et al., 2019; Wimpenny et al., 2019). It is argued that the “young” Pb-Pb ages of CAIs, determined from samples in the CV3 chondrites Efremovka (Connelly et al., 2012) and Allende (Amelin et al., 2010), could be the result of secondary alteration that both of those meteorites experienced (Bouvier and Wadhwa, 2010; Krot et al., 2021). Furthermore, there have been reports of older Pb-Pb ages of two CAIs, 2364-B1 from the CV3 chondrite NWA 2364 (Bouvier and Wadhwa, 2010) and 6691-B4 from the CV3 chondrite NWA 6691 (Bouvier et al., 2011b), with absolute Pb-Pb ages of 4568.2 (+0.2/-0.4) Ma and 4567.94 ± 0.31 Ma, respectively. Both D’Orbigny and NWA 6704, for example, are concordant when anchored to the 2364-B1 CAI age, in contrast to the Efremovka + Allende CAIs (Sanborn et al., 2019). However, the “old” Pb-Pb ages come with their own question marks. The U isotope composition of CAI 2364-B1 was not measured, but estimated using the Th/U ratio of the sample. This method has been shown to be unreliable, with a potential age correction of up to 4 Myr needed (Amelin et al., 2010; Brennecka et al., 2010). The U isotope composition of CAI 6691-B4 was measured, but that data has not been published in a peer-reviewed journal and remain available only in abstract form. A protracted formation interval of CAIs of up to 0.4 Myr, as suggested by Kawasaki et al. (2019, 2020), based on *in situ* ^{26}Al - ^{26}Mg dating, could potentially resolve the differences in absolute ages. This would, however, still require investigation into the absolute timing of such CAIs, and not necessarily impact the age of the oldest CAIs that define the initial $^{26}\text{Al}/^{27}\text{Al}$ ratio in the Solar System.

To summarize, other than ^{26}Al heterogeneity, the age gap between U-corrected Pb-Pb and ^{26}Al - ^{26}Mg ages in some achondrites could be the result of 1) differences in $^{238}\text{U}/^{235}\text{U}$

ratios between bulk meteorites and pyroxene fractions, where Pb-Pb ages were determined on leached pyroxenes, as seen in EC 002; 2) disturbance of the ^{26}Al - ^{26}Mg chronometer in some angrites and Asuka 881394; or 3) Pb-Pb ages of CAIs from the Efremovka and Allende meteorites that may have been affected by secondary alteration. Further advances in the analytical precision of both U and Pb isotope measurements could potentially reveal more and/or larger differences in ages between the ^{26}Al - ^{26}Mg and Pb-Pb chronometers.

While EC 002 shows relatively small age uncertainties for both ^{26}Al - ^{26}Mg and Pb-Pb ages and promises to be a useful anchor meteorite, its use for other short-lived chronometers such as the ^{53}Mn - ^{53}Cr and ^{182}Hf - ^{182}W chronometers has yet to be evaluated.

Table 20: Summary of Pb-Pb ages, initial $^{26}\text{Al}/^{27}\text{Al}$ ratios and anchored Al-Mg ages for EC 002 and eight other achondrites.

Sample	Pb-Pb age		Initial $^{26}\text{Al}/^{27}\text{Al}$		Al-Mg age rel. EC 002 [Ma]		Al-Mg age rel. D'Orbigny (2,3) [Ma]		Al-Mg age rel. CAI Connelly [Ma]		Pb-Pb sources	Al-Mg sources
	\pm		\pm	\pm	\pm	\pm	\pm	\pm	\pm	\pm		
Erg Chech 002	4565.87	0.28	8.89×10^{-6}	7.90×10^{-7}			4566.51	0.31	4565.59	0.19	this study	this study
			5.72×10^{-6}	0.07×10^{-6}			4566.09	0.29	4565.16	0.16		(1)
D'Orbigny	4563.51	0.29	3.98×10^{-7}	1.50×10^{-8}	4562.87	0.31			4562.58	0.17	(2), (3)	(4)
			5.06×10^{-7}	9.20×10^{-8}	4563.10	0.38			4562.82	0.26		(5)
Sahara 99555	4564.07	0.48	3.64×10^{-7}	1.80×10^{-8}	4562.78	0.31	4563.42	0.30	4562.50	0.18	(2), (6)	(4)
	4563.79	0.33	5.13×10^{-7}	1.90×10^{-7}	4563.11	0.54	4563.76	0.50	4562.83	0.42	(2), (7)	(5)
NWA 1670	4564.39	0.24	5.92×10^{-7}	5.90×10^{-8}	4563.25	0.33	4563.89	0.32	4562.97	0.20	(4)	(4)
NWA 7325	4563.4	2.6	3.03×10^{-7}	1.40×10^{-8}	4562.60	0.31	4563.25	0.30	4562.32	0.17	(8)	(8)
Asuka 881394	4564.95	0.53	1.48×10^{-6}	1.80×10^{-8}	4564.14	0.30	4564.78	0.29	4563.85	0.16	(9)	(9)
			1.28×10^{-6}	7.00×10^{-8}	4564.00	0.31	4564.64	0.30	4563.71	0.18		(10)
NWA 11119			1.69×10^{-6}	9.00×10^{-8}	4564.27	0.31	4564.91	0.30	4563.98	0.18		(11)
		+0.22/-										
NWA 6704	4562.76	0.30	3.15×10^{-7}	3.80×10^{-8}	4562.64	0.35	4563.28	0.33	4562.36	0.21	(12)	(13)
NWA 2976	4562.89	0.59	3.94×10^{-7}	1.60×10^{-8}	4562.86	0.31	4563.50	0.30	4562.57	0.17	(14)	(14)
			4.91×10^{-7}	4.60×10^{-8}	4563.07	0.33	4563.71	0.32	4562.79	0.20		(15)

References: (1) Barrat et al. (2021); (2) Tissot et al. (2017); (3) Amelin (2008a); (4) Schiller et al. (2015); (5) Spivak-Birndorf et al. (2009); (6) Amelin (2008b); (7) Connelly et al. (2008); (8) Koefoed et al. (2016); (9) Wimpenny et al. (2019); (10) Wadhwa et al. (2009); (11) Srinivasan et al. (2018); (12) Amelin et al. (2019); (13) Sanborn et al. (2019); (14) Bouvier et al. (2011c); (15) Schiller et al. (2010a).

5 Chronology and provenance of angrites

Angrites are basaltic achondrites that formed on a differentiated parent body and are, made up primarily of calcic olivine, Al-Ti-bearing diopside-hedenbergite (fassaite pyroxene) and anorthite (e.g., Keil, 2012). Their formation ages, determined by the Pb-Pb chronometer, range between 3 Ma and 11 Ma after CAI formation, representing some of the oldest crustal rocks of the Solar System (e.g., Amelin, 2008a, 2008b; Connelly et al., 2008; Brennecka and Wadhwa, 2012; Tissot et al., 2017). They are commonly grouped by their textures, into the fine-grained volcanic (or quenched) angrites and the coarse-grained plutonic angrites. The volcanic angrites cluster around absolute Pb-Pb ages of 4563 to 4564 Ma, whereas the plutonic angrites are dated at 4556 to 4557 Ma. So far, only the Pb-Pb ages of the paired angrites NWA 2999 and NWA 6291 have produced formation ages fully resolved from the other two groups, at ~4561 Ma (Amelin and Irving, 2007; Bouvier et al., 2011a; Tissot et al., 2017). Other chronometers, like the short-lived ^{182}Hf - ^{182}W chronometers, have dated angrite samples to similar ages and time intervals between the groups (Kleine et al., 2012).

Achondrites, and quickly cooled volcanic angrites in particular, are often used as anchor meteorites, where ages determined from short-lived chronometers (e.g., the ^{26}Al - ^{26}Mg chronometer) are anchored to the absolute Pb-Pb ages of the same sample. The volcanic angrite D'Orbigny has been widely used as an anchor for both the ^{26}Al - ^{26}Mg and ^{53}Mn - ^{53}Cr chronometers. The ^{26}Al - ^{26}Mg ages of D'Orbigny and other volcanic angrites however have repeatedly shown to be ~ 1 Myr younger than their Pb-Pb ages (Spivak-Birndorf et al., 2009; Schiller et al., 2015a). This age discrepancy has been attributed to disturbances in the Al-Mg systematics of volcanic angrites (Sanborn et al., 2015), spuriously young Pb-Pb ages of CAIs (Sanborn et al., 2019; Wimpenny et al., 2019), or to a lower initial ^{26}Al abundance in the inner Solar System where the angrites formed (Schiller et al., 2015a).

Bulk and mineral fractions of the two angrites NWA 8535 (dunite) and NWA 10463 (olivine-bearing angrite) were analyzed for their trace element abundances and their Mg isotope composition. In addition, a pyroxene and bulk fraction of NWA 10463 was dated using U-corrected Pb-Pb chronology. These analyses provide insight into their formation age and magmatic evolution on the angrite parent body.

5.1 Samples and Methods

5.1.1 Northwest Africa 10483

Previously described in conference abstracts by Santos et al. (2016, 2017), NWA 10463 consists of feldspar (37%), pyroxene (29%), olivine (26%) as well as minor phases of Fe-Ti oxides, Fe-sulfides, Cr-bearing spinel and phosphates (Figure 50). Feldspars (anorthite) and pyroxenes (Al- and Ti-rich fassaite) have typical angrite compositions. However, some textural features suggest that NWA 10463 may sample a hitherto unsampled part of the angrite parent body. Generally, the texture resembles that of plutonic angrites, but recurrent zoning and exsolution in minerals indicate that the sample did not equilibrate. Santos et al. (2016) suggest that NWA 10463 may represent an intermediate stage between plutonic and volcanic angrites.

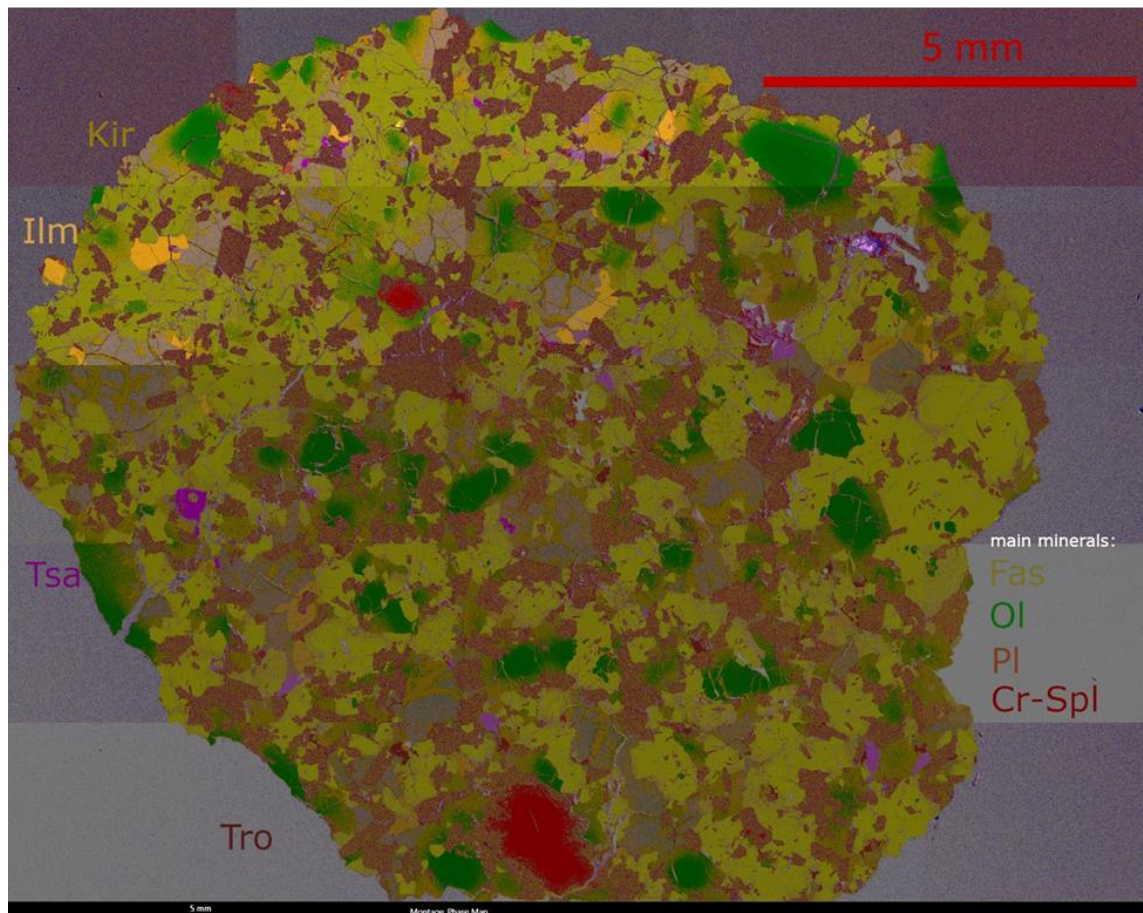


Figure 50: False-color EDS image of NWA 10463, with Al-Ti-bearing pyroxene (fassaite) in yellow, olivine in green, plagioclase in orange-brown and Cr-spinel in red. Accessory mineral phases include kirschsteinite, ilmenite, troilite and tsangpoite (Ca-phosphate).

5.1.2 Northwest Africa 8535

Northwest Africa (NWA) 8535 is the first dunitic angrite ever classified, and samples a new part of the angrite parent body. It consists of 90-95% zoned olivines (Fe-enriched rims), about 3% fassaite (Al- and Ti-bearing diopside) and accessory Al-spinel, Cr-spinel, troilite, as well as metal in the form of taenite and kamacite (Figure 51; Santos, 2016, Agee et al., 2015). The olivine composition overlaps with those of possible xenocrysts in the volcanic angrites Asuka 881371 and D'Orbigny (Agee et al., 2015), suggesting that there may be a petrogenetic relation between them and NWA 8535.

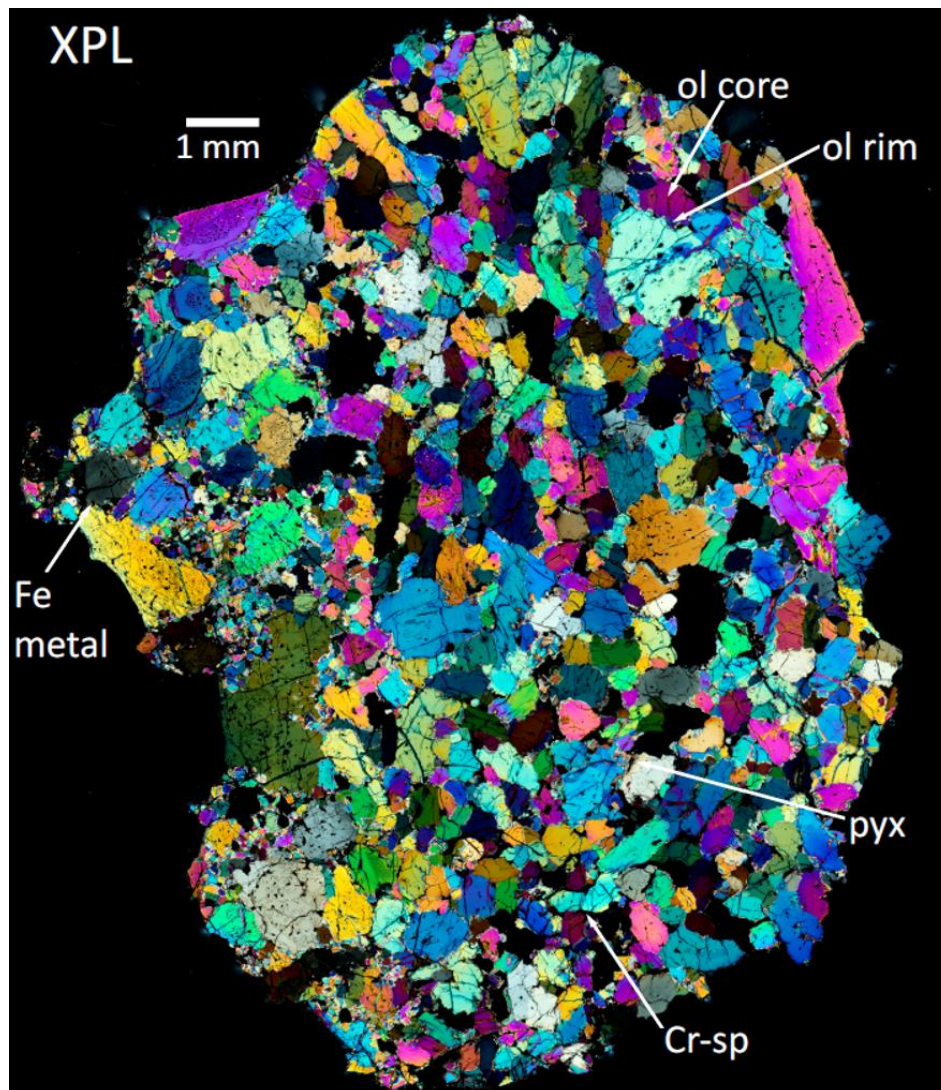


Figure 51: Image of NWA 8535 under cross-polarized light, from Santos (2016). This particular thin section is made up of ~ 96% olivine and 3% spinel, with accessory metal, sulfides, pyroxene and phosphates.

5.1.3 Methods

NWA 8535 was pre-cleaned with acetone to remove any terrestrial carbonates before being coarsely crushed in an agate mortar, from which multiple pure olivine grains without any visible inclusions were hand-picked under binoculars. Mineral separation procedure used for NWA 10463 is described in Chapter 2. In the end, roughly 65 mg pyroxene were hand-picked under binoculars for Pb chemistry, with the bulk sample making up ~ 150 mg.

The methods used to obtain the Mg, Pb and U isotope compositions, $^{27}\text{Al}/^{24}\text{Mg}$ ratios, as well as trace element abundances, are described in Chapter 2: Methods.

5.2 Results

5.2.1 Bulk and mineral REE abundances

Rare-earth element concentrations were analyzed in bulk and mineral fractions of NWA 10463. The re-combined bulk and pyroxene leachates, prepared for Pb chemistry, as well as the olivine and pyroxene fractions prepared for Mg isotope analysis were measured. In addition, the olivine fraction of NWA 8535 was also analyzed, and their abundances are listed in Table 21. Rare-earth element abundance patterns normalized to CI chondrites (Barrat et al., 2012) are displayed in Figure 56, Figure 57 and Figure 58.

Table 21: Rare-earth element concentrations in bulk and mineral fractions of NWA 10463 and NWA 8535. All concentrations are listed in ppm. n.m.: no measurement.

	NWA 10463 bulk	NWA 10463 Px (Pb)	NWA 10463 Px (Mg)	NWA 10463 Ol	NWA 8535 Ol
La	0.580	0.714	0.630	0.012	0.011
Ce	1.940	2.650	2.520	0.036	0.009
Pr	0.350	0.512	0.489	0.009	0.004
Nd	1.991	3.035	3.470	0.057	0.012
Sm	0.692	1.149	1.418	0.012	0.005
Eu	0.267	0.335	0.404	0.004	0.006
Gd	0.996	1.705	2.179	n.m.	0.003
Tb	0.182	0.321	0.379	0.009	0.002
Dy	1.179	2.090	2.502	0.081	0.011
Ho	0.244	0.435	0.536	0.012	0.002
Er	0.678	1.229	1.540	0.064	0.012
Tm	0.094	0.174	0.219	0.015	0.0005
Yb	0.605	1.152	1.442	0.141	0.049
Lu	0.092	0.177	0.221	0.021	0.004

5.2.2 Magnesium isotope compositions and Al/Mg ratios of achondrite fractions

Table 22: Al-Mg data for NWA 8535 and NWA 10463 fractions.

Sample	$^{27}\text{Al}/^{24}\text{Mg}$	$\delta^{25}\text{Mg}$ (‰)	2SE	$\delta^{26}\text{Mg}$ (‰)	2SE	$\delta^{26}\text{Mg}^*$ (‰)	2SE	n
NWA 8535 ol	0.005	-0.075	0.021	-0.173	0.032	-0.031	0.010	4
NWA 10463 ol	0.007	-0.016	0.015	-0.057	0.032	-0.025	0.007	4
NWA 10463 px	0.765	-0.415	0.017	-0.835	0.031	-0.024	0.005	4
NWA 10463 pl1	9.48	-0.429	0.022	-0.873	0.029	-0.037	0.008	6
NWA 10463 pl2	152	-0.898	0.031	-1.722	0.074	0.030	0.028	3
NWA 10463 pl3	81.9	-0.715	0.106	-1.016	0.177	0.378	0.043	3
NWA 10463 pl4	12.31	-0.640	0.026	-1.143	0.049	0.109	0.006	4

Mineral separates from the angrites Northwest Africa 8535, Northwest Africa 10463 and ungrouped achondrite Erg Chech 002 were analyzed for their $^{27}\text{Al}/^{24}\text{Mg}$ ratios by quadrupole ICP-MS and for their Mg isotope composition by MC-ICP-MS. The results are reported in Table 22. For NWA 8535, a dunitic angrite, only a single olivine fraction with a $^{27}\text{Al}/^{24}\text{Mg}$ ratio of 0.005 and $\delta^{26}\text{Mg}^*$ value of -0.030 ± 0.010 ‰ was analyzed. For NWA 10463, one pyroxene and one olivine fraction, as well as four plagioclase fractions were analyzed. The four plagioclase fractions have $^{27}\text{Al}/^{24}\text{Mg}$ ratios from 8.6 to 173, with their $\delta^{26}\text{Mg}^*$ values ranging from -0.039 ± 0.008 ‰ to 0.378 ± 0.043 ‰. Notably, however, the $\delta^{26}\text{Mg}^*$ values do not correlate with the $^{27}\text{Al}/^{24}\text{Mg}$ ratios over the whole dataset (Figure 52). The olivine fraction is comparable to the one from NWA 8535, with a $^{27}\text{Al}/^{24}\text{Mg}$ ratio of 0.007 and $\delta^{26}\text{Mg}^*$ value of -0.025 ± 0.007 ‰. The $\delta^{26}\text{Mg}^*$ value of the pyroxene fraction is equal within uncertainty to the olivine fraction (-0.024 ± 0.007 ‰), despite a $^{27}\text{Al}/^{24}\text{Mg}$ ratio of 0.765.

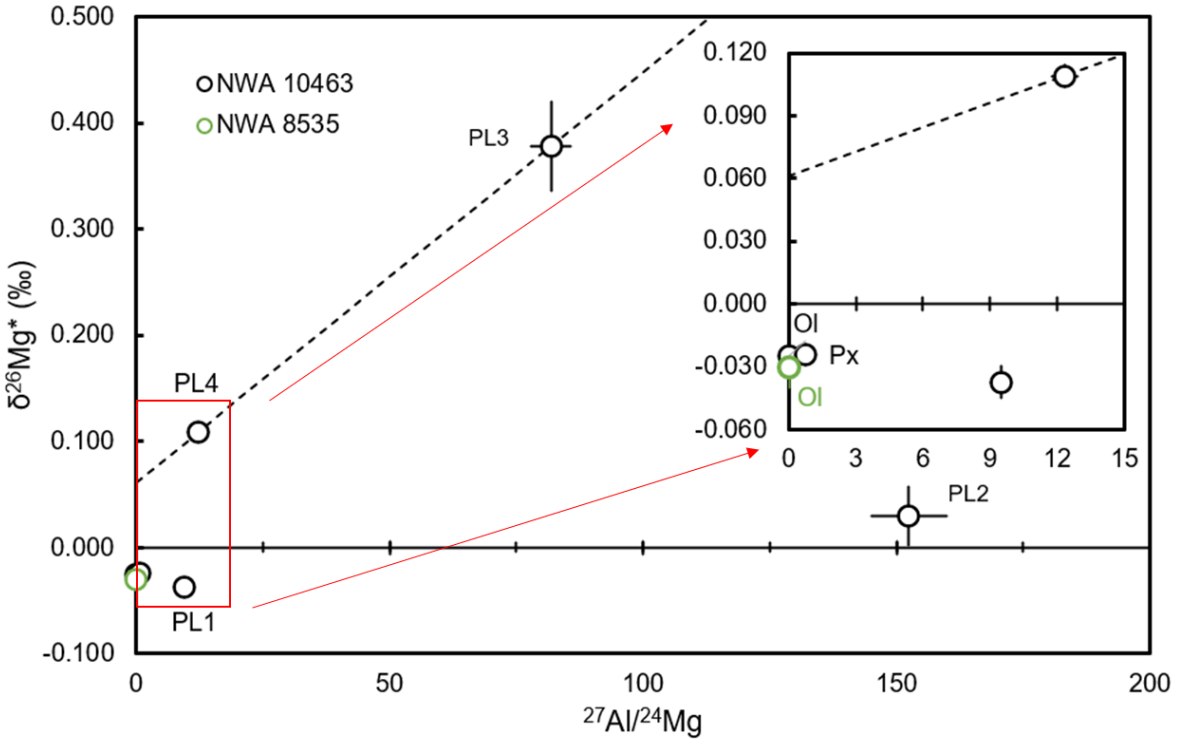


Figure 52: Al-Mg data of NWA 10463 and NWA 8535 fractions. Uncertainties in $^{27}\text{Al}/^{24}\text{Mg}$ ratios are $\pm 5\%$, and are within symbols where not visible. The regression line through PL3 and PL4 has a slope that corresponds to an initial $^{26}\text{Al}/^{27}\text{Al}$ ratio of $\sim 5.4 \times 10^{-7}$, in the range of the volcanic angrites.

5.2.3 U isotope composition of NWA 10463

The U isotope composition was measured on the combined leachates (L4 and later) and residue of both the pyroxene and the bulk fraction, at the Leibniz Universität in Hannover. The weighted mean of two measurement runs results in a $^{238}\text{U}/^{235}\text{U}$ ratio of 137.770 ± 0.110 . The relatively high uncertainty is due to the low amount of U in the sample, around 2.5 ng. The measured $^{238}\text{U}/^{235}\text{U}$ ratio is consistent with $^{238}\text{U}/^{235}\text{U}$ ratios of other angrite samples (Brennecka and Wadhwa, 2012; Tissot et al., 2017).

5.2.4 Pb-Pb chronology of NWA 10463

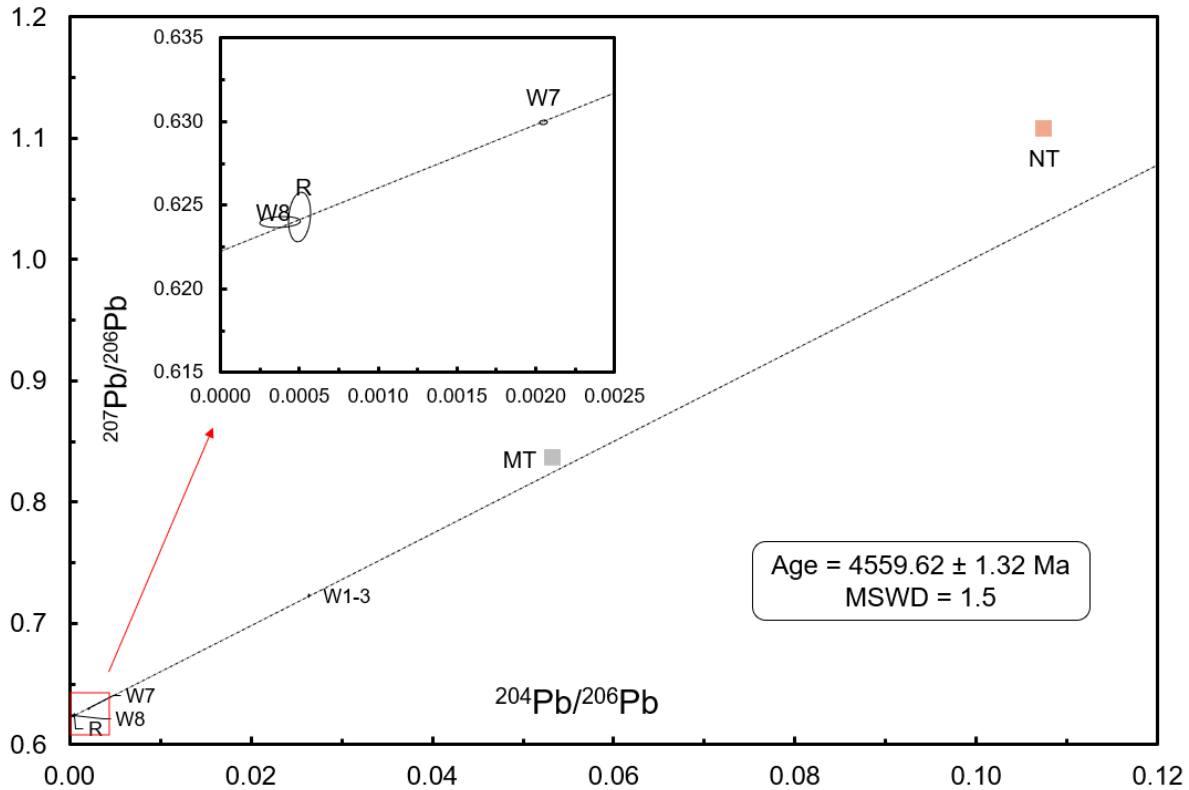


Figure 53: Pb-Pb isochron of Px fractions of NWA 10463 angrite.

The Pb isotope compositions of the leachates and residues of the bulk and pyroxene fractions are listed in Table 23: Pb isotope compositions of pyroxene and bulk leachates and residues of NWA 10463 angrite.

Sample	mass [mg]	Pb [ng]	U [ng]	Sample/Blank	$^{206}\text{Pb}/^{204}\text{Pb}$ raw	$^{204}\text{Pb}/^{206}\text{Pb}$	2SE [%]	$^{207}\text{Pb}/^{206}\text{Pb}$
Px W1-3	2.0	0.57	0.06	187	37.68	0.02640	0.24	
Px W4	8.1	8.2	0.35	1411	278.1	0.00358	4.53	
Px W5+6	0.8	1.5	0.02	132	347.5	0.00262	4.08	
Px W7	9.1	0.66	0.26	763	476.1	0.00205	1.03	
Px W8	13.4	0.44	0.07	159	1563	0.00038	28.2	
Px R	39.9	0.89	0.09	290	1563	0.00050	11.5	
bulk W1-3	24.3	6.2	0.54	3911	39.55	0.02528	0.10	
bulk W4	42.5	1.3	0.28	1096	56.02	0.01782	0.06	
bulk W5+6	8.1	0.53	0.08	160	61.53	0.01606	0.48	
bulk W7	2.1	0.51	0.87	1542	66.37	0.01505	0.06	
bulk W8	26.7	0.48	0.33	786	214.5	0.00461	0.42	
bulk R	62.5	0.12	0.30	415	89.13	0.01113	0.33	

. The leachates and residue of the pyroxene fraction have $^{206}\text{Pb}/^{204}\text{Pb}$ ratios ranging from 37.7 to 1562, while the bulk leachates and residues range from 39.6 to 216. Sample-to-blank ratios for the pyroxene fractions range from 132 to 1411 and from 160 to 3911 for the bulk fraction. The W1-3, W7, W8 leachates and the residue R of the pyroxene fraction define an isochron with a U-corrected age of 4559.61 ± 1.32 Ma (Figure 53). No combination of leachates and the residue of the bulk fractions define a statistically significant isochron. Including the W7 and W8 bulk leachates with the W7, W8 leachates and the residue R of the pyroxene fraction results in an isochron with a U-corrected age of 4560.25 ± 1.27 Ma (Figure 54).

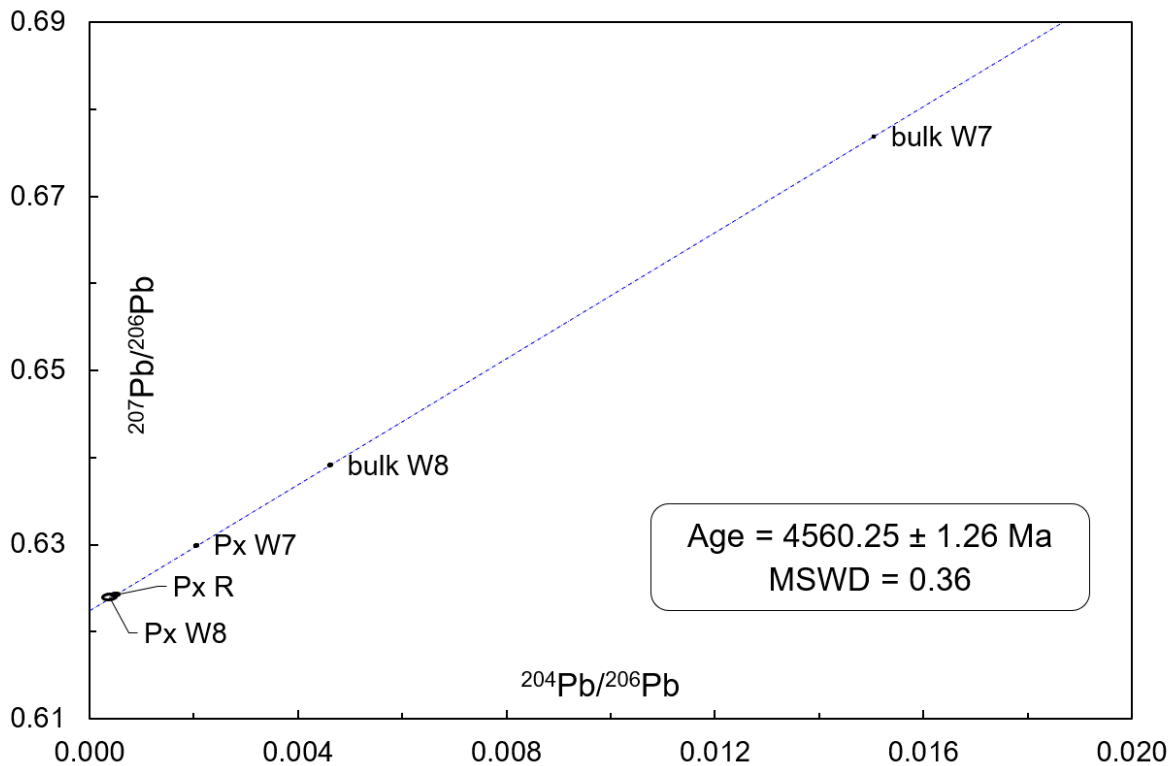


Figure 54: Pb-Pb isochron of pyroxene and bulk fractions of NWA 10463 angrite.

Table 23: Pb isotope compositions of pyroxene and bulk leachates and residues of NWA 10463 angrite.

Sample	mass [mg]	Pb [ng]	U [ng]	Sample/Blank	$^{206}\text{Pb}/^{204}\text{Pb}$ raw	$^{204}\text{Pb}/^{206}\text{Pb}$	2SE [%]	$^{207}\text{Pb}/^{206}\text{Pb}$	2SE [%]
Px W1-3	2.0	0.57	0.06	187	37.68	0.02640	0.24	0.72266	0.021
Px W4	8.1	8.2	0.35	1411	278.1	0.00358	4.53	0.62928	0.007
Px W5+6	0.8	1.5	0.02	132	347.5	0.00262	4.08	0.63055	0.042
Px W7	9.1	0.66	0.26	763	476.1	0.00205	1.03	0.62993	0.014
Px W8	13.4	0.44	0.07	159	1563	0.00038	28.2	0.62397	0.042
Px R	39.9	0.89	0.09	290	1563	0.00050	11.5	0.62425	0.023
bulk W1-3	24.3	6.2	0.54	3911	39.55	0.02528	0.10	0.71882	0.007
bulk W4	42.5	1.3	0.28	1096	56.02	0.01782	0.06	0.69094	0.004
bulk W5+6	8.1	0.53	0.08	160	61.53	0.01606	0.48	0.67828	0.034
bulk W7	2.1	0.51	0.87	1542	66.37	0.01505	0.06	0.67691	0.021
bulk W8	26.7	0.48	0.33	786	214.5	0.00461	0.42	0.63915	0.013
bulk R	62.5	0.12	0.30	415	89.13	0.01113	0.33	0.66096	0.016

5.3 Discussion

5.3.1 U-corrected Pb-Pb age of NWA 10463

The best-fit regression line through four pyroxene fractions of NWA 10463 (the residue plus L8 L7 and L1-3) results in an age of 4559.62 ± 0.41 Ma. Combining the pyroxene and bulk fractions, the best-fit regression line results in an age of 4560.34 ± 0.18 Ma. This regression includes the three most radiogenic pyroxene fractions (R, L8 and L7) as well as the two most radiogenic bulk leachates (L8 and L7). Both of these regression lines plot below the value for terrestrial Pb (Stacey and Kramers, 1975) indicating that no initial Pb was present at time of formation, akin to the volcanic angrite Sahara 99555 (Amelin, 2008a; Connelly et al., 2008). Since there is no evidence in any leachate that initial Pb is present as a third component, the inclusion of L1-3 in the isochron regression is justified, as it will contain only terrestrial and radiogenic Pb.

Propagating the uncertainty of the U isotope composition ($^{238}\text{U}/^{235}\text{U} = 137.770 \pm 0.110$) into the Pb-Pb age increases the uncertainty on them substantially. The uncertainty on the “bulk” isochron age increases to ± 1.26 Ma and the pyroxene isochron to ± 1.32 Ma.

The Pb-Pb age indicates that NWA 10463 falls into the intermediate age group of angrites, centered around 7.5 Ma after CAI formation between the older volcanic and the younger plutonic angrites, as defined by Kleine et al. (2012) using Hf-W chronology. This group also includes the NWA 2999/6291 pair (Amelin and Irving, 2007; Bouvier et al., 2011a; Tissot et al., 2017). This is consistent with the interpretation of the petrologic features that NWA 10463 likely is an intermediate sample between the volcanic and plutonic angrite groups.

5.3.2 Mg isotope compositions of olivine in NWA 10463 and NWA 8535

The low $\delta^{26}\text{Mg}^*$ values of the olivine from both NWA 8535 and NWA 10463 are within uncertainty of the Solar System initial (-0.0340 ± 0.0016 ; Schiller et al., 2010b). This indicates that very little radiogenic ingrowth of ^{26}Mg occurred between the beginning of the Solar System and the crystallization of both samples, and could be explained by fast accretion and early differentiation of the mantle (low Al/Mg) of the angrite parent body, before the samples crystallized. Comparable values were measured in olivine fractions of the volcanic angrites D’Orbigny and Sahara 99555 by Spivak-Birndorf et al. (2009), but the same meteorites have higher $\delta^{26}\text{Mg}^*$ values in the study by Schiller et al. (2015). Bulk Mg isotope compositions of

plutonic angrites show some resolved negative $\delta^{26}\text{Mg}^*$ anomalies (Schiller et al., 2010a) compared to the terrestrial value, which could indicate late formation from an Al-poor melt. It was previously suggested that NWA 8535 could have formed early in what would become the fine-grained angrite reservoir (Santos et al., 2017b).

5.3.3 ^{26}Mg excesses in NWA 10463 plagioclase: analytical artefact?

At an absolute age of ~ 4560 Ma, plagioclase fractions are not expected to show evidence of significant ^{26}Mg excesses. In that regard, results of the plagioclase fractions in NWA 10463 are unusual, in that some fractions with lower $^{27}\text{Al}/^{24}\text{Mg}$ ratios exhibit higher $\delta^{26}\text{Mg}^*$ values than those with higher $^{27}\text{Al}/^{24}\text{Mg}$ ratios (Figure 52). Thus, the question arises if the $\delta^{26}\text{Mg}^*$ values could have been the result of improper analytical protocols during chemistry or analysis rather than through natural effects. Possible causes of such effects are, a) mass fractionation during column chemistry and insufficient Mg recovery; or b) matrix effects during mass spectrometry, caused by insufficient Mg purification during column chemistry. Option a) can be discarded on the basis that mass fractionation during column chemistry would not result in any mass-independent fractionation of this amplitude, and has never been reported for Mg (e.g., Fujii et al., 2009). Furthermore, the chemistry procedure used for Mg separation was tested repeatedly, including with high Al/Mg rock standards, and Mg recovery in every case was $\geq 99.7\%$. For option b), the analyzed plagioclase fractions are all characterized by low amounts of Mg (1.8 to 5.8 μg) that were separated from relatively small total masses (1 mg or less) during cation-exchange chemistry. Expected candidates for isobaric interferences on the Mg isotope composition of plagioclase fractions are double-charged ions of ^{48}Ca , ^{48}Ti , ^{50}Ti , ^{50}Cr and ^{52}Cr . Particularly Ca is expected to be more highly concentrated in plagioclase, especially with increasing $^{27}\text{Al}/^{24}\text{Mg}$ ratios. Doubly charged ^{48}Ca however, would affect counts on ^{24}Mg , lowering $\delta^{26}\text{Mg}^*$ values, whereas only isobaric interference of double-charged ^{52}Cr would increase $\delta^{26}\text{Mg}^*$. In this dataset, there is no significant correlation between $\delta^{26}\text{Mg}^*$ values and Ca/Mg or Cr/Mg ratios in the plagioclase fractions. If purification of Mg during column chemistry was equally as insufficient in all plagioclase samples, it would be expected that $\delta^{26}\text{Mg}^*$ and the Ca or Cr content, respectively, exhibited some relationship. Additionally, the low Mg contents of the plagioclase fractions could raise the possibility of blank contributions affecting the Mg isotope composition. Full analytical blanks of the Mg chemistry and analyses

however never exceeded 5 ng, and generally were in the range of 1 to 3 ng, and should not have any impact on the samples. These arguments, along with the analysis of standard materials described in chapter 2, suggest that $\delta^{26}\text{Mg}^*$ values seen in the plagioclase fractions of NWA 10463 are not products of flawed analytical protocols.

5.3.4 Genetic heritage of NWA 8535 and NWA 10463

Having ruled out analytical artefacts as the origin of the unusual $\delta^{26}\text{Mg}^*$ values in the NWA 10463 plagioclase fractions, it is clear that radiogenic ingrowth of ^{26}Mg is the source in those samples with resolved excess ^{26}Mg . The lack of resolvable ^{26}Mg excesses in other fractions, including the one with the highest $^{27}\text{Al}/^{24}\text{Mg}$ ratio of 152, suggests that the plagioclase of NWA 10463 crystallized at different times and likely originated from (at least) two different reservoirs in the parent body. The two plagioclase fractions that do show resolvable ^{26}Mg excesses plot on a line with a slope equal to an initial $^{26}\text{Al}/^{27}\text{Al}$ ratio of $\sim 5.4 \times 10^{-7}$ (Figure 52). This is in a similar range to the volcanic angrites, about 0.3 Myr older than D'Orbigny, and could indicate that the different $\delta^{26}\text{Mg}^*$ values of plagioclase in NWA 10463 are reflective of their formation in either the volcanic angrite reservoir (earlier formed, with ^{26}Mg excesses) or the plutonic angrite reservoir (later formed, with no excess ^{26}Mg). It is, however, important to consider that this “isochron” may not have any chronological meaning, and could be the product of mixing between high Al/Mg plagioclase with higher radiogenic excesses in ^{26}Mg and low Al/Mg plagioclase or other Mg-rich phase without such excess. Further in-situ Al-Mg analyses by SIMS or LA-MC-ICPMS could shed light of potential Mg isotopic heterogeneities and age comparison with its own Pb-Pb age as well as with other angrites.

With the provenance of plagioclase in NWA 10463 somewhat unclear, it also casts some doubt on the accuracy of Pb-Pb isochrons that include leachates of the bulk fraction. For that reason, only the Pb-Pb age determined by isochron regression through data points from the pyroxene fractions is taken into consideration from this point. With that in mind, the suggested U-corrected Pb-Pb age of NWA 10463 is 4559.64 ± 1.32 Ma including uncertainties from U isotopic composition. Despite the larger uncertainty due to NWA 10463 U isotope composition, this age is resolved and intermediate between the volcanic angrites and plutonic angrites (Figure 55).

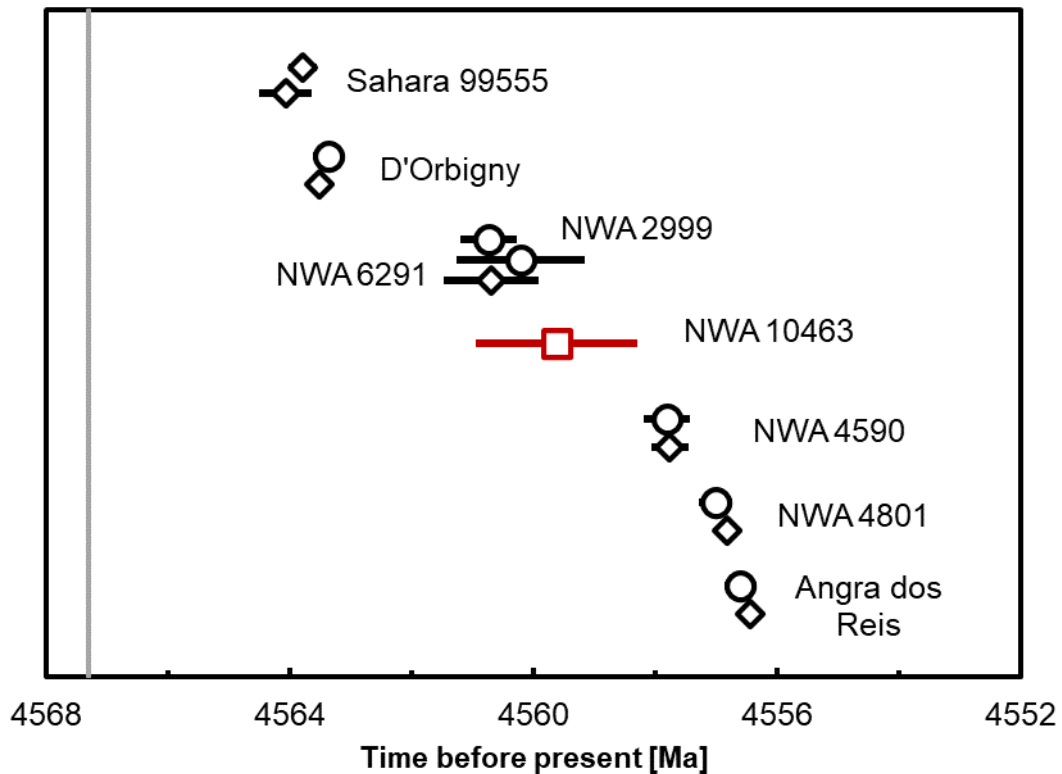


Figure 55: Comparison of U-corrected Pb-Pb ages of angrites, showing the age clusters of the volcanic angrites at ~4564 Ma, the plutonic angrites at ~4556-4557 Ma, and also the “intermediate” group of angrites at ~ 4560 Ma. Error bars are within the symbols if not visible, and include uncertainties of the U isotope compositions. Black diamonds are literature data from Tissot et al. (2017), black circles from Brennecka and Wadhwa (2012).

The Pb-Pb age established that NWA 10463 formed around the same time as the NWA 2999/6291 pair at ~4560 Ma (Amelin and Irving, 2007; Bouvier et al., 2011a; Brennecka and Wadhwa, 2012; Kleine et al., 2012; Tissot et al., 2017). This age is distinct from both the volcanic, fine-grained and plutonic, coarse-grained angrites at ~ 4564 Ma and ~4557 Ma, respectively (Amelin, 2008b; Tissot et al., 2017). The NWA 2999 and NWA 6291 pair are unusual angrites, in that they contain higher abundances of metal that was likely derived from an impactor (Humayun et al., 2007). NWA 2999 is a coarse-grained angrite that shows some evidence of possible arrested metamorphism, but NWA 6291 additionally exhibits both coarse- and fine-grained textures that is not seen in NWA 2999 (Bouvier et al., 2011a). Interestingly, the CI-normalized REE pattern of clinopyroxene in NWA 2999 is relatively flat and closer to the fine-grained than the coarse-grained angrites, whereas the bulk REE abundances are lower than

both angrite groups (Floss et al., 2003; Tissot et al., 2017; Sanborn and Wadhwa, 2021). NWA 10463 also exhibits petrologic characteristics that suggest it being a member of an intermediate group of angrites. While it is texturally similar to the coarse-grained plutonic angrites, larger olivine grains are chemically zoned and exhibit some exsolution lamellae, indicating that it did not equilibrate chemically as plutonic angrites did. Indeed, the REE patterns between bulk samples of NWA 10463 and NWA 2999 (Sanborn and Wadhwa, 2021) are remarkably similar (Figure 56). Both have lower REE abundances compared to volcanic angrites and plutonic angrites other than those paired with NWA 2999, i.e., NWA 4931, NWA 5167 and NWA 6291 (Riches et al., 2012; Baghdadi et al., 2015; Tissot et al., 2017). In both the olivine fraction (Figure 57) and pyroxene fractions (Figure 58) of NWA 10463, the REE patterns are comparable to NWA 2999 and are flatter than those of the coarse-grained plutonic angrites. The same can be observed in the REE pattern in olivine from NWA 8535, which more closely resembles the fine-grained volcanic angrites, and points towards a common heritage (Figure 57). This is supported by purported olivine xenocrysts in volcanic angrites Asuka 881371 and D'Orbigny overlapping NWA 8535 olivine compositions (Agee et al., 2015; Santos et al., 2017b). NWA 10463 and the NWA 2999/6291 pair having the same Pb-Pb ages (within uncertainty) further strengthens the case that their formations are linked, while the geochemical similarities point towards the same formation reservoir between NWA 8535, NWA 10463, NWA 2999/6291 and the fine-grained volcanic angrites.

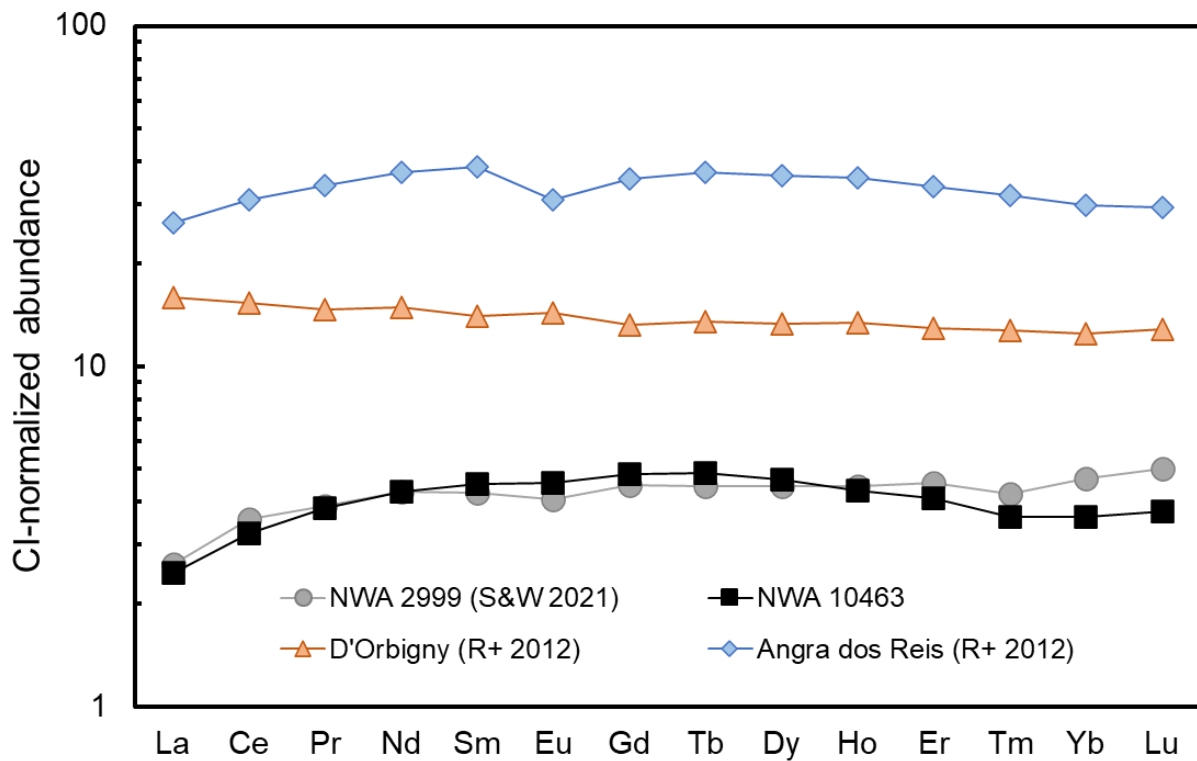


Figure 56: Bulk REE patterns for NWA 10463, NWA 2999, and the volcanic and plutonic angrites, represented by D'Orbigny and Angra dos Reis, respectively. R+ 2012: Riches et al. (2012). S&W 2021: Sanborn and Wadhwa (2021).

Given its low $\delta^{26}\text{Mg}^*$ value, NWA 8535 may be a sample from the early stages of the magmatic processes forming the fine-grained angrite source reservoir, as suggested by Santos et al. (2017b). Sanborn and Wadhwa (2021) suggested that this formation reservoir experienced protracted magmatic activity that lasted for at least 2 Myr after the volcanic angrites formed. The discovery of NWA 10463 with its intermediate petrology, geochemical and chronological affinity to the NWA 2999/6291 pair reinforces that argument. Plagioclase fractions of NWA 10463 with $\delta^{26}\text{Mg}^*$ values that do not reflect closed-system ingrowth of radiogenic ^{26}Mg on a whole-rock scale, along with the presence of both coarse- and fine-grained material in NWA 6291 furthermore suggest that some mixing between the respective formation reservoirs may have occurred. The presence of metal in NWA 2999/6291, along with the brecciated nature of NWA 2999, are consistent with their formation being linked to an impact event on the angrite parent body at ~ 4560 Ma. This scenario also explains the zoning in olivine grains in both NWA

8535 and NWA 10463, indicating more rapid cooling. An impact event could have excavated part of the angrite parent body and brought the formation reservoir of NWA 10463 and NWA 8535 closer to the surface where cooling rates would be higher.

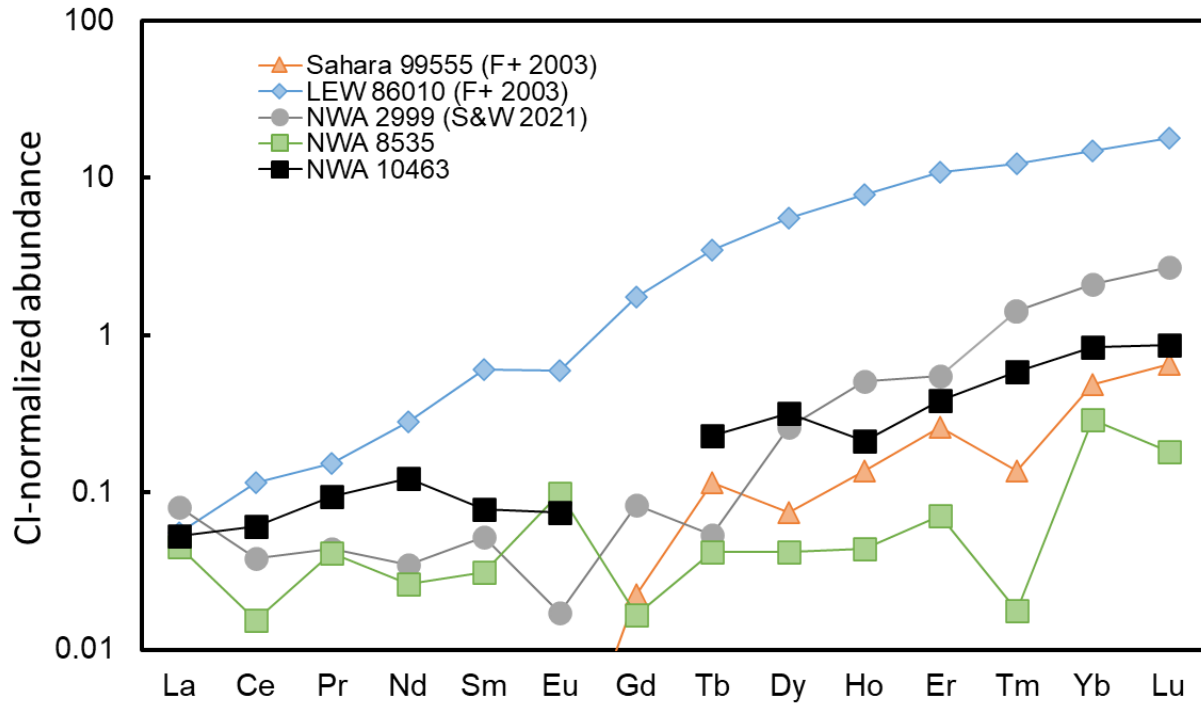


Figure 57: Olivine REE patterns for NWA 8535 and NWA 10463 compared to NWA 2999, volcanic angrite Sahara 99555 and plutonic angrite LEW 86010. F+ 2003: Floss et al. (2003). S&W 2021: Sanborn and Wadhwa (2021).

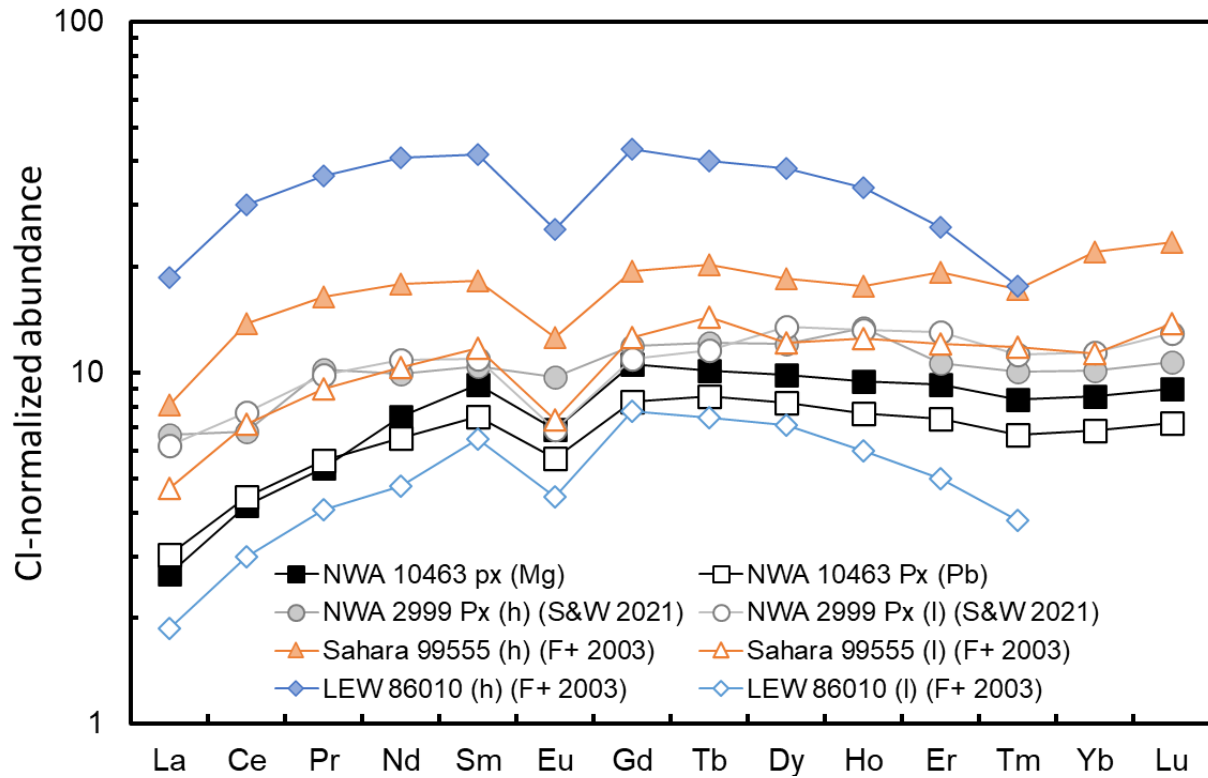


Figure 58: REE patterns in clinopyroxene of the angrites NWA 10463, NWA 2999, as well as volcanic angrite Sahara 99555 and plutonic angrite LEW 86010. ‘h’ and ‘l’ denote measurements with higher (filled symbols) or lower (empty symbols) REE concentration. Ytterbium and Lu measurements were reported as “below detection limit.” F+ 2003: Floss et al. (2003). S&W 2021: Sanborn and Wadhwa (2021).

6 Conclusions

6.1 Summary of Chapter 3

Chondrule ages, determined by the ^{26}Al - ^{26}Mg and Pb-Pb chronometer, and their ^{54}Cr nucleosynthetic anomalies are reported and discussed in Chapter 3. Chondrules have bulk Mg model ages that span the first 2 Myr after the formation of CAIs, whereas their *in situ* ^{26}Al - ^{26}Mg ages analyzed by SIMS give their formation ages span from 1.70 $^{+0.81}_{-0.44}$ Ma after CAI formation to 2.27 $^{+0.52}_{-0.34}$ Ma, consistent with previously reported ^{26}Al - ^{26}Mg ages in OC chondrules (e.g., Kita et al., 2010, Villeneuve et al., 2009; Pape et al., 2019). The bulk Mg model ages are believed to date Al/Mg fractionation, i.e., chondrule precursor formation, compared to *in situ* ^{26}Al - ^{26}Mg ages that date the last crystallization event. Nine chondrules were dated by the Pb-Pb chronometer, of which seven produced statistically significant isochrons. Three of these seven isochrons proved to be chronologically meaningless due to the presence of multiple U and Th carriers, after evaluating their $^{208}\text{Pb}/^{206}\text{Pb}$ and $^{204}\text{Pb}/^{206}\text{Pb}$ ratios. Three OC chondrules have old Pb-Pb ages, older or within error of the currently accepted absolute age of CAIs (Connelly et al., 2012), and range from 4568.21 ± 0.26 Ma to 4566.99 ± 0.73 Ma. When comparing these ages to the *in situ* ^{26}Al - ^{26}Mg ages, the same age gap of ~ 2 Myr is observed as in previous work (Bollard et al., 2019). This difference between Pb-Pb and Al-Mg ages has in the past been attributed to a heterogeneous distribution of ^{26}Al between the inner (NC) and outer (CC) Solar System, but that explanation has its own flaws. It has been previously speculated that Pb-Pb ages of bulk chondrules date U/Pb fractionation, i.e., precursor formation, rather than the last crystallization event (Blichert-Toft et al., 2020), analog to bulk Mg model ages. It is not entirely clear if Al/Mg and U/Pb fractionation occur at the same time or by the same processes, but the bulk Mg model ages and Pb-Pb ages are not consistent for individual chondrules.

The Cr isotope composition of OC chondrules are consistent with their formation in the NC reservoir, and define a positively correlated trend between their bulk Mg model ages and $\epsilon^{54}\text{Cr}$ values. This could reflect a change of infalling molecular cloud material or thermal processing of ^{54}Cr -poor material over time.

One chondrule from the CB_a chondrite QC 001 was analyzed alongside the OC chondrules. The Cr isotope composition is consistent with previously reported data of CB chondrules, whereas the Pb-Pb age is 0.90 ± 0.60 Myr older than the mean CB chondrule age, but does overlap with

two individual chondrule ages. Further evaluation of the isochron indicates that it may have been rotated due to some of the leachates potentially representing three-component mixtures of radiogenic, terrestrial and initial Pb, leading to a spuriously old age. This cannot be fully confirmed in this dataset, hence, the Pb-Pb age is interpreted as the older limit of chondrule formation of CB chondrites.

The two large igneous inclusions dated, Pap-II and NWA 12261-II, have *in situ* ^{26}Al - ^{26}Mg ages of $0.73^{+0.29}_{-0.22}$ and $2.92^{+1.06}_{-0.51}$ Ma after CAI formation, respectively. The old age of Pap-II inclusion is one of the oldest dated chondrule-like samples by SIMS, and provides an older limit on chondrule formation, thanks to the presence of a relict barred olivine chondrule within the inclusion. The Pb-Pb age for Pap-II is anomalously young at 4529.3 ± 2.1 Ma (~ 38 Ma after CAI formation), while for NWA 12261-II no age was determinable due to the lack of any radiogenic Pb. Coupled with a young I-Xe age of 126.5 Ma after CAI formation, Pap-II may have been subjected to late events that affected both the Pb-Pb and I-Xe chronometer, but not the ^{26}Al - ^{26}Mg chronometer. Thermal metamorphism could explain the Pb-Pb age of Pap-II, given similar ages Pb-Pb and U-Pb ages in equilibrated chondrites (Göpel et al., 1994; Amelin, 2000; Bouvier et al., 2007; Blackburn et al., 2017), but this is inconsistent with both the low petrologic type (3.2) and the unaffected Al-Mg systematics.

Based on these results from Pb-Pb and ^{26}Al - ^{26}Mg chronology, as well as literature data, the most consistent chronological data come from *in situ* ^{26}Al - ^{26}Mg ages, which are interpreted to reflect the currently best estimate of widespread chondrule formation, i.e., their last crystallization event. Chondrule formation could have been an ongoing process from CAI formation onwards, forming chondrules that were continuously or episodically recycled as precursors, as can be inferred from bulk Mg model ages. This is supported by the relict chondrule found within the igneous inclusion Pap-II in Paposo 004 L3 chondrite. The old ~ 0.7 Myr ^{26}Al - ^{26}Mg SIMS age of Pap-II is likely an outlier due to its large size and clast shape, that could have survived later flash heating events until accretion into the chondrite parent body.

The significance of Pb-Pb ages of individual chondrules remain inconclusive. Isochrons can be meaningless if multiple carriers of Th and U were incorporated into the chondrules or not fully reset during melting. Furthermore, the presence of statistically significant isochrons with anomalously young ages show that parent body processes may affect the Pb isotopic systematics compared to other more robust or short-lived and extinct radiochronometers.

6.2 Summary of Chapter 4

The unique achondrite Erg Chech 002 was dated by U-corrected Pb-Pb and ^{26}Al - ^{26}Mg chronology, and the results and their interpretation are reported in Chapter 4. Compared to a previous study that dated EC 002 by *in situ* ^{26}Al - ^{26}Mg analysis, the ^{26}Al - ^{26}Mg age determined by MC-ICP-MS analysis of seven mineral fraction, results in an age that is 0.43 ± 0.12 Myr older, at 1.71 ± 0.12 Ma after CAI formation and an absolute age of 4565.59 ± 0.19 Ma when anchored to the absolute age of CAIs. This age is consistent with the U-corrected Pb-Pb age of 4565.87 ± 0.28 Ma, determined by pyroxene residue and leachates, and makes EC 002 the oldest dated achondrite so far. The U isotope composition was determined for both a pyroxene and a bulk fraction, resulting in a notable difference between them that was likely caused by internal heterogeneities between mineral phases. For the calculation of the Pb-Pb age, the $^{238}\text{U}/^{235}\text{U}$ ratio of the (re-combined) leached pyroxenes was used.

The good agreement between the ^{26}Al - ^{26}Mg and Pb-Pb age suggest that ^{26}Al was distributed homogeneously in the inner Solar System (NC reservoir), in contrast to opposite interpretations (e.g., Schiller et al., 2015). Given its old age, agreement between the ^{26}Al - ^{26}Mg and Pb-Pb chronometer and straightforward thermal history, EC 002 shows promise to be used as an anchor to date other objects with short-lived chronometers. Anchoring the initial $^{26}\text{Al}/^{27}\text{Al}$ ratios of other achondrites to EC 002, the angrite D'Orbigny and two unique CC achondrites show concordant ^{26}Al - ^{26}Mg and Pb-Pb ages within the current level of uncertainties, whereas the ages of two other angrites and a unique NC achondrite are discordant. Given the good agreement between EC 002 (an NC achondrite) and CC achondrites, ^{26}Al heterogeneity does not seem to be the likely cause of the discordant ages between EC 002 and some NC achondrites. More likely, they could be attributed to internal U isotope heterogeneities between bulk meteorites and pyroxene fractions, disturbed ^{26}Al - ^{26}Mg systematics or spuriously young absolute ages of CAIs.

6.3 Summary of Chapter 5

Chapter 5 features the results and discussion of the REE abundances and Al-Mg systematics of mineral fractions from the angrites NWA 8535 and NWA 10463, as well as the U-corrected Pb-Pb age of the latter.

The mass-independent Mg isotope composition ($\delta^{26}\text{Mg}^*$) of olivine in both samples are within uncertainty of the Solar System initial value, suggesting they either formed early on their parent body, or late if they crystallized from an Al-poor melt. The REE pattern of olivine in NWA 8535

is similar to that of olivine in volcanic angrites and suggests a common heritage with that group, which would likely indicate early crystallization in that formation reservoir.

In two out of five plagioclase fractions from NWA 10463, significant ^{26}Mg excesses are found, but no correlation with $^{27}\text{Al}/^{24}\text{Mg}$ ratios. After analytical artefacts are deemed unfounded, the most likely explanation for this trait, is that NWA 10463 formed in a reservoir that experienced mixing between material with ^{26}Mg excesses similar to volcanic angrites and material without any ^{26}Mg excesses. The U-corrected Pb-Pb age of 4559.62 ± 1.32 Ma confirms that the ^{26}Mg excesses in some of the plagioclase fractions are likely from a different source. That age is not only distinct from the volcanic angrites, but also the plutonic angrites, but in good agreement with Pb-Pb ages of the paired angrites NWA 2999 and NWA 6291 (Amelin and Irving, 2007; Bouvier et al., 2011a; Tissot et al., 2017), suggesting a larger group of samples with intermediate ages. Furthermore, it confirms the inferences made from the petrology of the sample, with plutonic textures but evidence of quick cooling from zoned minerals which is not seen in plutonic angrites. The REE patterns of the bulk and mineral fractions of NWA 10463 are similar to those of NWA 2999 (Sanborn & Wadhwa, 2021) and indicate that they are more closely related to the fine-grained volcanic angrites (Floss et al., 2003). This suggests that magmatic activity in the fine-grained angrite reservoir extended at least for 2 Myr longer, and may have been excavated by an impact around ~ 4560 Ma to account for zoning in minerals of both NWA 8535 and NWA 10463. An impact-related formation has also been invoked for NWA 2999 due to its brecciated texture and metal-rich content.

In summary, both NWA 8535 and NWA 10463 are related to the fine-grained volcanic angrites, despite significantly different mineralogies. Likely, NWA 8535 initially formed early in the mantle (low Al/Mg), whereas NWA 10463 formed in a lower crust environment of the volcanic angrite reservoir. An impact occurring around 4560 Ma may have stripped the angrite parent body of some of its crust, leading to more rapid cooling and preservation of zoning in their minerals.

6.4 The wider context

In the wider context of early Solar System evolution and planetary formation, the results from Erg Chech 002 and the angrites NWA 8535 and NWA 10463 are examples of the increased diversity among the planetesimal population that furthers our understanding of the early Solar System. EC 002 has a unique mineralogy and is the oldest dated alkaline-rich achondrite,

suggesting varying differentiation processes taking place on early-formed planetesimals. The angrites parent body experienced a complex evolution, involving disruptive impact events, and with different formation reservoirs forming the different types of rocks found as meteorites.

The endogenous processes that shaped these achondrites is driven to a large extent by the energy created from the decay of ^{26}Al . The results from EC 002 and various OC chondrules do not indicate that ^{26}Al was distributed heterogeneously, as other have stated in the past, confirming that the ^{26}Al - ^{26}Mg chronometer can be applied to all early Solar System materials. On the other hand, the application of the Pb-Pb chronometer may be limited to the dating of mineral fractions, as variations of Th/U ratios in bulk chondrules can render “isochrons” meaningless. The importance of analyzing U isotope compositions in both bulk achondrites and its mineral fractions is re-stated by the internal heterogeneity of EC 002.

The chronology and formation of chondrules remains mysterious, but newly-found evidence indicates that chondrule formation occurred within the first 0.7 Myr after the first solids in the Solar System formed. Chondrule formation continued until at least 3.9 Ma after CAI formation in the outer Solar System, likely recycling previously formed chondrules until they were accreted to their parent bodies or the Solar nebula had dissipated.

6.5 Future work

Further chronological studies of both achondrites and chondrules may provide constraints on the distribution of ^{26}Al in the protoplanetary disk. In particular, chondrules in carbonaceous chondrites such as CR chondrites are prime candidates for the application of both the Pb-Pb and ^{26}Al - ^{26}Mg chronometers. Previously dated CR chondrules show a similar range of Pb-Pb ages to OC chondrules, but have yet to be dated by *in situ* ^{26}Al - ^{26}Mg analysis on the same samples. Such results would provide a direct comparison to the results of Bollard et al. (2019) and would either refute or confirm their interpretation of ^{26}Al heterogeneity between NC and CC chondrules, as well as the Pb-Pb ages dating the last crystallization of chondrules.

The number of angrites found has increased in recent years, and with them so has the diversity of samples of the angrite parent body. Chronologic, isotopic and geochemical investigations of these new samples will advance our understanding of the nature of the parent asteroid and its differentiation history.

References

- Abouchami W., Galer S. J. G. and Hofmann A. W. (2000) High precision lead isotope systematics of lavas from the Hawaiian Scientific Drilling Project. *Chem. Geol.* **169**, 187–209.
- Adcock C. T., Tschauer O., Hausrath E. M., Udry A., Luo S. N., Cai Y., Ren M., Lanzirotti A., Newville M., Kunz M. and Lin C. (2017) Shock-transformation of whitlockite to merrillite and the implications for meteoritic phosphate. *Nat. Commun.* **8**, 14667.
- Agee C. B., Miley H. . M., Ziegler K. and Spilde M. N. (2015) Northwest Africa 8535: Unique dunitic angrite. In *Lunar and Planetary Science Conference XLVI* p. 2681.
- Alexander C. M. O., Grossman J. N., Ebel D. S. and Ciesla F. J. (2008) The Formation Conditions of Chondrules and Chondrites. *Science (80-.)*. **320**, 1617–1619.
- Almeida N. V., Downes H., Smith C. L., Greenwood R. C., Hellmann J. L., Kleine T., Franchi I. A. and Russell S. S. (2017) Igneous Inclusions in the Barwell L6 Chondrite. In *80th Annual Meeting of the Meteoritical Society*, p. 6116.
- Amelin Y. (2008a) The U-Pb systematics of angrite Sahara 99555. *Geochim. Cosmochim. Acta* **72**, 4874–4885.
- Amelin Y. (2008b) U-Pb ages of angrites. *Geochim. Cosmochim. Acta* **72**, 221–232.
- Amelin Y. (2000) U-Th-Pb Systematics of Chondritic Phosphates: Implications for Chronology and Origin of Excess Pb. In *Lunar and Planetary Science* p. 1.
- Amelin Y., Ghosh A. and Rotenberg E. (2005) Unraveling the evolution of chondrite parent asteroids by precise U-Pb dating and thermal modeling. *Geochim. Cosmochim. Acta* **69**, 505–518.
- Amelin Y. and Irving A. J. (2007) Seven million years of evolution on the angrite parent body from Pb-isotopic data. *Chronol. Meteorites Early Sol. Syst.*, 20–21.
- Amelin Y., Kaltenbach A., Iizuka T., Stirling C. H., Ireland T. R., Petaev M. and Jacobsen S. B. (2010) U-Pb chronology of the Solar System's oldest solids with variable $^{238}\text{U}/^{235}\text{U}$. *Earth Planet. Sci. Lett.* **300**, 343–350.
- Amelin Y., Koefoed P., Iizuka T., Fernandes V. A., Huyskens M. H., Yin Q. and Irving A. J. (2019) U-Pb, Rb-Sr and Ar-Ar systematics of the ungrouped achondrites Northwest Africa 6704 and Northwest Africa 6693. *Geochim. Cosmochim. Acta*

245, 628–642.

- Amelin Y., Krot A. N., Hutcheon I. D. and Ulyanov A. A. (2002) Lead Isotopic Ages of Chondrules and Calcium-Aluminum – Rich Inclusions. **297**, 4–8.
- An Y. and Huang F. (2014) A review of Mg isotope analytical methods by MC-ICP-MS. *J. Earth Sci.* **25**, 822–840.
- Ancellin M. A., Vlastélic I., Samaniego P., Nauret F., Gannoun A. and Hidalgo S. (2019) Up to 1% Pb isotope disequilibrium between minerals hosted in dacites from the Guagua Pichincha volcano, Ecuador: Implication for tracing the source and crustal history of continental arc magmas. *Chem. Geol.* **525**, 177–189.
- Anders E. and Grevesse N. (1989) Abundances of the elements: Meteoric and solar. *Geochim. Cosmochim. Acta* **53**, 197–214.
- Andrews S. M. (2020) Observations of Protoplanetary Disk Structures. , 483–530.
- Asphaug E., Jutzi M. and Movshovitz N. (2011) Chondrule formation during planetesimal accretion. *Earth Planet. Sci. Lett.* **308**, 369–379.
- Baghdadi B., Jambon A. and Barrat J. (2015) Metamorphic angrite Northwest Africa 3164/5167 compared to magmatic angrites. *Geochim. Cosmochim. Acta* **168**, 1–21.
- Barrat J. A., Zanda B., Moynier F., Bollinger C., Liorzou C. and Bayon G. (2012) Geochemistry of CI chondrites: Major and trace elements, and Cu and Zn Isotopes. *Geochim. Cosmochim. Acta* **83**, 79–92.
- Barrat J., Chaussidon M., Yamaguchi A., Beck P., Villeneuve J., Byrne D. J., Broadley M. W. and Marty B. (2021) A 4,565-My-old andesite from an extinct chondritic protoplanet. *Proc. Natl. Acad. Sci.* **118**, e2026129118.
- Bermingham K. R., Worsham E. A. and Walker R. J. (2018) New insights into Mo and Ru isotope variation in the nebula and terrestrial planet accretionary genetics. *Earth Planet. Sci. Lett.* **487**, 221–229.
- Birnstiel T., Fang M. and Johansen A. (2016) Dust Evolution and the Formation of Planetesimals. *Space Sci. Rev.* **205**, 41–75.
- Bischoff A., Barrat J. A., Berndt J., Borovicka J., Burkhardt C., Busemann H., Hakenmüller J., Heinlein D., Hertzog J., Kaiser J., Maden C., Meier M. M. M., Morino P., Pack A., Patzek M., Reitze M. P., Rüfenacht M., Schmitt-Kopplin P., Schönbacher M., Spurný P., Weber I., Wimmer K. and Zirkund T. (2019) The

- Renchen L5-6 chondrite breccia – The first confirmed meteorite fall from Baden-Württemberg (Germany). *Chemie der Erde* **79**, 125525.
- Bizzarro M., Baker J. A. and Haack H. (2004) Mg isotope evidence for contemporaneous formation of chondrules and refractory inclusions. *Nature* **431**, 275–278.
- Blackburn T., Alexander C. M. O. D., Carlson R. and Elkins-Tanton L. T. (2017) The accretion and impact history of the ordinary chondrite parent bodies. *Geochim. Cosmochim. Acta* **200**, 201–217.
- Bland P. A., Alard O., Benedix G. K., Kearsley A. T., Menzies O. N., Watt L. E. and Rogers N. W. (2005) Volatile fractionation in the early solar system and chondrule - matrix complementarity. **102**.
- Blichert-Toft J., Göpel C., Chaussidon M. and Albarède F. (2020) Th/U variability in Allende chondrules. *Geochim. Cosmochim. Acta*.
- Blichert-Toft J., Zanda B., Ebel D. S. and Albarède F. (2010) The Solar System primordial lead. *Earth Planet. Sci. Lett.* **300**, 152–163.
- Bollard J., Connelly J. N. and Bizzarro M. (2015) Pb-Pb dating of individual chondrules from the CB_a chondrite Gujba: Assessment of the impact plume formation model. *Meteorit. Planet. Sci.* **50**, 1197–1216.
- Bollard J., Connelly J. N., Whitehouse M. J., Pringle E. A., Bonal L., Jørgensen J. K., Nordlund Å., Moynier F. and Bizzarro M. (2017) Early formation of planetary building blocks inferred from Pb isotopic ages of chondrules. *Sci. Adv.* **3**.
- Bollard J., Kawasaki N., Sakamoto N., Olsen M., Itoh S., Larsen K., Wielandt D., Schiller M., Connelly J. N., Yurimoto H. and Bizzarro M. (2019) Combined U-corrected Pb-Pb dating and ²⁶Al-²⁶Mg systematics of individual chondrules – Evidence for a reduced initial abundance of ²⁶Al amongst inner Solar System chondrules. *Geochim. Cosmochim. Acta* **260**, 62–83.
- Bouvier A., Blichert-Toft J., Moynier F., Vervoort J. D. and Albarède F. (2007) Pb-Pb dating constraints on the accretion and cooling history of chondrites. *Geochim. Cosmochim. Acta* **71**, 1583–1604.
- Bouvier A., Brennecka G. A., Sanborn M. E. and Wadhwa M. (2011a) U-Pb Chronology of a Newly Discovered Angrite. In *Lunar and Planetary Science Conference XLII* p. 2747.

- Bouvier A., Brennecka G. A. and Wadhwa M. (2011b) Absolute chronology of the first solids in the Solar System. In *Formation of the First Solids in the Solar System* p. 9054.
- Bouvier A., Gattacceca J., Grossman J. and Metzler K. (2017) The meteoritical bulletin, No. 105. *Meteorit. Planet. Sci.* **52**, 2411.
- Bouvier Audrey, Spivak-Birndorf L. J., Brennecka G. A. and Wadhwa M. (2011) New constraints on early Solar System chronology from Al-Mg and U-Pb isotope systematics in the unique basaltic achondrite Northwest Africa 2976. *Geochim. Cosmochim. Acta* **75**, 5310–5323.
- Bouvier A. and Wadhwa M. (2010) The age of the Solar System redefined by the oldest Pb – Pb age of a meteoritic inclusion. *Nat. Geosci.* **3**, 637–641.
- Bouvier A., Wadhwa M., Simon S. B. and Grossman L. (2013) Magnesium isotopic fractionation in chondrules from the Murchison and Murray CM2 carbonaceous chondrites. *Meteorit. Planet. Sci.* **48**, 339–353.
- Brasser R. and Mojzsis S. J. (2020) The partitioning of the inner and outer Solar System by a structured protoplanetary disk. *Nat. Astron.* **4**, 492–499.
- Brennecka Gregory A., Borg L. E., Hutcheon I. D., Sharp M. A. and Anbar A. D. (2010) Natural variations in uranium isotope ratios of uranium ore concentrates: Understanding the $^{238}\text{U}/^{235}\text{U}$ fractionation mechanism. *Earth Planet. Sci. Lett.* **291**, 228–233.
- Brennecka G. A., Budde G. and Kleine T. (2015) Uranium isotopic composition and absolute ages of Allende chondrules. *Meteorit. Planet. Sci.* **50**, 1995–2002.
- Brennecka G. A., Burkhardt C., Budde G., Kruijjer T. S., Nimmo F. and Kleine T. (2020) Astronomical context of Solar System formation from molybdenum isotopes in meteorite inclusions. *Science* **370**, 837–840.
- Brennecka G. A. and Wadhwa M. (2012) Uranium isotope compositions of the basaltic angrite meteorites and the chronological implications for the early Solar System. *Proc. Natl. Acad. Sci. U. S. A.* **109**, 9299–9303.
- Brennecka G. A., Weyer S., Wadhwa M., Janney P. E., Zipfel J. and Anbar A. D. (2010) $^{238}\text{U}/^{235}\text{U}$ variations in meteorites: Extant ^{247}Cm and implications for Pb-Pb Dating. *Science (80-.)*. **327**, 449–451.

- Bridges J. C. and Hutchison R. (1997) A survey of clasts and large chondrules in ordinary chondrites. *Meteorit. Planet. Sci.* **32**, 389–394.
- Budde G., Burkhardt C., Brennecka G. A., Fischer-Gödde M., Kruijer T. S. and Kleine T. (2016) Molybdenum isotopic evidence for the origin of chondrules and a distinct genetic heritage of carbonaceous and non-carbonaceous meteorites. *Earth Planet. Sci. Lett.* **454**, 293–303.
- Budde G., Kruijer T. S. and Kleine T. (2018) Hf-W chronology of CR chondrites: Implications for the timescales of chondrule formation and the distribution of ^{26}Al in the solar nebula. *Geochim. Cosmochim. Acta* **222**, 284–304.
- Burkhardt C., Dauphas N., Hans U., Bourdon B. and Kleine T. (2019) Elemental and isotopic variability in solar system materials by mixing and processing of primordial disk reservoirs. *Geochim. Cosmochim. Acta* **261**, 145–170.
- Burkhardt C., Kleine T., Oberli F., Pack A., Bourdon B. and Wieler R. (2011) Molybdenum isotope anomalies in meteorites: Constraints on solar nebula evolution and origin of the Earth. *Earth Planet. Sci. Lett.* **312**, 390–400.
- Catanzaro E. J., Murphy T. J., Garner E. L. and Shields W. R. (1966) Absolute Isotopic Abundance Ratios and Atomic Weight of Magnesium. *J. Res. Natl. Bur. Stand. Sect. A, Phys. Chem.* **70A**, 453–458.
- Catanzaro E. J., Murphy T. J., Shields W. R. and Garner E. L. (1968) Absolute isotopic abundance ratios of common, equal-atom, and radiogenic lead isotopic standards. *J. Res. Natl. Bur. Stand. - A Phys. Chem.* **72A**, 261.
- Chen H. W., Claydon J. L., Elliott T., Coath C. D., Lai Y. J. and Russell S. S. (2018) Chronology of formation of early solar system solids from bulk Mg isotope analyses of CV3 chondrules. *Geochim. Cosmochim. Acta* **227**, 19–37.
- Chen J. H., Papanastassiou D. A. and Wasserburg G. J. (2010) Ruthenium endemic isotope effects in chondrites and differentiated meteorites. *Geochim. Cosmochim. Acta* **74**, 3851–3862.
- Clayton R. N., Mayeda T. K., Goswami J. . and Olsen E. J. (1991) Oxygen isotope studies of ordinary chondrites. *Geochim. Cosmochim. Acta* **55**, 2317–2337.
- Clayton R. N., Onuma N. and Mayeda T. K. (1976) A classification of meteorites based on oxygen isotopes. *Earth Planet. Sci. Lett.* **30**, 10–18.

- Connelly J. N., Bizzarro M., Krot A. N., Nordlund Å., Wielandt D. and Ivanova M. A. (2012) The absolute chronology and thermal processing of solids in the solar protoplanetary disk. *Science (80-.)*. **338**, 651–655.
- Connelly J. N., Bizzarro M., Thrane K. and Baker J. A. (2008) The Pb-Pb age of Angrite SAH99555 revisited. *Geochim. Cosmochim. Acta* **72**, 4813–4824.
- Connelly J. N., Bollard J. and Bizzarro M. (2017) Pb–Pb chronometry and the early Solar System. *Geochim. Cosmochim. Acta* **201**, 345–363.
- Connolly H. C., Desch S. J., Ash R. D. and Jones R. H. (2006) Transient heating events in the protoplanetary nebula. In *Meteorites and the early solar system II* this volume. Univ. of Arizona, Tucson. pp. 383–397.
- Connolly Jr. H. C. and Love S. G. (1998) The Formation of Chondrules: Petrologic Tests of the Shock Wave Model. *Science (80-.)*. **280**, 62–67.
- Crowther S. A., Filtner M. J., Jones R. H. and Gilmour J. D. (2018) Old formation ages of igneous clasts on the L chondrite parent body reflect an early generation of planetesimals or chondrule formation. *Earth Planet. Sci. Lett.* **481**, 372–386.
- Crowther S. A., Mohapatra R. K., Turner G., Blagburn D. J., Kehm K. and Gilmour J. D. (2008) Characteristics and applications of RELAX, an ultrasensitive resonance ionization mass spectrometer for xenon. *J. Anal. At. Spectrom.* **23**, 938–947.
- Dauphas N. and Pourmand A. (2011) Hf-W-Th evidence for rapid growth of Mars and its status as a planetary embryo. *Nature* **473**, 489–492.
- Davis A. M., Richter F. M., Mendybaev R. A., Janney P. E., Wadhwa M. and McKeegan K. D. (2015) Isotopic mass fractionation laws for magnesium and their effects on ²⁶Al–²⁶Mg systematics in solar system materials. *Geochim. Cosmochim. Acta* **158**, 245–261
- Desch S. J. and Connolly H. C. (2002) A model of the thermal processing of particles in solar nebula shocks: Application to the cooling rates of chondrules. *Meteorit. Planet. Sci.* **37**, 183–207.
- Desch S. J. and Cuzzi J. N. (2000) The Generation of Lightning in the Solar Nebula. *Icarus* **143**, 87–105.
- Desch S. J., Dunlap D. R., Williams C. D. and Torrano Z. A. (2021) Statistical chronometry: Anchors away! In *84th Annual Meeting of the Meteoritical Society*, p.

6231.

- Dunlap D. R., Koefoed P. K., Amelin Y., Wadhwa M. and Agee C. B. (2018) Pb-Pb Age of the Ungrouped Achondrite Northwest Africa 11119: Timing of Extraterrestrial Silica-Rich Volcanism. In *Lunar and Planetary Science Conference XLIX*, p. 2302.
- Duprat J. and Tatischeff V. (2007) Energetic Constraints on In Situ Production of Short-Lived Radionuclei in the Early Solar System. *Astrophys. J.* **671**, L69–L72.
- Ellinger C. I., Young P. A. and Desch S. J. (2010) Collateral effects on solar nebula oxygen isotopes due to injection of ^{26}Al by a nearby supernova. *Astrophys. J.* **725**, 1495–1506.
- Fischer-Gödde M. and Kleine T. (2017) Ruthenium isotopic evidence for an inner Solar System origin of the late veneer. *Nature* **541**, 525–527.
- Fischer-Gödde M., Schwander D. and Ott U. (2018) Ruthenium Isotope Composition of Allende Refractory Metal Nuggets. *Astron. J.* **156**, 176.
- Florin G., Luais B., Alard O. and Rushmer T. (2021) Condensation and evaporation processes during CB chondrite formation: Insights from Ge isotopes and highly siderophile element abundances. *Meteorit. Planet. Sci.* **56**, 1191–1211.
- Floss C., Crozaz G., McKay G., Mikouchi T. and Killgore M. (2003) Petrogenesis of angrites. *Geochim. Cosmochim. Acta* **67**, 4775–4789.
- Fujii T., Moynier F. and Albarède F. (2009) The nuclear field shift effect in chemical exchange reactions. *Chem. Geol.* **267**, 139–156.
- Gattacceca J., McCubbin F. M., Bouvier A. and Grossman J. (2020a) The Meteoritical Bulletin, No. 107. *Meteorit. Planet. Sci.* **55**, 460–462.
- Gattacceca J., McCubbin F. M., Bouvier A. and Grossman J. N. (2020b) The meteoritical bulletin, No. 108. *Meteorit. Planet. Sci.* **55**, 1146–1150.
- Gattacceca J., McCubbin F. M., Grossman J., Bouvier A., Bullock E., Chennaoui Aoudjehane H., Debaille V., D’Orazio M., Komatsu M., Miao B. and Schrader D. L. (2021) The Meteoritical Bulletin, No. 109. *Meteorit. Planet. Sci.* **56**, 1626–1630.
- Gerber S., Burkhardt C., Budde G., Metzler K. and Kleine T. (2017) Mixing and Transport of Dust in the Early Solar Nebula as Inferred from Titanium Isotope Variations among Chondrules. *Astrophys. J.* **841**, L17.
- Gilmour J. D. and Crowther S. A. (2017) The I-Xe chronometer and its constraints on the

- accretion and evolution of planetesimals. *Geochem. J.* **51**, 69–80.
- Gilmour J. D. and Filtness M. J. (2019) Dissipation of the Solar System's debris disk recorded in primitive meteorites. *Nat. Astron.* **3**, 326–331.
- Glavin D. P., Kubny A., Jagoutz E. and Lugmair G. W. (2004) Mn-Cr isotope systematics of the D'Orbigny angrite. *Meteorit. Planet. Sci.* **39**, 693–700.
- Goldmann A., Brennecka G., Noordmann J., Weyer S. and Wadhwa M. (2015) The uranium isotopic composition of the Earth and the Solar System. *Geochim. Cosmochim. Acta* **148**, 145–158.
- Goodrich C. A., Kita N. T., Yin Q., Sanborn M. E., Williams C. D., Nakashima D., Lane M. D. and Boyle S. (2017) Petrogenesis and provenance of ungrouped achondrite Northwest Africa 7325 from petrology, trace elements, oxygen, chromium and titanium isotopes, and mid-IR spectroscopy. *Geochim. Cosmochim. Acta* **203**, 381–403.
- Göpel C., Manhès G. and Allègre C. J. (1994) U-Pb systematics of phosphates from equilibrated ordinary chondrites. *Earth Planet. Sci. Lett.* **121**, 153–171.
- Goswami J. N. (2004) Short-lived nuclides in the early solar system: The stellar connection. *New Astron. Rev.* **48**, 125–132.
- Gou L.-F., Jin Z., Galy A., Sun H., Deng L. and Xu Y. (2019) Effects of cone combinations on accurate and precise Mg-isotopic determination using multi-collector inductively coupled plasma mass spectrometry. *Rapid Commun. Mass Spectrom.* **33**, 351–360.
- Gounelle M. and Meibom A. (2007) Cite Gounelle, Matthieu, and Anders Meibom. "The oxygen isotopic composition of the Sun as a test of the supernova origin of ^{26}Al and ^{41}Ca ." *Astrophys. J. Lett.* **664**, 123–125.
- Gounelle M., Shu F. H., Shang H., Glassgold A. E., Rehm K. E. and Lee T. (2005) The Irradiation Origin of Beryllium Radioisotopes and Other Short-lived Radionuclides. **3**, 1163–1170.
- Greenwood R. C., Burbine T. H., Miller M. F. and Franchi I. A. (2017) Melting and differentiation of early-formed asteroids: The perspective from high precision oxygen isotope studies. *Chemie der Erde - Geochemistry* **77**, 1–43.
- Gregory T., Luu T.-H., Coath C. D., Russell S. S. and Elliott T. (2020) Primordial

- formation of major silicates in a protoplanetary disc with homogeneous $^{26}\text{Al}/^{27}\text{Al}$. *Sci. Adv.* **6**, eaay9626.
- Halliday A. N. and Lee D.-C. (1999) Tungsten isotopes and the early development of the Earth and Moon. *Geochim. Cosmochim. Acta* **63**, 4157–4179.
- Hellmann J. L., Kruijer T. S., Van Orman J. A., Metzler K. and Kleine T. (2019) Hf-W chronology of ordinary chondrites. *Geochim. Cosmochim. Acta* **258**, 290–309.
- Hewins R. H. and Connolly H. C. J. (1996) Peak temperatures of flash-melted chondrules. In *Chondrules and the Protoplanetary Disk* pp. 197–204.
- Hezel D. C. and Palme H. (2010) The chemical relationship between chondrules and matrix and the chondrule matrix complementarity. *Earth Planet. Sci. Lett.* **294**, 85–93.
- Humayun M., Irving A. J. and Kuehner S. M. (2007) Siderophile elements in metal from metal-rich angrite NWA 2999. In *Lunar and Planetary Science Conference XXXVIII*, p. 1221.
- Huss G. R., Rubin A. E. and Grossman J. N. (2006) Thermal Metamorphism in Chondrites. *Meteorites early Sol. Syst. II*, 567–586.
- Huyskens M. H., Amelin Y. and Yin Q.-Z. (2020) Uranium Isotopic Composition of Angrites. In *Lunar and Planetary Science Conference LI*, p. 1781.
- Huyskens M. H., Sanborn M. E., Yin Q. Z. and Agee C. B. (2018) Silica-Rich Magmatism in the Early Solar System: U-Pb and Al-Mg Chronology and Cr Isotopes of Ungrouped Achondrite Northwest Africa 11119. In *Lunar and Planetary Science Conference* p. 2311.
- Hyde B. C., Tait K. T., Moser D. E., Rumble D. and Thompson M. S. (2019) Accretionary mixing of a eucrite impactor and the regolith of the L chondrite parent body. *Meteorit. Planet. Sci.* **16**, 1–16.
- Izidoro A., Bitsch B. and Dasgupta R. (2021) The Effect of a Strong Pressure Bump in the Sun's Natal Disk: Terrestrial Planet Formation via Planetesimal Accretion Rather than Pebble Accretion. *Astrophys. J.* **915**, 62.
- Jacobsen B., Yin Q. zhu, Moynier F., Amelin Y., Krot A. N., Nagashima K., Hutcheon I. D. and Palme H. (2008) ^{26}Al - ^{26}Mg and ^{207}Pb - ^{206}Pb systematics of Allende CAIs: Canonical solar initial $^{26}\text{Al}/^{27}\text{Al}$ ratio reinstated. *Earth Planet. Sci. Lett.* **272**, 353–

364.

- Jaffey A. H., Flynn K. F., Glendenin L. E., Bentley W. C. and Essling A. M. (1971) Precision Measurement of Half-Lives and Specific Activities of ^{235}U and ^{238}U . *Phys. Rev. C* **4**, 1889–1906.
- Johansen A. and Lambrechts M. (2017) Forming Planets via Pebble Accretion. *Annu. Rev. Earth Planet. Sci.* **45**, 359–387.
- Johansen A., Low M. M. Mac, Lacerda P. and Bizzarro M. (2015) Growth of asteroids, planetary embryos, and Kuiper belt objects by chondrule accretion. *Sci. Adv.* **1**.
- Johansen A., Ronnet T., Bizzarro M., Schiller M., Lambrechts M., Nordlund A. and Lammer H. (2021) A pebble accretion model for the formation of the terrestrial planets in the solar system. *Sci. Adv.* **7**, 1–14.
- Jones R. H. and Danielson L. R. (1997) A chondrule origin for dusty relict olivine in unequilibrated chondrites. *Meteorit. Planet. Sci.* **32**, 753–760.
- Kawasaki N., Park C., Sakamoto N., Young S., Na H., Kuroda M. and Yurimoto H. (2019) Variations in initial $^{26}\text{Al}/^{27}\text{Al}$ ratios among fluffy Type A Ca – Al-rich inclusions from reduced CV chondrites. *Earth Planet. Sci. Lett.* **511**, 25–35.
- Kawasaki N., Wada S., Park C., Sakamoto N. and Yurimoto H. (2020) Variations in initial $^{26}\text{Al}/^{27}\text{Al}$ ratios among fine-grained Ca-Al-rich inclusions from reduced CV chondrites. *Geochim. Cosmochim. Acta* **279**, 1–15.
- Kebukawa Y., Ito M., Zolensky M. E., Greenwood R. C., Rahman Z., Suga H., Nakato A., Chan Q. H. S., Fries M., Takeichi Y., Takahashi Y., Mase K. and Kobayashi K. (2019) A novel organic-rich meteoritic clast from the outer solar system. *Sci. Rep.* **9**, 1–8.
- Keil K. (2012) Angrites, a small but diverse suite of ancient, silica-undersaturated volcanic-plutonic mafic meteorites, and the history of their parent asteroid. *Chemie der Erde* **72**, 191–218.
- Kita N. T., Nagahara H., Togashi S. and Morishita Y. (2000) A short duration of chondrule formation in the solar nebula: Evidence from ^{26}Al in Semarkona ferromagnesian chondrules. *Geochim. Cosmochim. Acta* **64**, 3913–3922.
- Kita N. T., Yin Q. Z., Macpherson G. J., Ushikubo T., Jacobsen B., Nagashima K., Kurahashi E., Krot A. N. and Jacobsen S. B. (2013) ^{26}Al - ^{26}Mg isotope systematics

- of the first solids in the early solar system. *Meteorit. Planet. Sci.* **48**, 1383–1400.
- Kleine T., Hans U., Irving A. J. and Bourdon B. (2012) Chronology of the angrite parent body and implications for core formation in protoplanets. *Geochim. Cosmochim. Acta* **84**, 186–203.
- Koefoed P., Amelin Y., Yin Q. Z., Wimpenny J., Sanborn M. E., Iizuka T. and Irving A. J. (2016) U-Pb and Al-Mg systematics of the ungrouped achondrite Northwest Africa 7325. *Geochim. Cosmochim. Acta* **183**, 31–45.
- Koike M., Sano Y., Takahata N., Iizuka T., Ono H. and Mikouchi T. (2020) Evidence for early asteroidal collisions prior to 4.15 Ga from basaltic eucrite phosphate U–Pb chronology. *Earth Planet. Sci. Lett.* **549**, 116497.
- Van Kooten E. M. M. E., Wielandt D., Schiller M., Nagashima K., Thomen A., Larsen K. K., Olsen M. B., Nordlund Å., Krot A. N. and Bizzarro M. (2016) Isotopic evidence for primordial molecular cloud material in metal-rich carbonaceous chondrites. *Proc. Natl. Acad. Sci.* **113**, 2011–2016. Available at:
- Kratter K. M. and Lodato G. (2016) Gravitational Instabilities in Circumstellar Disks.
- Krestianinov E., Datta C. and Amelin Y. (2021) Uranium Isotopic Composition of Volcanic Angrites Northwest Africa 12320, Northwest Africa 12004, and Northwest Africa 12774 and Ungrouped Achondrite Erg Chech 002. *LPI Contrib.* **2609**, 6059.
- Krot A. N., Amelin Y., Cassen P. and Meibom A. (2005) Young chondrules in CB chondrites from a giant impact in the early Solar System. **436**, 989–992.
- Krot A. N., Petaev M. I. and Nagashima K. (2021) Infiltration metasomatism of the Allende coarse-grained calcium-aluminum-rich inclusions. *Prog. Earth Planet. Sci.* **8**, 61.
- Krot A. N., Petaev M. I., Scott E. R. D., Choi B.-G., Zolensky M. E. and Keil K. (1998) Progressive alteration in CV3 chondrites: More evidence for asteroidal alteration. *Meteorit. Planet. Sci.* **33**, 1065–1085.
- Kruijjer T. S., Burkhardt C., Budde G. and Kleine T. (2017) Age of Jupiter inferred from the distinct genetics and formation times of meteorites. *Proc. Natl. Acad. Sci.* **114**, 201704461.
- Kruijjer T. S., Kleine T. and Borg L. E. (2020) The great isotopic dichotomy of the early Solar System. *Nat. Astron.* **4**, 32–40.

- Kruijer Thomas S., Kleine T., Fischer-Gödde M., Burkhardt C. and Wieler R. (2014) Nucleosynthetic W isotope anomalies and the Hf-W chronometry of Ca-Al-rich inclusions. *Earth Planet. Sci. Lett.* **403**, 317–327.
- Kruijer T. S., Touboul M., Fischer-Godde M., Bermingham K. R., Walker R. J. and Kleine T. (2014) Protracted core formation and rapid accretion of protoplanets. *Science (80-.)*. **344**, 1150–1154.
- Larsen K. K., Trinquier A., Paton C., Schiller M., Wielandt D., Ivanova M. A., Connelly J. N., Nordlund Å., Krot A. N. and Bizzarro M. (2011) Evidence for Magnesium Isotope Heterogeneity in the Solar Protoplanetary Disk. *Astrophys. J.* **735**, L37.
- Lee T., Papanastassiou D. A. and Wasserburg G. J. (1976) Demonstration of Mg-26 excess in Allende and evidence for Al-26. *Geophys. Res. Lett.* **3**, 41–44.
- Lee T., Shu F. H., Shang H., Glassgold A. E. and Rehm K. E. (1998) Protostellar Cosmic Rays and Extinct Radioactivities in Meteorites. *Astrophys. J.* **506**, 898.
- Leya, I., and Masarik, J. (2009). Cosmogenic nuclides in stony meteorites revisited. *Meteoritics & Planetary Science*, *44*(7), 1061-1086.
- Libourel G. and Krot A. N. (2007) Evidence for the presence of planetesimal material among the precursors of magnesian chondrules of nebular origin. *Earth Planet. Sci. Lett.* **254**, 1–8.
- Libourel G., Krot A. N. and Tissandier L. (2006) Role of gas-melt interaction during chondrule formation. *Earth Planet. Sci. Lett.* **251**, 232–240.
- Lichtenberg T., Golabek G. J., Dullemond C. P., Schönbächler M., Gerya T. V. and Meyer M. R. (2018) Impact splash chondrule formation during planetesimal recycling. *Icarus* **302**, 27–43.
- Liu B., Ormel C. W. and Johansen A. (2019) Growth after the streaming instability. *Astron. Astrophys.* **624**, A114.
- Lodders K. (2003) Solar System Abundances and Condensation Temperatures of the Elements. *Astrophys. J.* **591**, 1220–1247.
- Lodders K. and Fegley B. (1998) *The Planetary Scientist's Companion.*, Oxford University Press.
- Ludwig K. R. (2008) Isoplot version 4.15: a geochronological toolkit for microsoft Excel. *Berkeley Geochronol. Center, Spec. Publ.*, 247–270.

- Luu T.-H., Hin R. C., Coath C. D. and Elliott T. (2019) Bulk chondrite variability in mass independent magnesium isotope compositions – Implications for initial solar system $^{26}\text{Al}/^{27}\text{Al}$ and the timing of terrestrial accretion. *Earth Planet. Sci. Lett.* **522**, 166–175.
- Luu T. H., Young E. D., Gounelle M. and Chaussidon M. (2015) Short time interval for condensation of high-temperature silicates in the solar accretion disk. *Proc. Natl. Acad. Sci. U. S. A.* **112**, 1298–1303.
- Lyons J. R. and Young E. D. (2005) CO self-shielding as the origin of oxygen isotope anomalies in the early solar nebula. *Nature* **435**, 317–320.
- MacPherson G. J., Bullock E. S., Janney P. E., Kita N. T., Ushikubo T., Davis A. M., Wadhwa M. and Krot A. N. (2010) Early solar nebula condensates with canonical, not supracanonical, initial $^{26}\text{Al}/^{27}\text{Al}$ ratios. *Astrophys. J. Lett.* **711**, 117–121.
- MacPherson G. J., Bullock E. S., Tenner T. J., Nakashima D., Kita N. T., Ivanova M. A., Krot A. N., Petaev M. I. and Jacobsen S. B. (2017) High precision Al–Mg systematics of forsterite-bearing Type B CAIs from CV3 chondrites. *Geochim. Cosmochim. Acta* **201**, 65–82.
- Macpherson G. J., Davis A. M. and Zinner E. K. (1995) The distribution of aluminum-26 in the early Solar System - A reappraisal. *Meteoritics* **30**, 365–386.
- MacPherson G. J., Kita N. T., Ushikubo T., Bullock E. S. and Davis A. M. (2012) Well-resolved variations in the formation ages for Ca-Al-rich inclusions in the early Solar System. *Earth Planet. Sci. Lett.* **331–332**, 43–54.
- Mahan B., Moynier F., Siebert J., Gueguen B., Agranier A., Pringle E. A., Bollard J., Connelly J. N. and Bizzarro M. (2018) Volatile element evolution of chondrules through time. *Proc. Natl. Acad. Sci.*, 201807263.
- Marrocchi Y., Euverte R., Villeneuve J., Batanova V., Welsch B., Ferrière L. and Jacquet E. (2019) Formation of CV chondrules by recycling of amoeboid olivine aggregate-like precursors. *Geochim. Cosmochim. Acta* **247**, 121–141.
- McSween Jr H. Y. and Huss G. R. (2010) *Cosmochemistry.*, Cambridge University Press.
- Merle R., Amelin Y., Yin Q.-Z., Huyskens M. H., Sanborn M. E., Nagashima K., Yamashita K., Ireland T. R., Krot A. N. and Sieber M. J. (2020) Exploring the efficiency of stepwise dissolution in removal of stubborn non-radiogenic Pb in

- chondrule U-Pb dating. *Geochim. Cosmochim. Acta* **277**, 1–20.
- Metzler K., Bischoff A. and Stöffler D. (1992) Accretionary dust mantles in CM chondrites: Evidence for solar nebula processes. *Geochim. Cosmochim. Acta* **56**, 2873–2897.
- Miyamoto M., McKay D. S., McKay G. A. and Duke M. B. (1986) Chemical zoning and homogenization of olivines in ordinary chondrites and implications for thermal histories of chondrules. *J. Geophys. Res. Solid Earth* **91**, 12804–12816.
- Morris M. A., Boley A. C., Desch S. J. and Athanassiadou T. (2012) Chondrule formation in bow shocks around eccentric planetary embryos. *Astrophys. J.* **752**.
- Nanne J. A. M., Nimmo F., Cuzzi J. N. and Kleine T. (2019) Origin of the non-carbonaceous – carbonaceous meteorite dichotomy. *Earth Planet. Sci. Lett.* **511**, 44–54.
- Nicklas R., Day J., Gardner-Vandy K., Udry, A. (in review) Andesitic Magmatism on a Differentiated Asteroid. *Nature*.
- NuDat v3.0, National Nuclear Data Center (2021)
- Olsen M. B., Schiller M., Krot A. N. and Bizzarro M. (2013) Magnesium isotope evidence for single stage formation of CB chondrules by colliding planetesimals. *Astrophys. J. Lett.* **776**, 6–11.
- Olsen M. B., Wielandt D., Schiller M., Van Kooten E. M. M. E. and Bizzarro M. (2016) Magnesium and ^{54}Cr isotope compositions of carbonaceous chondrite chondrules – Insights into early disk processes. *Geochim. Cosmochim. Acta* **191**, 118–138.
- Van Orman J. A., Cherniak D. J. and Kita N. T. (2014) Magnesium diffusion in plagioclase: Dependence on composition, and implications for thermal resetting of the ^{26}Al - ^{26}Mg early solar system chronometer. *Earth Planet. Sci. Lett.* **385**, 79–88.
- Palme H., Lodders K. and Jones A. (2014) Solar System Abundances of the Elements. In *Treatise on Geochemistry* Elsevier. pp. 15–36.
- Pan L., Desch S. J., Scannapieco E. and Timmes F. X. (2012) Mixing of clumpy supernova ejecta into molecular clouds. *Astrophys. J.* **756**.
- Pape J., Mezger K., Bouvier A.-S. and Baumgartner L. P. (2019) Time and duration of chondrule formation: Constraints from ^{26}Al - ^{26}Mg ages of individual chondrules. *Geochim. Cosmochim. Acta* **244**, 416–436.

- Qin L., Alexander C. M. O. D., Carlson R. W., Horan M. F. and Yokoyama T. (2010) Contributors to chromium isotope variation of meteorites. *Geochim. Cosmochim. Acta* **74**, 1122–1145.
- Regelous M., Elliott T. and Coath C. D. (2008) Nickel isotope heterogeneity in the early Solar System. *Earth Planet. Sci. Lett.* **272**, 330–338.
- Render J., Brennecka G. A., Wang S.-J., Wasylenki L. E. and Kleine T. (2018) A Distinct Nucleosynthetic Heritage for Early Solar System Solids Recorded by Ni Isotope Signatures. *Astrophys. J.* **862**, 26.
- Riches A. J. V., Day J. M. D., Walker R. J., Simonetti A., Liu Y., Neal C. R. and Taylor L. A. (2012) Rhenium–osmium isotope and highly-siderophile-element abundance systematics of angrite meteorites. *Earth Planet. Sci. Lett.* **353–354**, 208–218.
- Richter S., Eykens R., Kühn H., Aregbe Y., Verbruggen A. and Weyer S. (2010) New average values for the $n(^{238}\text{U})/n(^{235}\text{U})$ isotope ratios of natural uranium standards. *Int. J. Mass Spectrom.* **295**, 94–97.
- Roebbert Y., Rosendahl C. D., Brown A., Schippers A., Bernier-Latmani R. and Weyer S. (2021) Uranium isotope fractionation during the anoxic mobilization of noncrystalline U(IV) by ligand complexation. *Environ. Sci. Technol.* **55**, 7959–7969.
- Le Roux L. J. and Glendenin L. E. (1963) Half-life of ^{232}Th . In *Proceedings of the National Meeting on Nuclear Energy, Pretoria, South Africa* p. 94.
- Rubin A. E., Rehfeldt A., Peterson E., Keil K. and Jarosewich E. (1983) Fragmental Breccias and the Collisional Evolution of Ordinary Chondrite Parent Bodies. *Meteorit. Planet. Sci.* **18**, 179–196.
- Russell S. S., Srinivasan G., Huss G. R., Wasserburg G. J. and MacPherson G. J. (1996) Evidence for widespread Al-26 in the solar nebula and constraints for nebula time scales. *Science (80-.)*. **273**, 757–762.
- Ruzicka A., Floss C. and Hutson M. (2008) Relict olivine grains , chondrule recycling , and implications for the chemical , thermal , and mechanical processing of nebular materials. *Geochim. Cosmochim. Acta* **72**, 5530–5557.
- Ruzicka A., Grossman J., Bouvier A. and Agee C. B. (2017) The meteoritical bulletin, No. 103. *Meteorit. Planet. Sci.* **52**, 1014.
- Ruzicka A., Grossman J., Bouvier A., Herd C. D. K. and Agee C. B. (2015) The

- Meteoritical Bulletin, No. 102. *Meteorit. Planet. Sci.* **50**, 1662–1662.
- Ruzicka A., Hiyagon H., Hutson M. and Floss C. (2007) Relict olivine, chondrule recycling, and the evolution of nebular oxygen reservoirs. *Earth Planet. Sci. Lett.* **257**, 274–289.
- Ruzicka A. M., Greenwood R. C., Armstrong K., Schepker K. L. and Franchi I. A. (2019) Petrology and oxygen isotopic composition of large igneous inclusions in ordinary chondrites: Early solar system igneous processes and oxygen reservoirs. *Geochim. Cosmochim. Acta*.
- Ruzicka A. M., Hellmann J. L. and Kleine T. (2018) Hf-W Chronology of Large Igneous Inclusions from Ordinary Chondrites. In *LPSC XLIX*.
- Ruzicka A. M., Hutson M., Floss C. and Hildebrand A. (2012) Large silica-rich igneous-textured inclusions in the Buzzard Coulee chondrite: Condensates, differentiates, or impact melts? *Meteorit. Planet. Sci.* **47**, 1809–1829.
- Ruzicka A. M., Snyder G. A. and Taylor L. A. (2000) Geochemical and isotopic evidence bearing on the origin of large, igneous-textured inclusions in ordinary chondrites. *Antarct. Meteor. Res.* **13**, 19–38.
- Ruzicka A. M., Snyder G. A. and Taylor L. A. (1998) Mega-chondrules and large igneous-textured clasts in Julesberg (L3) and other ordinary chondrites: Vapor-fractionation, shock-melting, and chondrule formation. *Geochim. Cosmochim. Acta* **62**, 1419–1442.
- Salmeron R. and Ireland T. R. (2012) Formation of chondrules in magnetic winds blowing through the proto-asteroid belt. *Earth Planet. Sci. Lett.* **327–328**, 61–67.
- Sanborn M. E., Carlson R. W. and Wadhwa M. (2015) $^{147,146}\text{Sm}$ - $^{143,142}\text{Nd}$, ^{176}Lu - ^{176}Hf , and ^{87}Rb - ^{87}Sr systematics in the angrites: Implications for chronology and processes on the angrite parent body. *Geochim. Cosmochim. Acta* **171**, 80–99.
- Sanborn M. E. and Wadhwa M. (2021) Trace element geochemistry of coarse-grained angrites from Northwest Africa: Implications for their petrogenesis on the angrite parent body. *Meteorit. Planet. Sci.* **56**, 482–499.
- Sanborn M. E., Wimpenny J., Williams C. D., Yamakawa A., Amelin Y., Irving A. J. and Yin Q. (2019) Carbonaceous achondrites Northwest Africa 6704/6693: Milestones for early Solar System chronology and genealogy. *Geochim. Cosmochim. Acta* **245**,

577–596.

- Santos, Alison R.. "New Insights into the Martian Crust and Angrite Parent Body Through Meteorites." (2016). https://digitalrepository.unm.edu/eps_etds/193
- Santos A. R., Agee C. B., Bell A. S. and Shearer C. K. (2017a) Northwest Africa 10463: A New Angrite Meteorite. In *80th Annual Meeting of the Meteoritical Society*, p. 6313.
- Santos A. R., Agee C. B., Shearer C. K., Bell A. S., Burger P. V. and McCubbin F. M. (2017b) Northwest Africa 8535: sampling a new portion of the angrite parent body. In *Lunar and Planetary Science Conference XLVIII*, p. 2266.
- Santos A. R., Agee C. B., Shearer C. K. and McCubbin F. M. (2016) Northwest Africa 8535 and Northwest Africa 10463: New Insights into the Angrite Parent Body. In *Lunar and Planetary Science Conference XLVII* pp. 2560.
- Schiller M., Baker J. A. and Bizzarro M. (2010a) ^{26}Al - ^{26}Mg dating of asteroidal magmatism in the young Solar System. *Geochim. Cosmochim. Acta* **74**, 4844–4864.
- Schiller M., Bizzarro M. and Fernandes V. A. (2018) Isotopic evolution of the protoplanetary disk and the building blocks of Earth and the Moon. *Nature* **555**, 507–510.
- Schiller M., Connelly J. N., Glad A. C., Mikouchi T. and Bizzarro M. (2015a) Early accretion of protoplanets inferred from a reduced inner solar system ^{26}Al inventory. *Earth Planet. Sci. Lett.* **420**, 45–54.
- Schiller M., Handler M. R. and Baker J. A. (2010b) High-precision Mg isotopic systematics of bulk chondrites. *Earth Planet. Sci. Lett.* **297**, 165–173.
- Schiller M., Van Kooten E., Holst J. C., Olsen M. B. and Bizzarro M. (2014) Precise measurement of chromium isotopes by MC-ICPMS. *J. Anal. At. Spectrom.* **29**, 1406–1416.
- Schiller M., Paton C. and Bizzarro M. (2015b) Evidence for nucleosynthetic enrichment of the protosolar molecular cloud core by multiple supernova events. *Geochim. Cosmochim. Acta* **149**, 88–102.
- Van Schmus W. R. and Wood J. A. (1967) A chemical-petrologic classification for the chondritic meteorites. *Geochim. Cosmochim. Acta* **31**, 747–765.
- Schneider J. M., Burkhardt C., Marrocchi Y., Brennecke G. A. and Kleine T. (2020)

- Early evolution of the solar accretion disk inferred from Cr-Ti-O isotopes in individual chondrules. *Earth Planet. Sci. Lett.* **551**, 116585.
- Schrader D. L., Nagashima K., Krot A. N., Ogliore R. C., Yin Q. Z., Amelin Y., Stirling C. H. and Kaltenbach A. (2017) Distribution of ^{26}Al in the CR chondrite chondrule-forming region of the protoplanetary disk. *Geochim. Cosmochim. Acta* **201**, 275–302.
- Scott E. R. D. (2007) Chondrites and the Protoplanetary Disk. *Annu. Rev. Earth Planet. Sci.* **35**, 577–620.
- Sedaghatpour F. and Teng F. Z. (2016) Magnesium isotopic composition of achondrites. *Geochim. Cosmochim. Acta* **174**, 167–179.
- Segura-Cox D. M., Schmiedeke A., Pineda J. E., Stephens I. W., Fernández-López M., Looney L. W., Caselli P., Li Z., Mundy L. G., Kwon W. and Harris R. J. (2020) Four annular structures in a protostellar disk less than 500,000 years old. *Nature* **586**, 228–231.
- Shields W. R., Murphy T. J., Catanzaro E. J. and Garner E. L. (1966) Absolute isotopic abundance ratios and the atomic weight of a reference sample of chromium. *J. Res. Natl. Bur. Stand. Sect. A Phys. Chem.* **70A**, 193.
- Shu F. H., Shang H., Glassgold A. E. and Lee T. (1997) X-rays and fluctuating x-winds from protostars. *Science (80-.)*. **277**, 1475–1479.
- Spitzer F., Burkhardt C., Budde G., Kruijer T. S., Morbidelli A. and Kleine T. (2020) Isotopic Evolution of the Inner Solar System Inferred from Molybdenum Isotopes in Meteorites. *Astrophys. J.* **898**, L2.
- Spitzer F., Burkhardt C., Nimmo F. and Kleine T. (2021) Nucleosynthetic Pt isotope anomalies and the Hf-W chronology of core formation in inner and outer solar system planetesimals. *Earth Planet. Sci. Lett.* **576**, 117211.
- Spivak-Birndorf L., Wadhwa M. and Janney P. (2009) ^{26}Al - ^{26}Mg systematics in D'Orbigny and Sahara 99555 angrites: Implications for high-resolution chronology using extinct chronometers. *Geochim. Cosmochim. Acta* **73**, 5202–5211.
- Srinivasan P., Dunlap D. R., Agee C. B., Wadhwa M., Coleff D., Ziegler K., Zeigler R. and McCubbin F. M. (2018) Silica-rich volcanism in the early solar system dated at 4.565 Ga. *Nat. Commun.* **9**, 1–8.

- Stacey J. S. and Kramers J. D. (1975) Approximation of terrestrial lead isotope evolution by a two-stage model. *Earth Planet. Sci. Lett.* **26**, 207–221.
- Steele R. C. J., Elliott T., Coath C. D. and Regelous M. (2011) Confirmation of mass-independent Ni isotopic variability in iron meteorites. *Geochim. Cosmochim. Acta* **75**, 7906–7925.
- Tatsumoto M., Knight R. J. and Allegre C. J. (1973) Time Differences in the Formation of Meteorites as Determined from the Ratio of Lead-207 to Lead-206. *Science* (80-.). **180**, 1279–1283.
- Teng F. Z., Li W. Y., Ke S., Marty B., Dauphas N., Huang S., Wu F. Y. and Pourmand A. (2010) Magnesium isotopic composition of the Earth and chondrites. *Geochim. Cosmochim. Acta* **74**, 4150–4166.
- Tenner T. J., Nakashima D., Ushikubo T., Tomioka N., Kimura M., Weisberg M. K. and Kita N. T. (2019) Extended chondrule formation intervals in distinct physicochemical environments: Evidence from Al-Mg isotope systematics of CR chondrite chondrules with unaltered plagioclase. *Geochim. Cosmochim. Acta* **260**, 133–160.
- Tissot F. L. H., Dauphas N. and Grove T. L. (2017) Distinct $^{238}\text{U}/^{235}\text{U}$ ratios and REE patterns in plutonic and volcanic angrites: Geochronologic implications and evidence for U isotope fractionation during magmatic processes. *Geochim. Cosmochim. Acta* **213**, 593–617.
- Trinquier A., Birck J. and Allegre C. J. (2007) Widespread ^{54}Cr Heterogeneity in the Inner Solar System. *Astrophys. J.* **655**, 1179–1185.
- Trinquier A., Elliott T., Ulfbeck D., Coath C., Krot A. N. and Bizzarro M. (2009) Origin of Nucleosynthetic Isotope Heterogeneity in the Solar Protoplanetary Disk. *Science* (80-.). **324**, 374–376.
- Valdes M. C., Bermingham K. R., Huang S. and Simon J. I. (2021) Calcium isotope cosmochemistry. *Chem. Geol.* **581**, 120396.
- Ventura P., Carini R. and D’Antona F. (2011) A deep insight into the Mg-Al-Si nucleosynthesis in massive asymptotic giant branch and super-asymptotic giant branch stars. *Mon. Not. R. Astron. Soc.* **415**, 3865–3871.
- Vermeesch P. (2018) IsoplotR: A free and open toolbox for geochronology. *Geosci.*

- Front.* **9**, 1479–1493.
- Villa I. M., Bonardi M. L., De Bièvre P., Holden N. E. and Renne P. R. (2016) IUPAC-IUGS status report on the half-lives of ^{238}U , ^{235}U and ^{234}U . *Geochim. Cosmochim. Acta* **172**, 387–392.
- Villeneuve J., Chaussidon M. and Libourel G. (2009) Homogeneous distribution of ^{26}Al in the solar system from the mg isotopic composition of chondrules. *Science (80-.)*. **325**, 985–988.
- Villeneuve J., Libourel G. and Soulié C. (2015) Relationships between type I and type II chondrules: Implications on chondrule formation processes. *Geochim. Cosmochim. Acta* **160**, 277–305.
- Vogl J., Rosner M., Kasemann S. A., Kraft R., Meixner A., Noordmann J., Rabb S., Rienitz O., Schuessler J. A., Tatzel M. and Vocke R. D. (2020) Intercalibration of Mg Isotope Delta Scales and Realisation of SI Traceability for Mg Isotope Amount Ratios and Isotope Delta Values. *Geostand. Geoanalytical Res.* **44**, 439–457.
- Wadhwa M., Amelin Y., Bogdanovski O., Shukolyukov A., Lugmair G. W. and Janney P. (2009) Ancient relative and absolute ages for a basaltic meteorite: Implications for timescales of planetesimal accretion and differentiation. *Geochim. Cosmochim. Acta* **73**, 5189–5201.
- Wang H., Weiss B. P., Bai X. N., Downey B. G., Wang Jun, Wang Jiajun, Suavet C., Fu R. R. and Zucolotto M. E. (2017) Lifetime of the solar nebula constrained by meteorite paleomagnetism. *Science (80-.)*. **355**, 623–627.
- Warren P. H. (2011) Stable-isotopic anomalies and the accretionary assemblage of the Earth and Mars: A subordinate role for carbonaceous chondrites. *Earth Planet. Sci. Lett.* **311**, 93–100.
- Wasserburg G. J., Busso M., Gallino R. and Nollett K. M. (2006) Short-lived nuclei in the early Solar System: Possible AGB sources. *Nucl. Phys. A* **777**, 5–69.
- Wasserburg G. J., Karakas A. I. and Lugaro M. (2017) Intermediate-mass Asymptotic Giant Branch Stars and Sources of ^{26}Al , ^{60}Fe , ^{107}Pd , and ^{182}Hf in the Solar System. *Astrophys. J.* **836**, 126.
- Wasserburg G. J., Wimpenny J. and Yin Q. Z. (2012) Mg isotopic heterogeneity, Al-Mg isochrons, And canonical $^{26}\text{Al}/^{27}\text{Al}$ in the early solar system. *Meteorit. Planet. Sci.*

- 47, 1980–1997.
- Weisberg M. K., McCoy T. J. and Krot A. N. (2006) Systematics and Evaluation of Meteorite Classification. *Meteorites early Sol. Syst. II*, 19–52.
- Weiss B. P., Wang H., Sharp T. G., Gattacceca J., Shuster D. L., Downey B., Hu J., Fu R. R., Kuan A. T., Suavet C., Irving A. J., Wang Jun and Wang Jiajun (2017) A nonmagnetic differentiated early planetary body. *Earth Planet. Sci. Lett.* **468**, 119–132.
- Weyer S., Anbar A. D., Gerdes A., Gordon G. W., Algeo T. J. and Boyle E. A. (2008) Natural fractionation of $^{238}\text{U}/^{235}\text{U}$. *Geochim. Cosmochim. Acta* **72**, 345–359.
- Weyrauch M., Zipfel J. and Weyer S. (2019) Origin of metal from CB chondrites in an impact plume – A combined study of Fe and Ni isotope composition and trace element abundances. *Geochim. Cosmochim. Acta* **246**, 123–137.
- White W. M., Albarède F. and Télouk P. (2000) High-precision analysis of Pb isotope ratios by multi-collector ICP-MS. *Chem. Geol.* **167**, 257–270.
- Williams J. P. and Cieza L. A. (2011) Protoplanetary disks and their evolution. *Annu. Rev. Astron. Astrophys.* **49**, 67–117.
- Wimpenny J., Sanborn M. E., Koefoed P., Cooke I. R., Stirling C., Amelin Y. and Yin Q. (2019) Reassessing the origin and chronology of the unique achondrite Asuka 881394: Implications for distribution of ^{26}Al in the early Solar System. *Geochim. Cosmochim. Acta* **244**, 478–501.
- Worsham E. A., Burkhardt C., Budde G., Fischer-gödde M., Kruijer T. S. and Kleine T. (2019) Distinct evolution of the carbonaceous and non-carbonaceous reservoirs : Insights from Ru , Mo , and W isotopes. *Earth Planet. Sci. Lett.* **521**, 103–112.
- Yamashita K., Maruyama S., Yamakawa A. and Nakamura E. (2010) ^{53}Mn - ^{53}Cr Chronometry of CB chondrite: Evidence for uniform distribution of ^{53}Mn in the early solar system. *Astrophys. J.* **723**, 20–24.
- Youdin A. N. and Shu F. H. (2002) Planetesimal Formation by Gravitational Instability. *Astrophys. J.* **580**, 494–505.
- Young E. D. and Galy A. (2004) The isotope geochemistry and cosmochemistry of magnesium. *Rev. Mineral. Geochemistry* **55**, 197–230.

Appendices

Appendix 1: SIMS data points of chondrules and clasts

Sample	$\delta^{26}\text{Mg}^*$	2SE	$^{27}\text{Al}/^{24}\text{Mg}$	2SE
<i>NWA 8007-C1</i>				
O11	0.043	0.071	0.009	3.67×10^{-4}
O12	-0.029	0.089	0.056	0.002
O13	-0.050	0.076	0.075	0.003
Pl4	1.029	0.264	8.54	0.579
Pl5	0.213	0.216	2.72	0.039
Pl6	-0.143	0.335	13.32	0.543
O17	0.058	0.079	0.078	0.003
O18	-0.031	0.086	0.077	0.003
Px9	0.070	0.106	0.131	0.005
Px10	0.029	0.093	0.122	0.005
Px11	-0.075	0.090	0.195	0.008
Pl12	2.508	0.631	23.45	3.086
O113	-0.074	0.065	0.077	0.003
O114	0.076	0.089	0.090	0.004
Pl15	0.947	0.201	3.45	0.150
Pl16	1.099	0.435	25.24	0.404
<i>NWA 8276-C1</i>				
O11	0.108	0.040	0.001	3.37×10^{-5}
O12	-0.024	0.074	0.001	3.12×10^{-5}
O13	-0.124	0.058	0.001	2.49×10^{-5}
G14	0.696	0.208	3.59	0.162
G15	0.426	0.210	4.27	0.064
G16	0.057	0.191	4.34	0.062
G17	0.096	0.171	3.29	0.044
O18	0.012	0.064	0.001	1.98×10^{-5}
O19	0.025	0.077	0.015	0.001
O110	-0.007	0.064	0.000	0.000
G111	0.176	0.176	2.73	0.031
G112	0.084	0.170	2.97	0.046
G113	0.242	0.187	3.57	0.094
O114	-0.120	0.064	0.001	2.73×10^{-5}
O115	0.157	0.078	0.030	0.001
G116	0.541	0.158	3.38	0.078
G117	-0.220	0.183	3.15	0.090
G118	-0.350	0.152	4.68	0.199
G119	-0.050	0.062	0.022	0.001
<i>NWA 8276-C2</i>				
O11	0.010	0.068	0.002	8.72×10^{-5}
O12	-0.029	0.074	0.005	1.98×10^{-4}

OI3	0.081	0.071	0.002	9.72×10^{-5}
OI4	-0.105	0.072	0.003	1.20×10^{-4}
GI5	1.560	0.513	35.96	0.354
GI6	0.734	0.227	4.33	0.195
GI7	1.424	0.601	38.32	0.362
OI8	-0.010	0.071	0.002	9.80×10^{-5}
OI9	-0.012	0.061	0.002	8.39×10^{-5}
GI10	0.755	0.904	38.50	0.387
GI11	0.123	0.405	13.12	0.176
OI13	0.098	0.063	0.003	1.09×10^{-4}
OI14	-0.037	0.074	0.002	9.34×10^{-5}
OI15	0.062	0.061	0.002	8.36×10^{-5}
GI16	1.524	0.968	46.27	0.469
GI17	0.522	0.470	19.30	0.205
OI19	0.008	0.078	0.002	9.18×10^{-5}
OI20	0.351	0.314	11.06	0.108
OI21	-0.070	0.101	0.003	1.12×10^{-4}
<i>NWA 10854-C2</i>				
OI1	0.033	0.076	0.005	2.18×10^{-4}
OI2	0.013	0.065	0.000	1.43×10^{-5}
OI3	0.046	0.059	0.001	3.88×10^{-5}
GI4	0.805	0.535	19.22	0.495
OI5	-0.116	0.088	0.001	3.09×10^{-5}
GI6	1.083	1.028	24.55	0.441
Px7	-0.124	0.080	0.419	0.023
OI8	0.147	0.069	0.000	1.20×10^{-5}
<i>NWA 10854-C6</i>				
OI1	-0.062	0.052	0.001	3.51×10^{-5}
OI2	0.003	0.067	0.004	1.69×10^{-4}
OI3	0.032	0.084	0.022	0.001
GI4	0.605	0.414	10.48	0.105
GI5	4.30	1.88	86.85	1.073
GI6	6.18	1.63	93.38	0.898
OI7	-0.033	0.061	0.001	6.51×10^{-5}
OI8	0.028	0.064	0.041	0.002
GI9	2.56	0.86	62.98	0.636
GI10	2.01	1.18	75.80	0.717
GI11	0.329	0.248	4.687	0.053
OI12	0.006	0.060	0.015	0.001
OI13	0.122	0.074	0.019	0.001
GI14	4.59	1.23	83.26	0.796
GI15	1.47	0.39	21.38	1.172
OI17	-0.057	0.063	0.000	1.99×10^{-5}
OI18	-0.042	0.070	0.003	1.11×10^{-4}

NWA 11672-C1

OI1	-0.124	0.060	0.001	4.07×10^{-5}
Px2	0.124	0.078	0.066	0.003
GI3	0.229	0.141	2.30	0.022
GI4	1.04	1.40	96.86	0.96

NWA 12261-II

Px1	0.002	0.072	0.013	0.001
Px2	-0.024	0.065	0.012	4.99E-04
OI3	-0.018	0.078	3.75×10^{-4}	1.57×10^{-5}
OI4	0.058	0.107	4.91×10^{-4}	2.04×10^{-5}
OI5	-0.007	0.090	4.00×10^{-4}	1.67×10^{-5}
GI6	-0.398	0.592	17.62	0.28
GI7	-0.005	0.530	17.62	0.26
GI8	-0.233	0.569	16.70	0.26
Px9	-0.013	0.083	0.011	4.59×10^{-4}
Px10	0.489	0.431	20.23	0.28
GI11	-0.648	0.515	16.33	0.22
GI12	0.474	0.453	19.09	0.23
GI13	-0.087	0.466	14.76	0.22
GI14	0.314	0.253	8.608	0.123
OI15	0.030	0.088	3.39×10^{-4}	1.42×10^{-5}
OI16	-0.026	0.099	4.35×10^{-4}	1.81×10^{-5}

Pap-II

OI1	-0.007	0.050	2.13×10^{-4}	8.95×10^{-6}
OI2	0.014	0.061	1.27×10^{-4}	5.50×10^{-6}
GI5	0.343	0.182	2.14	0.05
GI6	0.226	0.123	1.34	0.01
OI8	0.041	0.048	0.001	2.67×10^{-5}
OI9	-0.071	0.060	0.094	0.004
OI11	-0.107	0.058	2.69×10^{-4}	1.17×10^{-5}
OI12	0.152	0.064	3.14×10^{-4}	1.32×10^{-5}
OI13	0.043	0.062	2.90×10^{-4}	1.23×10^{-5}
OI14	-0.067	0.041	0.001	4.01×10^{-5}
RC15	0.077	0.090	0.247	0.011
RC16	0.003	0.077	0.071	0.003
RC17	-0.094	0.068	0.026	0.001
RC18	-0.119	0.064	0.121	0.005
RC19	-0.025	0.071	0.035	0.002
OI20	0.086	0.074	0.001	4.51×10^{-5}
OI21	0.073	0.060	0.005	2.31×10^{-4}
GI22	0.299	0.162	2.26	0.05
GI24	0.399	0.261	2.29	0.02

Appendix 2: NWA 8276-C1 EPMA data from UNM [in wt%]

Sample	Na ₂ O	MgO	Al ₂ O ₃	SiO ₂	K ₂ O	CaO	TiO ₂	Cr ₂ O ₃	MnO	FeO	NiO	Total
Pock1A Px1	0.008	21.6	4.5	50.4	0.005	10.7	0.37	1.27	0.43	8.7	0.029	98.02
Pock1A Px2	0.039	15.8	4.2	48.9	0.014	14.9	0.70	0.97	0.82	11.7	0.033	98.00
Pock1A E1	4.222	0.7	29.9	49.3	0.231	11.9	0.09	0.00	0.02	1.2	0.483	98.09
Pock1A Px3	0.011	27.7	3.9	52.2	0.017	2.8	0.26	1.09	0.43	10.4	0.012	98.73
Pock1A Px4	0.027	15.8	1.9	48.5	0.010	5.4	0.86	0.52	1.02	22.8	0.025	96.89
Pock1A Px4	0.025	18.0	2.5	49.3	0.059	4.4	0.84	0.60	1.13	21.6	0.015	98.36
Pock1A E2	4.529	1.5	29.0	52.3	0.698	6.1	0.30	0.01	0.06	1.1	0.882	96.36
Pock1A E3LT	2.415	1.7	29.4	46.5	0.327	13.2	0.19	0.03	0.06	2.0	0.623	96.49
Pock1A E4	2.969	4.2	24.9	49.3	0.990	7.1	0.30	0.07	0.23	4.5	1.254	95.90
Pock1A E5	0.012	20.1	4.4	50.5	0.031	12.9	0.49	0.66	0.43	8.6	0.053	98.10
Pock1B cpx	0.004	23.4	3.4	51.5	0.022	6.9	0.30	0.62	0.55	11.0	0.000	97.76
Pock1B OL	0.022	46.3	0.0	38.9	0.031	0.2	0.01	0.30	0.30	12.6	0.025	98.73
Pock1B E5BLT	2.541	1.3	29.1	48.9	0.870	11.2	0.15	0.02	0.07	1.5	0.346	95.98
Pock3 Mes1LT	0.977	3.0	26.6	50.1	0.033	14.4	0.27	0.01	0.09	3.6	0.025	99.08
Pock3 Mes2LT	1.070	1.1	25.9	54.0	0.035	13.4	0.18	0.00	0.02	1.4	0.026	97.09
Pock3 Mes3LT	0.954	0.6	26.5	54.9	0.032	14.2	0.17	0.00	0.01	1.0	0.023	98.32
Pock3 Mes4LT	0.683	5.6	21.6	52.5	0.026	11.3	0.34	0.05	0.23	8.2	0.000	100.46
Pock4 Mes1LT	2.482	3.6	25.8	48.9	0.661	11.5	0.28	0.07	0.22	4.0	0.477	98.00
Pock4 Mes2LT	3.701	2.1	26.9	47.8	0.969	8.8	0.16	0.02	0.10	2.5	0.606	93.63
Pock4 Px1	0.216	21.5	1.6	50.9	0.063	4.0	0.67	0.39	1.06	18.1	0.108	98.56
Pock4 Px2	0.000	33.7	0.6	56.0	0.019	0.4	0.05	0.65	0.22	7.2	0.069	98.95
Pock4 Mes3LT	4.279	2.2	27.7	50.5	0.943	7.6	0.33	0.04	0.18	2.9	0.521	97.27
Pock5 Mes1Dk	3.372	0.5	27.2	48.9	1.672	6.5	0.15	0.00	0.02	1.3	0.418	90.00
Pock5 Mes1Rep	3.231	0.5	30.8	48.8	0.415	12.2	0.18	0.00	0.03	1.6	0.189	97.86
Pock5 Mes2	3.199	0.2	32.9	48.9	0.469	13.6	0.09	0.00	0.02	1.0	0.073	100.39
Pock5 Px1	0.316	12.0	4.6	49.5	0.065	10.4	1.16	0.36	1.33	20.7	0.030	100.44
Pock5 Px2	0.004	29.5	1.5	54.5	0.028	1.8	0.15	0.99	0.47	9.7	0.000	98.70

Pock5 Mes2	3.357	0.8	25.5	44.1	1.469	8.5	0.19	0.01	0.05	1.8	0.422	86.19
Pock5A Mes1	3.579	0.4	27.0	52.2	2.074	1.8	0.11	0.00	0.04	1.4	0.459	88.99
Pock5A Mes2	3.997	0.5	24.7	50.2	1.883	3.3	0.11	0.00	0.02	1.3	0.505	86.48
Pock5A Mes3	4.282	0.3	28.9	49.8	0.343	10.7	0.11	0.00	0.02	1.1	0.188	95.75
Pock5A MesPx	0.124	11.7	2.3	48.7	0.053	12.0	1.42	0.38	1.25	20.6	0.066	98.65
Pock5A MesPx2	0.015	26.0	1.5	54.1	0.011	5.1	0.16	0.94	0.68	11.0	0.097	99.63
Pock5A MesPx3	0.000	29.3	1.0	55.3	0.036	2.2	0.12	0.87	0.58	10.5	0.016	100.01
Pock5A Px1	0.029	19.6	2.6	52.6	0.025	14.9	0.35	1.03	0.53	7.9	0.000	99.59
Pock5A Px2	0.008	33.930	0.671	57.706	0.035	0.500	0.066	0.683	0.275	8.146	0.059	102.079

Appendix 3: NWA 10854-C1 EPMA data from UNM [in wt%]

Sample	Na ₂ O	MgO	Al ₂ O ₃	SiO ₂	CaO	TiO ₂	Cr ₂ O ₃	MnO	FeO	Total
854C1 P1DK	0.00	31.3	1.77	55.2	1.66	0.13	0.66	0.18	8.0	98.9
854C1 P2DK	0.00	31.6	2.17	55.0	1.66	0.14	0.70	0.18	7.1	98.4
854C1 P3LT	0.00	45.3	0.11	39.4	0.15	0.03	0.07	0.20	13.1	98.4
854C1 P4LT	0.00	44.4	0.06	39.2	0.21	0.00	0.07	0.21	14.6	98.7
854C1 P5VDK	0.00	37.5	0.71	57.7	0.57	0.11	0.37	0.02	2.1	99.1
854C1 P6VDK	0.01	37.5	0.69	57.8	0.60	0.09	0.35	0.03	1.8	98.9
854C1 P7LT2	0.01	43.6	0.28	45.7	0.66	0.09	0.21	0.13	8.4	99.0
854C1 P8LT2	0.00	48.7	0.02	40.5	0.19	0.02	0.04	0.13	9.1	98.7
854C1 P9DK2	0.02	35.6	0.60	57.3	0.59	0.10	0.29	0.09	4.2	98.8
854C1 P11LT2	0.00	48.7	0.01	40.3	0.19	0.00	0.06	0.14	9.1	98.5

Appendix 4: NWA 10854-C3 EPMA data from BGI [in wt%]

Sample	SiO ₂	Na ₂ O	MnO	K ₂ O	FeO	MgO	Al ₂ O ₃	Cr ₂ O ₃	CaO	NiO	TiO ₂	P ₂ O ₅	Total
P1	55.7	0.00	0.35	0.013	12.2	29.8	0.72	0.95	0.92	0.008	0.06	0.006	100.73
P2	0.1	0.00	0.44	0.000	21.0	10.2	21.74	43.47	0.02	0.000	0.59	0	97.46
P3	52.6	0.03	0.62	0.024	16.2	20.6	2.08	0.89	7.17	0.017	0.27	0.004	100.46

P4	47.6	1.85	0.00	0.067	1.1	0.6	31.35	0.03	16.71	0.003	0.07	0.014	99.40
P5	48.0	1.79	0.00	0.044	0.9	0.5	31.72	0.00	16.80	0.000	0.05	0.032	99.78
P6	38.2	0.00	0.57	0.000	25.9	36.6	0.00	0.05	0.20	0.033	0.05	0.026	101.63
P7	39.2	0.02	0.39	0.001	20.1	41.4	0.02	0.45	0.09	0.000	0.02	0	101.60
P8	38.7	0.02	0.46	0.020	21.2	40.5	0.03	0.35	0.18	0.001	0.00	0.004	101.41
P9	38.6	0.00	0.46	0.008	22.0	39.7	0.03	0.27	0.19	0.002	0.02	0	101.29
P10	39.0	0.01	0.51	0.013	20.6	41.1	0.01	0.32	0.12	0.023	0.04	0.016	101.80
P11	38.7	0.00	0.50	0.000	21.6	40.1	0.00	0.18	0.20	0.000	0.01	0	101.24
P12	56.4	0.02	0.34	0.002	11.5	30.8	0.71	0.92	0.71	0.041	0.06	0	101.51
P13	38.7	0.00	0.49	0.000	20.9	41.1	0.02	0.40	0.13	0.018	0.01	0	101.82
P14	55.8	0.01	0.34	0.012	11.1	30.7	0.90	0.90	0.65	0.107	0.05	0.024	100.52
P15	56.3	0.02	0.37	0.013	11.0	31.2	0.66	0.89	0.58	0.000	0.01	0.032	101.04
P16	54.3	0.00	0.37	0.017	12.5	28.1	1.88	1.35	1.64	0.000	0.14	0	100.29
P17	39.2	0.02	0.34	0.026	17.8	43.9	0.02	0.48	0.08	0.000	0.00	0.018	101.85
P18	39.4	0.00	0.42	0.006	18.2	43.0	0.02	0.46	0.10	0.000	0.00	0	101.65
P19	55.0	0.00	0.50	0.000	12.4	28.8	1.45	1.25	1.29	0.000	0.12	0	100.74
P20	56.4	0.01	0.33	0.000	11.1	31.3	0.66	0.85	0.57	0.000	0.03	0.002	101.25
P21	56.4	0.00	0.35	0.003	10.9	31.2	0.64	0.76	0.55	0.015	0.08	0.050	101.01
P22	54.4	0.00	0.48	0.003	12.8	28.2	2.07	1.40	1.63	0.000	0.15	0.005	101.13
P23	56.6	0.00	0.30	0.000	10.9	31.5	0.61	0.89	0.55	0.005	0.08	0.007	101.37
P24	38.5	0.00	0.48	0.008	22.2	39.6	0.05	0.17	0.16	0.018	0.04	0.010	101.20
P25	38.6	0.00	0.46	0.009	22.9	39.4	0.02	0.21	0.13	0.015	0.03	0	101.75
P26	46.7	1.49	0.06	0.086	0.9	0.4	33.19	0.01	17.57	0.020	0.06	0.003	100.42
P27	2.9	0.01	0.06	0.007	2.4	1.9	170.60	0.10	0.67	0.000	0.08	0	178.75
P28	47.6	1.71	0.07	0.018	0.9	0.5	32.11	0.01	17.03	0.032	0.07	0.020	100.08
P29	48.0	1.64	0.06	0.015	0.7	0.5	32.00	0.00	17.21	0.016	0.04	0.058	100.26
P30	56.6	0.00	0.37	0.016	10.6	31.6	0.61	0.88	0.50	0.000	0.04	0.027	101.23
P31	56.4	0.01	0.40	0.013	10.7	31.4	0.56	0.74	0.56	0.000	0.07	0	100.92

Appendix 5: NWA 10854-C5 EPMA data from BGI [in wt%]

Sample	SiO ₂	Na ₂ O	MnO	K ₂ O	FeO	MgO	Al ₂ O ₃	Cr ₂ O ₃	CaO	NiO	TiO ₂	P ₂ O ₅	Total
P1	46.19	0.073	0.11	0.011	4.39	14.08	14.32	0.17	19.75	0.06	0.90	0.035	100.08
P2	47.91	0.572	0.12	0.261	2.75	9.11	17.19	0.11	17.18	0.10	0.35	0.028	95.68
P3	61.83	5.540	0.01	0.868	0.63	0.74	24.99	0.03	1.79	0.03	0.18	0.015	96.65
P4	41.07	0.030	0.14	0.005	10.03	49.57	0.03	0.15	0.18	0.08	0.00	0.057	101.34
P5	41.39	0.015	0.16	0.000	8.40	51.38	0.01	0.47	0.10	0.01	0.00	0.000	101.94
P6	58.01	0.000	0.10	0.000	5.39	36.10	0.53	0.50	0.42	0.06	0.06	0.005	101.18
P7	50.03	0.029	0.14	0.020	3.25	17.98	7.85	1.35	18.85	0.02	0.78	0.019	100.32
P8	58.31	0.027	0.17	0.000	5.39	36.05	0.53	0.42	0.42	0.00	0.07	0.003	101.40
P9	58.27	0.046	0.14	0.000	5.38	35.94	0.54	0.43	0.39	0.02	0.07	0.000	101.23
P10	38.91	0.016	0.07	0.000	7.84	49.92	0.01	0.11	0.14	0.02	0.01	0.000	97.04
P11	40.77	0.000	0.18	0.005	9.65	48.62	0.92	0.22	1.06	0.05	0.01	0.027	101.51
P12	52.69	0.000	0.17	0.017	4.26	22.13	5.05	1.05	14.81	0.00	0.50	0.000	100.68
P13	50.94	0.000	0.26	0.008	3.94	19.85	7.19	1.23	16.68	0.00	0.78	0.013	100.89
P14	41.36	0.000	0.22	0.000	8.98	51.04	0.01	0.12	0.15	0.03	0.00	0.040	101.95
P15	41.43	0.000	0.12	0.016	8.95	50.86	0.00	0.30	0.15	0.01	0.01	0.000	101.85
P16	47.48	0.027	0.17	0.014	3.79	15.35	12.44	0.59	19.81	0.00	0.96	0.000	100.64
P17	45.31	0.024	0.06	0.002	4.02	14.26	12.29	0.50	19.21	0.07	1.17	0.029	96.94
P18	50.24	0.036	0.15	0.000	7.07	28.82	12.26	0.42	1.61	0.02	0.49	0.000	101.11
P19	49.6	0.035	0.21	0.010	7.02	28.39	13.05	0.43	1.64	0.00	0.55	0.000	100.94
P20	58.21	0.029	0.14	0.000	5.04	36.07	0.78	0.51	0.49	0.00	0.12	0.016	101.40
P21	58.54	0.000	0.14	0.000	5.50	36.16	0.63	0.52	0.38	0.05	0.12	0.037	102.08
P22	57.71	0.013	0.13	0.000	5.63	35.79	0.44	0.60	0.33	0.00	0.05	0.002	100.69
P23	51.92	0.024	0.23	0.000	4.98	21.45	5.49	1.00	14.54	0.00	0.49	0.023	100.15
P24	41.24	0.028	0.20	0.015	8.77	50.99	0.01	0.45	0.14	0.00	0.00	0.000	101.84
P25	41.33	0.005	0.13	0.008	8.49	50.78	0.01	0.55	0.14	0.00	0.00	0.010	101.46
P26	41.43	0.008	0.15	0.010	8.28	50.98	0.00	0.69	0.12	0.04	0.03	0.000	101.74
P27	43.97	0.059	0.16	0.000	3.21	13.53	17.92	0.74	19.76	0.02	0.86	0.032	100.26
P28	41.33	0.019	0.09	0.000	7.85	51.49	0.01	0.28	0.10	0.03	0.00	0.014	101.21
P29	41.32	0.013	0.14	0.003	8.53	50.83	0.01	0.59	0.13	0.02	0.00	0.000	101.59

P30 53.62 0.000 0.17 0.020 5.85 28.24 5.36 0.95 6.12 0.03 0.45 0.025 100.84

Appendix 6: NWA 11672-C1 EPMA data from BGI [in wt%]

Sample	SiO ₂	Na ₂ O	MnO	K ₂ O	FeO	MgO	Al ₂ O ₃	Cr ₂ O ₃	CaO	NiO	TiO ₂	P ₂ O ₅	Total
P8	39.43	0.021	0.30	0.023	15.49	44.89	0.02	0.06	0.20	0	0.05	0.000	100.48
P9	40.09	0.000	0.24	0.016	15.86	45.25	0.01	0.10	0.18	0.000	0.00	0.000	101.73
P10	36.27	1.160	0.03	0.107	1.64	2.57	22.14	0.09	17.10	0.000	0.03	0.050	81.19
P11	39.7	0.021	0.26	0.000	16.07	45.05	0.05	0.06	0.21	0.014	0.12	0.008	101.56
P12	39.49	0.018	0.28	0.000	15.99	44.91	0.04	0.14	0.24	0.025	0.12	0.015	101.28
P13	39.71	0.013	0.28	0.000	16.08	44.36	0.28	0.04	0.22	0.018	0.02	0.026	101.05
P14	46.22	1.430	0.02	0.000	1.10	0.56	32.69	0.00	17.54	0.014	0.05	0.000	99.62
P15	39.68	0.000	0.27	0.014	15.10	45.47	0.05	0.14	0.30	0.037	0.04	0.000	101.10
P16	39.88	0.019	0.21	0.000	15.03	45.62	0.06	0.07	0.22	0.008	0.04	0.041	101.20
P17	51.39	0.835	0.17	0.120	6.47	17.18	13.52	0.80	9.65	0.041	0.31	0.026	100.51
P18	46.62	1.530	0.04	0.000	1.14	0.36	32.71	0.03	17.46	0.000	0.02	0.000	99.90
P19	40.1	0.005	0.32	0.010	14.97	45.65	0.03	0.07	0.24	0.000	0.02	0.000	101.41
P20	46.93	1.690	0.07	0.023	1.07	0.33	33.27	0.01	16.99	0.000	0.02	0.017	100.42
P21	40.1	0.000	0.22	0.020	14.89	45.96	0.04	0.07	0.24	0.000	0.02	0.000	101.55
P22	47.12	1.710	0.00	0.021	1.05	0.42	32.60	0.00	17.30	0.007	0.04	0.000	100.26
P23	46.43	1.420	0.03	0.000	1.03	0.29	33.11	0.03	17.87	0.013	0.03	0.000	100.24
P24	53.84	0.002	0.28	0.014	9.85	27.70	2.89	1.01	4.40	0.000	0.43	0.028	100.44
P25	39.99	0.032	0.26	0.005	14.81	46.01	0.02	0.03	0.24	0.000	0.02	0.028	101.45
P26	39.91	0.004	0.27	0.000	14.82	45.93	0.03	0.10	0.21	0.037	0.04	0.000	101.35
P27	39.97	0.000	0.34	0.000	15.19	45.78	0.03	0.07	0.21	0.022	0.01	0.000	101.63
P28	40.29	0.012	0.25	0.016	13.81	46.47	0.07	0.15	0.26	0.039	0.08	0.023	101.47
P29	47.38	1.550	0.01	0.001	0.86	0.54	33.74	0.07	17.28	0.014	0.05	0.049	101.55
P30	46.28	1.370	0.01	0.003	0.96	0.42	33.98	0.06	17.64	0.025	0.04	0.000	100.79
P32	46.24	1.440	0.01	0.046	1.08	0.61	31.51	0.02	17.39	0.001	0.03	0.001	98.37
P33	54	0.089	0.31	0.027	10.35	26.97	2.38	0.94	4.26	0.010	1.27	0.005	100.62
P34	48.61	0.000	0.16	0.007	5.94	17.36	4.53	1.56	17.64	0.000	3.71	0.000	99.52

P35	50.97	0.048	0.26	0.013	9.31	21.78	2.77	0.79	10.13	0.000	0.61	0.017	96.70
P36	42.45	0.900	0.11	0.033	7.60	20.12	18.69	0.22	8.78	0.029	0.04	0.028	99.00
P37	39.42	0.121	0.22	0.058	15.34	43.06	0.41	0.70	0.31	0.006	0.05	0.011	99.71
P38	39.55	0.000	0.23	0.002	16.41	44.79	0.03	0.09	0.21	0.009	0.09	0.000	101.41

Appendix 7: Pap-I1 EPMA Data from UWO [in wt%]: Olivine

Sample	SiO ₂	Al ₂ O ₃	Na ₂ O	MgO	FeO	MnO	NiO	Cr ₂ O ₃	TiO ₂	CaO	K ₂ O	Total
Ol_d_01	40.3	nd	0.002	44.86	14.23	0.28	0.02	0.24	0.009	0.06	0.003	99.99
Ol_d_02	40.6	0.019	0.004	45.80	12.86	0.29	0.05	0.17	0.009	0.07	nd	99.82
Ol_d_03	40.6	nd	0.038	45.89	13.26	0.33	0.03	0.35	0.005	0.06	0.002	100.52
Ol_d_04	40.6	nd	0.021	46.52	12.21	0.28	0.01	0.29	nd	0.07	nd	100.00
Ol_d_05	40.4	0.017	0.012	44.56	14.44	0.37	0.02	0.10	0.006	0.07	nd	99.97
Ol_d_06	42.0	0.028	0.005	52.62	5.65	0.07	0.05	0.11	0.010	0.15	nd	100.73
Ol_d_07	40.2	0.010	0.015	44.13	15.35	0.31	nd	0.23	nd	0.07	nd	100.31
Ol_d_08	40.1	0.010	0.006	44.73	14.14	0.28	0.07	0.23	0.017	0.07	nd	99.69
Ol_d_09	40.5	0.005	nd	45.77	13.06	0.25	0.05	0.23	0.011	0.06	0.001	99.95
Ol_d_10	60.5	0.158	nd	38.17	1.82	0.08	0.03	0.47	0.036	0.17	0.005	101.40
Ol_b_01	37.6	0.086	0.019	35.13	24.86	0.48	0.10	0.11	0.010	0.17	0.019	98.62
Ol_b_02	37.8	0.019	0.014	33.35	27.57	0.64	0.05	0.06	0.015	0.14	0.004	99.64
Ol_b_03	37.8	nd	nd	33.71	26.79	0.59	0.00	0.08	0.003	0.18	0.002	99.11
Ol_b_04	38.3	0.004	0.007	36.51	23.56	0.49	nd	0.12	0.009	0.17	nd	99.13
Ol_b_05	37.5	nd	0.003	33.62	27.43	0.58	0.04	0.06	nd	0.15	0.003	99.39
Ol_b_06	38.0	0.070	0.004	36.07	24.41	0.54	0.05	0.18	0.012	0.28	nd	99.64
Ol_b_07	36.5	0.025	nd	29.13	32.75	0.57	0.07	0.07	0.031	0.21	0.012	99.38
Ol_b_08	37.3	0.025	0.010	32.19	28.88	0.66	0.02	0.08	0.020	0.18	0.004	99.37
Ol_b_09	37.5	0.001	0.023	33.61	27.28	0.63	0.02	0.09	0.000	0.10	0	99.30
Ol_b_10	37.5	0.012	0.007	34.38	27.07	0.59	0.04	0.10	0.012	0.05	nd	99.79

Appendix 8: Pap-I1 EPMA Data from UWO [in wt%]: Pyroxene (relict chondrule)

Sample	SiO ₂	Al ₂ O ₃	Na ₂ O	MgO	FeO	MnO	NiO	Cr ₂ O ₃	TiO ₂	CaO	K ₂ O	Total
Px_01	56.21	0.11	0.040	27.30	15.05	0.56	0.01	0.86	0.025	0.59	0.001	100.76
Px_02	56.61	0.14	0.042	28.74	13.64	0.51	nd	0.67	0.031	0.54	0.004	100.94
Px_03	57.05	0.12	0.023	29.32	12.54	0.39	nd	0.60	0.013	0.47	nd	100.51
Px_04	53.24	0.85	0.328	18.37	16.16	0.63	0.01	1.66	0.129	8.35	0.002	99.73
Px_05	55.32	0.14	0.069	25.77	16.13	0.61	nd	0.83	0.029	1.08	0.001	99.98
Px_06	56.17	0.12	0.036	27.99	14.02	0.47	0.02	0.72	0.021	0.72	0.003	100.29
Px_07	55.33	0.23	0.053	26.00	15.28	0.55	0.02	0.85	0.042	1.16	nd	99.52
Px_08	56.32	0.14	0.036	28.08	13.99	0.48	0.02	0.71	0.037	0.63	nd	100.43
Px_09	55.09	0.24	0.068	25.56	15.98	0.57	0.02	0.93	0.036	1.29	nd	99.79
Px_10	56.27	0.16	0.028	29.17	12.10	0.41	0.01	0.63	0.025	0.49	nd	99.30

Appendix 9: Pap-I1 EPMA Data from UWO [in wt%]: Glassy mesostatis

Sample	SiO ₂	Al ₂ O ₃	Na ₂ O	MgO	FeO	MnO	TiO ₂	CaO	K ₂ O	Total
Glass_01	63.13	13.53	8.68	2.05	7.30	0.05	0.35	1.22	0.11	96.41
Glass_02	62.74	14.41	8.99	3.09	5.95	0.07	0.39	2.39	0.11	98.14
Glass_03	58.91	13.66	7.83	5.08	9.00	0.21	0.26	4.08	0.11	99.13
Glass_04	61.61	12.88	7.63	3.83	7.68	0.14	0.48	4.52	0.09	98.84
Glass_05	64.34	14.94	9.78	3.22	5.95	0.10	0.46	0.52	0.09	99.39
Glass_06	66.53	17.89	5.73	0.45	1.49	0.03	0.43	0.44	3.40	96.38
Glass_07	57.20	5.39	2.86	15.85	12.83	0.49	0.26	5.41	0.07	100.36
Glass_08	66.46	16.80	10.21	0.63	4.37	0.08	0.46	0.69	0.24	99.94
Glass_09	64.93	18.62	10.44	0.58	3.59	0.01	0.11	0.57	0.19	99.05
Glass_10	65.98	17.19	9.82	1.84	3.49	0.11	0.46	1.88	0.27	101.03

Curriculum Vitae

Name: Philip Michael Reger

Post-secondary Education and Degrees: University of Western Ontario
London, Ontario, Canada
2017 – present, Ph.D. candidate in Geology and Planetary Science

Eidgenössische Technische Hochschule Zürich
Zürich, Switzerland
2014-2016, MSc ETH in Earth Sciences with specialization in Mineralogy and Geochemistry

Eidgenössische Technische Hochschule Zürich
Zürich, Switzerland
2010-2014, BSc ETH in Earth Sciences, Focus Geology

Honours and Awards: Province of Ontario Graduate Scholarship
2020-2021

Related Work Experience

Teaching Assistant
The University of Western Ontario
2017-2020

Teaching Assistant
Eidgenössische Technische Hochschule Zürich
2013-2015

Publications: Hunt, A. C., Cook, D. L., Lichtenberg, T., **Reger, P. M.**, Ek, M., Golabek, G. J., & Schönbächler, M. (2018). Late metal–silicate separation on the IAB parent asteroid: Constraints from combined W and Pt isotopes and thermal modelling. *Earth and Planetary Science Letters*, 482, 490-500.